UNIVERSITATEA DIN
BUCUREȘTI
VIRTUTE ET SAPIENTIA

UNIVERSITY OF BUCHAREST
Faculty of Physics
Doctoral School of Physics

European Organization for Nuclear Research

Alexandra-Gabriela ŞERBAN

Low-energy interactions of protons in FLUKA for radiation damage studies and α-particle scattering on $N = Z$ nuclei

Doctoral thesis

Scientific advisors:
Dr. Neculai Săndulescu
Dr. Francesc Salvat-Pujol

Bucharest, 2025

Rezumat

FLUKA este un cod Monte Carlo pentru simularea transportului radiaţiilor prin materie, fiind utilizat, printre alte aplicaţii, pentru evaluarea producerii evenimentelor de tip *single-event upset* (SEU) în dispozitive electronice expuse radiaţiilor. Studii recente privind producerea evenimentelor de tip SEU în memorii statice cu acces aleator (SRAMs) comerciale iradiate cu protoni au dezvăluit un acord foarte bun între valorile experimentale şi estimările FLUKA pentru secţiunea eficace de producere a evenimentelor de tip SEU la energii ale protonilor mai mari de 20-30 MeV. Cu toate acestea, pentru energii mai joase ale protonilor, unde secţiunea eficace creşte drastic în componente cu sarcină critică redusă, FLUKA subestima valorile experimentale cu până la două ordine de mărime. Analize preliminare au indicat că această subestimare era cauzată în mare parte de lipsa modelării împrăştierii elastice nucleare a protonilor sub 10 MeV în versiunile FLUKA până la v4-3.4.

Pentru a depăşi această limitare, împrăştierea elastică Coulomb şi nucleară a protonilor pe nuclee a fost revizuită. S-au utilizat atât metoda undelor distorsionate bazată pe modele de potenţial optic dependente de spin, cât şi distribuţii unghiulare experimentale. Astfel, a fost generată o bază de date numerică a secţiunilor eficace diferenţiale pentru împrăştierea elastică a protonilor cu energii între bariera Coulomb şi 250 MeV pe nuclee ţintă cu numere de masă de până la $A = 252$. Pentru a minimiza cerinţele de memorie, o expresie parametrizată bazată pe limita discului negru (*black-disk limit*) a fost fitată bazei de date numerice, reducând-o la un număr mic de coeficienţi dependenţi de energia protonilor incidenţi şi de numărul de masă al nucleului ţintă. De asemenea, această expresie parametrizată păstrează cele mai relevante caracteristici ale secţiunii eficace diferenţiale şi oferă totodată un mijloc sistematic de separare a împrăştierilor elastice Coulomb şi nucleare. Noul model dezvoltat pentru împrăştierea elastică nucleară a protonilor cu energii de la bariera Coulomb la 250 MeV a fost inclus în FLUKA v4-4.0, înlocuind modelul anterior disponibil doar pentru protoni cu energii peste 10 MeV. Acesta îmbunătăţeşte cu un ordin de mărime acordul dintre estimările FLUKA şi secţiunile eficace experimentale pentru producerea evenimentelor de tip SEU în SRAM-uri iradiate cu protoni în intervalul energetic 1–10 MeV. De asemenea, noul model oferă o descriere mai precisă a coliziunilor elastice nucleare la unghiuri mari de împrăştiere pentru energii ale protonilor până la 250 MeV comparativ cu modelul anterior. O altă limitare privind estimarea secţiunii eficace de producere a evenimentelor de tip SEU în SRAM-uri comerciale iradiate cu protoni era considerarea inadecvată a reculurilor din împrăştierea elastică Coulomb. Pentru a include contribuţia eveniment-cu-eveniment a acestora la producerea evenimentelor de tip SEU, generarea şi transportul lor explicit au fost implementate pentru protoni (ca particule incidente) într-o versiune internă a FLUKA.

Cu aceste două modele dezvoltate şi implementate în FLUKA, producerea evenimentelor de tip SEU indusă de protoni a fost investigată în trei SRAM-uri comerciale fabricate pe diferite noduri tehnologice CMOS (*complementary metal-oxide-semiconductor*), variind între 250 nm şi 40 nm. Geometria dispozitivelor a fost descrisă printr-un model paralelipipedic dreptunghiular (RPP), având drept parametri volumul sensibil şi sarcina critică. Parametrii optimi care maximizează acordul dintre secţiunile eficace simulate şi cele experimentale au fost identificaţi pentru cele trei SRAM-uri studiate. Dependenţa parametrilor modelului RPP de nodul tehnologic a fost identificată şi validată prin studii

independente din literatură ale altor componente electronice. Aceasta oferă estimări inițiale ale volumului sensibil și sarcinii critice pentru modelarea componentelor electronice fabricate pe alte noduri tehnologice.

Împrăștierea elastică nucleară joacă un rol semnificativ și în dozimetria cu protoni, o aplicație pentru care noul model inclus în FLUKA v4-4.0, dedicat acestui mecanism de interacție al protonilor, a fost validat explicit. În acest scop, a fost utilizat un set recent de date experimentale, constând în doze absorbite într-o fantomă de apă iradiată cu protoni la energii de 100 MeV, 160 MeV și 225 MeV; dozele experimentale au fost publicate în referința originală ca funcție de adâncimea în fantoma de apă, pentru diferite distanțe radiale față de fasciculul de protoni incident. Două versiuni FLUKA au fost utilizate pentru simularea dozelor experimentale: v4-3.4, bazată pe un model anterior al împrăștierii elastice nucleare a protonilor, și v4-4.0, bazată pe modelul dezvoltat în această teză. Acordul îmbunătățit obținut cu FLUKA v4-4.0 față de dozele experimentale absorbite este discutat, iar rolul jucat de împrăștierea elastică nucleară a protonilor, printre alte mecanisme de interacție, este elucidat. Mai mult decât atât, acest test comparativ a evidențiat importanța caracterizării cât mai precise a parametrilor fasciculului de protoni incident și a geometriei adoptate pentru simulări Monte Carlo.

În final, având în vedere interesul crescut față de fasciculele de heliu pentru aplicații în hadronoterapie sau în producerea evenimentelor de tip SEU, a fost investigată împrăștierea elastică a particulelor alfa (pentru care împrăștierea elastică nucleară lipsește momentan în FLUKA). Distribuția unghiulară a particulelor alfa împrăștiate elastic pe nuclee ușoare cu $N = Z$ prezintă o creștere semnificativă la unghiuri de împrăștiere mari, cunoscută sub denumirea de efect de împrăștiere anormală (ALAS). Pentru a investiga ipoteza conform căreia efectul ALAS se datorează corelațiilor din interiorul nucleului țintă, în această teză s-a adoptat un potențial de tip *folding* simplu. Acesta rezultă în urma unei integrări de convoluție simple dintre un potențial alfa-nucleon și densitatea nucleului țintă, derivată din modele de câmp mediu microscopice și incorporând explicit corelații nucleare. Rolul jucat de corelațiile de 2-corpuri (*pairing*) și de 4-corpuri (*quartetting*) a fost, astfel, explorat. Această metodă simplă de calcul s-a dovedit eficientă în a oferi o descriere corespunzătoare a secțiunii eficace diferențiale.

Abstract

FLUKA is a general-purpose code for the Monte Carlo simulation of radiation transport used, among other applications, for the assessment of single-event upset (SEU) production in electronic devices exposed to radiation. Recent studies of SEU production in commercial static random access memories (SRAMs) under proton irradiation revealed very good agreement between experimental measurements and FLUKA estimates of the SEU production cross section for proton energies above 20-30 MeV. However, at lower proton energies, where the cross section for SEU production in low-critical-charge components increases drastically, a FLUKA underestimation of up to two orders of magnitude was observed. Preliminary analyses indicated that this underestimation was in great measure due to the lack of nuclear elastic scattering of protons below 10 MeV in FLUKA up to version v4-3.4.

To overcome this limitation, the Coulomb and nuclear elastic scattering of protons on nuclei has been revisited, combining partial-wave analyses, which rely on spin-dependent optical potential models for protons of up to 250 MeV in the vicinity of nuclei, and experimental angular distributions. A numerical database of differential cross sections for the elastic scattering of protons with energies from Coulomb barrier up to 250 MeV on target nuclei with mass numbers up to $A = 252$ has been evaluated. To minimize memory requirements, an effective parametrized expression based on the black-disk limit has been fitted to the numerical database, reducing it to a handful of energy- and A-dependent coefficients, while still capturing the most relevant features in the differential cross section and providing a systematic means of disentangling Coulomb and nuclear elastic scattering. This model supersedes the legacy model for proton nuclear elastic scattering employed up to FLUKA v4-3.4 (available only above 10 MeV). The newly developed model, covering the nuclear elastic scattering of protons from Coulomb barrier up to 250 MeV, has been included in FLUKA v4-4.0 and it leads to an order-of-magnitude improvement in the agreement between FLUKA and experimental cross sections for the production of SEUs in SRAMs under proton irradiation in the 1–10 MeV energy domain. Furthermore, it also gives an overall better description of large-angle nuclear elastic collisions of protons up to 250 MeV compared to the effective legacy model in use up to FLUKA v4-3.4. A further limitation for estimating the SEU production cross section in commercial SRAMs under proton irradiation with FLUKA was the improper account of recoils from Coulomb single scattering. Thus, to account for the event-by-event contribution of Coulomb recoils to SEU production, in this work their explicit production and transport have been implemented for proton projectiles in a development version of the code.

In view of these two new model developments, SEU production induced by protons has been investigated with FLUKA in three commercial bulk planar SRAMs manufactured on different complementary metal-oxide-semiconductor (CMOS) technology nodes, from 250 nm to 40 nm. A rectangular parallelepiped (RPP) model has been adopted to describe the device geometry, relying on the sensitive volume and the critical charge as effective parameters. Optimal parameters, which maximize the agreement between simulated and experimental SEU production cross sections, have been found for the three considered devices. RPP-model parameter trends have been therefore identified across technology nodes. These have been further validated by RPP-model parameters from independent

literature studies of other devices, thus providing practical guidelines when modelling components manufactured on other technology nodes.

The new model for the nuclear elastic scattering of protons below 250 MeV included in FLUKA v4-4.0 necessitated an explicit validation also for proton dosimetry applications, where this interaction mechanism plays a significant role. A benchmark has been carried out against a recent experimental dataset consisting of radial-depth maps of absorbed dose in a water phantom under irradiation by protons of 100 MeV, 160 MeV, and 225 MeV. Two FLUKA versions have been employed to simulate these experimental radial-depth dose maps: v4-3.4, relying on a legacy model for proton nuclear elastic scattering, and v4-4.0, relying on the model developed in this work. The enhanced agreement with experimental absorbed doses obtained with FLUKA v4-4.0 is discussed, and the role played by proton nuclear elastic scattering, among other interaction mechanisms, in various regions of the radial-depth dose maps is elucidated. Furthermore, this benchmark is sensitive enough to showcase the importance of characterizing as accurately as possible the beam parameters and the scattering geometry for Monte Carlo simulations.

Finally, in view of a rising interest in ^{4}He beams for, *e.g.*, hadron therapy and SEU production, the elastic scattering of α particles (for which nuclear elastic scattering is currently missing in FLUKA) has been addressed. Specifically, the angular distribution of α particles elastically scattered off light $N = Z$ nuclei exhibits significant enhancement at large scattering angles, *i.e.*, the anomalous large-angle scattering (ALAS) effect. To investigate whether ALAS arises from correlations inside the target nucleus, a single-folding interaction potential has been adopted, relying on a simple α-nucleon potential folded with the target nuclear density derived from microscopic mean field models and explicitly accounting for nuclear correlations. The role played by pairing and quartetting correlations has therefore been explored and an accurate description of the differential cross section has been provided based on this straightforward yet effective prescription.

Acknowledgements

I would like to extend my deepest gratitude to my supervisors, Dr. Nicolae Sandulescu and Dr. Francesc Salvat-Pujol. The encouragement I received from Dr. Sandulescu has supported me to pursue a research topic that truly suited my interests. Moreover, his belief in my abilities has provided me with the freedom to explore innovative ideas, while ensuring I remained grounded in rigorous academic standards. Equally, the profound insights and intellectual rigor of Dr. Salvat-Pujol have not only inspired me, but also broadened my academic and professional horizons, encouraging me to think critically and approach challenges with a fresh perspective and determination. Their dedicated time, patient mentorship, and thoughtful feedback have been invaluable throughout the elaboration of this dissertation and have contributed immensely to my growth as a researcher.

I am profoundly grateful to CERN for the opportunity to be a doctoral student within the SY-STI-BMI section. Being part of the development team for the general-purpose Monte Carlo code FLUKA has been a unique scientific journey from which I have gained invaluable knowledge and experience. My gratitude extends also to the Theoretical Physics Department of the "Horia Hulubei" National Institute of Physics and Nuclear Engineering for welcoming me as a Research Scientific Assistant since my master programme.

I would like to further express my gratitude to my colleagues at CERN, the university, and the institute for their invaluable discussions, collaboration, and unwavering support.

Lastly, but certainly not least, I am deeply thankful to my family and friends for their unconditional support throughout my time at CERN. Their encouragement, patience, and belief in me have been a constant source of strength, motivating me to persevere and achieve this significant milestone.

Contents

List of Abbreviations

Abbreviation	Definition
ALAS	Anomalous large-angle scattering
BCS	Bardeen-Cooper-Schrieffer
BEOL	Back-end of line
CB	Coulomb barrier
CM	Center of mass
CMOS	Complementary metal-oxide-semiconductor
CPU	Central processing unit
DW	Distorted wave
DXS	Differential cross section
FLUKA	Fluktuierende Kaskade
G4SEE	Geant4-based Single Event Effect
Geant4	Geometry and tracking
HF	Hartree-Fock
ISSI	Integrated Silicon Solution Inc.
LET	Linear energy transfer
MB	Megabyte
MC	Monte Carlo
MCS	Multiple Coulomb scattering
NN	nucleon-nucleon
OPM	Optical potential model
QCM	Quartet condensation model
R2E	Radiation to electronics
RHB	Relativistic-Hartree-Bogoliubov
RMF	Relativistic mean field
RPP	Rectangular parallelepiped
SEE	Single-event effect
SEU	Single-event upset
SRAM	Static random access memory
SV	Sensitive volume
WS	Wood-Saxon
nn	neutron-neutron
ph	particle-hole
pn	proton-neutron
pp	proton-proton

Chapter 1

Introduction

Electronic devices used in space missions, avionics, and particle accelerator facilities may be damaged as a result of exposure to radiation fields [1–3]. These devices are particularly sensitive to single-event effects (SEEs), which are difficult to predict and mitigate [4, Sec. 1.2], and pose considerable operational risks, ranging from data corruption to system failures [5–7]. To assess these risks, the radiation environment relevant to SEE production is typically characterized relying on the fluence of hadrons with energies higher than 20 MeV [8]. This approximation is tantamount to assuming that the production of SEEs is governed by the energy deposition of fragments and residual nuclei from nuclear reactions of high-energy hadrons, thereby neglecting contributions from direct ionization by hadrons, as well as from their elastic scattering on target atoms. However, recent studies showed that the production of SEEs, and particularly of single-event upsets (SEUs), induced by protons below 20 MeV, where the SEU production cross section typically rises drastically, is indeed dominated by direct ionization [9–11] and elastic scattering [11–15].

The role played by these interaction mechanisms, and others, in SEU production can be assessed by means of Monte Carlo (MC) simulation tools, such as the general-purpose MC code FLUKA [19–21]. FLUKA simulates the coupled hadronic and electromagnetic showers set up in complex material geometries by more than 60 particle species, with energies from keV to PeV; neutrons are exceptionally tracked down to thermal energies (0.01 meV). Furthermore, it features among the simulation tools employed by the Radiation to Electronics (R2E) team at CERN [4, 22, 23], which ensures the successful operation of the accelerator infrastructure taking into account the effects of radiation exposure on electronic components and systems. In a recent R2E study [12, 13], the production of SEUs in a commercial SRAM [16] under proton irradiation was assessed with FLUKA. Figure 1.1 displays the cross section for SEU production, σ_{SEU}, in this device as a function of the proton energy. Dots display the experimental measurements, for which the uncertainty is smaller than the symbol size, while the crosses (connected with a solid line to guide the eye) represent the FLUKA v4-3.4 estimation. For proton energies above 20-30 MeV, where SEU production is driven by nuclear reactions [11], and where the aforementioned high-energy hadron approximation holds, remarkable agreement was obtained. However, in the 1–10 MeV range, where σ_{SEU} increases by five orders of magnitude towards lower energies, FLUKA exhibits an underestimation of up to two orders of magnitude. This energy range is particularly relevant for space applications in view of the considerable flux attained by the vastly dominating contribution of protons in the galactic cosmic ray flux (transported through an aluminum shielding), as illustrated in Fig. 1.2. Preliminary R2E analyses suggested that in the 1–10 MeV range, proton nuclear elastic scattering significantly contributes to SEU production in the ISSI SRAM [12]. However, this interaction mechanism was not available for protons below 10 MeV as of FLUKA v4-3.4. Furthermore, above 10 MeV, a too simplistic account of large-scattering-angle deflections was provided, often over- or under-estimating their importance. These deflections, however,

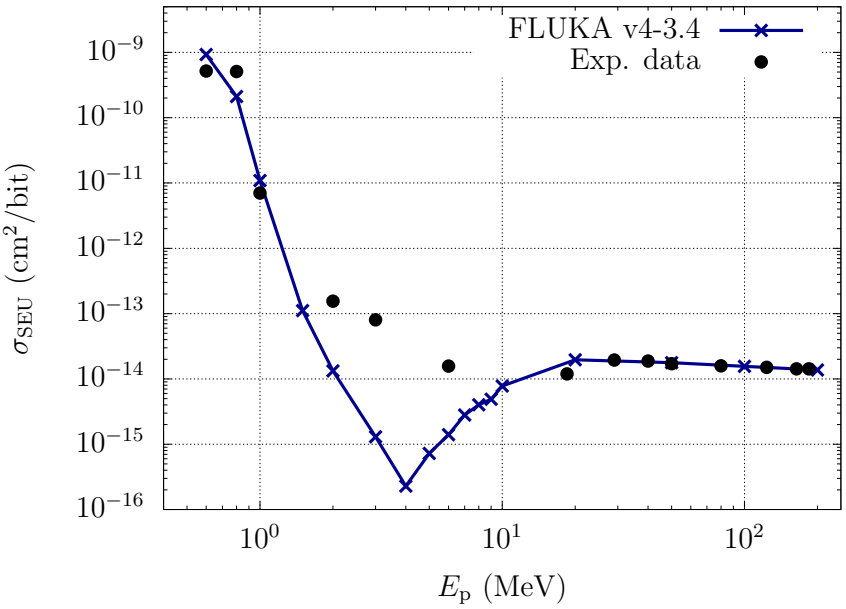

Figure 1.1: Comparison between experimental SEU production cross section (dots; uncertainties are smaller than the symbol size) [12, 13] and FLUKA v4-3.4 predictions (crosses with solid line to guide the eye) induced by low-energy protons in the ISSI (Integrated Silicon Solution Inc.) SRAM [16].

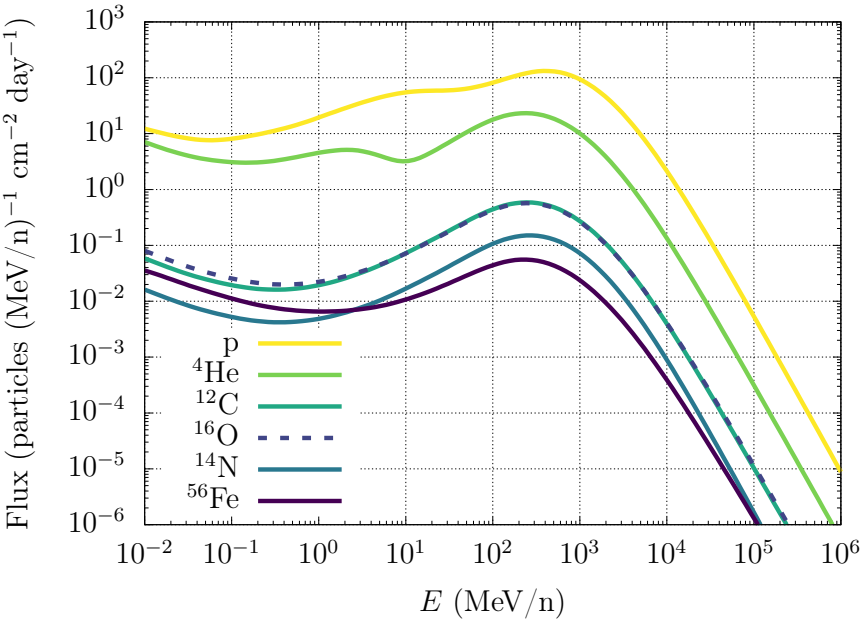

Figure 1.2: Galactic cosmic rays fluxes (based on the Badhwar-O'Neill 2020 model [17]) as a function of the energy per nucleon for the circular Earth orbit environment at an altitude of 35786 km and an inclination of 0 deg with respect to the equator. The fluxes have been transported through an aluminium shielding of 0.254 cm using OLTARIS [18].

contribute significantly to the production of SEUs, even at energies of $\mathcal{O}(100)$ MeV [12].

To overcome the aforementioned limitations, a new model for the nuclear elastic scattering of protons from Coulomb barrier up to 250 MeV, constituting the core of this thesis, has been developed. It combines partial-wave analyses and experimental angular distributions into a database of differential cross sections (DXSs) which prescribe the angular distribution of a proton of a given kinetic energy elastically scattered from a specified nucleus. To minimize memory requirements, an effective parametrized expression has been fitted onto the calculated DXS database. This newly developed model has been included in FLUKA v4-4.0, publicly released on February 14, 2024.

A further limitation identified in Refs. [12, 13] for the simulation of SEU production in the ISSI SRAM under proton irradiation with FLUKA concerned its improper closing of the kinematics in Coulomb single scattering mechanism. In the course of a Coulomb single scattering event, the direction of the charged projectile is updated, while its energy is not. This approximation, while reasonable at high energies, becomes questionable towards low energies. To quantify the event-by-event contribution of Coulomb recoils to SEU production, a proper closing of the kinematics, where the elastic recoil is explicitly generated and transported (if above transport threshold), has been implemented for proton projectiles in a development version of the code.

In the aforementioned SEU production study, the FLUKA simulation geometry describing the sensitive region of an SRAM is based on the rectangular parallelepiped (RPP) model [9, 12, 24]. This approach relies on two parameters: the sensitive volume, in which energy deposition is collected, and the critical energy deposition (or displaced critical charge) that needs to be exceeded to trigger an SEU. These parameters are generally inferred from experimental SEU production cross sections induced by protons, as well as heavy ions [9, 13, 25, 26]. The wealth of necessary SEU production cross sections hinders the application of such prescriptions to novel devices which have not yet been irradiated. Instead, in this work, RPP-model parameter trends have been sought for modelling SEU production in various commercial bulk planar SRAMs manufactured on different complementary metal-oxide-semiconductor (CMOS) technology nodes. These provide a simple prescription to set initial RPP-model simulation parameters, without relying on *a priori* available experimental SEU cross sections, and therefore facilitate SEU production simulations for devices which have not yet undergone irradiation.

Proton nuclear elastic scattering plays a significant role, not only in the production of SEUs in electronic components [11, 14, 27], but also in dosimetry applications [28]. It contributes to the angular spread of proton showers as they pass through matter, directly influencing depth-dose distributions, particularly out-of-field, and thus the dose delivered to nearby healthy tissue in proton therapy applications. The inclusion in FLUKA v4-4.0 of the new model for proton nuclear elastic scattering developed in this thesis [27] required an assessment of the code performance for proton dosimetry applications prior to public release. A dedicated benchmark has been carried out consisting of FLUKA simulations of a recently published experimental dataset of radial-depth dose maps in a water phantom under proton irradiation [29]. A comparison between simulated and experimental absorbed dose has been performed with two FLUKA versions: v4-3.4, relying on a legacy model for proton nuclear elastic scattering [30], and v4-4.0, relying on the model presented in this thesis. With the latter, better agreement has been obtained between simulated and experimental absorbed doses. These detailed radial-depth dose maps allow one to elucidate the physical origin of the improvements obtained with FLUKA v4-4.0 and the role played by proton nuclear elastic scattering, among other interaction mechanisms, in

various regions of these maps. Furthermore, this benchmark is sensitive enough to allow one to highlight the importance of accurately characterizing the beam parameters and the scattering geometry for MC simulation purposes.

Finally, given a growing interest in ^{4}He beams for applications in both hadron therapy [31] and SEU production [32], α-scattering processes with large-angle deflections (leading to large energy transfers from the α particle to the material), such as nuclear elastic scattering, may become particularly relevant. However, the nuclear elastic scattering of α particles is currently missing in FLUKA. The approach adopted in this work for the nuclear elastic scattering of protons based on a global optical potential model (OPM) is more challenging for α particles: global OPMs [33] have difficulties in capturing the angular distribution of α particles on $N = Z$ nuclei at large scattering angles. In this particular angular domain, there is a strong enhancement of the DXS, known as the anomalous large-angle scattering (ALAS) [34]. Several studies [35, 36] suggested that ALAS may be due to α-like correlations present in $N = Z$ nuclei. This premise has been investigated as a preliminary endeavor before a more systematic modelling. The DXS for the elastic scattering of α particles on $N = Z$ nuclei has been evaluated in this work using a partial-wave approach based on a single-folding potential. The latter depends on a simple α-nucleon interaction potential and the target nucleon density, evaluated within microscopic mean field theories and explicitly incorporating nuclear correlations. Thus, this approach allows one to investigate the role played by α-cluster correlations inside the target nucleus by means of the target nucleon density. Furthermore, opposed to global OPMs, this straightforward prescription provides an accurate description of the DXS of α particles elastically scattered off $N = Z$ nuclei in the full angular domain.

This thesis is structured as follows. In Chapter 2 the nuclear elastic scattering of protons relying on the legacy model employed up to FLUKA v4-3.4 is outlined and the development and implementation in FLUKA v4-4.0 of a new model for the nuclear elastic scattering of protons below 250 MeV is presented in detail. In Chapter 3, the interplay between Coulomb and nuclear elastic scattering is assessed, especially around Coulomb barrier, and an explicit account of recoils from Coulomb single scattering is discussed. Next, in Chapters 4 and 5, the new model for the nuclear elastic scattering of protons is benchmarked in two applications: the production of SEUs in commercial SRAMs under proton irradiation and the out-of-field dose deposition by proton beams in water phantoms. In Chapter 6 the elastic scattering of α particles on $N = Z$ nuclei, relying on the single-folding potential, is discussed. Finally, Chapter 7 concludes the thesis by summarizing its contributions, while auxiliary derivations are included in the Appendix.

Chapter 2

Nuclear elastic scattering of protons in FLUKA

Proton nuclear elastic scattering is the process in which an incoming proton is scattered off the nuclear potential of a target nucleus (which remains in the ground state), thereby exchanging energy and momentum, as schematically depicted in Fig. 2.1. This interaction mechanism opens at proton energies above Coulomb barrier (CB). While the elastic scattering of protons on the electrostatic potential leads to a strongly forward-peaked differential cross section (DXS), which decreases sharply with increasing center-of-mass (CM) scattering angle as $\sim 1/\sin^4(\theta/2)$ [see Chapter 3], nuclear elastic scattering dominates the large scattering angles, *i.e.*, small impact parameters, and is qualitatively distinguishable from the former.

To illustrate this behaviour in a simplified way, one may consider the elastic scattering of a proton on a point-like nucleus, as depicted in Fig. 2.2, which shows the Rutherford DXS (dashed curve) for 25 MeV protons elastically scattered off ^{28}Si (as a point-like object). However, the nuclear charge distribution is not point-like, but rather extended: the DXS of a proton elastically scattered on such an extended charge distribution, *e.g.*, a homogeneously charged sphere (solid teal curve in Fig. 2.2) is lower than the Rutherford DXS at large scattering angles (small impact parameters) since the electrostatic potential inside the nucleus is finite. Finally, when the contribution of the short-range nuclear potential (modelled by, *e.g.*, a Woods-Saxon potential) is considered in addition to the electrostatic interaction, the corresponding DXS (solid green curve in Fig. 2.2) is enhanced. This allows one to qualitatively distinguish between the scattering of protons on the electrostatic potential of the nucleus, dominating small scattering angles, and their nuclear elastic scattering, governing the large scattering angles, which correspond to large energy transfers, and are therefore relevant for single-event upset (SEU) production.

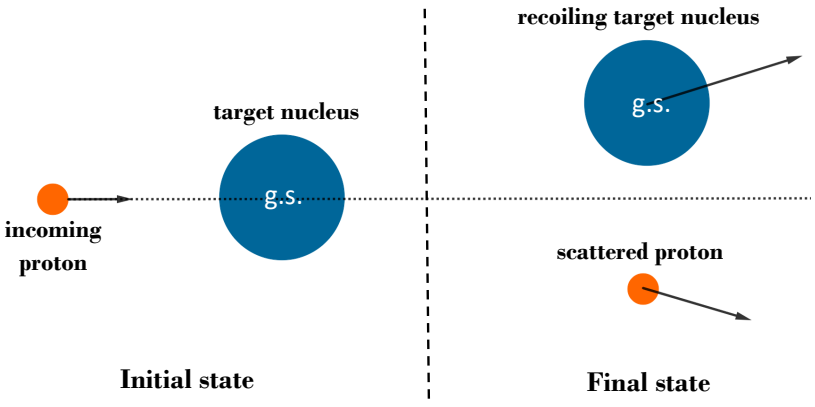

Figure 2.1: Schematic of the elastic scattering of a proton on a nucleus.

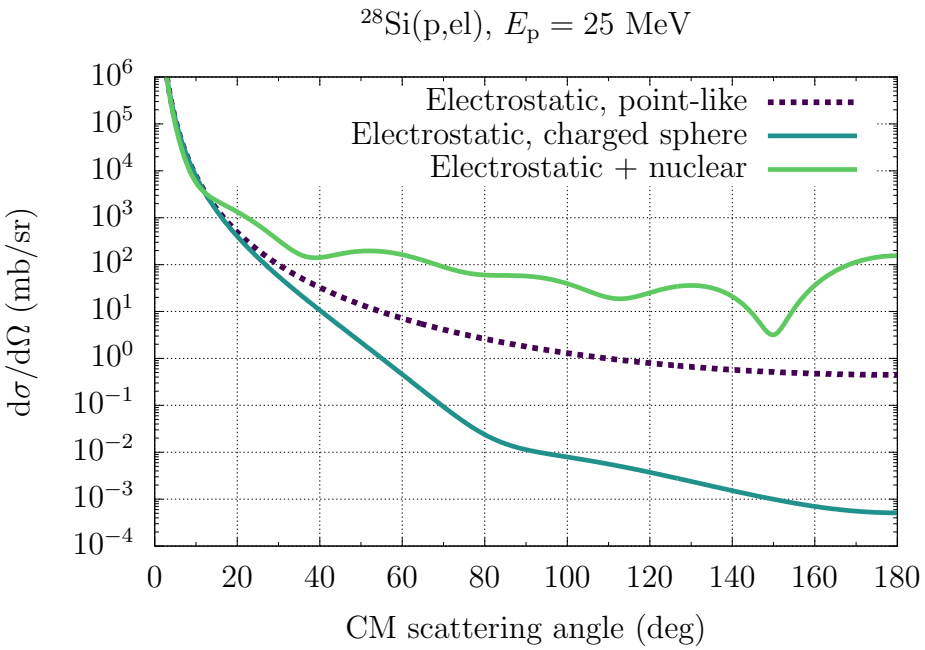

Figure 2.2: Comparison of the elastic scattering of 25 MeV protons on ^{28}Si due to three different potentials: the electrostatic potential of a point-like nucleus (dashed), the electrostatic potential of a homogeneously charged sphere (solid teal), and a combined electrostatic and nuclear potential (solid green).

Up to FLUKA v4-3.4, the DXS for the nuclear elastic scattering of protons above 10 MeV was modelled as [30]:

$$\frac{\mathrm{d}\sigma(\theta)}{\mathrm{d}\hat{\Omega}} \approx \begin{cases} A^{1.63}e^{14.5A^{0.66}t} + 1.4A^{0.33}e^{10t}, & \text{if } A < 62 \\ A^{1.33}e^{60A^{0.33}t} + 0.4A^{0.40}e^{10t}, & \text{if } A \geq 62, \end{cases} \tag{2.1}$$

where θ is the CM scattering angle, $t = -2p^2(1 - \cos\theta)$ is the square of the 4-momentum transfer, p is the CM momentum, and A is the mass number of the nucleus. Figure 2.3a displays the DXS for the elastic scattering of 65 MeV protons on ^{28}Si as a function of the CM scattering angle. The experimental angular distribution [37, 38] is represented by dots (uncertainties are smaller than the symbol size), while the DXS for nuclear elastic scattering sampled from FLUKA v4-3.4 is displayed by the dashed curve; the solid curve is discussed in Section 2.1. Equation (2.1) attempts to capture the forward-scattering peak with the first exponential function, and the large-scattering-angle domain with the second exponential function. The dominant forward scattering feature extending up to ~30 deg is indeed reasonably reproduced by Eq. (2.1). However, at large scattering angles there is an order-of-magnitude discrepancy, which is even more accentuated for heavier nuclei and higher proton energies, see, *e.g.*, Fig. 2.3b for 160 MeV protons elastically scattering on ^{208}Pb. Unfortunately, as discussed in Section 4.1, elastic collisions with large scattering angle strongly contribute to SEU production. Accordingly, particular focus has been devoted to characterize such collisions in the modelling work discussed in this chapter.

A new FLUKA model for the nuclear elastic scattering of protons from CB up to 250 MeV has been therefore developed in this thesis. The global optical potential model (OPM) of Koning and Delaroche [39] has been employed to effectively describe the

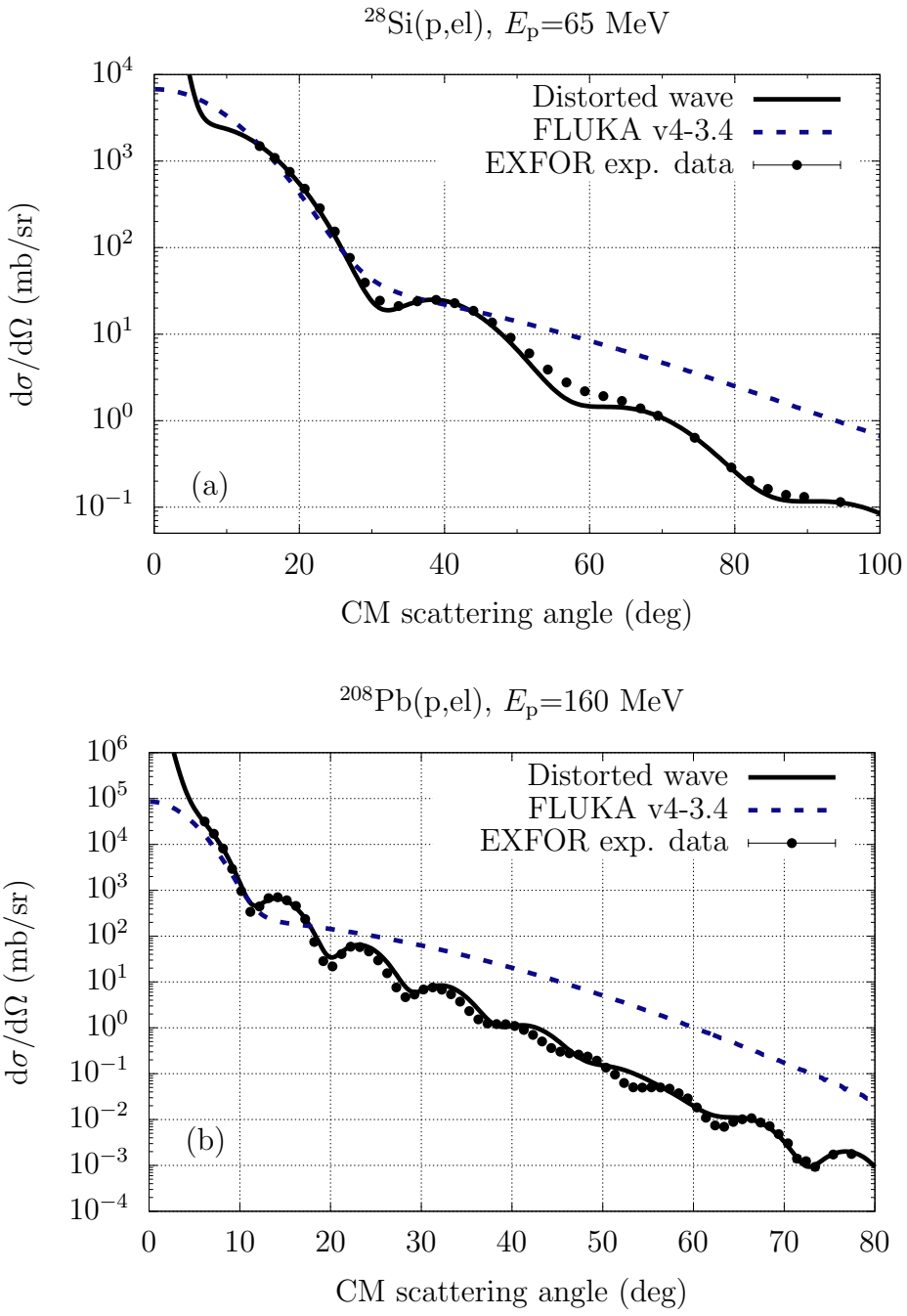

Figure 2.3: Differential cross section for the elastic scattering of protons on ^{28}Si at 65 MeV (a) and on ^{208}Pb at 160 MeV (b).

interaction of protons of up to 250 MeV with nuclei with mass number $A \geq 20$[†], and to evaluate a database of DXSs by means of a partial-wave analysis (see Section 2.1). To minimize memory requirements, an effective parametrized expression depending on 7 parameters has been fitted onto the evaluated DXS database (see Section 2.2). For nuclei with $A \leq 20$, where OPMs are scarcer, the parametrized expression has been directly fitted onto available experimental angular distributions (see Section 2.3). An algorithm to numerically sample nuclear elastic scattering events has been developed (see Section 2.5). Finally, an effective integrated cross section for proton nuclear elastic scattering has been obtained by numerical integration of the aforementioned parametrized expression (see Section 2.6). This model, discussed in detail in this chapter, has been implemented and released in FLUKA v4-4.0 (February 14, 2024), and led to a dedicated publication [27] on which this chapter is based.

2.1 Partial-wave analysis

The elastic scattering of protons at kinetic energies much lower than the proton mass (938 MeV/c^2) on nuclei can be treated on the basis of the Schrödinger equation for an effective interaction potential energy, $V(r)$, assumed to depend only on the relative distance r between the proton and the nucleus:

$$\left[-\frac{\hbar^2}{2\mu}\nabla^2 + V(r)\right]\psi_{\boldsymbol{k}}(\boldsymbol{r}) = E\psi_{\boldsymbol{k}}(\boldsymbol{r}), \tag{2.2}$$

where $\hbar$ is the reduced Planck constant, $\boldsymbol{k}$ is the CM wavevector, and

$$\mu = \frac{m_\mathrm{p} m_\mathrm{t}}{m_\mathrm{p} + m_\mathrm{t}}, \tag{2.3}$$

is the reduced mass, where m_p and m_t are the proton and the target nucleus masses, respectively. In Eq. (2.2) the CM motion has been already factored out via a separation of variables [40]. Since the interaction potential is central, $V(\boldsymbol{r}) = V(r)$, Eq. (2.2) can be expressed in spherical coordinates and using separation of variables one obtains an angular equation, whose solutions are the spherical harmonics, and a radial equation:

$$-\frac{\hbar^2}{2\mu}\frac{d^2P_{E\ell}(r)}{dr^2} + \left[\frac{\hbar^2\ell(\ell+1)}{2\mu r^2} + V(r)\right]P_{E\ell}(r) = EP_{E\ell}(r), \tag{2.4}$$

where $P_{E\ell}(r)$ are the radial functions and ℓ is the orbital angular momentum.

In absence of an interaction potential energy term, $V(r) = 0$, the solutions of the Schrödinger equation (2.2) are plane waves, which can be expanded as:

$$\mathrm{e}^{i\boldsymbol{k}\cdot\boldsymbol{r}} = 4\pi\sum_{\ell=0}^{\infty} i^\ell j_\ell(kr)\sum_{m_\ell=-\ell}^{\ell} Y_{\ell m_\ell}(\hat{\boldsymbol{r}})Y^*_{\ell m_\ell}(\hat{\boldsymbol{k}}), \tag{2.5}$$

where $j_\ell(kr)$ are the spherical Bessel functions, $Y_{\ell m_\ell}(\hat{\boldsymbol{r}})$ are the spherical harmonics, and m_ℓ is the projection of the orbital angular momentum along the quantization axis. Instead, when a central interaction potential is considered, $V(r) \neq 0$, the solutions become distorted plane waves: while the angular part of the wavefunction remains unaltered, the spherical

[†]Slightly below the strict domain of applicability ($A \geq 24$) of the Koning and Delaroche OPM.

Bessel functions of the radial part are replaced by the aforementioned radial functions, allowing for phase shifts δ_ℓ:

$$\psi_{\boldsymbol{k}}(\boldsymbol{r}) = \frac{4\pi}{kr}\sum_{\ell=0}^{\infty} i^\ell e^{i\delta_\ell} P_{E\ell}(kr) \sum_{m_\ell=-\ell}^{\ell} Y_{\ell m_\ell}(\hat{\boldsymbol{r}}) Y^*_{\ell m_\ell}(\hat{\boldsymbol{k}}). \tag{2.6}$$

The factor $1/r$ appears due to the expansion in terms of spherical waves, while the additional factor $1/k$ ensures dimensionlessness; see Appendix A for further details. The phase shifts δ_ℓ measure how much the introduction of an effective interaction potential shifts the radial functions with respect to the corresponding zero-potential solutions. For protons, which have spin $s = 1/2$, Eq. (2.6) becomes:

$$\psi_{\boldsymbol{k}m_s}(\boldsymbol{r}) = \frac{4\pi}{kr}\sum_{\ell=0}^{\infty} \sum_{j=\left|\ell-\frac{1}{2}\right|}^{\ell+\frac{1}{2}} \sum_{m=-j}^{j} i^\ell e^{i\delta_{\ell j}} \mathcal{P}_{k\ell j}(kr) \sum_{m_\ell=-\ell}^{\ell} Y^*_{\ell m_\ell}(\hat{\boldsymbol{k}}) \Omega^\ell_{jm}(\hat{\Omega}) \left\langle jm \mid \ell \frac{1}{2} m_\ell m_s \right\rangle, \tag{2.7}$$

where j is the total angular momentum, and

$$\begin{aligned} \Omega^\ell_{jm}(\hat{\Omega}) = \langle \hat{\Omega} \mid jm \rangle &= \sum_{m_\ell=-l}^{\ell} \sum_{m_s=-\frac{1}{2}}^{\frac{1}{2}} \left\langle \hat{\Omega} \mid \ell \frac{1}{2} m_\ell m_s \right\rangle \left\langle \ell \frac{1}{2} m_\ell m_s \mid jm \right\rangle \\ &= \sum_{m_\ell=-l}^{\ell} \sum_{m_s=-\frac{1}{2}}^{\frac{1}{2}} Y_{\ell m_\ell}(\hat{\Omega}) \chi_{m_s} \left\langle \ell \frac{1}{2} m_\ell m_s \mid jm \right\rangle, \end{aligned} \tag{2.8}$$

are the spherical spinors, where m is the projection of the total angular momentum along the quantization axis, $\hat{\Omega} = (\theta, \varphi)$, where θ and φ are the polar and azimuthal CM scattering angles, respectively, χ_{m_s} is the unit spinor, and $\left\langle jm \mid \ell \frac{1}{2} m_\ell m_s \right\rangle$ are Clebsch-Gordan coefficients.

To effectively model the proton-nucleus potential energy, optical potential models (OPMs) are generally employed. In this work, the global OPM of Koning and Delaroche [39], strictly valid for nuclei with mass numbers $A \geq 24$, has been adopted. As an example, Fig. 2.4 displays the Koning and Delaroche OPM potential energy of a 100 MeV proton in the vicinity of ^{28}Si (excluding spin-orbit coupling terms).

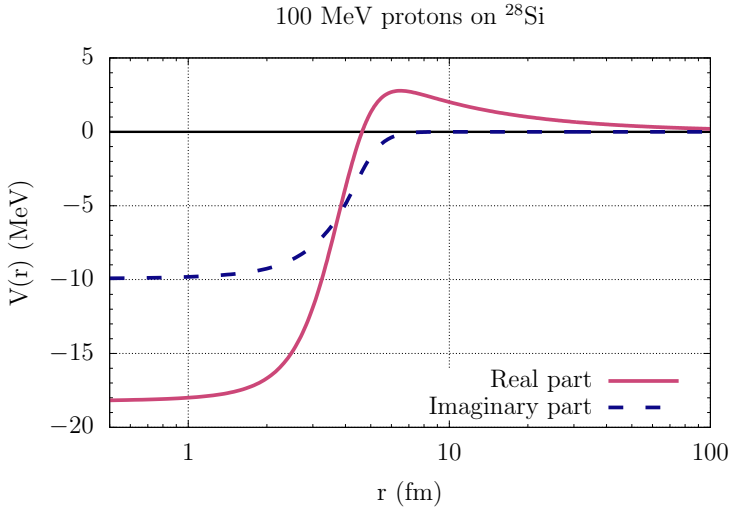

Figure 2.4: Interaction potential energy of 100 MeV protons on ^{28}Si for orbital angular momentum $\ell = 0$.

The radial Schrödinger equation for protons on nuclei has been solved numerically for the OPM of Koning and Delaroche [39] for each orbital angular momentum ℓ in the partial-wave series, using the RADIAL Fortran subroutine package [41] which provides the phase shifts $\delta_{\ell j}$. The DXS for proton elastic scattering as a function of θ has been evaluated as [42]:

$$\frac{\mathrm{d}\sigma}{\mathrm{d}\hat{\Omega}} = \left|f(\hat{\Omega})\right|^2 + \left|g(\hat{\Omega})\right|^2, \tag{2.9}$$

where

$$f(\hat{\Omega}) = f_{\mathrm{C}}(\theta) + \frac{1}{2ik}\sum_{\ell=0}^{\infty} P_\ell(\cos\theta)\,\mathrm{e}^{\mathrm{i}2\Delta_\ell}\left[(\ell+1)\,\mathrm{e}^{i2\tilde{\delta}_{\ell,\ell+1/2}} + \ell\,\mathrm{e}^{i2\tilde{\delta}_{\ell,\ell-1/2}} - (2\ell+1)\right] \tag{2.10}$$

and

$$g(\hat{\Omega}) = \frac{1}{2ik}\mathrm{e}^{i\varphi}\sum_{\ell=1}^{\infty} P_\ell^1(\cos\theta)\left(\mathrm{e}^{i2\delta_{\ell,\ell+1/2}} - \mathrm{e}^{i2\delta_{\ell,\ell-1/2}}\right) \tag{2.11}$$

are the direct and the spin flip scattering amplitudes, respectively, $P_\ell(\cos\theta)$ are the Legendre polynomials, $P_\ell^m(\cos\theta)$ are the associated Legendre polynomials, $\Delta_\ell = \arg\Gamma(\ell+1+i\eta)$, where Γ is the Gamma function, and $\tilde{\delta}_{\ell j}$ are the Coulomb and the inner phase shifts, respectively, verifying $\delta_{\ell j} = \Delta_\ell + \tilde{\delta}_{\ell j}$, while

$$f_{\mathrm{C}}(\theta) = -\eta\frac{\exp\left[2i\Delta_0 - i\eta\ln\left(\sin^2\dfrac{\theta}{2}\right)\right]}{2k\sin^2\dfrac{\theta}{2}} \tag{2.12}$$

is the Coulomb scattering amplitude on a point nucleus, where

$$\eta = \frac{Z_{\mathrm{p}}Z_{\mathrm{t}}e^2}{\hbar v} \tag{2.13}$$

is the Sommerfeld parameter, where $Z_{\mathrm{p}} = 1$ and Z_{t} are the atomic numbers of the proton and of the target nucleus, respectively, e is the elementary charge, and v is the non-relativistic velocity of the proton far from the origin of coordinates [41]. Defining

$$f_{\mathrm{N}}(\theta) = \frac{1}{2ik}\sum_{\ell=0}^{\infty} P_\ell(\cos\theta)\,\mathrm{e}^{\mathrm{i}2\Delta_\ell}\left[(\ell+1)\,\mathrm{e}^{i2\tilde{\delta}_{\ell,\ell+1/2}} + \ell\,\mathrm{e}^{i2\tilde{\delta}_{\ell,\ell-1/2}} - (2\ell+1)\right] \tag{2.14}$$

and inserting Eq. (2.10) in Eq. (2.9), the DXS becomes

$$\frac{\mathrm{d}\sigma}{\mathrm{d}\hat{\Omega}} = \left|g(\hat{\Omega})\right|^2 + \left|f_{\mathrm{C}}(\theta)\right|^2 + \left|f_{\mathrm{N}}(\theta)\right|^2 + 2\,\mathrm{Re}\left[f_{\mathrm{C}}^*(\theta)f_{\mathrm{N}}(\theta)\right]. \tag{2.15}$$

While the first three terms are positive, the remaining interference term between Coulomb and nuclear elastic scattering can be either positive or negative. This formally precludes treating nuclear and Coulomb elastic scattering as additive (separate) interaction mechanisms, especially at energies near CB, hence the lack of nuclear elastic scattering below 10 MeV up to FLUKA v4-3.4. In Section 3.1.2 an effective scheme is proposed.

Relying on the partial-wave scheme outlined above, a database of DXSs for the elastic scattering of protons on nuclei has been evaluated on a grid of 14 nuclei, and on a roughly

logarithmic grid of 37 proton energies, from CB up to 250 MeV. To confirm the soundness of the implemented partial-wave scheme, a systematic benchmark has been performed, wherein calculated DXSs have been compared with experimental DXSs [37, 38]. Overall, good agreement has been obtained[‡], as shown in Fig. 2.3, where the solid black curves represent the DXSs calculated with the partial-wave scheme adopted here. At most, deviations in the order of 20-30% are occasionally encountered in narrow angular domains, due to the use of a globally fitted OPM instead of a local fit on a per-isotope basis.

2.2 Parametrized differential cross section

A database of tabulated partial-wave DXSs, calculated as outlined above, could have been readily adopted for sampling proton nuclear elastic scattering events in FLUKA. However, a database evaluation in a sufficiently dense grid of proton energies, nuclei, and scattering angles would promptly lead to memory requirements in the order of tens or even hundreds of megabytes (MB). Allocating such an amount of memory for a single interaction mechanism (nuclear elastic scattering) of a single particle species (protons) in a restricted energy range (from CB to 250 MeV) would be excessive in the framework of a general-purpose multi-particle tracking code such as FLUKA.

Instead, an effective analytical DXS has been sought with sufficient flexibility to reasonably reproduce the structure of maxima and minima of the actual DXS. In a spirit similar to that of Refs. [43–45], the DXS for the elastic scattering of a particle on a fully absorptive imaginary potential in the so-called black-disk limit [44] has been recast as follows:

$$\frac{\mathrm{d}\sigma_0(\theta,\boldsymbol{\alpha})}{\mathrm{d}\hat{\Omega}} = \alpha k^2 R^4 \left[\left(\frac{J_1(Rq\delta_1)}{Rq} \right)^2 e^{-\beta_1 Rq} + \gamma J_0^2(Rq\delta_0) e^{-\beta_0 Rq} \right], \tag{2.16}$$

where $\boldsymbol{\alpha} = \{\alpha, \beta_{0,1}, \gamma, \delta_{0,1}\}$ are 6 dimensionless fit parameters (whose role is clarified below), J_1 and J_0 are Bessel functions of the 1$^{\mathrm{st}}$ kind, $R = 1.2A^{1/3}$ is the nuclear radius in fm, which provides a built-in scaling with the mass number A of the nucleus, and

$$q = 2k \sin\frac{\theta}{2} \tag{2.17}$$

is the CM wavevector transfer expressed as a function of the CM wavevector k and the CM scattering angle θ.

As an example, the thick black curve in Fig. 2.5 displays the DXS for the elastic scattering of 70 MeV protons on ^{107}Ag calculated within the partial-wave approach discussed in the foregoing section, while the thin orange curve represents the DXS obtained by fitting parametrized expression (2.16), yielding $\alpha = 6.141$, $\beta_0 = 0.296$, $\beta_1 = 0.369$, $\gamma = 0.008$, and $\delta_0 = \delta_1 = 1.105$. The drastic rise of the DXS as the scattering angle approaches 0 deg is instead a feature captured by Coulomb scattering, discussed in Section 3.1.2. The dashed green and blue curves in Fig. 2.5 show the contributions of the J_1 and J_0 terms of Eq. (2.16). Their minima and maxima are in phase opposition, allowing to capture the structure of minima and maxima of the actual DXS with a sufficient degree of flexibility, as needed. The 6 fit parameters play different roles: α is a mere scaling factor; β_1 and β_0 adjust the slope of the DXS; δ_1 and δ_0 allow one to better capture the

[‡]Also for isotopes slightly beyond the strict domain of applicability of the employed OPM, *e.g.*, ^{20}Ne and ^{238}U.

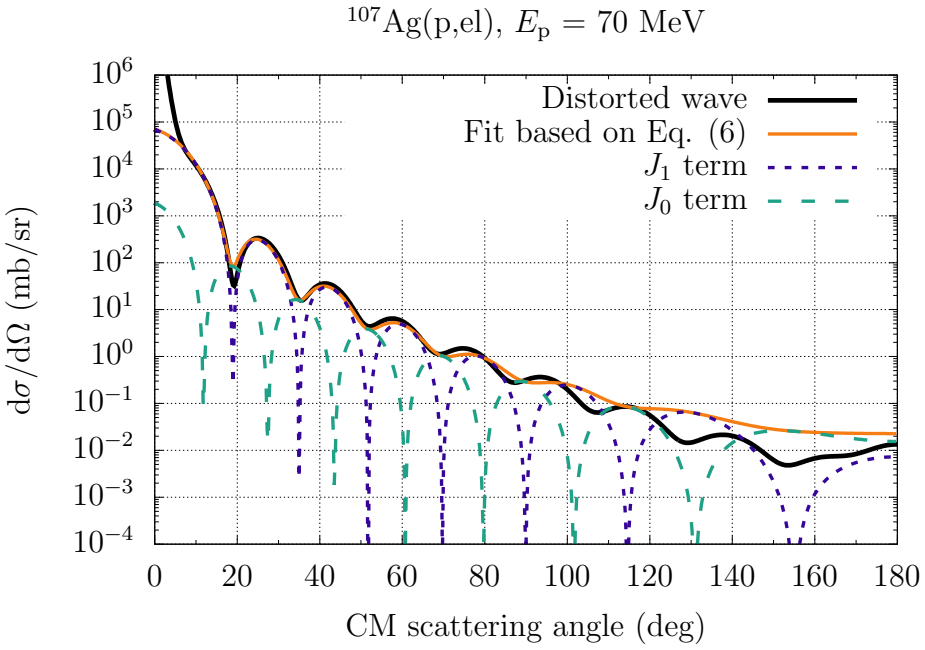

Figure 2.5: Differential cross section for the elastic scattering of 70 MeV protons on ^{107}Ag.

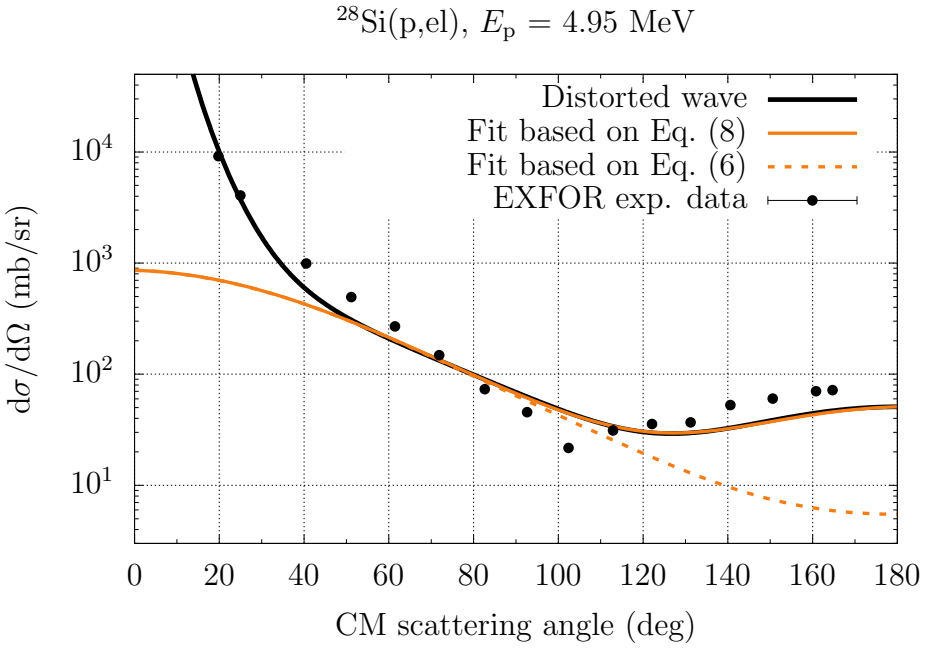

Figure 2.6: Differential cross section for the elastic scattering of 4.95 MeV protons on ^{28}Si.

position of the minima and maxima of the DXS, while γ drives the depth of the minima in the DXS.

As shown in Fig. 2.5, the proposed parameterized expression (2.16) is able to reproduce not only the main forward scattering feature extending up to ~20 deg, but also a considerable amount of minima and maxima at large scattering angles. Occasional difficulties are however encountered when trying to capture accentuated backscattering features. Therefore, it has been decided to provide Eq. (2.16) with a symmetrized term, prefaced by an additional fit parameter ζ,

$$\frac{\mathrm{d}\sigma(\theta,\boldsymbol{\alpha})}{\mathrm{d}\hat{\Omega}} = \frac{\mathrm{d}\sigma_0(\theta,\boldsymbol{\alpha})}{\mathrm{d}\hat{\Omega}} + \zeta\frac{\mathrm{d}\sigma_0(\pi-\theta,\boldsymbol{\alpha})}{\mathrm{d}\hat{\Omega}}, \tag{2.18}$$

which facilitates the fit of DXS features at large scattering angles. The effect of this additional term is highlighted in Fig. 2.6 which displays in thick black curve the DXS calculated within the partial-wave scheme of Section 2.1, in dashed orange the DXS obtained by fitting Eq. (2.16), missing the prominent backscattering feature, and in solid orange the DXS obtained by fitting Eq. (2.18), which is in very good agreement with the distorted-wave calculated DXS.

2.3 Nuclear elastic scattering on light nuclei

The Koning and Delaroche OPM is not strictly applicable to model the elastic scattering of protons on nuclei with mass number $A < 24$. The Watson OPM [46], instead, has parameters adjusted for incident proton energies up to a few tens of MeV on nuclei with $6 \leq A \leq 16$. This OPM was tentatively envisaged in this work for protons with energies from CB to 250 MeV on nuclei with $A < 24$. Figure 2.7 displays a comparison between these distorted-wave (dark blue) and experimental (black symbols) DXSs for 12.8 MeV protons elastically scattered on ^{10}B (a) and for 121.8 MeV protons on ^{14}N (b); the dark red curves are discussed below. While at low proton energies the agreement is reasonable, as shown in Fig. 2.7a, towards higher proton energies, the distorted-wave DXS evaluated with the Watson OPM (in dark-blue) exhibits deep minima, in disagreement with the experimental DXS, as displayed in Fig. 2.7b.

Other global OPMs for protons on light nuclei are not readily available. Thus, a complementary strategy has been adopted: instead of partial-wave DXSs, available experimental DXSs [37, 38] have been considered for 13 nuclei with $2 \leq A \leq 16$, for proton energies below 250 MeV. Where lacking, partial-wave DXSs based on the OPM of Koning and Delaroche have been adopted, albeit strictly outside the domain of applicability. These DXSs, displayed by the dark red curves in Fig. 2.7, are still in very good agreement with experimental DXSs. Table 2.1 outlines for each light nucleus whether distorted-wave and/or experimental DXSs have been adopted.

Parametrized expression (2.18) can be fitted equally well to experimental angular distributions rather than partial-wave DXSs. Figure 2.8 displays its good fit (represented by the solid orange lines) on the experimental DXSs (in black dots; uncertainties are smaller than the symbol size) for the elastic scattering of protons of various energies on ^{4}He (first column) and ^{16}O (second column). The proton-proton nuclear elastic scattering model has not been altered with respect to FLUKA v4-3.4.

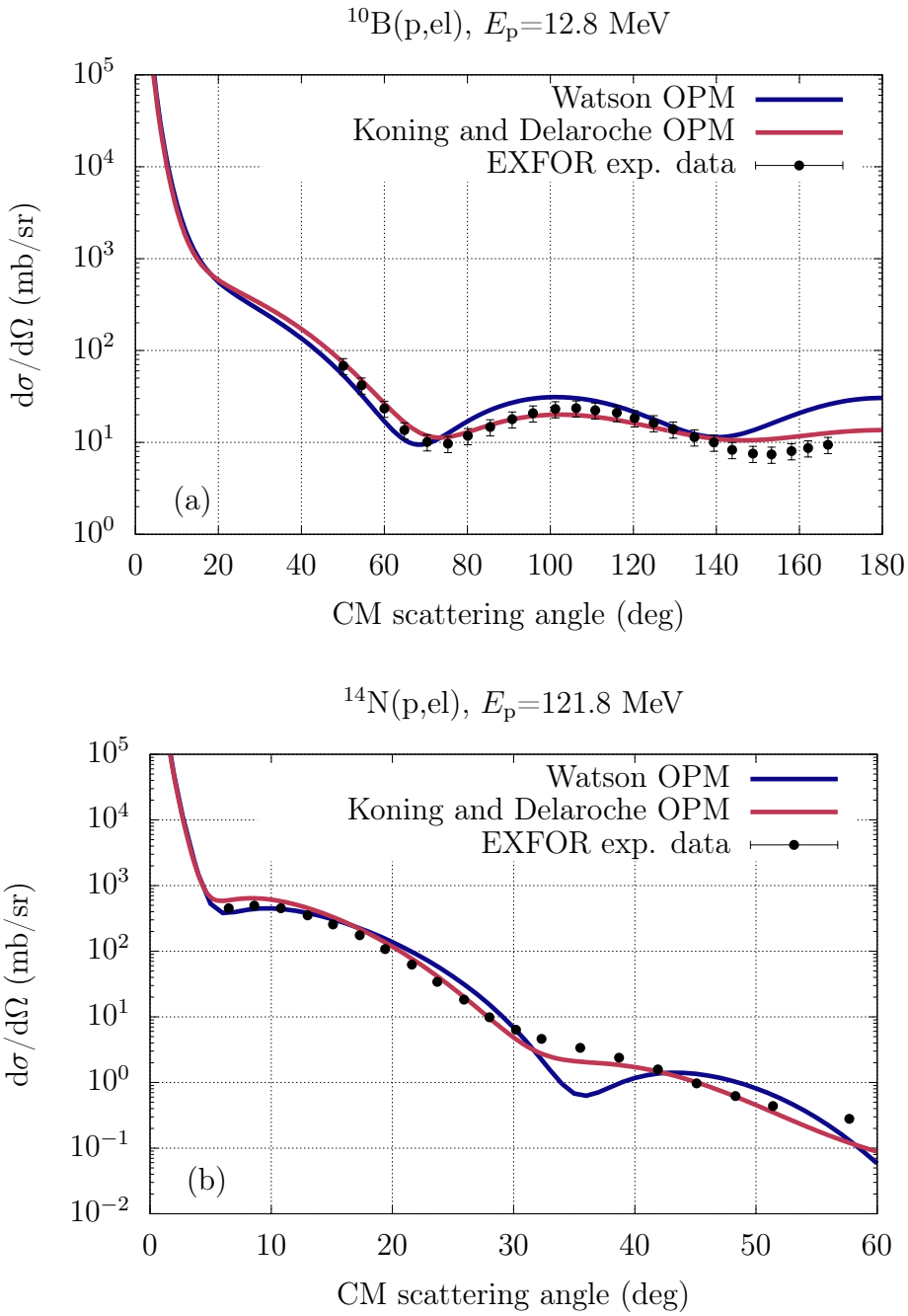

Figure 2.7: Differential cross section for the elastic scattering of protons on ^{10}B at 12.8 MeV (a) and on ^{14}N at 121.8 MeV (b).

Table 2.1: Experimental vs. distorted-wave DXSs used to fit Eq. (2.18) for light nuclei.

Nucleus	Experimental DXS	Distorted-wave DXS
^{2,3}H	✓	✗
^{3,4}He	✓	✗
^{6,7}Li	✓	✓
^{9}Be	✓	✓
^{10,11}B	✓	✓
^{12}C	✓	✗
^{14,15}N	✓	✓
^{16}O	✓	✗

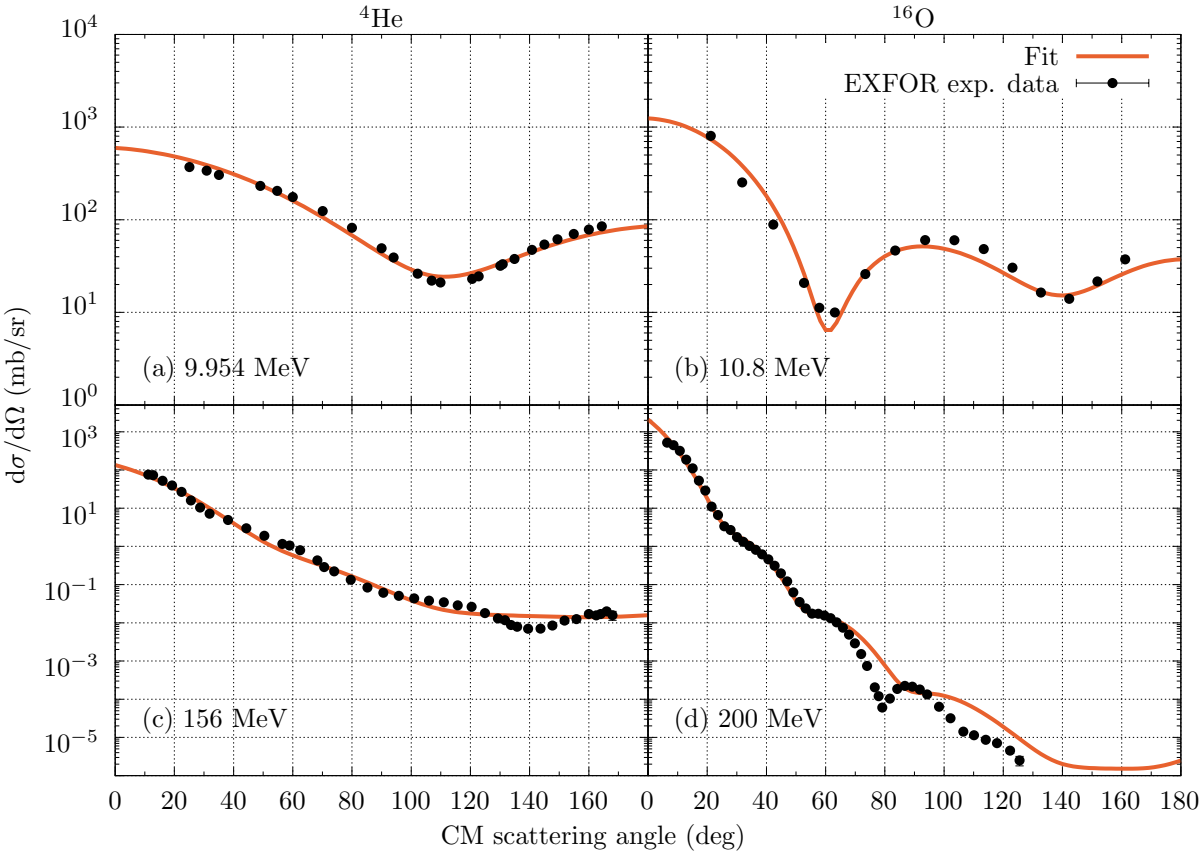

Figure 2.8: Fitted parametrized expression (2.18) (solid orange curves) compared with experimental DXSs (black dots; uncertainties are smaller than the symbol size) [37, 38] for protons of various energies on ^{4}He (left) and ^{16}O (right).

2.4 Least-squares minimization and goodness-of-fit

The adopted parametrized DXS (2.18), relying on 7 energy- and nucleus-dependent parameters $\boldsymbol{\alpha} = \{\alpha, \beta_{0,1}, \gamma, \delta_{0,1}, \zeta\}$, has been fitted to partial-wave DXSs for $\{^{20}$Ne, ^{24}Mg, ^{27}Al, ^{28}Si, ^{32}S, ^{40}Ca, ^{60}Co, ^{90}Zr, ^{107}Ag, ^{137}Cs, ^{197}Au, ^{208}Pb, ^{232}Th, and ^{238}U$\}$ and to partial-wave and/or experimental DXSs for the light nuclei in Table 2.1 by means of a dedicated least-squares minimization of

$$\chi^2 = \sum_{i=1}^{N} \left(\log \frac{\mathrm{d}\sigma(\theta_i, \boldsymbol{\alpha})}{\mathrm{d}\hat{\Omega}} - \log \left. \frac{\mathrm{d}\sigma(\theta_i, \boldsymbol{\alpha})}{\mathrm{d}\hat{\Omega}} \right|_{\mathrm{DW/exp}} \right)^2 W(\theta_i) \tag{2.19}$$

with respect to the fit parameters $\boldsymbol{\alpha}$, where $\dfrac{\mathrm{d}\sigma(\theta_i, \boldsymbol{\alpha})}{\mathrm{d}\hat{\Omega}}$ is the fitted DXS (2.18) at scattering angle θ_i, $\left. \dfrac{\mathrm{d}\sigma(\theta_i, \boldsymbol{\alpha})}{\mathrm{d}\hat{\Omega}} \right|_{\mathrm{DW/exp}}$ is the partial-wave/experimental DXS at θ_i, and N is the number of CM scattering angles. To equally weight differences across decades, a logarithmic instead of a linear difference has been adopted in Eq. (2.19).

Furthermore, weights $W(\theta_i)$ have been introduced to enhance the agreement between the fitted and the partial-wave/experimental DXSs at small and intermediate scattering angles, and to provide an overall reasonable description of the large scattering angles which, for high energies, are orders of magnitude below forward scattering. In this spirit, the following weights have been prescribed:

$$W(\theta_i) = \begin{cases} 100, & \text{for } \theta_i < \theta_0, \\ 70, & \text{for } \theta_i < 2\theta_0, \\ 15, & \text{for } \theta_i < 3\theta_0, \\ a\theta_i + b, & \text{for } \theta_i \geq 3\theta_0, \end{cases} \tag{2.20}$$

where θ_0 is the angle corresponding to the first minimum of the distorted-wave/experimental DXS; if a minimum scattering angle had not been found, *e.g.*, for Rutherford-like angular distributions at proton energies near CB, θ_0 has been set to 180 deg. The constants a and b have been determined such that $W(3\theta_0) = 10$ and $W(\pi) = 1$. For fitted DXSs underestimating the distorted-wave/experimental DXSs by more than an order of magnitude, the weights have been multiplied by an additional factor 50 to reduce discrepancies. Furthermore, since the distorted-wave DXS is divergent as the scattering angle approaches 0 deg due to Coulomb scattering, as discussed in Section 3.1.2, an angle from which the fitting procedure starts, θ_{fit}, has been determined based on θ_0 as:

$$\theta_{\mathrm{fit}} = \begin{cases} \dfrac{\theta_0}{2.5}, & \text{for } E_{\mathrm{p}} \leq 50\,\mathrm{MeV}, \\ \dfrac{\theta_0}{2.85}, & \text{for } E_{\mathrm{p}} > 50\,\mathrm{MeV}, \end{cases} \tag{2.21}$$

where the denominators have been chosen empirically.

First, a coarse fitting has been carried out in which a broad range of parameter values set on the equispaced grid outlined in Table 2.2 has been explored. The fit parameter α has

Table 2.2: Minimum and maximum of each parameter, and the corresponding number of evaluation points for the first fitting step.

Parameter	Min.	Max.	N_p
α	$0.15\alpha_0$	$1.20\alpha_0$	7
β_1	0.1	1.4	7
β_0	0.1	1.4	7
δ_1	0.8	2.0	8
δ_0	0.75	1.5	8
γ	0.005	0.2	7

been initially estimated from the asymptotic behaviour of the partial-wave/experimental DXSs as the scattering angle is approaching 0 deg,

$$\alpha_0 = \frac{1}{k^2 R^4} \frac{\mathrm{d}\sigma(\theta_{\mathrm{fit}}, \boldsymbol{\alpha})}{\mathrm{d}\hat{\Omega}}\bigg|_{\mathrm{DW/exp}} . \tag{2.22}$$

Furthermore, ζ has been set for each considered nucleus and incident proton energy as

$$\zeta = \max\left(0, \frac{\dfrac{\mathrm{d}\sigma(\theta=\pi, \boldsymbol{\alpha})}{\mathrm{d}\hat{\Omega}}\bigg|_{\mathrm{DW/exp}} - \dfrac{\mathrm{d}\sigma(\theta=\pi, \boldsymbol{\alpha})}{\mathrm{d}\hat{\Omega}}}{\dfrac{\mathrm{d}\sigma(\theta=0, \boldsymbol{\alpha})}{\mathrm{d}\hat{\Omega}}}\right), \tag{2.23}$$

and has, therefore, not been fitted. For the fit parameter γ, a logarithmic evaluation grid has been adopted since it spans several orders of magnitude. The coarse fitting allows one to quickly identify a promising region in the parameter space and provide a good starting point for a second more refined fitting. Next, a narrower range of parameters, restricted to ±10% around the approximate fit parameters found in the first fitting step, has been probed.

As an example, Fig. 2.9 displays all relevant fit parameters (α is not needed for numerical sampling purposes) as a function of the proton energy for the nuclear elastic scattering of protons on ^{40}Ar. At energies above a few tens of MeV, the energy dependence is smooth since the parametrized expression (2.18) relies on the black-disk limit, *i.e.*, it works best at high proton energies. At lower energies, the fit parameters exhibit a less smooth behaviour, nevertheless their values do not significantly deviate from $O(1)$. To minimize posterior interpolation errors at low energies, the energy grid on which the fit parameters have been tabulated is roughly logarithmic.

This fit has effectively reduced the memory requirements from ~10s of MB to a mere tabulation of 7 parameters for 14 nuclei and 37 tabular proton energies, amounting to ~0.1 MB. To provide an overview of the fit performance, Fig. 2.10 displays the DXS for the elastic scattering of protons on ^{28}Si, ^{90}Zr and ^{232}Th (first, second, and third column, respectively) at 10 MeV, 70 MeV, and 200 MeV (first, second, and third row, respectively). The thick black curves have been evaluated with the partial-wave approach discussed in Section 2.1, while the thin orange curves have been obtained by fitting parametrized

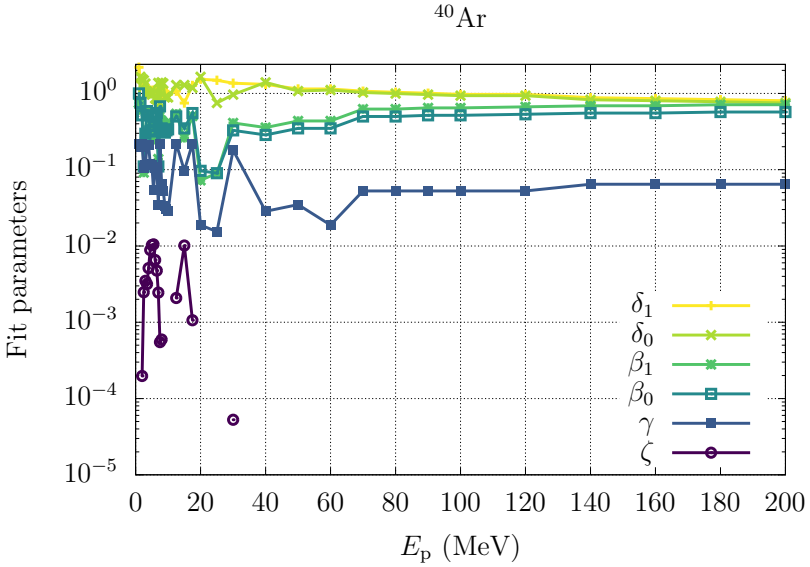

Figure 2.9: Fit parameters as a function of proton energy for ^{40}Ar.

expression (2.18). Finally, the dashed curves have been obtained by sampling nuclear elastic scattering events from FLUKA v4-3.4 (relying on a cruder model [30] for proton nuclear elastic scattering) and scaling the resulting (unit-normalized) angular distributions by a crude neutron-based integrated cross section [47]. The FLUKA v4-3.4 DXSs generally capture the forward scattering feature, but tend to provide a too coarse account of the large-scattering-angle domain, missing the rich structure of maxima and minima exhibited by the actual DXSs. Moreover, subfigure (c) exemplifies a case in which the FLUKA v4-3.4 integrated cross section for nuclear elastic scattering provides insufficient intensity (see also Section 3.1.2). Instead, parametrized expression (2.18) captures not only the forward-scattering feature, but also a considerable number of minima and maxima at large scattering angles, especially at high energies and for large mass numbers, as shown by the thin orange curves in subfigures (f), (h) and (i). However, for low mass numbers, at localized energies in the few tens of MeV, the agreement is occasionally less optimal at large scattering angles (where, nevertheless, the DXSs have already dropped by several orders of magnitude), as shown in subfigures (d), (e) and (g). Furthermore, for intermediate and large mass numbers and proton energies near CB, mild wiggling of the fitted parametrized expression around the actual DXS is encountered, as seen in subfigure (c). Nonetheless, the parametrized expression fulfills its original purpose to provide a good effective description of the forward-scattering peak, as well as a fairly resolved account of the structure of minima and maxima at larger scattering angles, relying only on 7 fit parameters.

As illustrated in Fig. 2.10, the fitted parametrized expression (2.18) provides satisfactory agreement with the actual DXS. A goodness-of-fit test has been conducted to quantify this agreement, *i.e.*, to test the null hypothesis $\mathcal{H}_0$ = "The distorted-wave/experimental DXSs are well described by the fitted DXSs". For each considered nucleus and incident proton energy pair, the statistic

$$\hat{\chi}^2 = \sum_{i=1}^{N} \frac{(O_i - E_i)^2}{(\sigma_i E_i)^2} \tag{2.24}$$

has been evaluated. The observables O_i, where $i = 1, \ldots, N$, are the fitted DXS at each

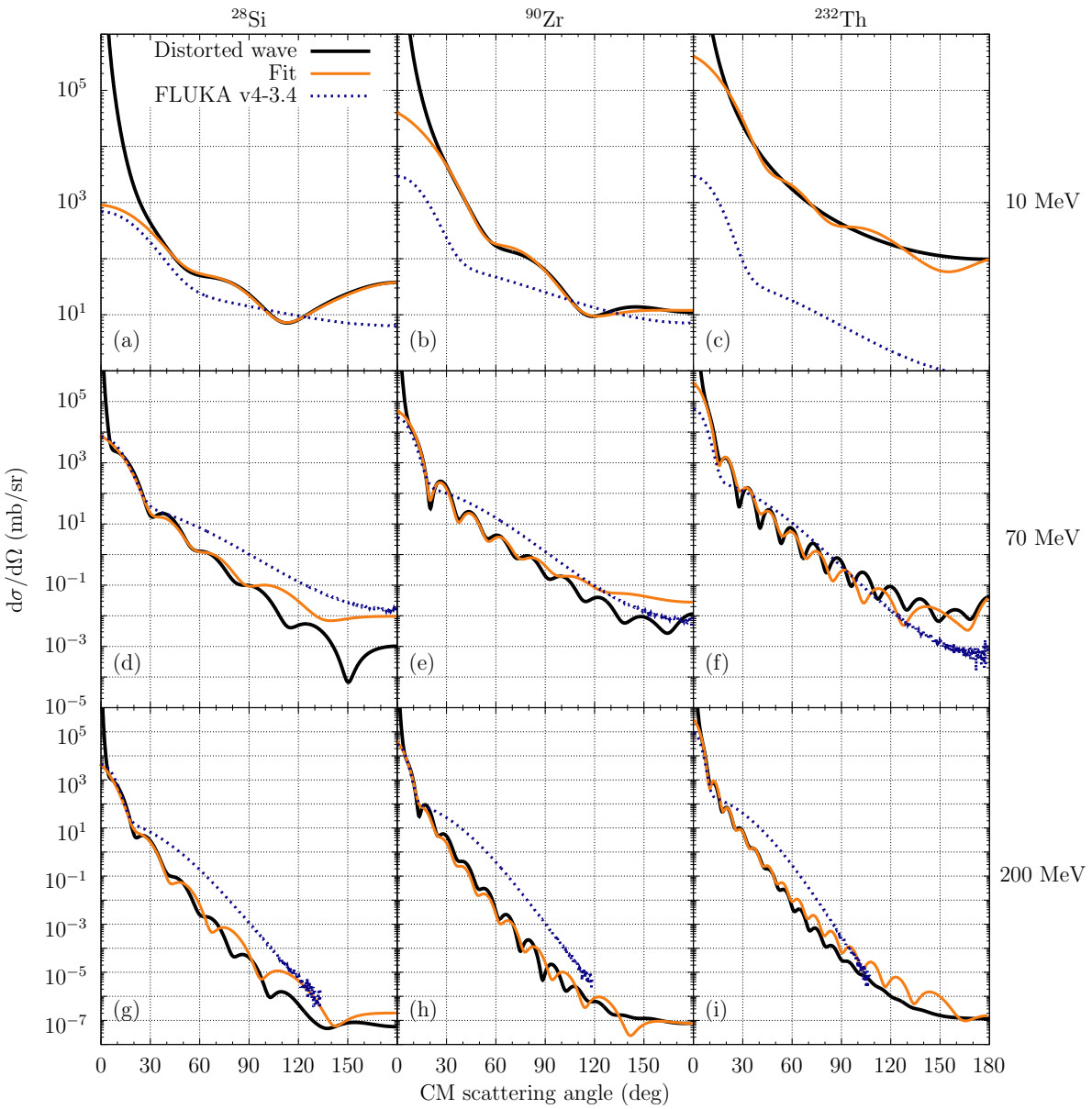

Figure 2.10: Fitted parametrized expression (2.18) (thin orange curves) compared with DXSs evaluated within the partial-wave approach (2.9) (thick black curves) for protons of 10 MeV, 70 MeV, and 200 MeV (first, second, and third row, respectively) elastically scattering on ^{28}Si, ^{90}Zr, and ^{232}Th (first, second, and third column, respectively), and with the FLUKA v4-3.4 sampled DXSs for nuclear elastic scattering (dashed curves).

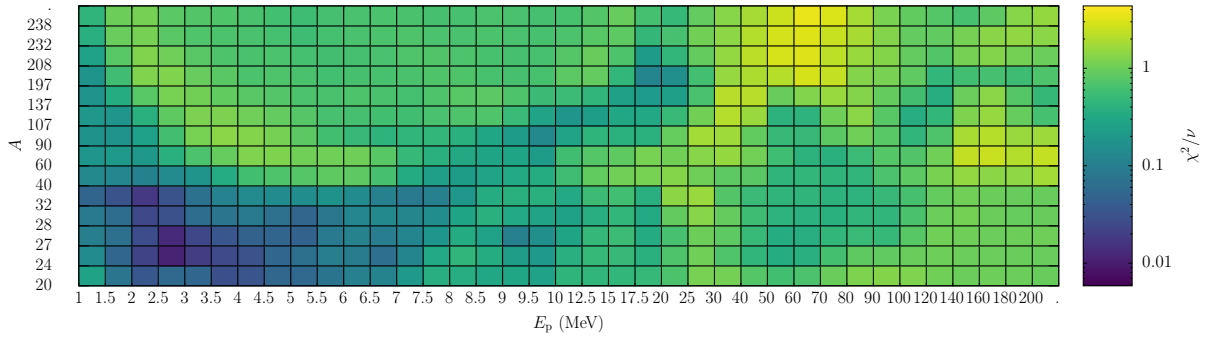

Figure 2.11: Ratio of $\hat{\chi}^2/\nu$.

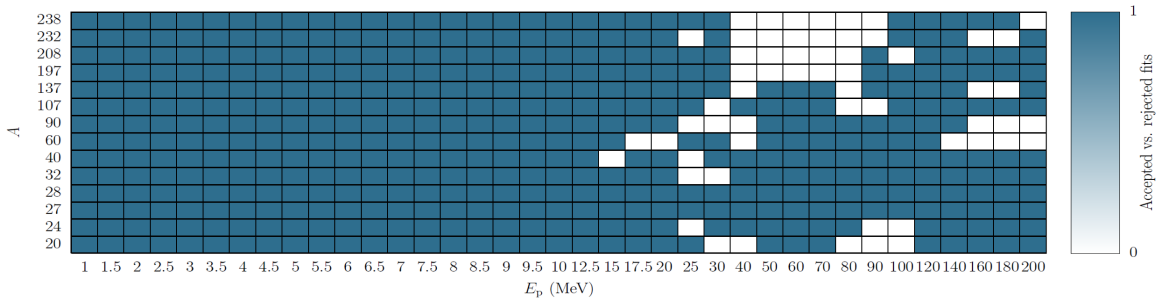

Figure 2.12: Accepted vs. rejected fits.

scattering angle θ_i, while the expectation values E_i are the corresponding distorted-wave or experimental DXS at θ_i. The uncertainty of the observables around their respective expectation values has been estimated as

$$\sigma_i = 0.3\frac{\theta_i}{\theta_0}, \tag{2.25}$$

in view of the occasional variation of 20-30% of the partial-wave DXSs around experimental DXSs (themselves subject to uncertainties) due to the globally fitted OPM instead of a local per-isotope fit. Furthermore, the N points considered in the evaluation of $\hat{\chi}^2$ have been restricted from θ_{fit} to $3\theta_0$ (see Eqs. (2.20) and (2.21)) since particular care has been devoted to fitting the small and intermediate scattering angles.

The probability to obtain a value equal or higher than $\hat{\chi}^2$ is [48]

$$p_{\hat{\chi}^2} = \int_{\hat{\chi}^2}^{\infty} \frac{e^{-\frac{x}{2}} x^{\frac{\nu}{2}}}{2^{\frac{\nu}{2}}\Gamma\left(\frac{\nu}{2}\right)} \mathrm{d}x, \tag{2.26}$$

where $\nu = N - m$ is the number of degrees of freedom, $m = 6$ is the number of free fit parameters (ζ is not obtained by fitting, but it is evaluated from Eq. (2.23)) and $\Gamma(x)$ is the Gamma function. If this probability is lower than a predefined confidence level, which in this work has been set to 5%, the null hypothesis $\mathcal{H}_0$ is rejected, otherwise it is not. Furthermore, if $\mathcal{H}_0$ is not rejected, $\hat{\chi}^2$ is expected to be approximately equal to ν. Figure 2.11 displays the ratio $\hat{\chi}^2/\nu$ which is indeed very close to 1 overall, and especially for high proton energies, where expression (2.18) is intended to work best, albeit Fig. 2.11 shows only the heavy nuclei for which the energy grid on which the fit parameters are tabulated is fixed.

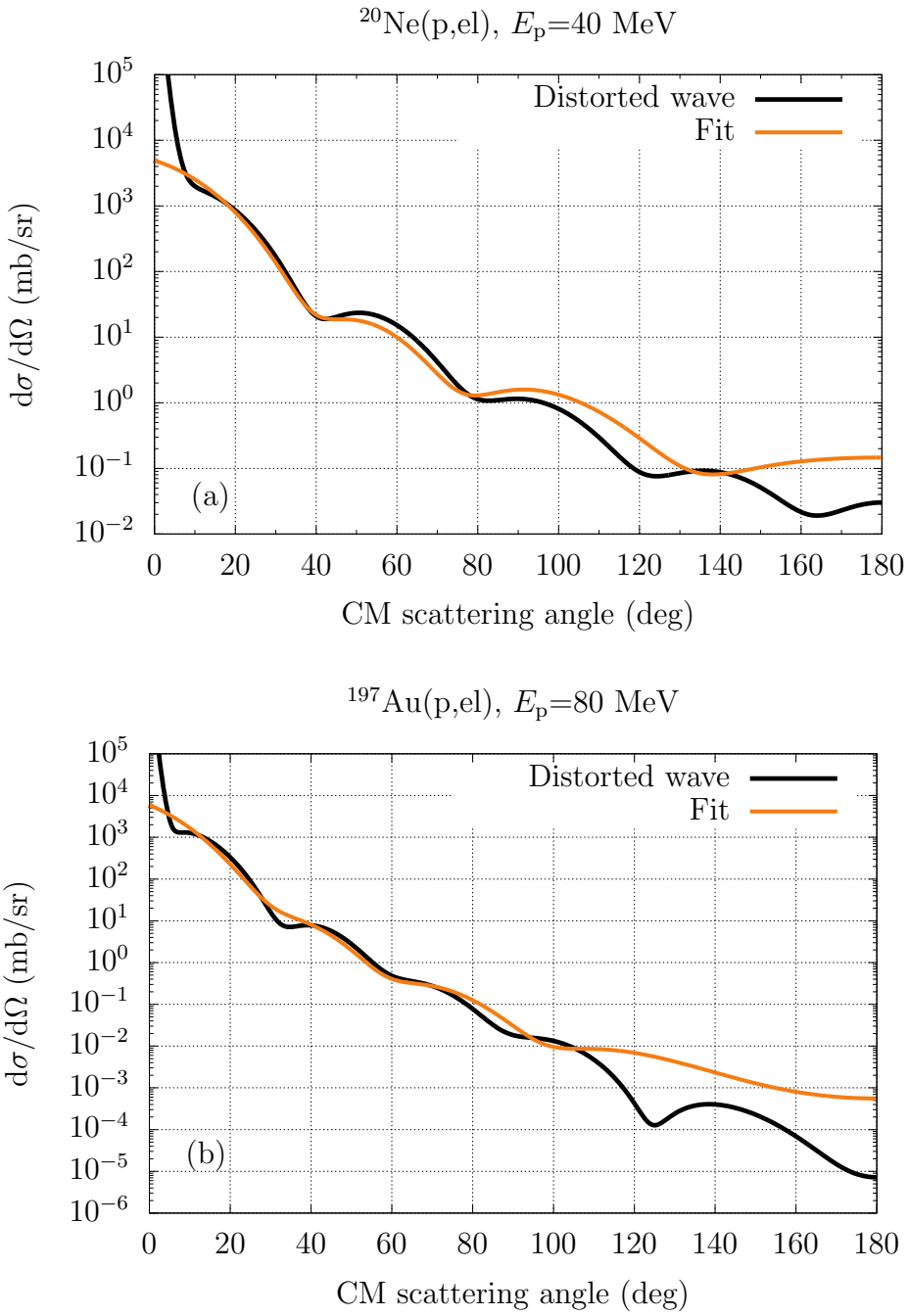

Figure 2.13: Differential cross section for the elastic scattering of protons on ^{20}Ne at 40 MeV (a) and on ^{197}Au at 80 MeV (b).

This goodness-of-fit test has revealed that the fit parameters can be accepted with a confidence level of 5% in 88.6% of the considered proton energy and heavy nucleus tuples and in 88.9% of the considered proton energy and light nucleus tuples. As an example, Fig. 2.12 provides an overview of the rejected fits in white and the accepted fits in blue for the heavy nuclei (for which the proton energy grid on which the fit parameters are tabulated is fixed). To illustrate that the fit remains reasonably effective even for the cases rejected by the goodness-of-fit test, Fig. 2.13 depicts the fitted parametrized expression (2.18) (in orange) and the distorted-wave DXS (in black) for the elastic scattering for protons of 40 MeV on ^{20}Ne (a) and of 80 MeV on ^{197}Au (b), which are still in fairly reasonable agreement over several orders of magnitude.

2.5 Rejection sampling scheme

A sampling scheme has been implemented in FLUKA v4-4.0 for the simulation of proton nuclear elastic scattering events from the fitted parametrized expression (2.18). For clarity, expression (2.16) has been be used in the following derivation. Inserting Eq. (2.17) in Eq. (2.16) one has

$$\frac{d\sigma_0(\theta,\boldsymbol{\alpha})}{d\hat{\Omega}} = \alpha k^2 R^4 \left[\left(\frac{J_1(R2k\sin\frac{\theta}{2}\delta_1)}{R2k\sin\frac{\theta}{2}} \right)^2 e^{-\beta_1 R2k\sin\frac{\theta}{2}} + \gamma J_0^2\left(R2k\sin\frac{\theta}{2}\delta_0\right) e^{-\beta_0 R2k\sin\frac{\theta}{2}} \right]. \quad (2.27)$$

Since an analytical sampling algorithm appears out of reach for this probability density function, a rejection sampling scheme has been adopted instead. To better precondition Eq. (2.27) for numerical sampling, the trigonometric identity $\sin\frac{\theta}{2} = \sqrt{\frac{1-\cos\theta}{2}} = \sqrt{\mu}$ has been used, implying

$$\frac{d\sigma_0(\theta,\boldsymbol{\alpha})}{d\hat{\Omega}} = \alpha k^2 R^4 \left[\left(\frac{J_1(R2k\sqrt{\mu}\delta_1)}{R2k\sqrt{\mu}} \right)^2 e^{-\beta_1 R2k\sqrt{\mu}} + \gamma J_0^2\left(R2k\sqrt{\mu}\delta_0\right) e^{-\beta_0 R2k\sqrt{\mu}} \right], \quad (2.28)$$

where the variable μ is convenient for numerical sampling purposes.

The main steps of the rejection sampling scheme are detailed below and illustrated through a flow diagram in Fig. 2.14.

1. **Decide to sample from the J_1 or J_0 Bessel-function terms of Eq. (2.28).**

   One evaluates

   $$\mathcal{R} = \frac{\int_0^1 \left(\frac{J_1(R2k\sqrt{\mu}\delta_1)}{R2k\sqrt{\mu}} \right)^2 e^{-\beta_1 R2k\sqrt{\mu}} \mathrm{d}\mu}{\int_0^1 \left[\left(\frac{J_1(R2k\sqrt{\mu}\delta_1)}{R2k\sqrt{\mu}} \right)^2 e^{-\beta_1 R2k\sqrt{\mu}} + \gamma J_0^2\left(R2k\sqrt{\mu}\delta_0\right) e^{-\beta_0 R2k\sqrt{\mu}} \right] \mathrm{d}\mu} \quad (2.29)$$

   and generates a random number $\eta \sim \mathcal{U}[0,1)$. If $\eta < \mathcal{R}$, the J_1 term is selected, otherwise the J_0 term.

2. **Sample μ from the exponential terms in Eq. (2.28).**

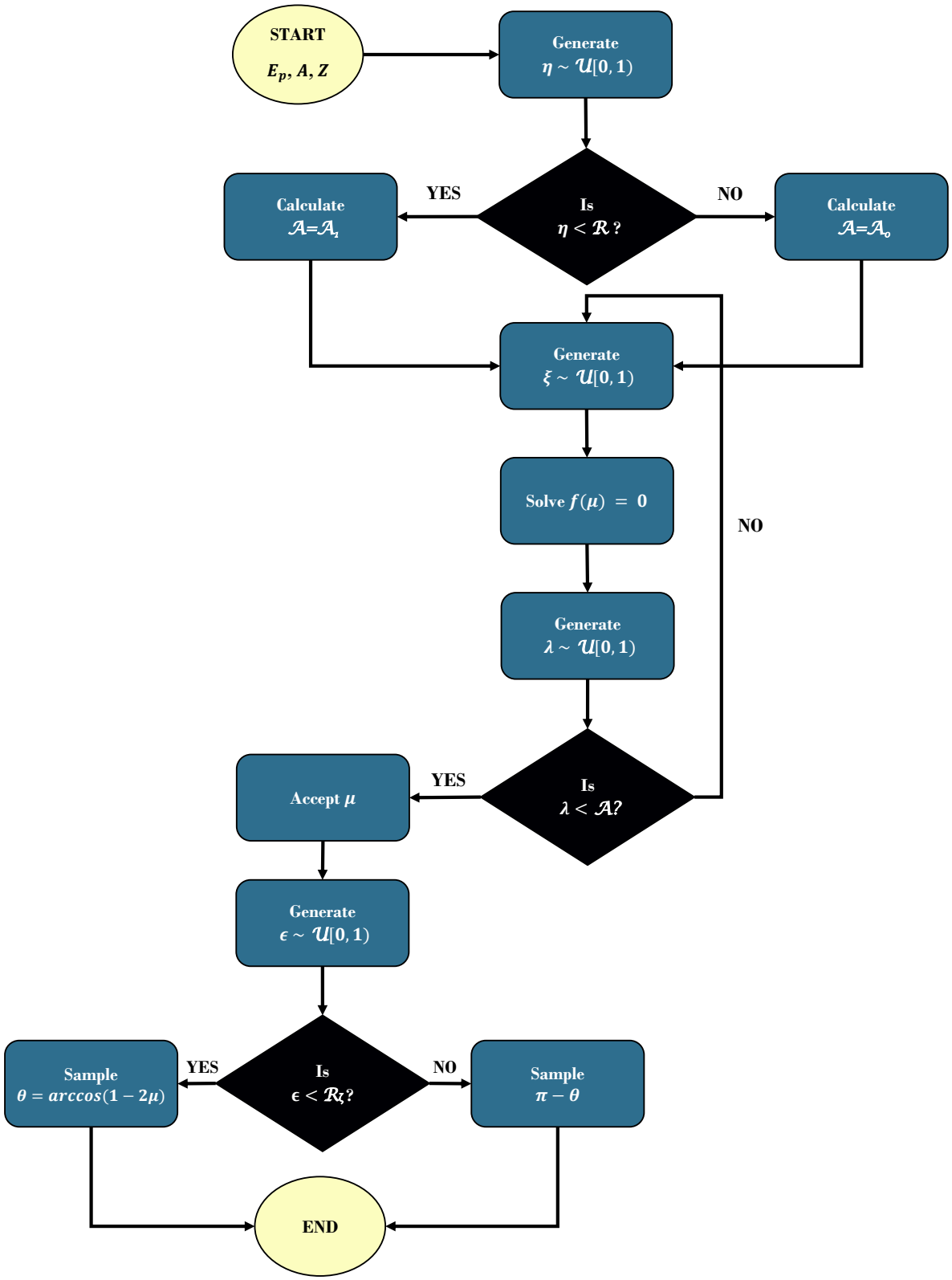

Figure 2.14: Flow diagram of the rejection sampling scheme implemented in FLUKA v4-4.0.

The exponential terms in Eq. (2.28) have been adopted as reasonable envelope functions:

$$p(\mu) = \mathcal{N} e^{-z\sqrt{\mu}}, \tag{2.30}$$

where $z = R2k\beta_1$ for the J_1 term, and $z = R2k\beta_0$ for the J_0 term, and the normalization constant $\mathcal{N}$ follows from:

$$1 = \int_0^1 \mathrm{d}\mu\, p(\mu) = \mathcal{N} \int_0^1 \mathrm{d}\mu\, e^{-z\sqrt{\mu}} = \frac{2\mathcal{N}}{z^2}\left[1 - e^{-z}(z+1)\right], \tag{2.31}$$

i.e.,

$$\mathcal{N} = \frac{z^2}{2\left[1 - e^{-z}(z+1)\right]}. \tag{2.32}$$

Thus, Eq. (2.30) becomes:

$$p(\mu) = \frac{z^2}{2\left[1 - e^{-z}(z+1)\right]} e^{-z\sqrt{\mu}}. \tag{2.33}$$

The sampling equation is:

$$\xi = \int_0^\mu \mathrm{d}\mu'\, p(\mu'), \tag{2.34}$$

where $\xi \sim \mathcal{U}[0,1)$ is a random number. Inserting Eq. (2.33) into Eq. (2.34), yields:

$$\xi = \frac{z^2}{2\left[1 - e^{-z}(z+1)\right]} \int_0^\mu \mathrm{d}\mu'\, e^{-z\sqrt{\mu'}} = \frac{1 - e^{-z\sqrt{\mu}}\left(1 + z\sqrt{\mu}\right)}{1 - e^{-z}(z+1)} \tag{2.35}$$

For simplicity, denoting $\kappa = 1 - e^{-z}(z+1)$ yields:

$$f(\mu) = 1 - e^{-z\sqrt{\mu}}\left(1 + z\sqrt{\mu}\right) - \xi\kappa = 0. \tag{2.36}$$

Equation (2.36) does not have an analytical solution. Therefore, it has to be solved numerically. Since $\mu \in [0,1]$, the values of the function at the ends of the interval are:

$$\begin{aligned} f(0) &= -\xi\kappa \\ f(1) &= (1-\xi)\kappa, \end{aligned} \tag{2.37}$$

which have opposite signs: $f(0)f(1) < 0$. Therefore, the bisection method has been employed to solve Eq. (2.36) and find μ for a given ξ.

3. **Accept** μ.

   While the exponential terms have been used as envelope functions, the remaining Bessel-function terms of Eq. (2.28) have been used as acceptance weights:

$$\begin{aligned} \mathcal{A}_1 &= \alpha k^2 R^4 \left(\frac{J_1(R2k\sqrt{\mu}\delta_1)}{R2k\sqrt{\mu}}\right)^2, \\ \mathcal{A}_0 &= \alpha k^2 R^4 \gamma J_0^2\left(R2k\sqrt{\mu}\delta_0\right). \end{aligned} \tag{2.38}$$

   A random number $\lambda \sim \mathcal{U}[0,1)$ is generated. If λ is less than the acceptance weight, the solution μ is accepted, otherwise go back to step 2.

4. **Decide to sample θ or $\pi - \theta$.**

   Finally, to sample either the first (forward scattering) or the second (back-scattering) term on the right-hand side of Eq. (2.18), a random number $\epsilon \sim \mathcal{U}[0, 1)$ is generated and compared with the ratio $\mathcal{R}_\zeta = 1/(1 + \zeta)$. If $\epsilon < \mathcal{R}_\zeta$, the scattering angle $\theta = \arccos(1 - 2\mu)$ is sampled directly, otherwise $\pi - \theta$ is sampled.

2.6 Integrated cross section for proton nuclear elastic scattering

Up to FLUKA v4-3.4, an effective integrated cross section for proton nuclear elastic scattering $\sigma_{(\mathrm{p,el})}^{\text{v4-3.4}}$ was obtained not as the integral of the differential cross section, but based on parametrizations of the total and nuclear reaction cross sections of neutrons [47]. One could have kept $\sigma_{(\mathrm{p,el})}^{\text{v4-3.4}}$ in FLUKA v4-4.0 and beyond, but such an approach proved to be untenable. To emphasize this point, the solid blue curve in Fig. 2.15 represents the DXS for the nuclear elastic scattering of 50 MeV protons on ^{208}Pb sampled as a unit-normalized angular distribution employing the prescription presented in the foregoing section and scaled with $\sigma_{(\mathrm{p,el})}^{\text{v4-3.4}}$. The resulting DXS exhibits the correct shape, but an intensity of a factor of 8 lower than that of the fitted DXS, Eq. (2.18), shown in dashed dark-orange in Fig. 2.15. Thus, such an approach would result in a considerably underestimated proton nuclear elastic scattering rate.

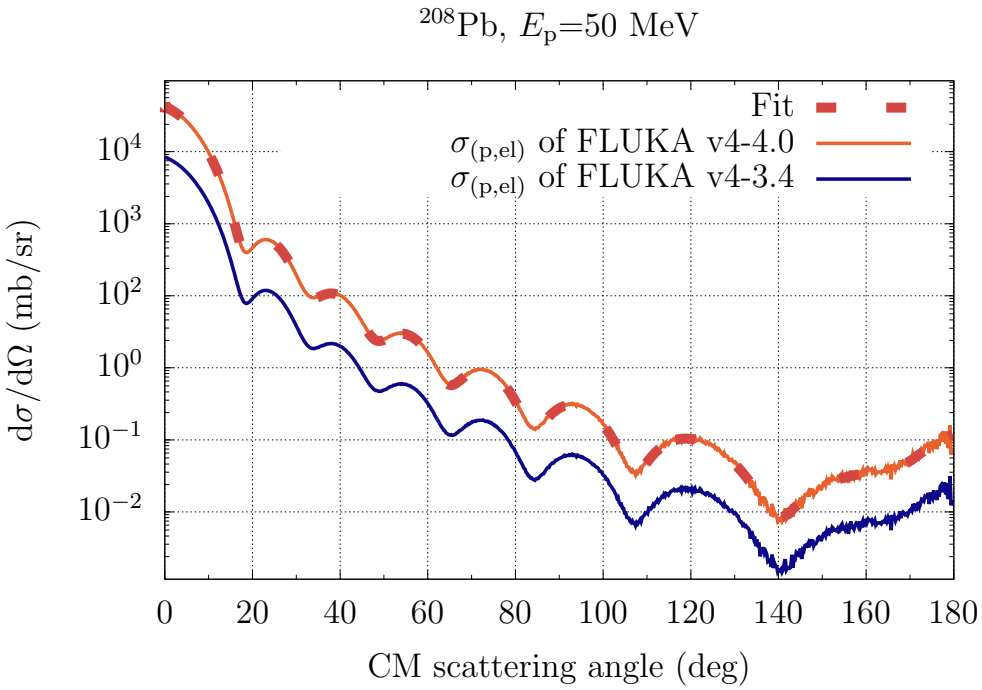

Figure 2.15: Differential cross section for the nuclear elastic scattering of 50 MeV protons on ^{208}Pb based on fitted parametrized expression (2.18) (dashed dark-orange curve) vs. the sampled DXS obtained when using the proton nuclear elastic scattering integrated cross section of FLUKA v4-3.4 (solid blue curve) vs. when using that of FLUKA v4-4.0 (solid red curve). Statistical uncertainties are omitted for clarity.

Instead, a self-consistent scheme has been adopted, wherein the integrated cross section for proton nuclear elastic scattering has been estimated by numerically integrating Eq. (2.18), which can be recast as follows:

$$\sigma_{(\mathrm{p,el})}^{\text{v4-4.0}} = \int \mathrm{d}\hat{\boldsymbol{\Omega}} \frac{\mathrm{d}\sigma(\theta, \boldsymbol{\alpha})}{\mathrm{d}\hat{\boldsymbol{\Omega}}} = (1+\zeta)\, 2\pi\alpha R^2 \mathcal{F}_1 + (1+\zeta)\, \frac{2\pi\alpha R^2 \gamma}{\delta_0^2} \mathcal{F}_0, \tag{2.39}$$

where

$$\mathcal{F}_1 = \int_0^{2kR\delta_1} \frac{1}{x_1} J_1^2(x_1)\, e^{-\frac{\beta_1}{\delta_1} x_1} \mathrm{d}x_1, \tag{2.40}$$

$$\mathcal{F}_0 = \int_0^{2kR\delta_0} x_0 J_0^2(x_0)\, e^{-\frac{\beta_0}{\delta_0} x_0} \mathrm{d}x_0, \tag{2.41}$$

where $x_{0,1} = Rq\delta_{0,1}$; for the full derivation of Eqs. (2.40) and (2.41) see Appendix B. The integrals (2.40) and (2.41) have been evaluated numerically once using an adaptive Gaussian quadrature and tabulated on a grid of the fit parameters δ_1 and δ_0, and the ratios β_1/δ_1 and β_0/δ_0.

A function taking as input the atomic and mass numbers of the nucleus and the kinetic energy of the incident proton has been written in FLUKA to interpolate the tabulated integrals (2.40) and (2.41) and return the integrated cross section for proton nuclear elastic scattering in mb. The solid red curve in Fig. 2.15 displays the sampled DXS obtained with this self-consistent approach, which is in perfect agreement with the fitted DXS, not only in shape, but also in intensity, *i.e.*, in proton nuclear elastic interaction rate.

Chapter 3

Coulomb and nuclear elastic scattering of protons in FLUKA

The elastic scattering of protons on nuclei is a process mediated both by the nuclear and the Coulomb forces. While proton nuclear elastic scattering has been extensively discussed in Chapter 2, in this chapter the focus is on Coulomb scattering, *i.e.*, scattering off the electrostatic potential of the nucleus (screened by the atomic electrons). This contributes to the broadening of the angular distribution due to many Coulomb scattering events when a proton passes through matter. Coulomb collisions can be treated individually in Monte Carlo (MC) simulations. However, the mean free path for, *e.g.*, 20 MeV protons undergoing Coulomb scattering on ^{208}Pb is of ~10s of nm [19]. Therefore, detailed simulations are highly computationally intensive, making such an approach untenable for general-purpose multi-particle Monte Carlo codes like FLUKA. Instead, condensed-history approaches are favoured, which imply an aggregate description of the effect of multiple elastic collisions of protons on the electrostatic potential of atoms along macroscopic particle steps. Specifically, FLUKA relies on the Molière multiple Coulomb scattering (MCS) theory [49], in which the angular distribution per unit solid angle after a path length s is

$$F(\theta; s) \approx f^{(0)}(\vartheta) + \frac{1}{B} f^{(1)}(\vartheta) + \frac{1}{B^2} f^{(2)}(\vartheta) + \ldots, \tag{3.1}$$

where the reduced angle $\vartheta = \theta/(\chi_c B^{1/2})$ depends on the characteristic scattering angle χ_c and the material-dependent dimensionless parameter B [50], while

$$f^{(n)}(\vartheta) = \frac{1}{n!} \int_0^\infty \omega \exp\left(-\frac{\omega^2}{4}\right) \left[\frac{\omega^2}{4} \ln\left(\frac{\omega^2}{4}\right)\right]^n J_0(\vartheta\omega) d\omega, \tag{3.2}$$

where J_0 is the Bessel function of the first kind. The term $f^{(0)}(\vartheta) = 2\exp(-\vartheta^2)$ represents the Gaussian core of the distribution, while the next two functions, $f^{(1)}(\vartheta)$ and $f^{(2)}(\vartheta)$, account for the non-Gaussian tails of the distribution, and are evaluated by numerical integration [51]. A more comprehensive discussion is presented in Ref. [50].

The Molière MCS theory has several virtues: the angular distribution is nearly analytical and it can be applied to any charged particle species. Nevertheless, it also has some limitations: the underlying single-scattering differential cross section (DXS) is a screened Rutherford DXS, the small angle approximation is assumed, and the path length s has to be 10-20 times larger than the mean free path for Coulomb scattering. When the assumptions of the Molière theory do not hold or for particular applications, *e.g.*, scattering in very thin geometries, FLUKA offers the possibility to switch to single scattering, sampling individual Coulomb collisions explicitly (at a significant cost in terms of central processing unit (CPU) time).

Unfortunately, the underlying screened Rutherford single-scattering DXS adopted by Molière precludes the use of an arbitrary DXS, such as that of Eq. (2.9). Therefore, nuclear

elastic scattering has to be treated as a dedicated interaction mechanism in FLUKA, along with Coulomb scattering. As mentioned in the discussion of Eq. (2.15), this approach is formally questionable. In this chapter, the interplay between Coulomb and nuclear elastic scattering is investigated and the error stemming from their necessary additive treatment is quantified. Furthermore, the improper treatment of elastic recoils from Coulomb single scattering up to FLUKA v4-3.4 is addressed, as it represents an additional limitation of FLUKA for single-event upset (SEU) production [12].

3.1 Coulomb elastic scattering of protons in FLUKA

Coulomb scattering in FLUKA is predicated on a Rutherford DXS, accounting for electron screening according to an expression derived by Molière [49, 52]:

$$\left.\frac{\mathrm{d}\sigma}{\mathrm{d}\hat{\Omega}}\right|_{\mathrm{Cou}} = \left[\frac{Z_{\mathrm{p}}^2 Z_{\mathrm{t}}^2 e^4}{4c^4\beta^2 E^2 \sin^4\frac{\tilde{\theta}}{2}}\right]\left[\frac{(1-\cos\tilde{\theta})^2}{\left(1-\cos\tilde{\theta}+\frac{\chi_{\mathrm{a}}^2}{2}\right)^2}\right], \tag{3.3}$$

where Z_{p} and Z_{t} are the atomic numbers of the projectile and of the target nucleus, respectively, the constants e and c are the elementary charge and the speed of light, respectively; E is the kinetic energy of the projectile, β is the ratio between the velocity of the projectile and c, χ_{a} is the screening angle [49], and $\tilde{\theta}$ is the scattering angle. The latter is sampled in FLUKA in the laboratory frame as:

$$\tan^2\frac{\tilde{\theta}}{2} = \frac{\eta\chi_{\mathrm{a}}^2}{(1-\eta)\left(4+\chi_{\mathrm{a}}^2\right)}, \tag{3.4}$$

where η is a uniformly distributed random number, as discussed in Appendix C.

While the DXS for Coulomb scattering is evaluated in the laboratory frame, the partial-wave DXS for nuclear elastic scattering, discussed in Chapter 2, is evaluated in the center-of-mass (CM). To investigate the combined effect of Coulomb and nuclear elastic scattering, both DXSs have to be expressed in the same reference frame. The transformation of angular distributions from the lab to the CM is:

$$\frac{\mathrm{d}\sigma}{\mathrm{d}\hat{\Omega}_{\mathrm{CM}}} = \frac{\mathrm{d}\sigma}{\mathrm{d}\hat{\Omega}_{\mathrm{lab}}}\frac{\gamma(1+\xi\cos\theta)}{\left[\gamma^2(\cos\theta+\xi)^2+\sin^2\theta\right]^{3/2}}, \tag{3.5}$$

where γ is the Lorentz factor for the boost from the lab to the CM, θ is the CM scattering angle and

$$\xi = \frac{\beta E'_{\mathrm{p}}}{p}, \tag{3.6}$$

where E'_{p} and p are the total CM energy and CM momentum, respectively, of the proton after the elastic collision; see Appendix D for the derivation of Eq. (3.5).

To assess the disparity of FLUKA sampling Eq. (3.3) in the laboratory frame instead of the CM frame, as evaluated in Eq. (2.12), Fig. 3.1a depicts Eq. (3.3) (solid yellow) sampled from FLUKA in the laboratory frame and boosted to the CM using Eq. (3.5), and Eq. (2.12) (dashed black) evaluated in the CM for 5 MeV protons on ^{6}Li. Minor discrepancies of $O(1)$ are observed at very large scattering angles, which are however substantially suppressed compared to forward scattering. Figure 3.1b displays the same

benchmark for 200 MeV protons on ^{208}Pb, where no noticeable differences are observed. Therefore, the disparity between FLUKA sampling Eq. (3.3) in the laboratory frame and Eq. (2.12) evaluated in the CM is negligible for the proton energies and nuclei treated in this thesis.

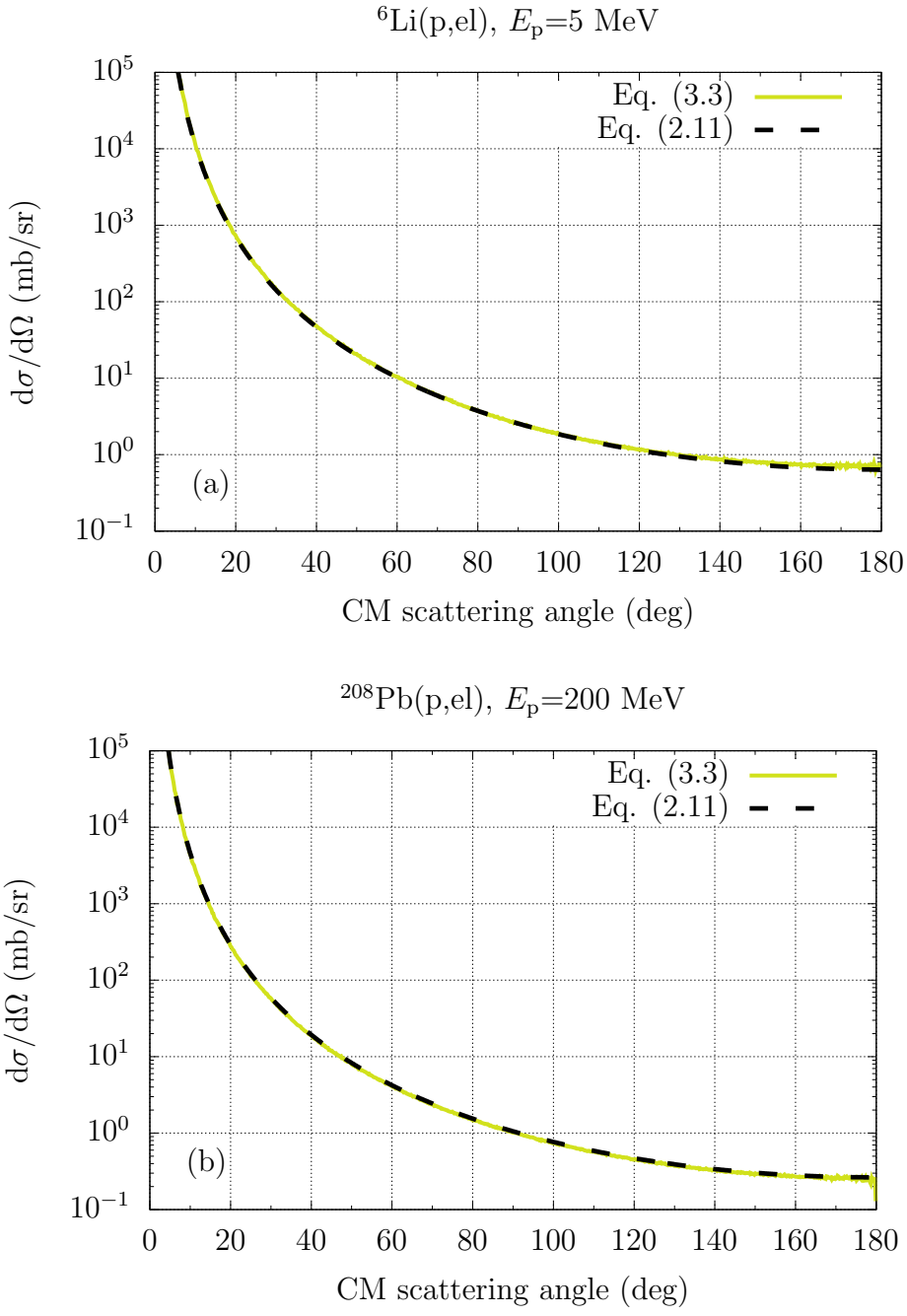

Figure 3.1: Comparison between the Molière differential cross section sampled by FLUKA from Eq. (3.3) in the laboratory frame and that evaluated in the CM with Eq. (2.12) for the elastic scattering of protons on ^{6}Li at 5 MeV (a) and on ^{208}Pb at 200 MeV (b).

3.1.1 Nuclear finite-size form factors

Equation (3.3) describes the Coulomb scattering off a point-like nucleus. However, the nucleus has an extended distribution of charge, which can be effectively accounted for by means of nuclear finite-size form factors $F(q^2)$ [53]. Accordingly, the DXS for Coulomb single scattering in FLUKA, Eq. (3.3), is modified as [52]:

$$\left.\frac{\mathrm{d}\sigma}{\mathrm{d}\hat{\Omega}}\right|_{\mathrm{Cou}} = \left[\frac{z^2 Z^2 e^4}{4c^4\beta^2 E^2 \sin^4\frac{\tilde{\theta}}{2}}\right]\left[\frac{(1-\cos\tilde{\theta})^2}{\left(1-\cos\tilde{\theta}+\frac{\chi_{\mathrm{a}}^2}{2}\right)^2}\right]\times\left|F(q^2)\right|^2. \tag{3.7}$$

Since the charge distribution leads to a decrease in the probability of large-angle scattering events, the nuclear finite-size form factors have the role of suppressing large-angle deflections. To investigate their behaviour as a function of energy, the nuclear finite-size form factors employed by FLUKA [53] have been extracted for protons at various energies on different nuclei. Figure 3.2 displays a comparison between FLUKA nuclear finite-size form factors (dashed curves) and partial-wave estimates, set as the ratio of the full (Coulomb + nuclear) partial-wave DXS to the Molière DXS (solid black curves), for the elastic scattering of 50 MeV protons on ^{208}Pb (a) and of 1 MeV protons on ^{28}Si (b); the solid red curves are discussed below. At high energies, the FLUKA nuclear finite-size form factors are excessively suppressive and lack structure, as shown in Fig. 3.2a. Even at energies below Coulomb barrier (CB), where one expects a Rutherford-like DXS and nuclear finite-size form factors equal to unity, they substantially suppress large scattering angles, as displayed in Fig. 3.2b.

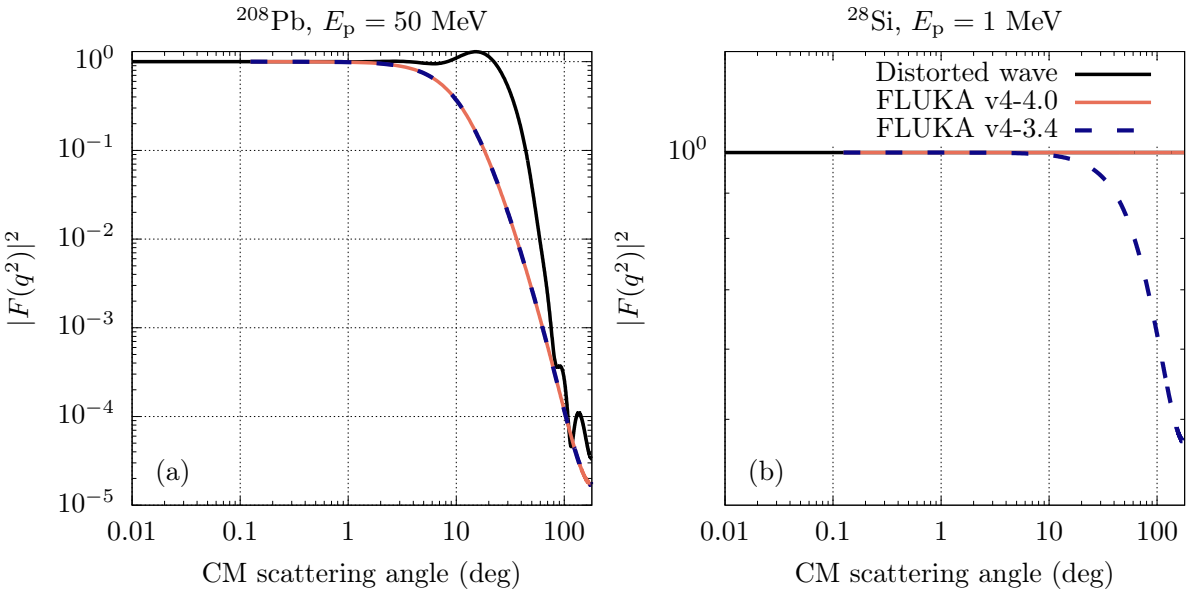

Figure 3.2: Nuclear finite-size form factors for 50 MeV protons elastically scattering on ^{208}Pb (a) and 1 MeV protons on ^{28}Si (b).

To understand whether the unexpected behaviour observed below CB stems from the nuclear finite-size form factors or from the CB energies in FLUKA, the latter have been extracted and compared with partial-wave estimates, set as the energies where the DXS deviates by more than 5% from a Rutherford-like shape. Figure 3.3 displays with empty black dots and with filled blue dots the distorted-wave-estimated and the FLUKA

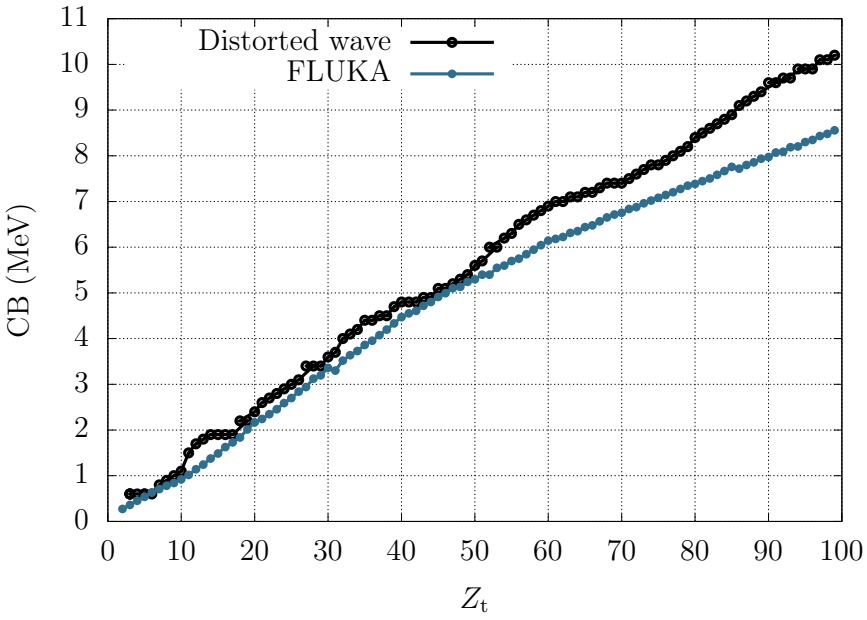

Figure 3.3: Coulomb barrier energies for protons as a function of the atomic number of the target nucleus.

CB energies, respectively, as a function of the atomic number of the target nucleus, Z_t. Since the CB energies are comparable, they have been left unaltered in FLUKA v4-4.0. Therefore, the FLUKA nuclear finite-size form factors suppressed the large-angle deflections excessively for proton energies below CB, where the DXS should be Rutherford-like with no nuclear effects taken into account.

Thus, as far as elastic scattering is concerned, in FLUKA v4-4.0 special care has been devoted to ensure that at energies below CB only Coulomb scattering is accounted for and that proton nuclear elastic scattering is inactive. Below CB, nuclear finite-size form factors in Coulomb scattering have been set to unity, as illustrated in Fig. 3.2b by the solid red curves, and the integrated cross section for proton nuclear elastic scattering has been set to zero. In an energy window of ±5% of the CB, the nuclear finite-size form factors are allowed to deviate from 1 and the integrated cross section for proton nuclear elastic scattering is gradually switched on. Finally, at higher energies, both quantities take their full values. As an example, Fig. 3.2a depicts the FLUKA v4-4.0 nuclear finite-size form factors in solid red, which are unaltered with respect to those of FLUKA v4-3.4.

3.1.2 Error incurred when treating Coulomb and nuclear elastic scattering as additive interaction mechanisms

In this section the error incurred by treating Coulomb and nuclear elastic scattering as separate (additive) interaction mechanisms has been assessed. A dedicated benchmark has been carried out, whereby Coulomb and nuclear elastic scattering events have been sampled with FLUKA v4-4.0. The combined DXS resulting from the sum of Coulomb and nuclear elastic scattering events (each scaled with their respective integrated cross section) has been compared in absolute units of mb/sr with the corresponding experimental and/or partial-wave DXS for light or heavy nuclei, respectively. This comparison has been performed for a series of 27 target nuclei (from ^{2}H to ^{238}U) on a grid of 30 proton energies (from CB up to 250 MeV).

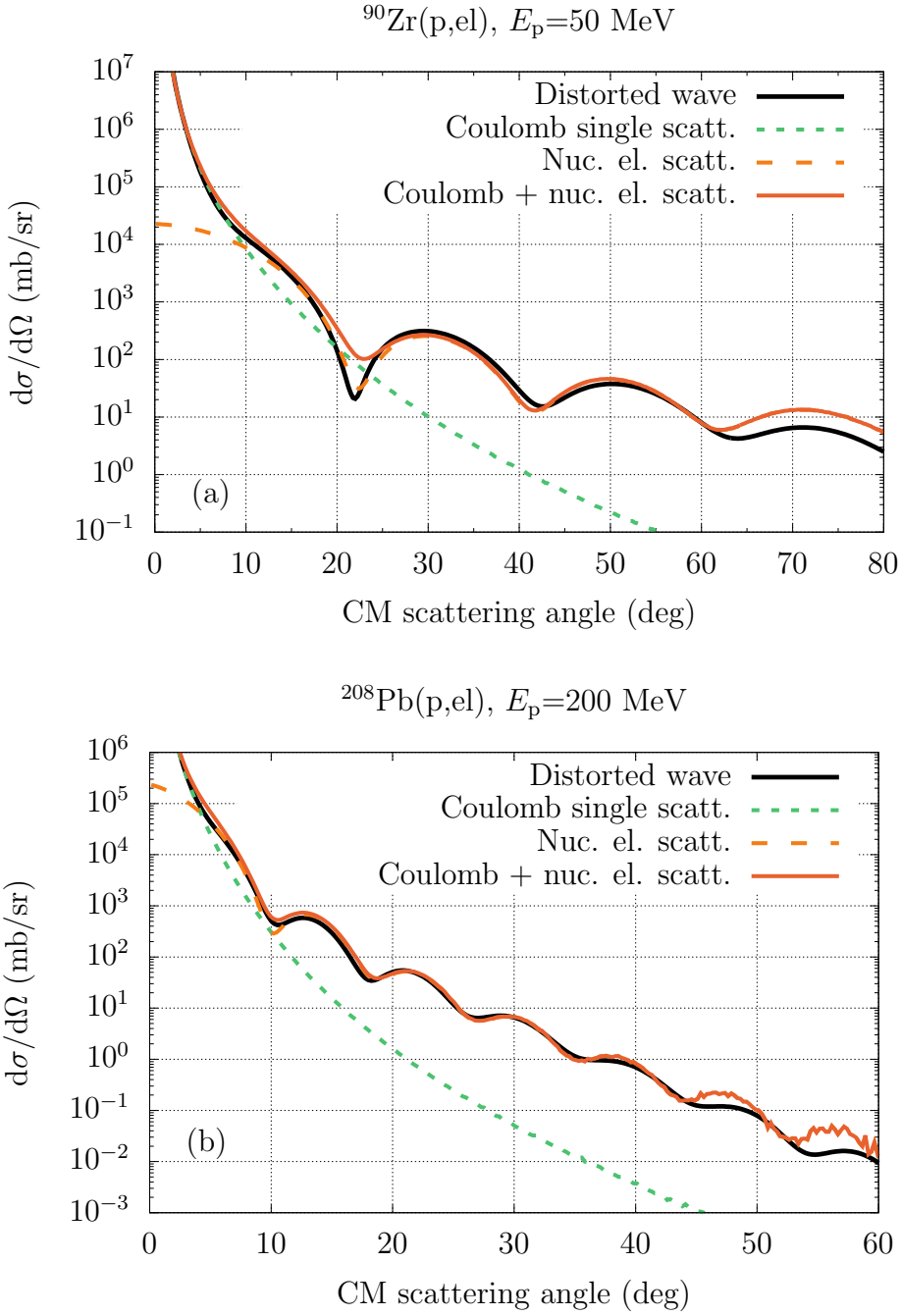

Figure 3.4: Error incurred when treating Coulomb and nuclear elastic scattering as separate interaction mechanisms for protons on ^{90}Zr at 50 MeV (a) and on ^{208}Pb at 200 MeV (b), exposed as mild differences between the solid red and the thick solid black curves near the first minimum of the distorted-wave DXS.

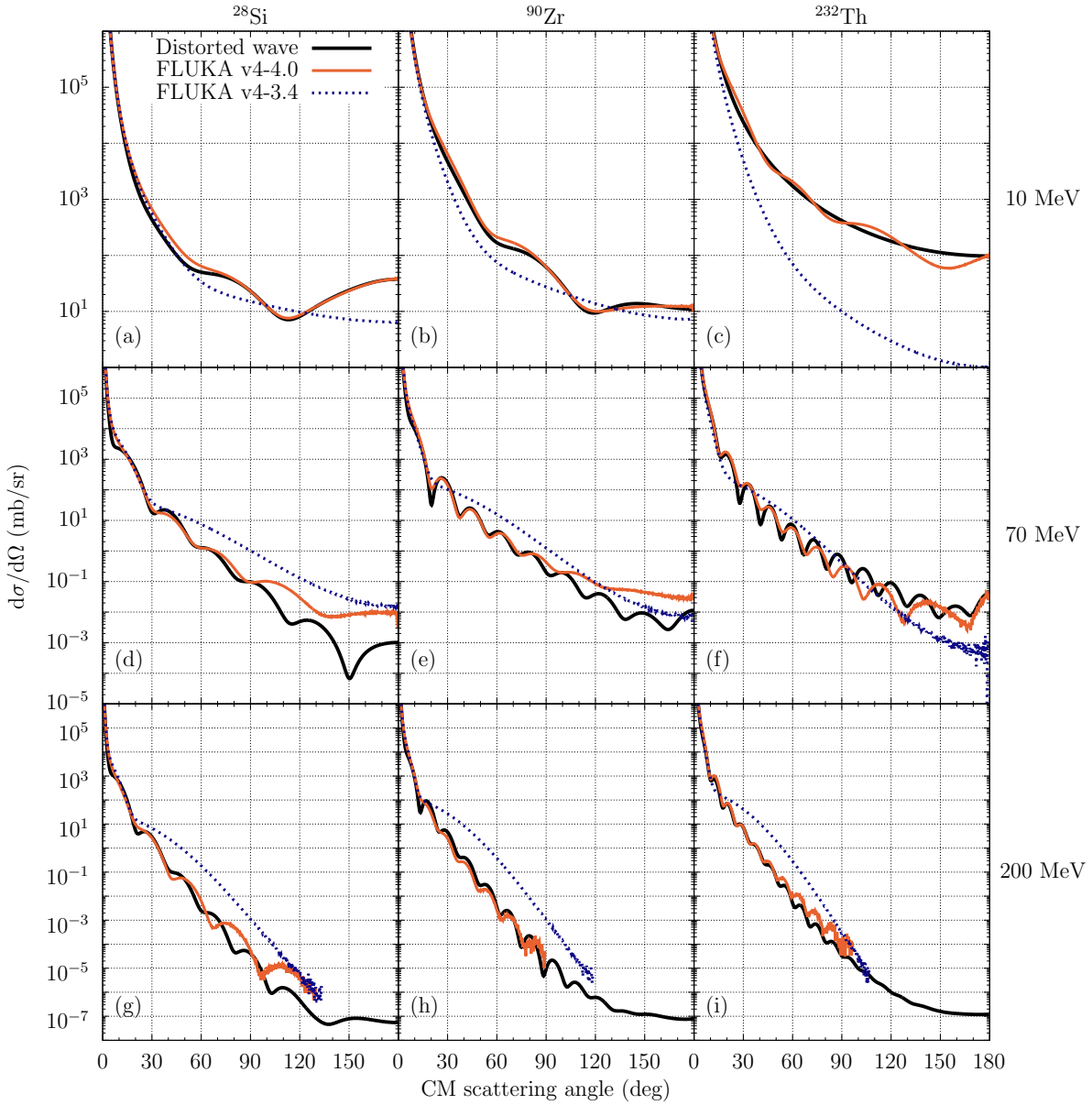

Figure 3.5: Same as Fig. 2.10 for the full (Coulomb plus nuclear) elastic scattering of protons on nuclei.

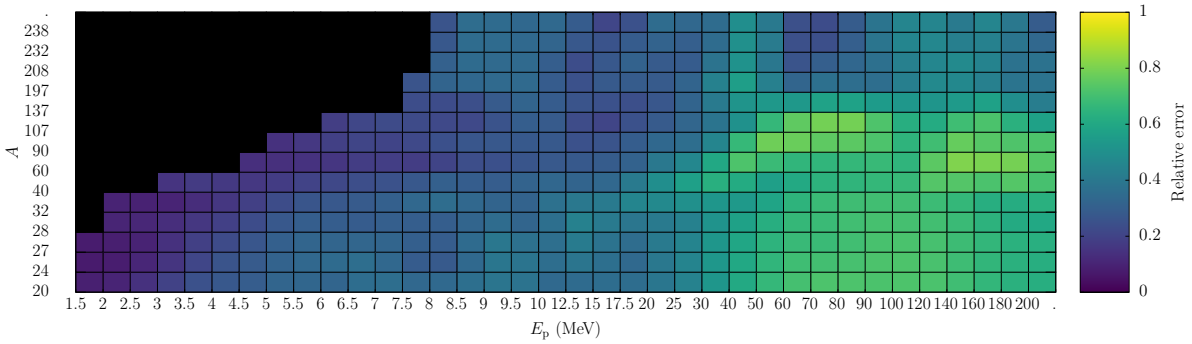

Figure 3.6: Maximum relative difference between partial-wave/experimental and fitted differential cross sections for heavy target nuclei.

Figure 3.4a displays the output of this benchmark for 50 MeV protons elastically scattered from ^{90}Zr. The thick solid black curve represents the DXS calculated with the partial-wave scheme of Section 2.1, the dotted dark-green curve represents the angular distribution of Coulomb single scattering events sampled with FLUKA v4-4.0, the dashed orange curve represents the angular distribution for nuclear elastic scattering sampled with the model presented in this work, while the solid red curve is the sum of the last two curves. At this intermediate energy, and especially for light and intermediate nuclei, localized overestimations of several 10% at intermediate scattering angles are observed, where the Coulomb single scattering DXS is not yet sufficiently suppressed. Instead, at large scattering angles (relevant for the radiation-to-electronics effects assessment in Chapter 4) the agreement is by construction reasonable. Finally, for heavy nuclei, the incurred error is minimal since the Coulomb single scattering DXS decreases swiftly, as shown in Fig. 3.4b.

To quantify the error incurred by treating Coulomb and nuclear elastic scattering as separate interaction mechanisms, the maximum relative difference between partial-wave/experimental and fitted DXSs has been evaluated for the proton energies and target nuclei considered in this work. For instance, Fig. 3.6 displays the maximum relative difference calculated for heavy nuclei (for which the proton energy grid on which fit parameters are tabulated is fixed). The largest errors have been obtained for light and intermediate nuclei at intermediate and high proton energies, where the Coulomb single scattering DXS is not yet sufficiently suppressed, as shown in Fig. 3.4a. Instead, for heavy nuclei, this artefact does not persist and the errors are considerably smaller, as illustrated in Fig. 3.4b. For all nuclei at low proton energies, the errors are at most a few 10%. Note that the black squares in Fig. 3.6 at proton energies below ~10 MeV are due to the absence of nuclear elastic scattering below CB, where concerning elastic scattering, only Coulomb scattering is active.

To further visualize the incurred error, Fig. 3.5 extends Fig. 2.10 with the inclusion of Coulomb elastic scattering, directly sampled from FLUKA v4-4.0 - with the relevant difference that now the thin red curves are sampled from (and not a direct evaluation of) parametrized expression (2.18). This comparison reveals the typically negligible error incurred by the separate treatment of Coulomb and nuclear elastic scattering, and an overall very good agreement, both in the forward scattering and in the large-scattering-angle domains. Additionally, Fig. 3.5 shows that the proton nuclear elastic scattering model employed up to FLUKA v4-3.4 tends to either under- or over-estimate the actual DXS at large scattering angles. For heavy nuclei, for which the CB for protons approaches 10 MeV, the FLUKA v4-3.4 DXS for the elastic scattering (Coulomb plus nuclear) of protons with energies slightly above Coulomb barrier may underestimate the partial-wave DXS by orders of magnitude, as illustrated in subfigure (c). Instead, the FLUKA v4-4.0 model for proton nuclear elastic scattering presented here does not suffer from these artefacts. Incidentally, this benchmark also probes the good performance of the integrated cross section scheme (discussed in Section 2.6) in scaling correctly the angular distribution for proton nuclear elastic scattering.

3.2 Coulomb-single-scattering recoils

In Ref. [12], a further limitation of FLUKA impacting the simulation of SEU production in the ISSI SRAM [16] under proton irradiation was identified. Up to FLUKA v4-3.4, in the course of a Coulomb-single-scattering event, the direction of the charged projectile is

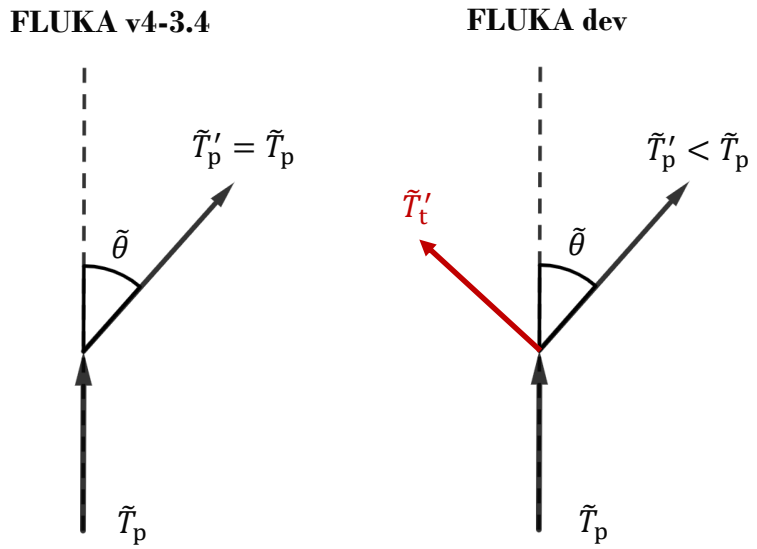

Figure 3.7: Schematic of a Coulomb single scattering event in FLUKA v4-3.4 (left) and in a development version of FLUKA (right).

updated, while its energy is not, as illustrated in the left panel of Fig. 3.7. The energy transferred to target atoms in the course of multiple Coulomb collisions is accounted for in an average way along macroscopic particle steps via a nuclear stopping power term. However, this approach prevents event-by-event analyses, and therefore does not allow to assess the contribution of individual Coulomb collisions to the production of SEUs. Nevertheless, Coulomb collisions may contribute to SEU production, especially those with large scattering angle. Suppressed as they may be, when they do occur there is a risk of triggering an SEU [14]. To quantify their event-by-event contribution to SEU production, a tentative closing of the Coulomb-single-scattering kinematics (as well as the explicit transport of the recoil where applicable) has been implemented in a development version of FLUKA. This model ingredient, amounting to an event-by-event account of nuclear-stopping-power effects, has been developed and tested only for proton projectiles.

Consider a proton with mass m_{p} and momentum $\tilde{\boldsymbol{p}}_{\mathrm{p}}$ which scatters elastically on a target nucleus with mass m_{t}, originally at rest. Before the collision, the total four-momentum of the system in the lab is

$$\tilde{\boldsymbol{\mathcal{P}}} = \tilde{\boldsymbol{\mathcal{P}}}_{\mathrm{p}} + \tilde{\boldsymbol{\mathcal{P}}}_{\mathrm{t}} = \left(m_{\mathrm{p}} + \tilde{T}_{\mathrm{p}} + m_{\mathrm{t}}, \tilde{\boldsymbol{p}}_{\mathrm{p}}\right) \equiv (\tilde{E}, \tilde{\boldsymbol{p}}_{\mathrm{p}}). \tag{3.8}$$

Its inner product gives the s invariant of the system:

$$s = \tilde{\boldsymbol{\mathcal{P}}} \cdot \tilde{\boldsymbol{\mathcal{P}}} = \tilde{E}^2 - \tilde{p}_{\mathrm{p}}^2 = \left(m_{\mathrm{p}} + m_{\mathrm{t}}\right)^2 + 2\tilde{T}_{\mathrm{p}} m_{\mathrm{t}}. \tag{3.9}$$

For simplicity, the system of Cartesian coordinates is orientated such that the z-axis is parallel to the direction of the incident proton:

$$\tilde{\boldsymbol{p}}_{\mathrm{p}} = \tilde{p}_{\mathrm{p}} \hat{\boldsymbol{z}}. \tag{3.10}$$

The boost to the CM frame is

$$\boldsymbol{\beta} = \frac{\tilde{p}_{\mathrm{p}}}{\tilde{E}} \hat{\boldsymbol{z}}, \tag{3.11}$$

and the Lorentz factor is

$$\gamma = \frac{1}{\sqrt{1-\beta^2}} = \frac{\tilde{E}}{\sqrt{s}}. \tag{3.12}$$

Their product is

$$\beta\gamma = \frac{\tilde{p}_{\mathrm{p}}}{\sqrt{s}}. \tag{3.13}$$

Finally, the CM momentum is

$$p = \frac{\tilde{p}_{\mathrm{p}} m_{\mathrm{t}}}{\sqrt{s}}. \tag{3.14}$$

The CM scattering angle, *i.e.*, the angle between the incoming and outgoing directions of the proton is given by:

$$\cos\theta = \hat{\boldsymbol{p}}_{\mathrm{p}} \cdot \hat{\boldsymbol{p}}'_{\mathrm{p}}, \tag{3.15}$$

where the CM momentum of the proton after the elastic collision is

$$\boldsymbol{p}'_{\mathrm{p}} = p\,(\sin\theta, 0, \cos\theta)\,, \tag{3.16}$$

where the x and y axes have been oriented such that $p_{\mathrm{p}y} = 0$. An arbitrary rotation around $\hat{\boldsymbol{z}}$ leaves the kinematics unchanged. The four-momentum of the proton in the laboratory frame can be obtained by performing a Lorentz-boost:

$$\tilde{\boldsymbol{\mathcal{P}}}'_{\mathrm{p}} = \begin{pmatrix} \tilde{E}'_{\mathrm{p}}(\tilde{\theta}) \\ \tilde{p}'_{\mathrm{p}}(\tilde{\theta})\sin\tilde{\theta} \\ 0 \\ \tilde{p}'_{\mathrm{p}}(\tilde{\theta})\cos\tilde{\theta} \end{pmatrix} = \begin{pmatrix} \gamma & 0 & 0 & \beta\gamma \\ 0 & 1 & 0 & 0 \\ 0 & 0 & 1 & 0 \\ \beta\gamma & 0 & 0 & \gamma \end{pmatrix} \begin{pmatrix} E'_{\mathrm{p}} \\ p\sin\theta \\ 0 \\ p\cos\theta \end{pmatrix} = \begin{pmatrix} \gamma E'_{\mathrm{p}} + \beta\gamma p\cos\theta \\ p\sin\theta \\ 0 \\ \gamma p\cos\theta + \beta\gamma E'_{\mathrm{p}} \end{pmatrix}, \tag{3.17}$$

which is the starting point for evaluating the kinetic energy of the elastic recoil. From Eq. (3.17) one can extract:

$$\begin{aligned} \tilde{p}'_{\mathrm{p}}\sin\tilde{\theta} &= p\sin\theta \\ \tilde{p}'_{\mathrm{p}}\cos\tilde{\theta} &= \gamma p\cos\theta + \gamma\beta E'_{\mathrm{p}}. \end{aligned} \tag{3.18}$$

Dividing the above relations yields:

$$\tan\tilde{\theta} = \frac{p\sin\theta}{\gamma p\cos\theta + \gamma\beta E'_{\mathrm{p}}} = \frac{\sin\theta}{\gamma\cos\theta + \gamma\xi}, \tag{3.19}$$

where $\xi = \dfrac{\beta E'_{\mathrm{p}}}{p}$. Rearranging the terms gives:

$$\gamma\tan\tilde{\theta}\cos\theta + \gamma\xi\tan\tilde{\theta} = \sin\theta. \tag{3.20}$$

Using the trigonometric identity $\sin^2\theta + \cos^2\theta = 1$ further implies

$$\gamma\tan\tilde{\theta}\left(\pm\sqrt{1-\sin^2\theta}\right) = \sin\theta - \gamma\xi\tan\tilde{\theta}. \tag{3.21}$$

Squaring Eq. (3.21) and rearranging the terms yields a quadratic equation in $\sin\theta$:

$$\left(1+\gamma^2\tan^2\tilde{\theta}\right)\sin^2\theta - \left(2\gamma\xi\tan\tilde{\theta}\right)\sin\theta + \gamma^2(\xi^2-1)\tan^2\tilde{\theta} = 0. \tag{3.22}$$

The discriminant of this equation is

$$\Delta = 4\gamma^2 \tan^2\tilde{\theta}\left[1+\gamma^2(1-\xi^2)\tan^2\tilde{\theta}\right]. \tag{3.23}$$

Hence, the solution of Eq. (3.22) is

$$\sin\theta = \frac{\xi \pm \sqrt{1+\gamma^2(1-\xi^2)\tan^2\tilde{\theta}}}{\dfrac{1}{\gamma\tan\tilde{\theta}}+\gamma\tan\tilde{\theta}}. \tag{3.24}$$

Since $\theta \in [0,\pi]$, the solution of Eq. (3.24) has to be in the interval $[0,1]$.

From Eq. (3.18), the momentum of the proton after the elastic collision is

$$\tilde{p}'_{\mathrm{p}} = p\frac{\sin\theta}{\sin\tilde{\theta}}, \tag{3.25}$$

and its lab kinetic energy is

$$\tilde{T}'_{\mathrm{p}} = \sqrt{\tilde{p}'^2_{\mathrm{p}} + m^2_{\mathrm{p}}} - m_{\mathrm{p}}. \tag{3.26}$$

Finally, the kinetic energy of the elastic recoil is evaluated in FLUKA as:

$$\tilde{T}'_{\mathrm{t}} = \tilde{T}_{\mathrm{p}} - \tilde{T}'_{\mathrm{p}}. \tag{3.27}$$

It can take values between 0 and a maximum kinetic energy transfer, $T^{\max}_{\mathrm{t}} = 2\tilde{p}^2_{\mathrm{p}}\, m_{\mathrm{t}}/s$, which can be derived from the inverse Lorentz boost, Eq. (3.17), for the target nucleus by setting $\theta = \pi$.

The closing of the Coulomb single scattering kinematics has been implemented in a development version of FLUKA. Coulomb recoils are transported if their energy is above threshold, otherwise their energy is deposited locally. Thanks to this development, the explicit contribution of Coulomb recoils to SEU production can be quantified and it is accessible in a development version of FLUKA (see Chapter 4).

Chapter 4

SEU production in commercial SRAMs under proton irradiation

A single-event upset (SEU) is a random single bit flip induced in an electronic component by direct ionization from traversing swift charged projectiles and/or by recoils from nuclear elastic/inelastic interactions. Although non-destructive, SEUs can still lead to data corruption, incorrect computations, and disruptions in operation, among other operational risks [5–7]. Quantifying and understanding the impact of SEUs in electronic devices exposed to high-radiation environments is therefore essential.

SEU production can be assessed experimentally but, while quantitative, measurements face several challenges [54, 55]: they involve beam time costs and entail significant complexity in campaign planning (given the potential unavailability of irradiation facilities), data acquisition, and post-processing. Conversely, simulation techniques provide complementary insights by enabling detailed event-by-event modelling of radiation transport within electronic devices, thus offering a microscopic picture of SEU production also for devices which have not yet been irradiated.

To simulate SEU production in electronic devices, various numerical methods have been proposed in the literature. These methods range from comprehensive three-dimensional cell device modelling [56–58], sometimes combined with explicit representations of the circuit layout [59], to Monte Carlo (MC) particle transport calculations integrated with drift-diffusion models for accurate charge collection description [60], and circuit simulators [15, 61–63], to name but a few. One particularly effective approach [13, 64–66] uses general-purpose MC codes [19–21, 67, 68] to simulate energy deposition in the sensitive region of the device, effectively modelled as a rectangular parallelepiped (RPP), from which SEU-production cross sections can be extracted [13, 27]. In this approach, the device is characterized by two parameters: the sensitive volume (SV), where deposited energy is collected, and the critical charge (Q_{crit}), which must be exceeded to induce an SEU. In view of its effectiveness, the RPP-approach has been adopted in this work.

Experimental and simulation assessements of SEU production are performed at CERN by the Radiation to Electronics (R2E) team [4, 22, 23], which ensures the successful operation of the accelerator infrastructure taking into account the effects of radiation exposure on electronic components and systems. Recent R2E simulations [12, 13] of SEU production with FLUKA in an ISSI (Integrated Silicon Solutions Inc.) SRAM [16] under proton irradiation revealed discrepancies of up to two orders of magnitude with respect to experimental cross sections in the 1–10 MeV proton energy range (see Fig. 1.1). This underestimation was attributed to the lack of nuclear elastic scattering of protons below 10 MeV in FLUKA up to v4-3.4, as well as to an improper account of recoils in Coulomb single scattering. Both shortcomings have been addressed in this work, in Chapters 2 and 3, respectively.

The aim of this chapter is twofold. First, the significant role played by recoils from

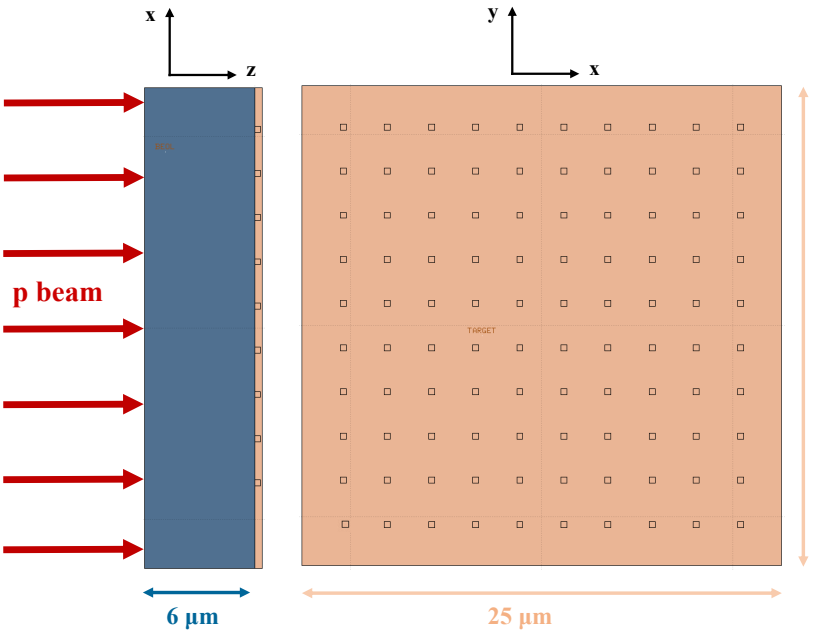

Figure 4.1: ISSI SRAM simulation geometry in FLUKA.

nuclear elastic scattering and Coulomb single scattering in the production of SEUs in the ISSI SRAM under irradiation by 1–10 MeV protons is substantiated. Second, the RPP-model parameters employed for modelling SEU production in SRAMs under proton irradiation with FLUKA are scrutinized.

4.1 SEU production in an ISSI SRAM under 1–10 MeV proton irradiation

In this section, the aforementioned R2E simulations for the ISSI SRAM are revisited with FLUKA v4-4.0 to elucidate the role of elastic recoils from proton nuclear elastic scattering in SEU production. Furthermore, a development version of the code is employed to quantify the event-by-event contribution of recoils from Coulomb single scattering.

A simulation geometry similar to that employed in Ref. [12] has been adopted. The SV of the ISSI SRAM is modelled in FLUKA as a 10×10 array of silicon cubes, each having a length of 310 nm, embedded in a silicon matrix placed on a back-end-of-line (BEOL) layer composed of SiO_2, as illustrated schematically in Fig. 4.1. The considered parallel proton beam, with energies ranging from 600 keV to 200 MeV, fully covers the transverse surface of the SRAM. For each considered energy, the average energy deposition spectrum in a cube, $\mathrm{d}N/\mathrm{d}E_{\mathrm{dep}}$, has been scored on an event-by-event basis.

For instance, the simulated $\mathrm{d}N/\mathrm{d}E_{\mathrm{dep}}$ for 8 MeV protons (thick black curve) is depicted in Fig. 4.2. Exploiting the particle-latching capabilities of FLUKA, the spectrum is further resolved into contributions from various particle histories. The main peak (dashed yellow curve) corresponds to proton histories involving only direct ionization and Coulomb scattering by incident protons. The additional features extending up to ~600 keV arise from energy depositions by recoiling nuclei from nuclear elastic scattering (teal curve) and from Coulomb single scattering (green curve), along with energy depositions from fragments and residual nuclei from nuclear reactions (dashed blue curve). The maximum kinetic energy transfer (T_{max}) during an elastic collision of an 8 MeV proton with a ^{28}Si or

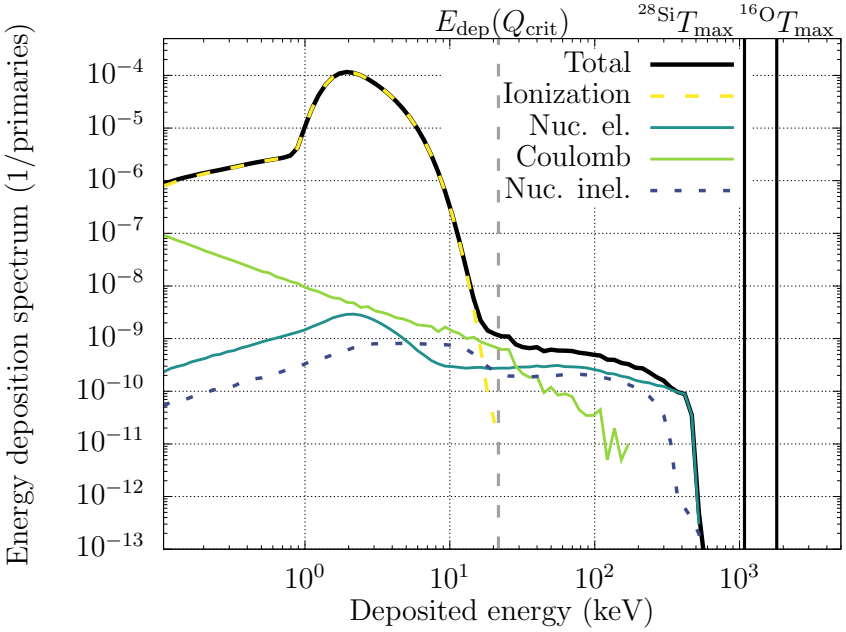

Figure 4.2: Energy deposition histogram of 8 MeV protons in the ISSI SRAM, displaying the contributions from various kinds of particle histories.

^{16}O nucleus is approximately 1 MeV and 1.8 MeV, respectively, as indicated by the black vertical lines in Fig. 4.2. The maximum recoil energy is rarely fully deposited within the SV: some δ rays (knock-on electrons) produced by the elastic recoil may escape from the SV. Nonetheless, energies of the order of several hundred keV, significantly higher than those typically imparted by direct ionization from protons, are easily deposited in the SV.

To trigger an SEU, a threshold energy deposition $E_{\mathrm{dep}}^{\mathrm{th}}$ must take place in the SV. This is typically given in terms of a threshold displaced charge (electron-hole pairs), the so-called critical charge Q_{crit}, given in fC by:

$$Q_{\mathrm{crit}} = E_{\mathrm{dep}}^{\mathrm{th}}(\mathrm{GeV})\ \frac{1\,\mathrm{eV}}{10^{-9}\,\mathrm{GeV}}\ \frac{1}{3.6\,\mathrm{eV}}\ 1.6\times10^{-19}\,\mathrm{C}\ \frac{1\,\mathrm{fC}}{10^{-15}\,\mathrm{C}}, \tag{4.1}$$

where 3.6 eV represents the average energy required to create an electron-hole pair in silicon [69], while 1.6×10^{-19} C is the elementary charge.

For the ISSI SRAM, Q_{crit} is 0.96 fC [12, 13], corresponding to a critical deposited energy $E_{\mathrm{dep}}(Q_{\mathrm{crit}})$ = 21.6 keV, evaluated using Eq. (4.1) and indicated by the vertical dashed grey line in Fig. 4.2. The energy deposited in the SV through direct ionization does not exceed $E_{\mathrm{dep}}(Q_{\mathrm{crit}})$. Consequently, for 8 MeV protons, direct ionization has a negligible impact on SEU production in the ISSI SRAM, which is instead driven by nuclear interactions. Although energy depositions in the SV from Coulomb recoils (green curve) can reach $E_{\mathrm{dep}}(Q_{\mathrm{crit}})$ at this proton energy, this contribution is several orders of magnitude less effective at producing significant energy depositions compared to those in which a nuclear elastic scattering (teal curve) occurred.

The cross section for the production of SEUs, σ_{SEU}, for a given proton energy E_{p}, is given by:

$$\sigma_{\mathrm{SEU}}(Q_{\mathrm{crit}};E_{\mathrm{p}}) = \frac{1}{\Phi}\int_{E_{\mathrm{dep}}(Q_{\mathrm{crit}})}^{\infty} \mathrm{d}E_{\mathrm{dep}}\ \frac{\mathrm{d}N}{\mathrm{d}E_{\mathrm{dep}}}, \tag{4.2}$$

where $\Phi = 1.1\times10^{5}$ cm^{-2} is the incoming beam fluence in the simulation. Figure 4.3 displays

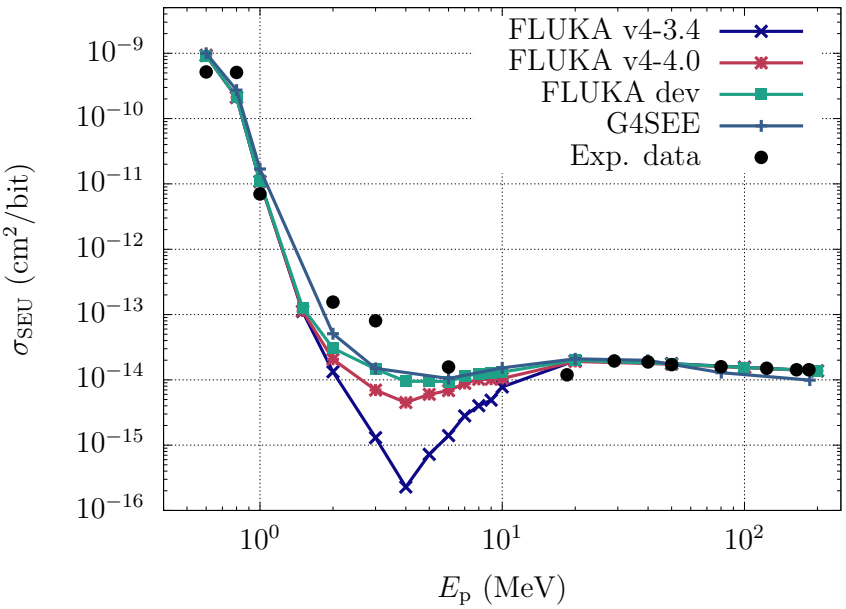

Figure 4.3: SEU production cross section in the ISSI SRAM as a function of the incident proton energy.

$\sigma_{\mathrm{SEU}}(Q_{\mathrm{crit}}; E_{\mathrm{p}})$ as a function of proton energy. Experimental SEU cross sections [12, 13] are shown as black dots, with uncertainties smaller than the symbol size (see the discussion on page 43). Estimates of the SEU production cross section obtained with Eq. (4.2) from FLUKA v4-3.4 are represented by crosses (connected by a solid line to guide the eye) and exhibit the aforementioned underestimation by two orders of magnitude compared to experimental SEU cross sections in the 1–10 MeV energy range. In contrast, SEU production cross sections obtained with FLUKA v4-4.0, which incorporates the new model for proton nuclear elastic scattering discussed in Chapter 2, are indicated by stars. Notably, within the 1–10 MeV energy range, the agreement with experimental SEU cross sections improves by a factor of 20. This improvement is largely attributable to the fact that prior to FLUKA v4-3.4, nuclear elastic scattering of protons below 10 MeV was not included. To further illustrate the origin of this improvement, Fig. 4.4 displays the differential cross section (DXS) for the elastic scattering of 4.95 MeV protons on ^{28}Si (a) and 6.48 MeV protons on ^{16}O (b), as implemented in FLUKA v4-3.4 (dashed blue curves), greatly underestimating the experimental angular distributions by up to several orders of magnitude due to the lack of the nuclear elastic scattering contribution, and FLUKA v4-4.0 (solid red curves), reasonably matching the experimental angular distributions. To produce a ^{28}Si (^{16}O) recoil having at least the critical deposited energy of 21.6 keV, a proton must be elastically scattered by an angle greater than 23 deg (17 deg). As shown in Fig. 4.4, it is precisely at scattering angles exceeding these thresholds, marked by vertical black lines, where the DXS has significantly improved from FLUKA v4-3.4 to FLUKA v4-4.0.

Furthermore, SEU production cross sections obtained with a development version of FLUKA (which includes an explicit treatment of elastic recoils in Coulomb single scattering, along with an ad-hoc biasing scheme for nuclear elastic scattering), represented by squares in Fig. 4.3, show a slightly improved agreement with experimental cross sections in the 2–6 MeV energy range. Comparable results are obtained with other MC tools, such as G4SEE [68], a Geant4-based application [67], as indicated by the curve with plus symbols in Fig. 4.3. The minor differences between the predictions of FLUKA (squares)

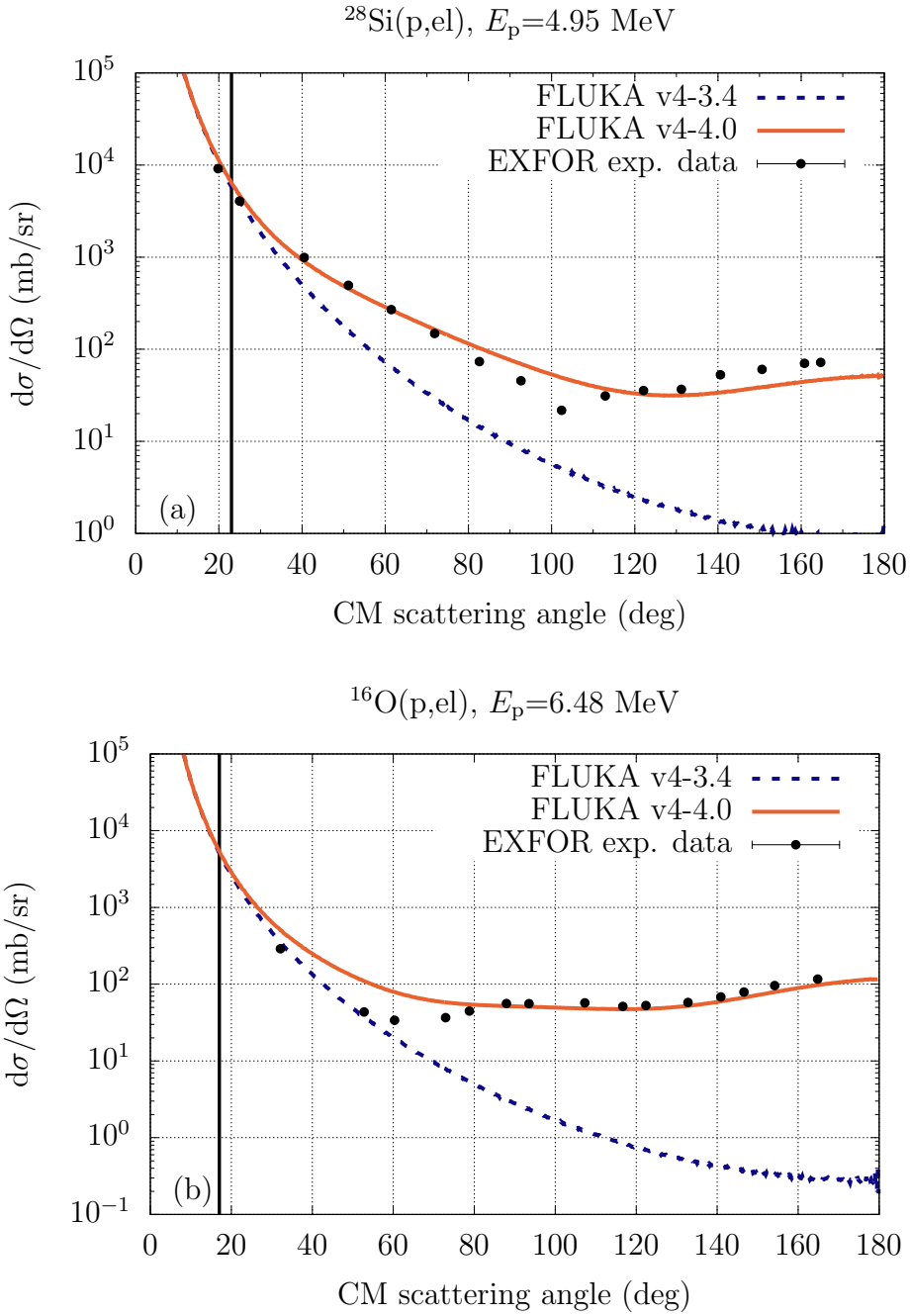

Figure 4.4: Differential cross section for the elastic scattering of 4.95 MeV protons on ^{28}Si (a) and protons of 6.48 MeV on ^{16}O (b). Statistical uncertainties are omitted for clarity.

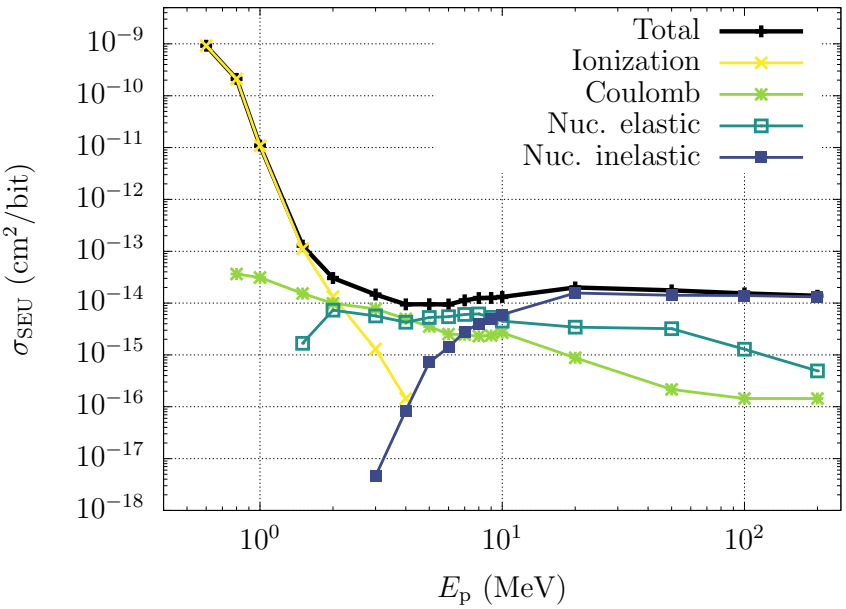

Figure 4.5: SEU production cross section in the ISSI SRAM induced by protons resolved into contributions from various kinds of particle histories.

and G4SEE (plus symbols) can be attributed to slight differences in the treatment of proton ionization and elastic scattering in these two codes. However, at energies between 2 and 5 MeV, significant discrepancies remain when compared to experimental cross sections, themselves subject to uncertainties . These discrepancies may stem from uncertainties in the determination of Q_{crit} or from approximations and simplifications in the simulation setup (such as approximations of the SV dimensions or a simplified BEOL composition). Nevertheless, the overall agreement with experimental SEU cross section is remarkable.

Finally, Fig. 4.5 illustrates the contribution to σ_{SEU} from various kinds of particle histories, allowing one to identify the interaction mechanisms governing SEU production in the ISSI SRAM across different proton energy ranges. For proton energies below ~2 MeV, direct ionization by incident protons is the dominant mechanism triggering SEUs. In the energy range from 2 to 8 MeV, energy depositions by recoils from nuclear elastic and Coulomb single scattering become the primary contributors. At energies above ~8 MeV, SEU production is mainly driven by energy depositions by recoiling residuals and fragments from nuclear reactions.

4.2 RPP-model parameter trends for SEU production simulations

The benchmark of the foregoing section for the ISSI SRAM [16] has been extended in this section to two other commercial bulk planar SRAMs: the Cypress SRAM [70] and the ESA Monitor SRAM [71], which have been extensively tested and characterized in previous studies [13, 24]. Furthermore, the RPP-model parameters adopted to simulate SEU production in the considered SRAMs under proton irradiation with FLUKA have been scrutinized. The contents of this section have led to a dedicated publication [72].

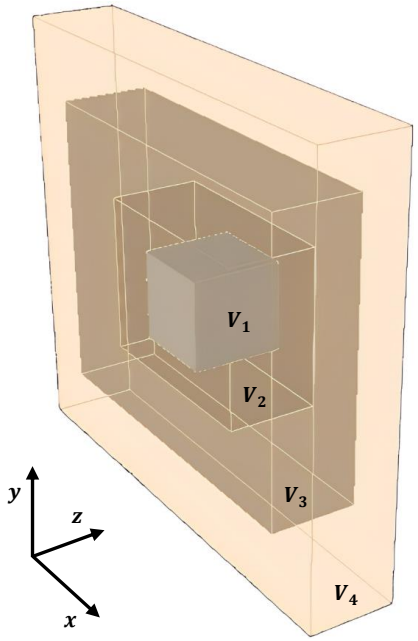

Figure 4.6: Schematic 3D view of a nested RPP. All volumes have the same depth along the z-axis.

4.2.1 MC simulation of SEU production in the RPP model

The SV of an SRAM can be modelled as either a single or a nested RPP [9], [12, Sec. 3.3]. In the latter, multiple encapsulated SVs are used, as illustrated in Fig. 4.6. The central region of these SVs represents the p-n junction of the two transistors in the OFF state (the sensitive nodes where charge is collected), while the outer regions account for more distant areas from which charge can diffuse towards the sensitive nodes. However, RPPs are not intended to replicate the physical structure of the SRAM cell, but rather to effectively model the overall response of the device. The transverse dimensions (x and y) and thickness (z) of the innermost volume (V_1) can be initially assumed equal and are estimated as

$$x = y = z = \sqrt{\max[\sigma_{\mathrm{SEU}}(E_{\mathrm{p}})]}, \tag{4.3}$$

where $\max[\sigma_{\mathrm{SEU}}(E_{\mathrm{p}})]$ is the maximum experimental SEU production cross section due to proton direct ionization [13] (when available), displayed in Fig. 4.7 as a function of proton energy E_{p}. For the encapsulating volumes $V_2, \ldots, V_N$, the thickness is set equal to that of V_1, while their transverse dimensions are inferred from experimental SEU cross sections induced by heavy ions, $\sigma_{\mathrm{SEU},2}, \ldots, \sigma_{\mathrm{SEU},N}$, listed in Table 4.2, as:

$$x_i = y_i = \sqrt{\sigma_{\mathrm{SEU},i}}, \quad i = 2, \ldots, N, \tag{4.4}$$

as further detailed in Refs. [9], [12, Sec. 5.1], [13]. Each SV is assigned a different charge collection efficiency coefficient (α) to account for charge drift and diffusion processes [64]. The innermost SV is assigned $\alpha = 1$, while for each encapsulating SV α is determined as follows. Using the aforementioned heavy ion induced SEU production cross sections sorted increasingly, the α of the i^{th} SV is set as:

$$\alpha_i = \frac{\mathrm{LET}_{\mathrm{p}}}{\mathrm{LET}_i}, \quad i = 2, \ldots, N, \tag{4.5}$$

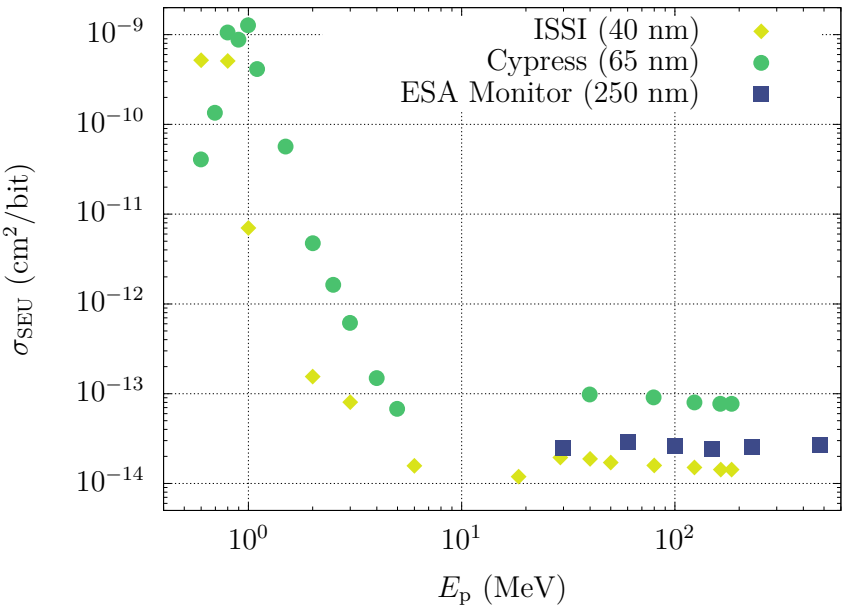

Figure 4.7: Experimental SEU production cross sections as a function of the incident energy induced by protons in the ISSI (yellow diamonds), Cypress (green circles), and ESA Monitor (blue squares) SRAMs [12, Sec. 4.3] [4, Sec. 5.2].

Table 4.1: Main characteristics of the bulk planar CMOS technology SRAMs considered in this work [24], [12, Sec. 4.2, Sec. 5.1], [73].

SRAM	Technology node (nm)	Size (bits)	Transistors per cell	Cell dimensions (μm^2)
ISSI	40	32M	6	0.2-0.25
Cypress	65	16M	6	0.5-0.7
ESA Monitor	250	16M	6	9.765

where $\mathrm{LET_p}$ is the linear energy transfer (LET) for which the maximum proton-induced SEU production cross section is attained and LET_i is the LET of the i^{th} heavy ion [9], [12, Sec. 5.1], [13], summarized in Table 4.3. By setting $\alpha = 0$ for all encapsulating volumes, except for the innermost one, the single RPP limit is recovered.

The extensive amount of experimental SEU-production cross sections required to apply the aforementioned RPP modeling approach significantly conditions its use for new devices which have not undergone irradiation (the analysis in Section 4.2.2 offers a substantially simpler method). To induce an SEU, a threshold energy must be deposited in the SV, corresponding to a critical charge Q_{crit} which must be collected. The latter is determined such that a good overall agreement between simulated and experimental SEU production cross sections is ensured across the full probed energy range [12, Sec. 3.3]. In the case of nested SVs, separate simulations are performed for each SV. The energy deposition spectra are weighted by the respective charge collection efficiency coefficient α of each SV, while Q_{crit} remains the same for all SVs.

The smallest technology node considered in this study is 40 nm, represented by the ISSI SRAM [16, 74], whose SV has been modelled as a single RPP. The initial SV dimensions were determined following the above prescription for the innermost volume and were then adjusted iteratively until the best overall agreement between simulated and

Table 4.2: SEU production cross section induced by heavy ions [13].

Index	Ion	Energy (MeV)	$\sigma_{\mathrm{SEU},i}$ (cm^2/bit)
2	Ar	1050	9.7×10^{-9}
3	Ar	548	2.6×10^{-8}
4	Xe	2700	1×10^{-7}

Table 4.3: Maximum proton LET and heavy ion LET [13].

Ion	Energy (MeV)	LET (MeV cm^2/mg)
p	0.5-5	0.3
Ar	1050	5.2
Ar	548	8.1
Xe	2700	43.5

experimental SEU production cross sections was achieved, yielding $x = y = z = 310$ nm, for $Q_{\mathrm{crit}} = 0.96$ fC [13].

The intermediate technology node examined in this study is 65 nm, represented by the Cypress SRAM [70]. Previous studies [12, Sec. 5.1] revealed that modelling its SV as a single RPP leads to underestimations of up to a factor of 3 between simulated and experimental SEU production cross sections in the high-energy proton range for $Q_{\mathrm{crit}} = 0.86$ fC. To address this shortcoming, the depth of the single RPP can be adjusted until an improved description of the simulated SEU production cross section is obtained at high proton energies. However, this approach would lead to an overestimated SEU response at low and intermediate proton energies. Therefore, to properly account for charge drift and diffusion processes [64], which increase SEU production cross sections at high proton energies without affecting the response at lower energies, it was proposed in Ref. [12, Sec. 5.1] to model the SV of this SRAM using four nested RPPs, as shown in Fig. 4.6; the chosen number of nested RPPs is explained below. This approach resulted in better agreement with experimental SEU production cross sections in the high-energy proton range, as discussed in Ref. [13] and further elaborated below. The transverse dimensions, thicknesses, and charge collection efficiency coefficients for each RPP, determined using

Table 4.4: Initial transverse dimensions, thicknesses, and charge collection efficiency coefficients for the nested RPPs of the Cypress SRAM [13].

SV index	$x = y$ (nm)	z (nm)	α
V_1	360	360	1
V_2	984	360	0.057
V_3	1612	360	0.037
V_4	3160	360	0.007

Table 4.5: Initial SV and BEOL thicknesses, critical charges, and critical deposited energies for the ISSI, Cypress, and ESA Monitor SRAMs [13] [4, Sec. 5.3].

SRAM	SV z (nm)	BEOL z (μm)	Q_{crit} (fC)	$E_{\mathrm{dep}}(Q_{\mathrm{crit}})$ (keV)
ISSI (40 nm)	310	6	0.96	21.6
Cypress (65 nm)	360	10	0.86	19.35
ESA Monitor (250 nm)	625	6.7	9.8	220.5

the nested volumes method, are summarized in Table 4.4.

The largest technology node considered in this work is 250 nm, represented by the ESA Monitor SRAM [71]. Since no SEU production cross sections are currently available for this SRAM in the low-energy proton range, the method described above for determining the SV dimensions cannot be applied. However, following previous guidelines [32], a single cubic SV with a size of 625 nm is used as representative for this technology node, and a critical charge of 9.8 fC is adopted [4, Sec. 5.3].

The SVs of each SRAM are embedded in a silicon matrix placed on a BEOL layer. The latter may consist of various materials, such as silicon dioxide, aluminum, copper, and tungsten [4, Sec. 5.3]. However, to focus this study on the variation of the SEU-production cross section with SV thickness and Q_{crit}, the simulated BEOL for all three SRAMs was modelled using only SiO_2. Since manufacturing details on the BEOL are not available for the ISSI and Cypress SRAMs, its thickness was set to 6 μm and 10 μm, respectively, following the guidelines provided in Ref. [12, Sec. 5.1]. For the ESA Monitor SRAM, a BEOL thickness of 6.7 μm [4, Sec. 5.3] was used based on technical specifications from the manufacturer. Table 4.5 summarizes the key initial simulation parameters for the three SRAMs under consideration. The simulation geometries described above are irradiated by a monoenergetic proton beam with zero angular divergence, which impinges perpendicularly on and fully covers the BEOL, as illustrated in Fig. 4.8.

The energy deposition spectrum deposited per SV, $\mathrm{d}N(\mathrm{SV})/\mathrm{d}E_{\mathrm{dep}}$, has been scored using FLUKA on an event-by-event basis for incident proton kinetic energies ranging from 600 keV–500 MeV. For each proton energy E_{p}, the cross section for SEU production can be estimated from these FLUKA simulations using Eq. (4.2). The critical deposited energy, $E_{\mathrm{dep}}(Q_{\mathrm{crit}})$, of each SRAM is listed in Table 4.5. While the ISSI and Cypress SRAMs have comparable critical deposited energies, $E_{\mathrm{dep}}(Q_{\mathrm{crit}}) = 21.6$ keV and $E_{\mathrm{dep}}(Q_{\mathrm{crit}}) = 19.35$ keV respectively, the ESA Monitor SRAM has $E_{\mathrm{dep}}(Q_{\mathrm{crit}}) = 220.5$ keV, which is one order of magnitude higher. Consequently, recent devices like the ISSI and Cypress SRAMs require less collected charge to trigger an upset compared to older devices such as the ESA Monitor SRAM [9, 75].

Fig. 4.9 illustrates a selection of simulated energy deposition spectra (thick black curves) for the ISSI, Cypress, and ESA Monitor SRAMs (first, second, and third columns, respectively) at sufficiently close proton kinetic energies for which experimental SEU production cross sections are available. The particle latching capabilities of FLUKA enable further filtering of these spectra into contributions from different kinds of particle histories. The main peak (dashed yellow curve) arises from energy deposition in the SV by primary protons that undergo no nuclear interactions along their path, *i.e.*, they undergo only ionization losses (in addition to Coulomb scattering). Additional features at energy

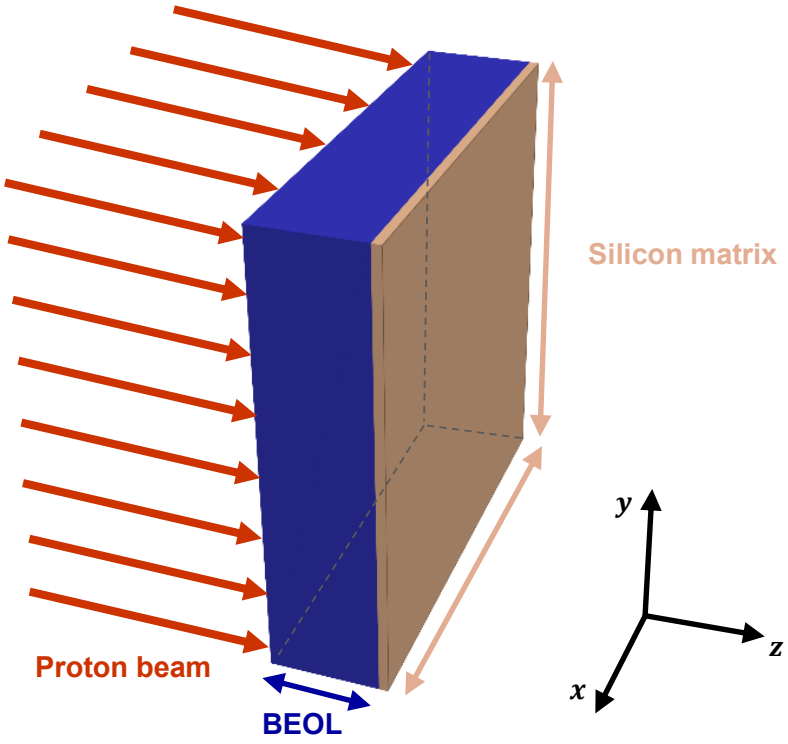

Figure 4.8: 3D schematic of the FLUKA simulation geometry showing the BEOL, the silicon matrix embedding the sensitive volumes, and the extended proton beam covering the entire transverse face of the device.

depositions exceeding several tens of keV correspond to contributions from recoils due to proton nuclear elastic scattering (teal curve), recoils from Coulomb single scattering events (green curve), or residuals and fragments produced from nuclear reactions (dashed blue curve). The vertical dashed grey lines in Fig. 4.9 represent $E_{\mathrm{dep}}(Q_{\mathrm{crit}})$ for each SRAM, allowing one to identify the interaction mechanisms driving SEU production. For instance, at proton energies of several tens of MeV, *e.g.*, Fig. 4.9c for the ISSI SRAM, Fig. 4.9f for the Cypress SRAM, and Figs. 4.9g–i for the ESA Monitor SRAM, SEU production is mainly driven by fragments and residuals from nuclear reactions. At intermediate proton energies between 2 MeV and 10 MeV, elastic recoils significantly contribute to SEU production, as seen in Fig. 4.9b for the ISSI SRAM and Fig. 4.9e for the Cypress SRAM. At proton energies of ~1 MeV, SEU production is dominated by proton direct ionization, exemplified in Fig. 4.9a for the ISSI SRAM. Although SEU production was not consistently assessed experimentally at the same proton energies for all SRAMs, both the ISSI and Cypress SRAMs were irradiated with 3 MeV protons. At this energy, SEU production in the ISSI SRAM is governed by both proton direct ionization and Coulomb recoils, as shown in Fig. 4.9b (where the contribution of proton direct ionization reaches $\sim 7 \times 10^{-9}$, while that of Coulomb recoils is $\sim$2-3 $\times 10^{-9}$). In contrast, SEU production in the Cypress SRAM is predominantly due to proton direct ionization, as indicated in Fig. 4.9d (where the contribution of direct ionization reaches 10^{-7}, and that of Coulomb recoils remains at a much lower level of $\sim$3-4 $\times 10^{-9}$). This highlights that SEU production in different components may be driven by different interaction mechanisms, even at the same proton energy.

This detailed filtering of particle histories based on the undergone interaction mechanism

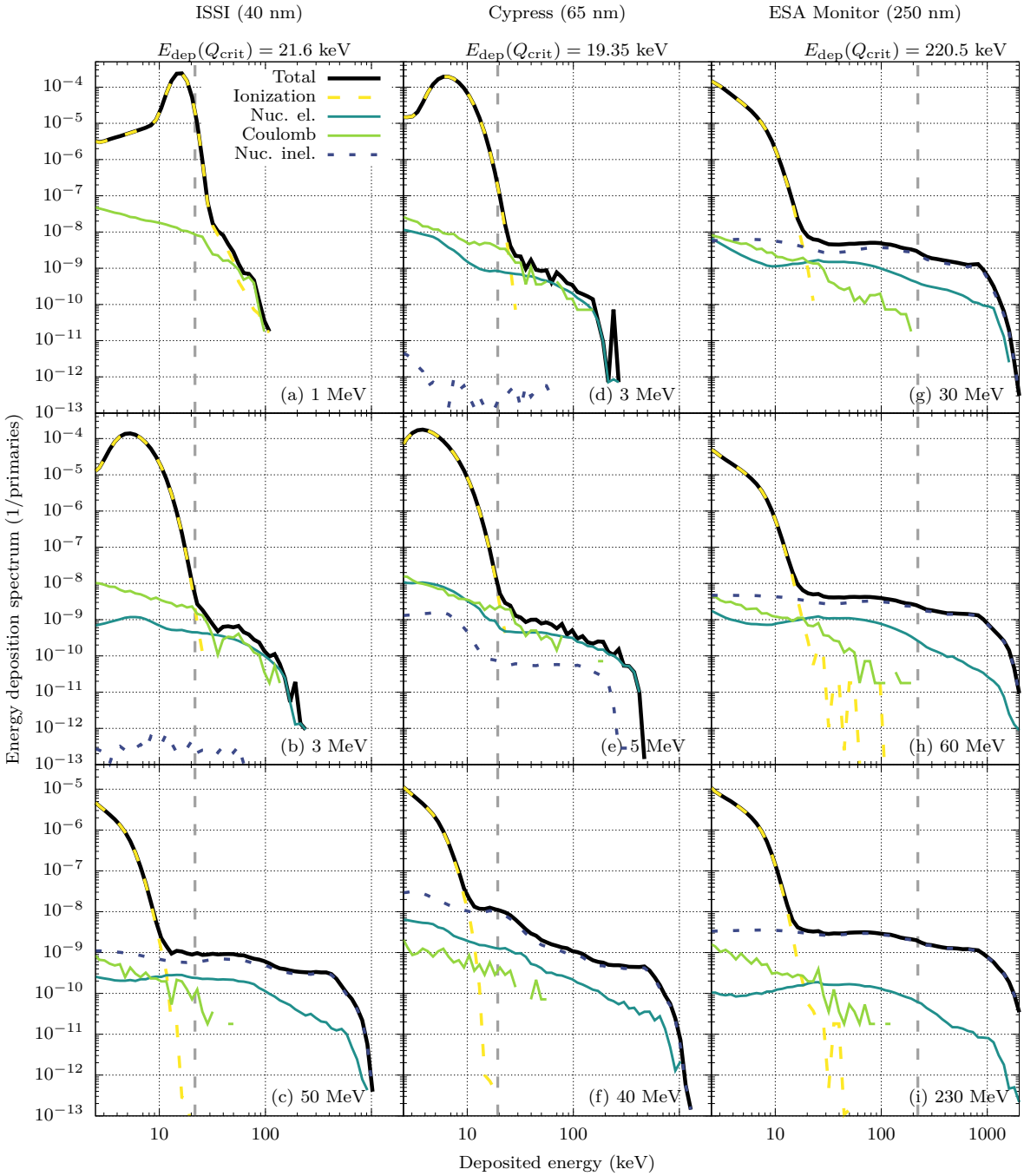

Figure 4.9: Energy deposition histograms in the ISSI, Cypress, and ESA Monitor SRAMs (first, second, and third column, respectively), displaying the contributions from various kinds of particle histories. Statistical error bars are omitted for clarity.

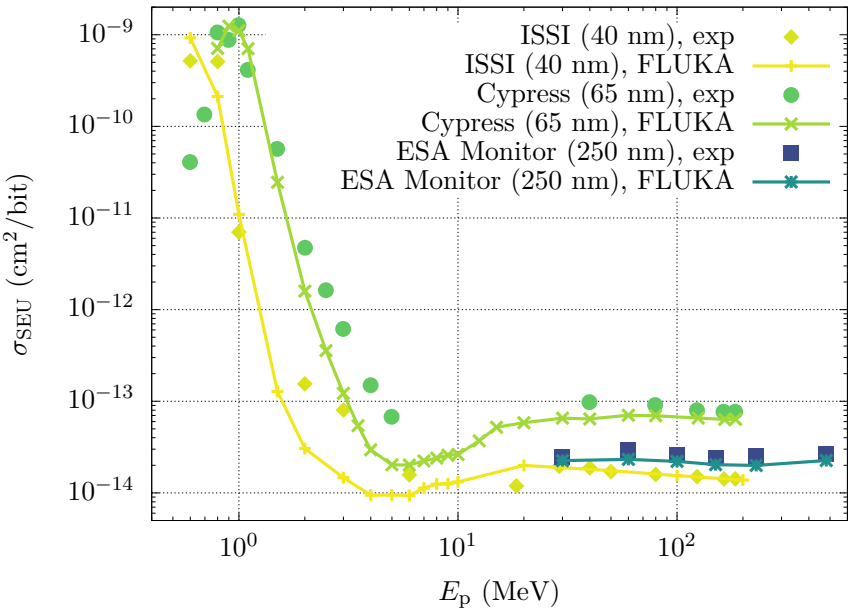

Figure 4.10: SEU production cross section as a function of proton energy in the ISSI, Cypress, and ESA Monitor SRAMs.

reveals that SEU production in devices with high Q_{crit}, such as the ESA Monitor SRAM, is primarily driven by nuclear reactions. In contrast, for devices with lower Q_{crit}, like the ISSI and Cypress SRAMs, proton direct ionization and elastic scattering play a more significant role [9, 14, 75, 76]. The latter two interaction mechanisms contribute to an increase in the SEU production cross sections at lower proton energies [77], as shown in Fig. 4.10, which displays experimental and simulated SEU production cross sections as a function of proton energy for the considered SRAMs. Available experimental SEU production cross sections for the ISSI, Cypress, and ESA Monitor SRAMs are represented by yellow diamonds, green circles, and blue squares, respectively, with uncertainties smaller than the symbol size [4, Sec. 5.2], [12, Sec. 4.3]. The estimates from the development version of FLUKA, obtained using the initial parameters outlined in Table 4.5, are depicted by matching coloured symbols connected by solid lines. The qualitative agreement between the experimental and FLUKA-simulated SEU cross sections across the considered wide range of proton energies validates the prescribed method for determining the SV dimensions and Q_{crit}. However, notable discrepancies remain. For the ISSI and Cypress SRAMs, differences of up to factors of 5.5 and 5, respectively, are observed in the 2 to 6 MeV energy range. In contrast, for the ESA Monitor SRAM, the discrepancies are smaller, up to a factor of 1.3, within the available proton energy range. These differences highlight uncertainties in the initially proposed SV thickness and Q_{crit}.

Incidentally, the Cypress SRAM is the only SRAM in this study for which the nested RPP approach was used to model the SV, as initially proposed by Refs. [12, Sec. 5.1], [13], since a single SV was insufficient to replicate the experimental SEU production cross section across the entire probed proton energy range. To address this shortcoming, first, the SV surface area and Q_{crit} were adjusted to achieve satisfactory agreement between simulated and experimental SEU cross sections around 1 MeV, where direct ionization dominates. Then, the agreement at energies above 10 MeV was improved, where indirect ionization becomes significant, by optimizing the number of SVs, taking into account that changes in the RPP-model parameters have a greater impact on SEU cross sections at

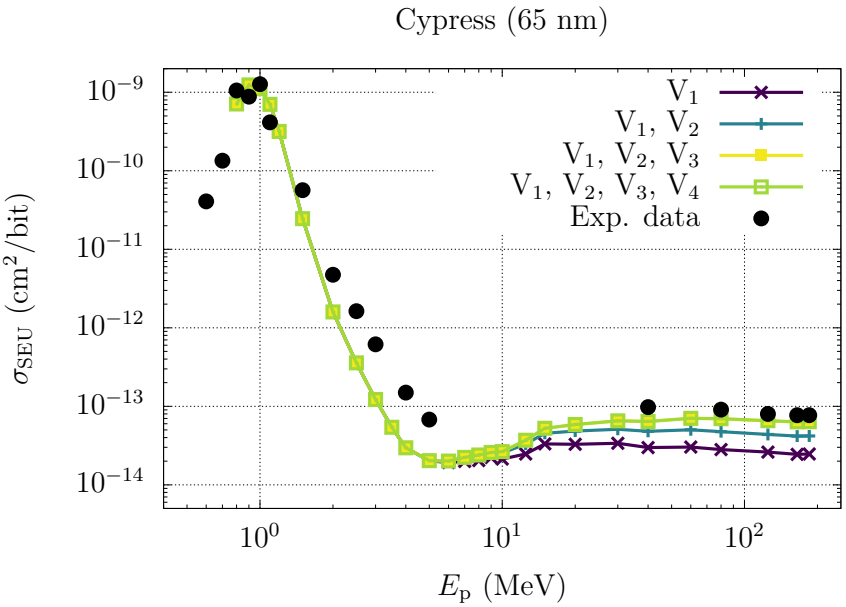

Figure 4.11: Effect of the encapsulating SVs on the FLUKA-simulated SEU production cross section as a function of proton energy in the Cypress SRAM.

low and intermediate proton energies compared to high energies, as will be discussed in Section 4.2.2. Figure 4.11 illustrates the effect of adding encapsulating SVs, each with its charge collection efficiency coefficient α, to account for charge drift and diffusion [64]. The purple curve displays FLUKA predictions using only a single SV (the innermost one). While this is sufficient to describe SEU production at low energies, where ionization dominates (as shown in Fig. 4.9), it underestimates experimental SEU cross sections by up to a factor of 3 for protons above 10 MeV, where nuclear reactions dominate. By successively adding one (blue), two (yellow), and three (green) SVs, the agreement at low energies remains unaffected, while that at high proton energies improves progressively until a satisfactory match is achieved. Fig. 4.11 shows that adding a fourth nested RPP results only in a modest increase in SEU cross sections compared to three RPPs. Therefore, adding further volumes would not significantly enhance the accuracy, as four nested RPPs are sufficient to reasonably describe the SEU response of the Cypress SRAM across the considered proton energy range. Each of the four nested RPPs was simulated individually, and their energy deposition spectra have been combined based on their respective α (as per Table 4.4). Reasonable agreement between simulated and experimental SEU production cross sections has been achieved at both low proton energies (~1 MeV), where direct ionization is dominant, and at higher energies (above 10 MeV), where indirect ionization becomes relevant. The remaining discrepancies at proton energies between 2–5 MeV, where elastic collisions play a significant role, are addressed in the following section.

4.2.2 Optimization of critical charge and sensitive volume thickness across technology nodes

Residual discrepancies between FLUKA-estimated and experimental SEU production cross sections remain for the three SRAMs when using the SV thickness and Q_{crit} prescribed in the previous section, following standard methods based on experimental SEU production cross sections. Therefore, in this section the variation of these two RPP-model parameters

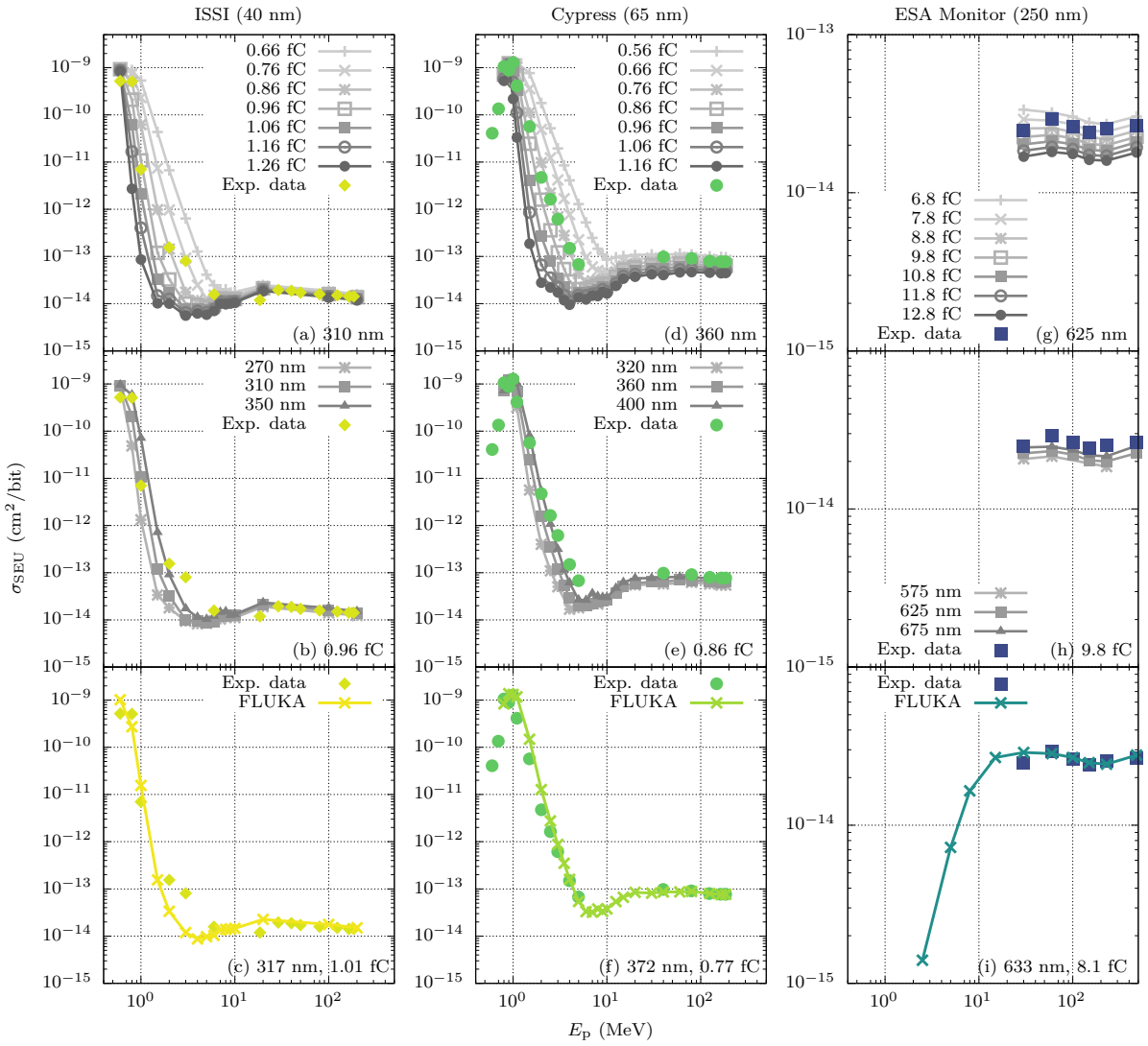

Figure 4.12: Variation of the FLUKA simulated SEU production cross section induced by low-energy protons with the critical charge and SV thickness in the ISSI, Cypress, and ESA Monitor SRAMs (first, second, and third column, respectively).

is explored with the aim of identifying optimal parameters that maximize the agreement between simulated and experimental SEU production cross sections. For simplicity, in the case of the Cypress SRAM the transverse dimensions of the four nested RPPs are kept constant, while only the SV thickness and Q_{crit} are adjusted.

The impact of varying each of the two RPP-model parameters on the simulated SEU production cross section is assessed separately. First, the SV thickness is kept constant while Q_{crit} is varied in steps of ~10%. Figures 4.12a, 4.12d, and 4.12g show the changes in the simulated SEU production cross section as Q_{crit} is varied for a constant SV thickness of the ISSI, Cypress, and ESA Monitor SRAMs (first, second, and third columns, respectively). For the ISSI and Cypress SRAMs, small variations in Q_{crit} significantly affect the FLUKA-simulated SEU production cross sections below 10 MeV, where proton direct ionization and elastic collisions dominate SEU production, as illustrated in Figs. 4.12a and 4.12d. This arises from the swift decrease of the $dN(SV)/dE_{dep}$ spectra in Fig. 4.9 when crossing the energy range at which protons no longer induce upsets by direct ionization. Next, Q_{crit} is kept constant while the SV thickness is varied in steps of ~10%. Figures 4.12b, 4.12e,

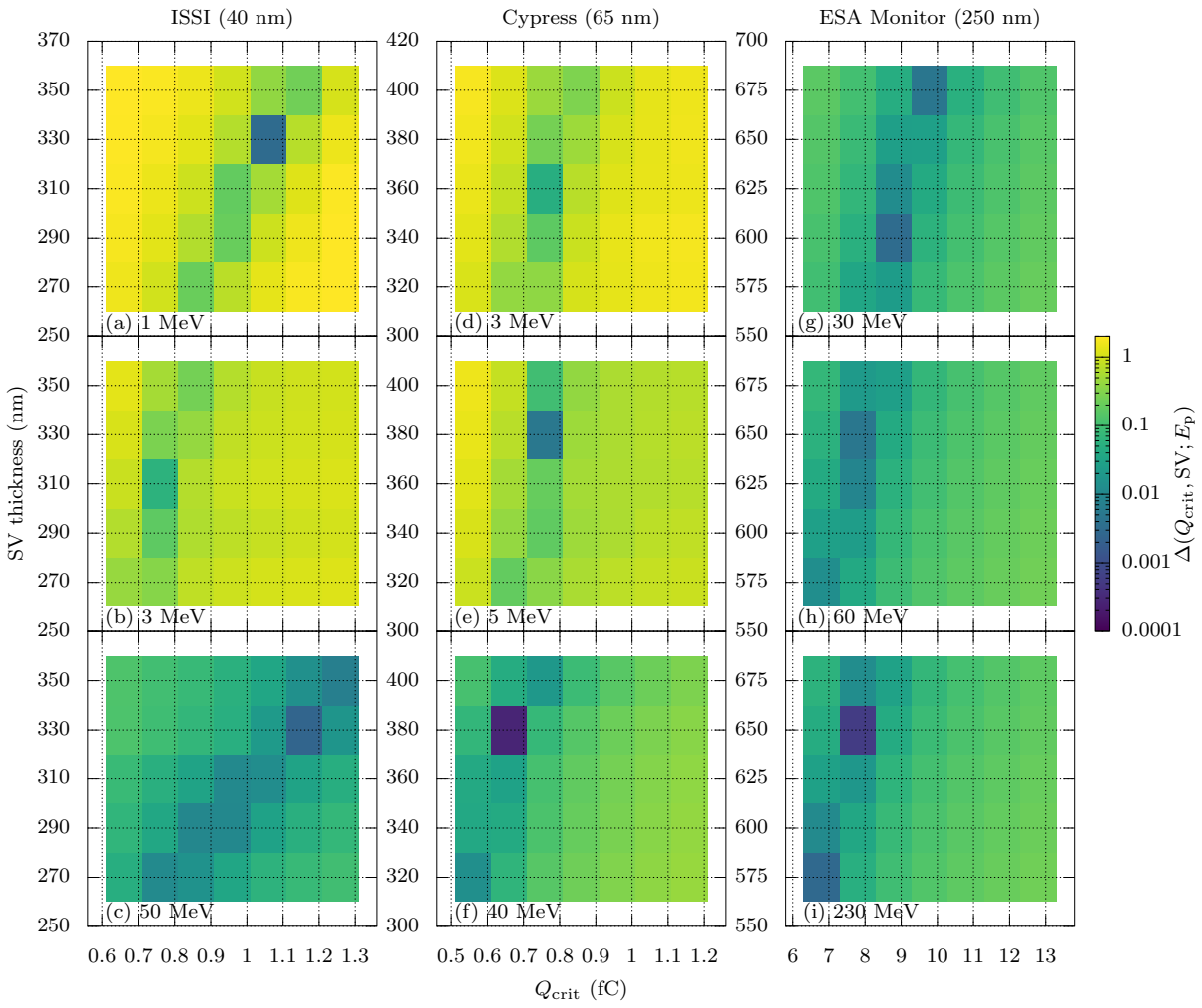

Figure 4.13: Variation of the FLUKA simulated SEU production cross section induced by low-energy protons as a function of the SV thickness and critical charge for the ISSI, Cypress, and ESA Monitor SRAMs (first, second, and third column, respectively), at a selection of experimental proton kinetic energies.

and 4.12h show how changes in SV thickness affect the simulated SEU production cross section for a constant Q_{crit} of the ISSI, Cypress, and ESA Monitor SRAMs (first, second, and third columns, respectively). As seen in Figs. 4.12b and 4.12e, variations in SV thickness can lead to changes in the SEU production cross section by up to an order of magnitude, particularly at energies below 2 MeV. In both cases, whether varying Q_{crit} or SV thickness, the SEU production cross section tends to stabilize above 10 MeV, where nuclear reactions dominate. This occurs due to most of events depositing an energy well above $E_{dep}(Q_{crit})$, making the SEU production cross section less sensitive to changes in either Q_{crit} or SV thickness for all three SRAMs.

The analysis has been extended to investigate the effect of varying both Q_{crit} and SV thickness. To quantify differences between simulated and experimental SEU production cross sections over several orders of magnitude, the geometric relative difference

$$\Delta(Q_{crit}, SV; E_p) = \left| \log \frac{\sigma_{SEU}^{FLUKA}(Q_{crit}, SV; E_p)}{\sigma_{SEU}^{exp}(E_p)} \right| \tag{4.6}$$

has been adopted, where $\sigma_{SEU}^{FLUKA}(Q_{crit}, SV; E_p)$ is the SEU production cross section ob-

Table 4.6: Average SV thickness and Q_{crit} determined for the ISSI, Cypress, and ESA Monitor SRAMs in the probed parameter space.

SRAM	<SV thickness> (nm)	<Q_{crit}> (fC)
ISSI (40 nm)	317 ± 5.8	1.01 ± 0.03
Cypress (65 nm)	372 ± 5.2	0.77 ± 0.03
ESA Monitor (250 nm)	633 ± 11.5	8.10 ± 0.06

Table 4.7: Average SV thickness and Q_{crit} extracted from independent literature studies of bulk planar devices manufactured on other technology nodes.

Technology node (nm)	<SV thickness> (nm)	<Q_{crit}> (fC)	Ref.
32	238	0.93	[60]
65	235	0.5	[78]
90	308	1.0	[78]
130	414	2.0	[78]
180	526	4.0	[78]
250	626	8.0	[32]
600	1000	44.0	[79]

tained with the development version of FLUKA for a given Q_{crit}, SV thickness, and proton energy E_{p}, while $\sigma_{\mathrm{SEU}}^{\mathrm{exp}}(E_{\mathrm{p}})$ is the experimental SEU cross section at E_{p}. Figure 4.13 shows $\Delta(Q_{\mathrm{crit}}, \mathrm{SV}; E_{\mathrm{p}})$ as a function of Q_{crit} and SV thickness for the ISSI, Cypress, and ESA Monitor SRAMs (first, second, and third column respectively) for a selection of experimental proton kinetic energies. For the ESA Monitor SRAM, experimental SEU production cross sections are available only for proton energies above 30 MeV, where nuclear reactions dominate SEU production. The stabilization tendency of the SEU cross section in this energy range leads to the rather monotonic behaviour of $\Delta(Q_{\mathrm{crit}}, \mathrm{SV}; E_{\mathrm{p}})$, shown in Figs. 4.13g–i. For each SRAM, at the three displayed energies, there is a local minimum of $\Delta(Q_{\mathrm{crit}}, \mathrm{SV}; E_{\mathrm{p}})$ at which the best agreement between simulated and experimental SEU production cross sections is found. However, there is no unique (Q_{crit}, SV thickness) pair providing optimal agreement with experimental SEU production cross sections at all considered proton energies. This is due to different interaction mechanisms governing SEU production at different proton energies. Nevertheless, throughout the available experimental proton energies, the (Q_{crit}, SV thickness) pairs which yield optimal agreement with experimental SEU cross sections for each SRAM, corresponding to the local minima of $\Delta(Q_{\mathrm{crit}}, \mathrm{SV}; E_{\mathrm{p}})$ in Fig. 4.13, do not differ by more than ~20%. This variation exceeds the resolution of ~10% with which Q_{crit} and SV thickness have been probed. Hence, this uncertainty is not driven by the adopted resolution, but arises from the SEU response of the device at different proton energies. This relatively low uncertainty suggests that the RPP-model is able to effectively capture the essential features for describing SEU production in the considered SRAMs, in spite of its simplicity.

For each SRAM, the average Q_{crit} and SV thickness across the available experimental

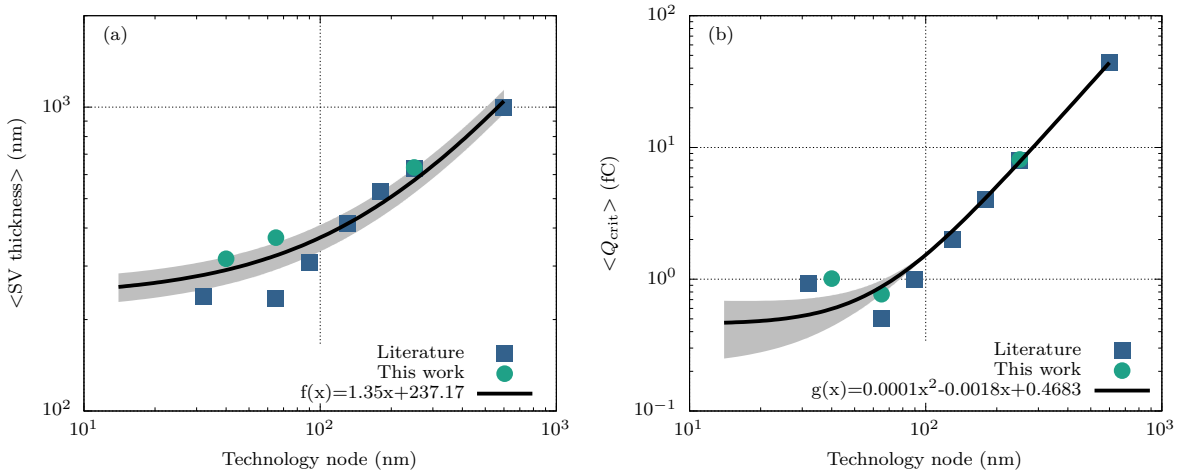

Figure 4.14: Average SV thickness (a) and average critical charge (b) of the SRAMs presented in this work (teal dots) and of SRAMs from independent literature studies (blue squares) as a function of the technology node. The black solid lines represent linear (a) and quadratic (b) functions fitting the data. The variable x in the aforementioned functions is the technology node in nm.

proton energies, yielding minimal discrepancies with respect to the experimental SEU cross sections, have been evaluated. These are summarized in Table 4.6, along with their associated uncertainties due to the finite resolution of the probed SV thickness and Q_{crit} domains. When calculating the average over SV thickness, the optimal Q_{crit} for each SV thickness and proton energy has been considered (and vice versa). The remarkable agreement between FLUKA-simulated and experimental SEU cross sections, achieved by employing these optimal parameters, is illustrated in Fig. 4.12c, 4.12f, and 4.12i. For the ESA Monitor SRAM, the optimal SV thickness and Q_{crit} derived from the available experimental SEU cross sections at high proton energies have been employed to extend the FLUKA SEU cross section predictions to lower proton energies. Although experimental SEU cross sections are not currently available in this lower energy range, the downward trend in SEU cross section observed in Fig. 4.12i is consistent with that reported for low-energy neutron irradiation [4, Sec. 5.2]. Nonetheless, residual discrepancies with respect to the experimental SEU cross sections are still observed in Fig. 4.12, particularly for the ISSI SRAM in the 2–3 MeV range. Given that the focus of this study was on the impact of uncertainties in SV thickness and Q_{crit} on the simulated SEU production cross sections under a simplified BEOL composition, the remaining differences may stem from this simplification or from uncertainties in the experimental SEU cross sections. The evaluated average SV thickness and Q_{crit} are depicted as a function of the technology nodes in Figs. 4.14a and 4.14b, respectively, by the teal dots, with calculated uncertainties smaller than the symbol size, as reported in Table 4.6.

In addition to the optimal pairs of Q_{crit} and SV thickness obtained in this study for the ISSI, Cypress, and ESA Monitor SRAMs, RPP-model parameters reported independently by other research groups have been gathered from the literature for devices fabricated on different bulk planar technology nodes. Since the RPP volumes described in these studies are not necessarily cubic, their average SV thickness has been approximated as the cubic root of the given arbitrary RPP volume. The extracted RPP-model parameters from the literature for different technology nodes are summarized in Table 4.7 and are

represented by blue squares in Fig. 4.14. Linear and quadratic functions, shown as solid black lines in Fig. 4.14, were fitted to the SV thickness ($f(x) = 1.35x + 237.17$) and Q_{crit} ($g(x) = 0.0001x^2 - 0.0018x + 0.4683$) data, respectively, where x denotes the technology node in nm. The shaded grey bands in Fig. 4.14 represent the fit uncertainties. These fitted trends across different technology nodes provide practical guidelines for estimating the SV thickness and Q_{crit} required for simulating bulk planar devices within the RPP model. This approach is particularly useful in situations where only the technology node is known and experimental SEU production cross sections are unavailable. Therefore, the technology trends identified in this work extend beyond Ref. [13], which relies on an extensive amount of experimental SEU cross sections to determine RPP-model parameters for simulating SEU production in the analyzed SRAMs. These trends provide a straightforward evaluation of the simulation parameters based solely on the technology node and offer a more flexible methodology for device modelling in the absence of experimental SEU production cross sections.

4.2.3 Nuclear interaction contributions across technology nodes

Within the RPP model, differences in SEU production among SRAMs manufactured on different technology nodes under proton irradiation can be attributed to distinct fragments and residual nuclei resulting from nuclear interactions, which ultimately deposit energy in the SV. Thus, it is insightful to examine the location (SV, silicon matrix, BEOL) where these nuclear interactions occur, as well as the distribution of the produced residual nuclei.

Figure 4.15 depicts the energy deposition spectrum for 40 MeV protons (thick black curve) on the Cypress (top) and ESA Monitor (bottom) SRAMs. The solid purple curve represents energy depositions by residuals and fragments from nuclear reactions. The particle-latching capabilities of FLUKA allow one to inquire the region where each nuclear inelastic interaction occurred, and to transfer this information to the generated secondary particles. The latter carry a flag indicating the region where they were produced, and upon reaching the SV, their contribution to the deposited energy is filtered into various curves based on this flag. Specifically, the dotted yellow, dash-dotted blue, and dashed green curves in Figs. 4.15a and 4.15c correspond to particle histories where a nuclear inelastic scattering occurred within the SV, in the surrounding silicon matrix, and in the BEOL, respectively, for the Cypress and ESA Monitor SRAMs. The analysis reveals that energy depositions by residuals and fragments originating from nuclear interactions in the BEOL dominate in both SRAMs. However, for the Cypress SRAM, interactions occurring directly within the SV significantly contribute to the low energy depositions, with their contribution diminishing at higher energy depositions. Conversely, for the ESA Monitor SRAM, due to its larger SV thickness, interactions within the SV become increasingly significant at higher energy depositions, as more particles are able to deposit substantial energy within the SV.

To identify which nuclear reaction channels contribute most significantly to SEU production in the examined geometries, the nuclear inelastic contribution (solid purple curve in Figs. 4.15a and 4.15c) has been further resolved according to the species of the residual nucleus, as shown in Figs. 4.15b and 4.15d for the Cypress and ESA Monitor SRAMs, respectively. The SV and the surrounding silicon matrix consist of Si in natural composition (92.2% ^{28}Si, 4.7% ^{29}Si, 3.1% ^{30}Si), while the BEOL is composed of both Si and O (99.759% ^{16}O, 0.037% ^{17}O, 0.204% ^{18}O) in natural composition. Thus, in the considered energy range, the possible residual nuclei are C, N, O, and F from proton-induced reactions

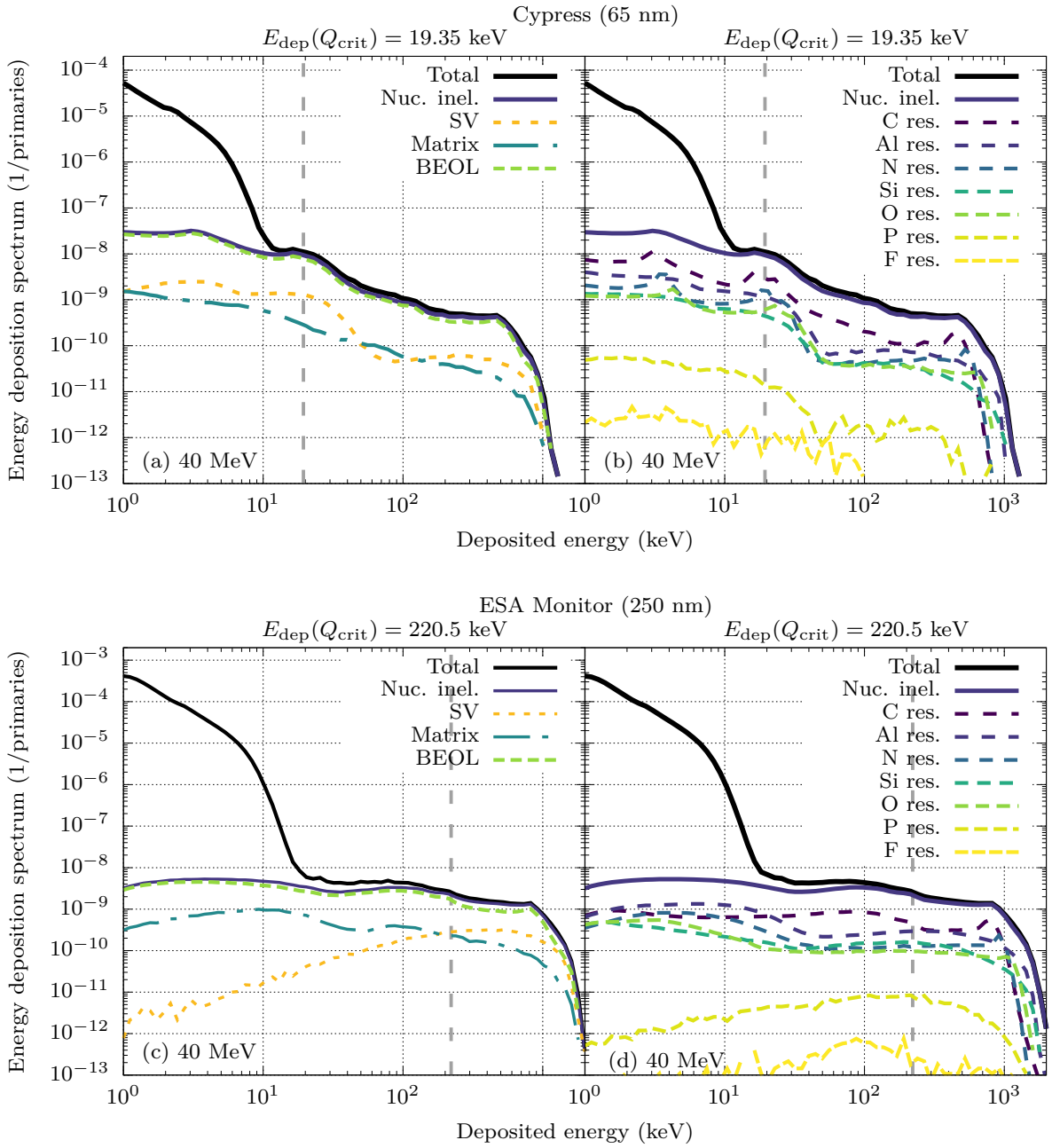

Figure 4.15: Energy deposition histogram of 40 MeV protons showing the contribution of different kinds of particle histories to the nuclear reactions curve by splitting according to the region where the event happened (a) for the Cypress (65 nm) SRAM; (c) for the ESA Monitor (250 nm) SRAM. Energy deposition histogram of 40 MeV protons showing the contribution of different kinds of particle histories to the nuclear reactions curve by splitting according to the recoiling residual particle species (b) for the Cypress (65 nm) SRAM; (d) for the ESA Monitor (250 nm) SRAM.

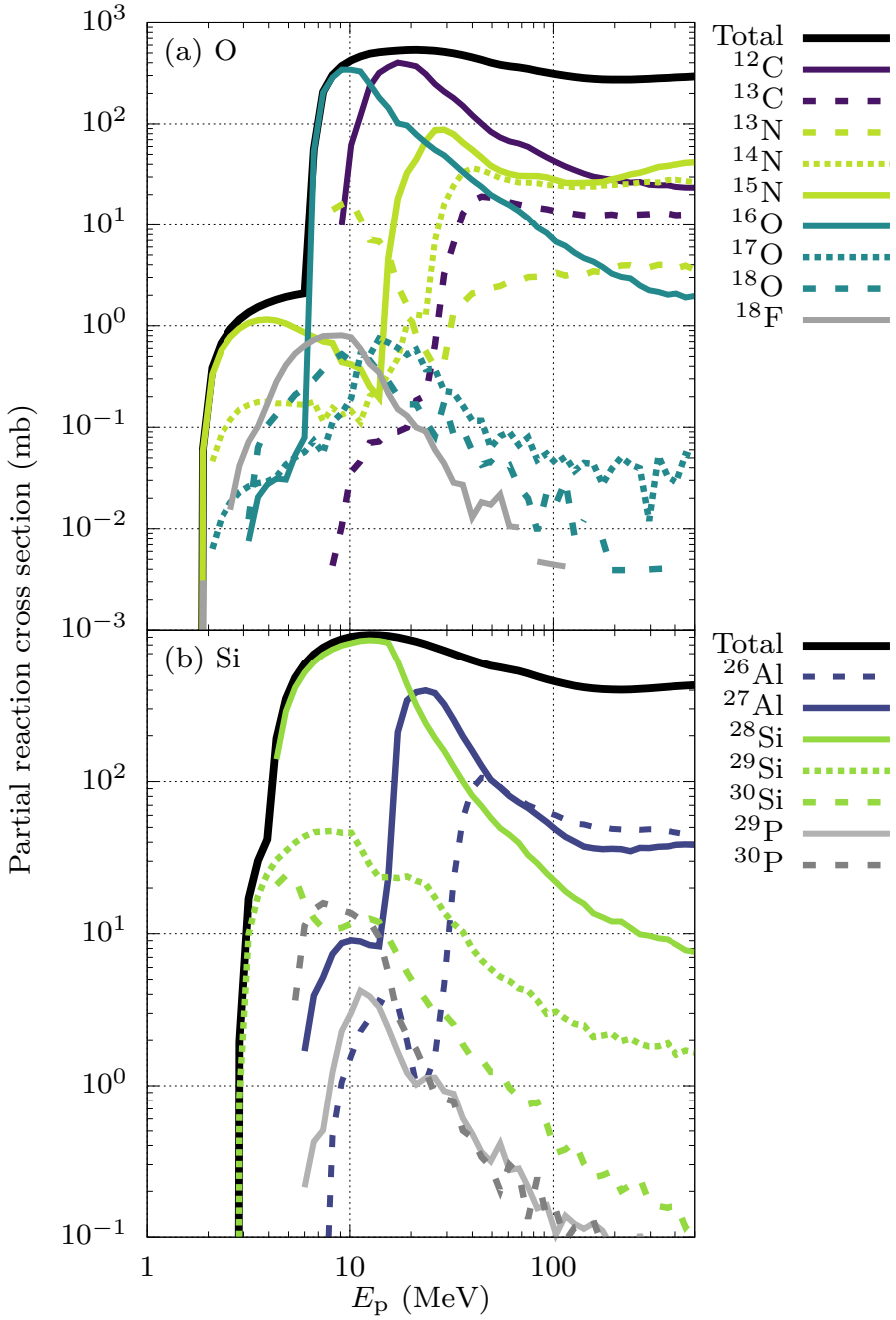

Figure 4.16: (a) Partial reaction cross sections as a function of proton energy for protons on natural O. (b) Same as (a) for protons on natural Si.

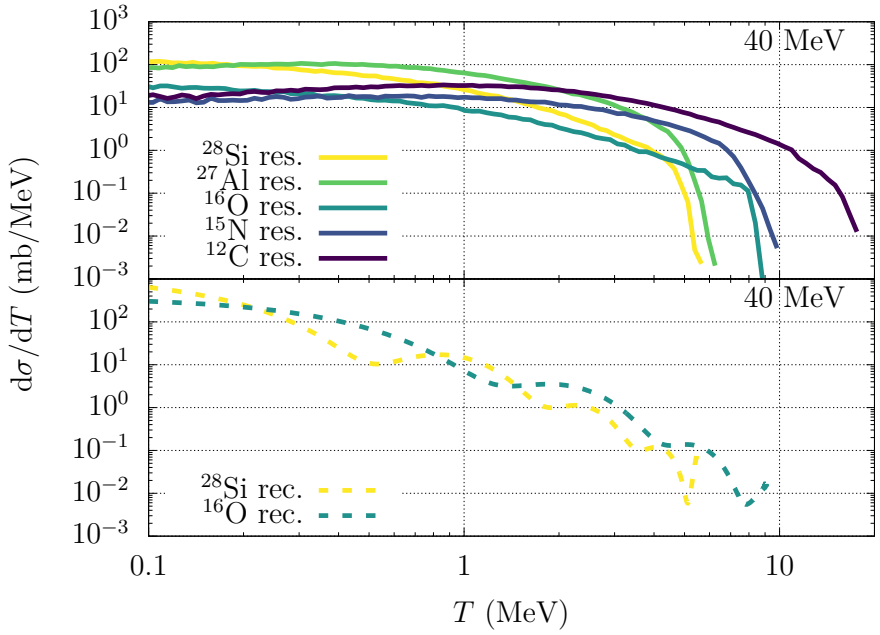

Figure 4.17: Differential cross section as a function of the recoil kinetic energy for 40 MeV protons elastically scattered on ^{16}O (dashed purple) and ^{28}Si (dashed yellow). Differential cross section as a function of the residual kinetic energy (with solid lines) for 40 MeV protons undergoing nuclear reactions on natural Si and natural O.

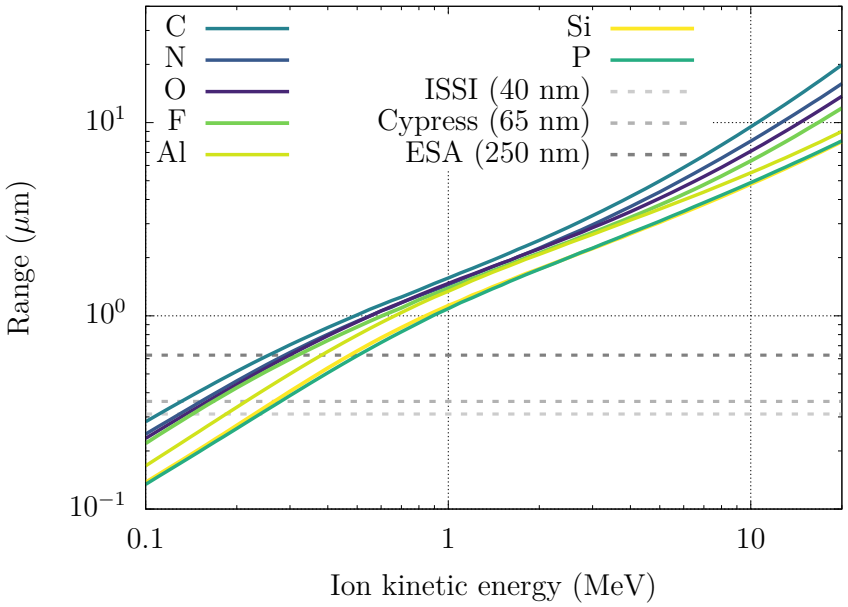

Figure 4.18: Range of C, N, O, F, Al, Si, and P ions in silicon extracted from SRIM [80].

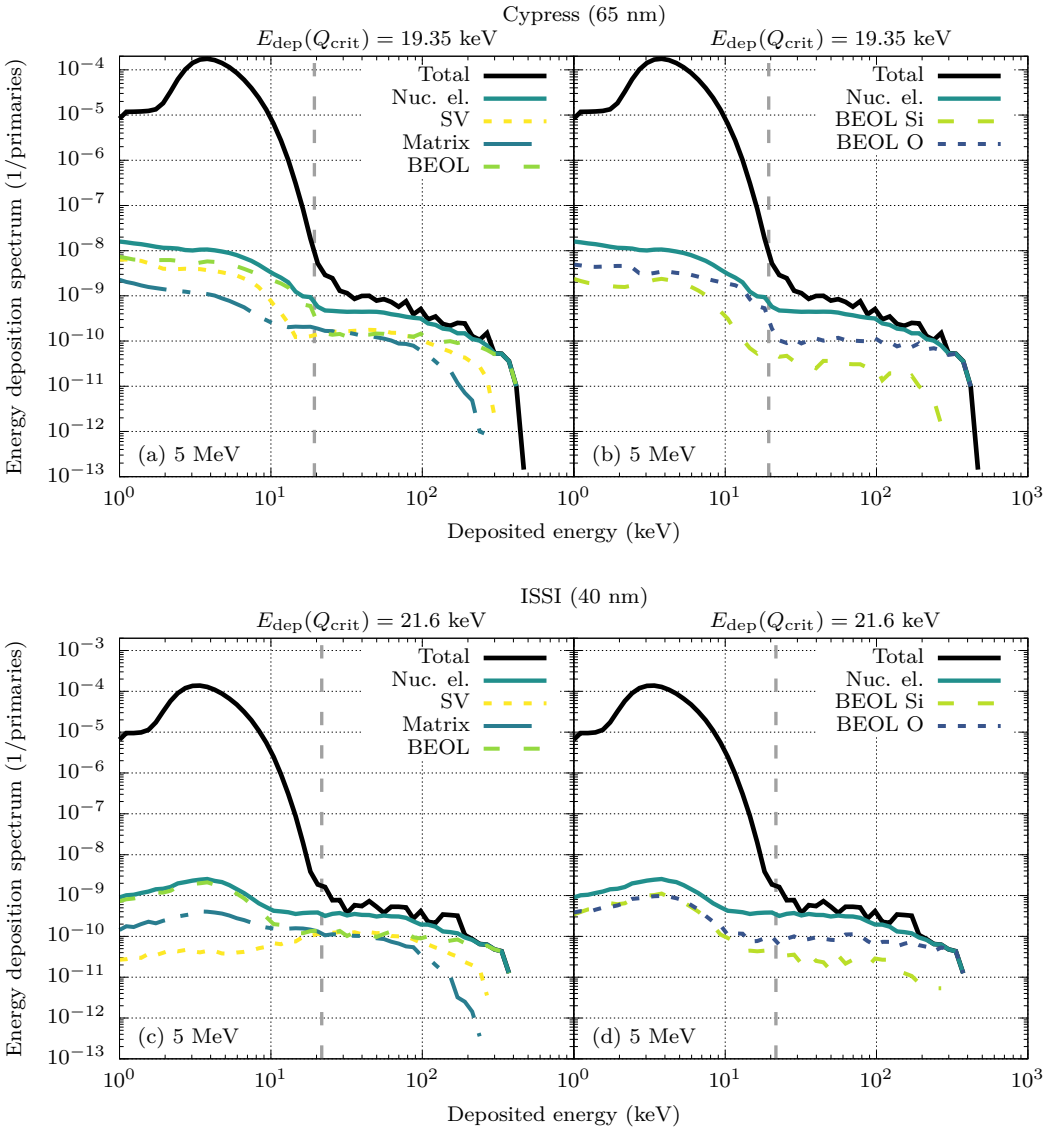

Figure 4.19: Energy deposition histogram of 5 MeV protons showing the contribution of different kinds of particle histories to the nuclear elastic scattering curve by splitting according to the region where the event happened (a) for the Cypress (65 nm) SRAM; (c) for the ISSI (40 nm) SRAM. Energy deposition histogram of 5 MeV protons showing the contribution of different kinds of particle histories to the nuclear elastic scattering curve by splitting according to the recoiling residual particle species (b) for the Cypress (65 nm) SRAM; (d) for the ISSI (40 nm) SRAM.

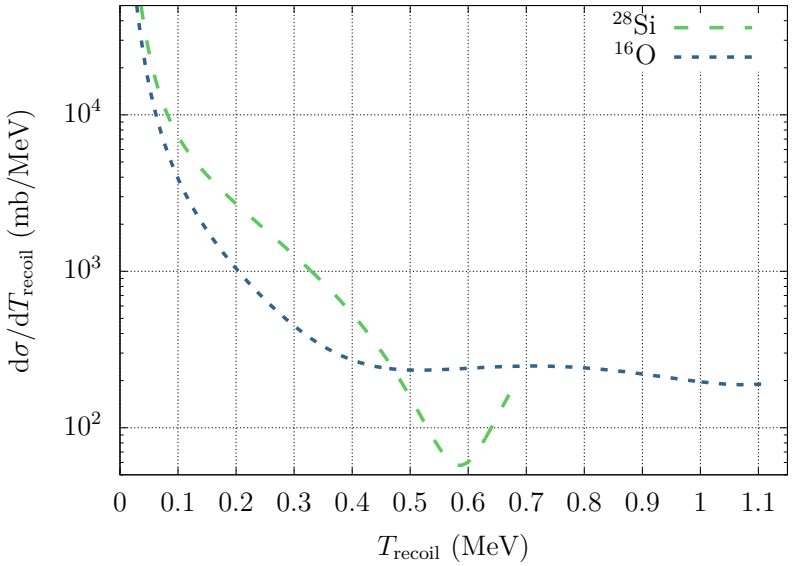

Figure 4.20: Differential cross section as a function of the recoil kinetic energy for 5 MeV protons elastically scattered on ^{16}O and ^{28}Si.

on O, as well as Al, Si, and P from reactions of protons on Si.

The partial reaction cross sections as a function of proton kinetic energy for protons on Si and O, shown in Fig. 4.16, indicate which residual nuclei are most likely to be produced. For 40 MeV protons, the dominant residuals are ^{12}C, ^{15}N, ^{14}N, ^{16}O, and ^{13}C from nuclear reactions on O, while for nuclear reactions on Si, the primary residuals are ^{26}Al, ^{27}Al, and ^{28}Si. As depicted in Fig. 4.15b, ^{12}C residuals generated in the BEOL and travelling into the SV dominate the higher energy depositions for the Cypress SRAM. This is consistent with Fig. 4.16, where ^{12}C has the highest production cross section. Additionally, due to their relatively light mass, C residuals can acquire a significant fraction of the kinetic energy during their production, as shown in Fig. 4.17. Their low charge also results in an extended range within silicon, as indicated in Fig. 4.18, which illustrates ion ranges in silicon extracted from SRIM [80]. Consequently, a substantial number of C residuals from BEOL interactions reach the SV and contribute to energy deposition. In contrast, for the ESA Monitor SRAM, both C and Al residuals are prominent contributors to the energy deposition. Notably, the ESA Monitor exhibits a relatively steady trend of the deposited energy, whereas the Cypress SRAM shows a decreasing trend, with fewer high-energy depositions. The different behaviours are attributed to the SV thicknesses of the two SRAMs, which vary by a factor of 1.7. This difference in SV thickness affects the range of ions, with many ions exhausting their range within the thicker SV of the ESA Monitor SRAM. The ISSI SRAM has been omitted in Fig. 4.15 because its SV thickness and Q_{crit} are comparable to those of the Cypress SRAM; their energy deposition trends (both in terms of the location of the nuclear interactions and the generated residuals) are therefore very similar.

In addition to nuclear reactions, nuclear elastic scattering significantly contributes to SEU production, particularly within the 1–10 MeV proton energy range. Figure 4.19 depicts the energy deposition spectrum (thick black curve) for 5 MeV protons incident on the Cypress (top) and ISSI (bottom) SRAMs. The teal solid curve represents the spectrum of energy deposited by recoils from nuclear elastic scattering occurring anywhere in the RPP-geometry (SV, silicon matrix, and BEOL). The dotted yellow, dash-dotted

blue, and dashed green curves indicate the contributions from recoils due to nuclear elastic scattering within the SV, the Si matrix, and the BEOL, respectively, as shown in Figs. 4.19a and 4.19c for the Cypress and ISSI SRAMs. Notably, contributions from all three regions are comparable in both SRAMs due to their similar SV thicknesses. Contributions from the BEOL have been further resolved according to the charge of the recoil nucleus, as shown in Figs. 4.19b and 4.19d, which display Si recoils in dashed green and O recoils in dotted blue. Oxygen recoils dominate for two reasons: first, due to their lower mass, a larger fraction of kinetic energy is transferred to O recoils compared to Si recoils during elastic collisions with protons [81], as shown in Fig. 4.20, which depicts the DXS for the elastic scattering of 5 MeV protons on ^{16}O and ^{28}Si as a function of the recoil kinetic energy. Second, O recoils exhibit a higher range in silicon, as illustrated in Fig. 4.18, owing to their lighter mass relative to Si.

This detailed microscopic analysis not only elucidates the location of nuclear interaction events, particularly those leading to significant energy depositions, but also provides an overview of the spectra of residual nuclei generated in these interactions. Moreover, it provides a deeper understanding of the differences in SEU production across different technology nodes.

Chapter 5

Out-of-field dose deposition by proton beams in water phantoms

Proton nuclear elastic scattering plays a crucial role, not only in evaluating radiation effects on electronics [11, 14, 27], as discussed in the foregoing chapter, but also in hadron therapy [28]. Specifically, proton nuclear elastic scattering contributes to the angular spread of proton showers in matter, directly affecting depth-dose distributions, especially in out-of-field regions (and thus influencing the dose delivered to healthy tissue nearby). Prior to the public release of FLUKA v4-4.0, a dedicated FLUKA simulation was conducted based on a recently published experimental dataset of radial-depth (r-z) dose maps in a water phantom under proton irradiation [29] to validate the new model for proton nuclear elastic scattering [27] developed in this work.

In this chapter, the improved performances of FLUKA v4-4.0 vs. v4-3.4 are highlighted and the role of proton nuclear elastic scattering is elucidated, particularly in capturing features across different regions of the aforementioned experimental r-z dose maps. Additionally, the importance of accurately characterizing the radiation source and the scattering geometry for Monte Carlo (MC) simulations is emphasized.

The contents of this chapter have led to a dedicated publication [82].

5.1 Experimental r-z maps of absorbed dose in water

In a recent study [29], detailed r-z maps of absorbed dose in a water phantom irradiated with protons of 100 MeV, 160 MeV, and 225 MeV were reported. This section provides a summary of the key aspects of the experimental setup relevant to the FLUKA simulations discussed below; further details can be found in the original reference [29].

The r-z maps of absorbed dose were obtained using a two-dimensional array of 1020 ionization chambers arranged in a square grid and placed within a water phantom measuring 40 cm in length. Each cylindrical chamber had a diameter of 0.42 cm, and the center of the proton beam was aligned with the center of one ionization chamber, as detailed in Ref. [29]. The uncertainties reported for each experimental point were 2.5% in the absorbed dose, ±0.07 cm in depth, and ±0.01 cm in the radial position. Additionally, the experimental r-z dose maps were not provided in absolute units, but rather normalized to the dose at 3 cm on the beam axis.

In the original reference, there are inaccuracies in the labels on the y-axis for the 100 MeV proton beam at a radial distance of 2.29 cm. The correct experimental absorbed doses were provided directly by the authors of the original paper [29].

5.2 FLUKA simulation setup

In Ref. [29], the spatial distribution and angular spread of the proton beam at the entrance of the water phantom are described by the Fermi-Eyges theory [83–85], which models the probability density of finding a proton at a position $\boldsymbol{r}$ after traversing a path length s as:

$$\Phi(s; \boldsymbol{r}, \theta_x, \theta_y) = F(z; x, \theta_x) F(z; y, \theta_y), \tag{5.1}$$

where

$$F(z; x, \theta_x) = \frac{1}{4\pi\sqrt{B(z)}} \exp\left(-\frac{A_0(z)x^2 - 2A_1(z)x\theta_x + A_2(z)\theta_x^2}{4B(z)}\right) \tag{5.2}$$

represents the probability density for a proton at depth z to be at a transverse position x, while its direction of motion projected onto the xz-plane makes an angle θ_x with the z-axis. A similar expression applies for the projections onto the yz-plane [84]. The beam parameters are the variance of the angular distribution ($2A_0$), the variance of the spatial distribution ($2A_2$), and their covariance ($2A_1$). The emittance of the proton beam is $B = A_0A_2 - A_1^2$. Transverse positions and angles are sampled as [29]:

$$x = \mu_x + \sqrt{2A_2}\xi_1, \tag{5.3}$$

$$\theta_x = \mu_{\theta_x} + \sqrt{\frac{2A_1^2}{A_2}}\xi_1 + \sqrt{\frac{2B}{A_2}}\xi_2, \tag{5.4}$$

where μ_x is the mean position, μ_{θ_x} is the mean angle, and $\xi_{1,2}$ are two normally distributed pseudo-random variables. Due to the assumed axial symmetry around the z-axis, these expressions apply to both the x- and y-components with the same parameters. For completeness, Table 5.1 lists the proton beam parameters at the entrance of the water phantom for 100 MeV, 160 MeV, and 225 MeV, as suggested by Ref. [29].

Table 5.1: Fermi-Eyges proton beam parameters for 100 MeV, 160 MeV, and 225 MeV at the entrance of the water phantom [29].

	100 MeV	**160 MeV**	**225 MeV**
E (MeV)	100.150	160.244	225.142
σ_E (MeV)	0.614	0.835	0.513
$\sqrt{2A_2(0)}$ (cm)	0.536	0.334	0.320
$2A_1(0)$ (cm mrad)	1.320	0.809	0.773
$\sqrt{2A_0(0)}$ (mrad)	6.01	3.52	3.90
μ_x (cm)	0	0	0
μ_θ (mrad)	0	0	0

To simulate the r-z dose maps of Ref. [29], the adopted FLUKA geometry is set up using the Flair graphical interface [86, 87]. As shown in Fig. 5.1, it consists of a cylindrical water phantom with a length of 35 cm and a radius of 15 cm, aligned with the z-axis. The proton beam is initiated at its entrance and the initial position and direction of the primary protons is sampled according to the Fermi-Eyges theory, Eq. (5.1). Separate

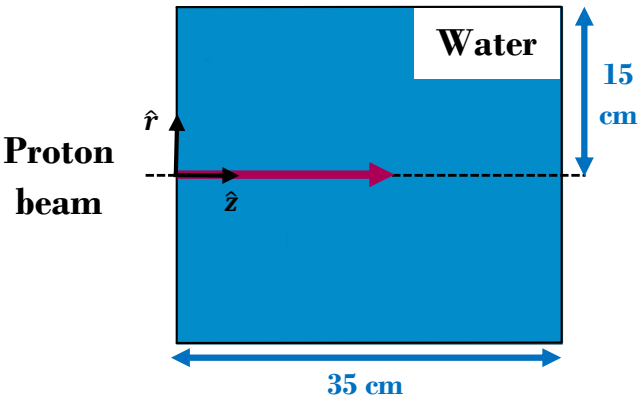

Figure 5.1: Schematic FLUKA simulation geometry showing the proton beam starting at the entrance of the water phantom.

simulations are performed for three different proton energies: 100 MeV, 160 MeV, and 225 MeV; 2.5×10^8 primary protons are simulated in each case.

For each energy, absorbed dose is scored in the water phantom at various radial distances from the beam axis using a cylindrical mesh (`USRBIN`). A radial bin width of 0.42 cm is adopted, corresponding to the diameter of the ionization chamber used experimentally [29]. Table 5.2 provides the radial binnings employed for each proton energy. Consistent with Ref. [29], a bin width of 1 mm along the z-axis is chosen.

Table 5.2: Radial binning employed in FLUKA to score the absorbed dose by 100 MeV, 160 MeV, and 225 MeV protons in water.

$r_j^{\min,\max}$ (cm)	**100 MeV**	**160 MeV**	**225 MeV**
$r_1^{\min}$	0.00	0.00	0.00
$r_1^{\max}$	0.42	0.42	0.42
$r_2^{\min}$	0.55	1.31	1.31
$r_2^{\max}$	0.97	1.73	1.73
$r_3^{\min}$	2.08	2.84	2.08
$r_3^{\max}$	2.50	3.26	2.50
$r_4^{\min}$	2.84	4.36	7.41
$r_4^{\max}$	3.26	4.78	7.83
$r_5^{\min}$	4.36	5.89	9.69
$r_5^{\max}$	4.78	6.31	10.11
$r_6^{\min}$	5.89	7.41	10.46
$r_6^{\max}$	6.31	7.83	10.88

In the performed FLUKA simulations, electron transport and production thresholds are set at 50 keV. This choice, while slightly excessive (50 keV electrons in water have a range of ~43 μm) ensures that electron histories are stopped when they have practically no chance to contribute to any other r-z bin and prevents particle-range-induced artefacts.

Photon production and transport thresholds are set to 100 eV; those for hadrons are set at 100 keV; neutrons are transported down to 0.01 meV; light ions (d, t, ^{3}He, ^{4}He) down to 100 keV, while heavier ions have thresholds scaled from those of ^{4}He by the mass numbers ratio. Lastly, the mean excitation energy of water is set to $I = 78$ eV [88].

5.3 FLUKA *r*-*z* dose maps

The experimental *r*-*z* dose maps have been simulated using the setup outlined in the foregoing section with two versions of FLUKA: v4-3.4, relying on the legacy model for proton nuclear elastic scattering [30], and v4-4.0, incorporating the model developed in this work for this interaction mechanism [27]. Figure 5.2 depicts *r*-*z* maps of absorbed dose in the water phantom for the 225 MeV proton beam. The black dots correspond to the experimental absorbed dose [29], while the solid curves are simulated with FLUKA v4-3.4 (blue) and v4-4.0 (green); dashed curves are discussed later. The dose maps are plotted as a function of depth, but are not integrated over the transverse plane; instead, the radial distance specified in each panel is considered (see Table 5.2 for the employed radial binning). The absorbed doses are shown in arbitrary units as reported in Ref. [29], *i.e.*, normalized to the dose on axis at $z = 3$ cm. At radial distances of $r = 0$ cm and $r = 1.52$ cm (panels 5.2a and 5.2b), where the dose is relatively high, both FLUKA versions exhibit excellent agreement with the experimental absorbed doses. At $r = 2.29$ cm (panel 5.2c), where the dose has decreased by almost two orders of magnitude, FLUKA v4-4.0 shows a slight improvement at depths beyond 20 cm, where the dose remains significant. A more notable improvement is observed at $r = 7.62$ cm (panel 5.2d) at depths between 25 cm and 30 cm. Additionally, better agreement is achieved at $r = 9.90$ cm and $r = 10.67$ cm (panels 5.2e and 5.2f), although some minor discrepancies persist, which are addressed at the end of Section 5.4.

The comparison for the 160 MeV proton beam is shown in Fig. 5.3 (see Table 5.2 for the corresponding radial binnings). The FLUKA v4-4.0 simulation results at $r = 0$ cm, $r = 1.52$ cm, and $r = 4.57$ cm (panels 5.3a, 5.3b, and 5.3d) show a slight but noticeable improvement in agreement with the experimental absorbed dose compared to those from v4-3.4. However, for $r = 1.52$ cm (panel 5.3b), the significant overestimation of the experimental absorbed dose by FLUKA v4-3.4 is only minimally reduced in v4-4.0. A similar discrepancy with experimental absorbed doses was observed also in Ref. [29] for simulations performed using other MC codes. In contrast, for $r = 3.05$ cm (panel 5.3c), the agreement is considerably improved with FLUKA v4-4.0. However, at $r = 6.10$ cm and $r = 7.62$ cm (panels 5.3e and 5.3f), the discrepancies between the experimental absorbed doses and the FLUKA v4-3.4 estimates persist and are not mitigated with v4-4.0: the simulated doses remain significantly lower than the experimental doses. Additionally, the feature observed at depths between 15 and 20 cm is not captured, particularly for $r = 7.62$ cm, as discussed further in Section 5.4.

Lastly, Fig. 5.4 illustrates the same comparison for the 100 MeV proton beam (see Table 5.2 for the corresponding radial binnings). The performances of FLUKA v4-3.4 and v4-4.0 are comparable across all considered radial distances. The agreement with experimental absorbed doses at $r = \{0, 0.76, 2.29\}$ cm (panels 5.4a, 5.4b, and 5.4c) is reasonable. However, at $r = \{3.05, 4.57, 6.10\}$ cm (panels 5.4d, 5.4e, and 5.4f) significant discrepancies persist.

Before further exploring in Section 5.4 the source of the discrepancies at $r = 6.10$ cm and $r = 7.62$ cm for the 160 MeV proton beam and at $r = \{3.05, 4.57, 6.10\}$ cm for the 100 MeV

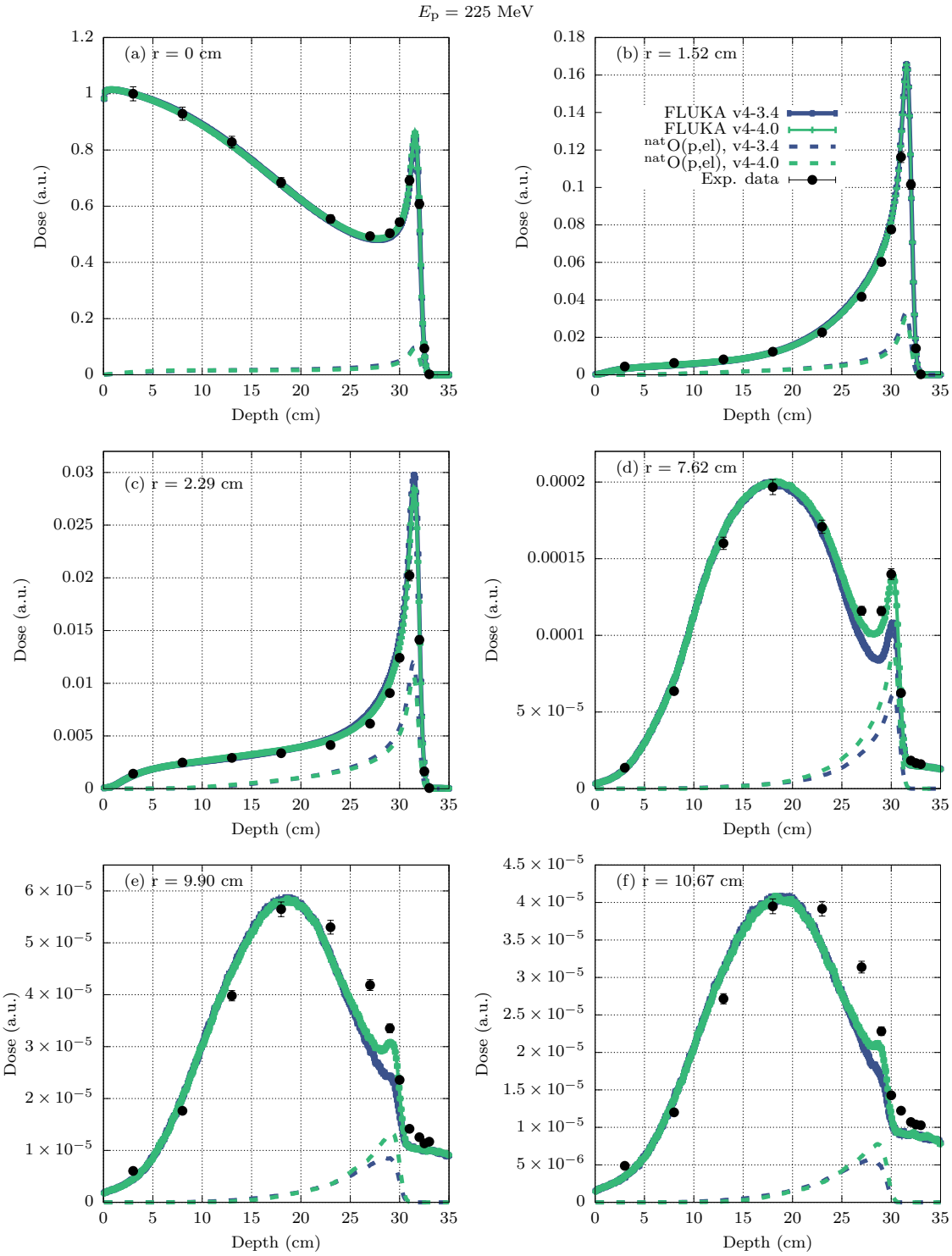

Figure 5.2: Absorbed dose in arbitrary units as a function of depth by 225 MeV protons in water scored with FLUKA v4-3.4 (solid blue) and v4-4.0 (solid green) at the various indicated radial distances. The black dots represent experimental absorbed doses [29]. The blue and green dashed curves show the contribution from particle histories where protons underwent a nuclear elastic scattering event on oxygen, scored with FLUKA v4-3.4 and v4-4.0, respectively.

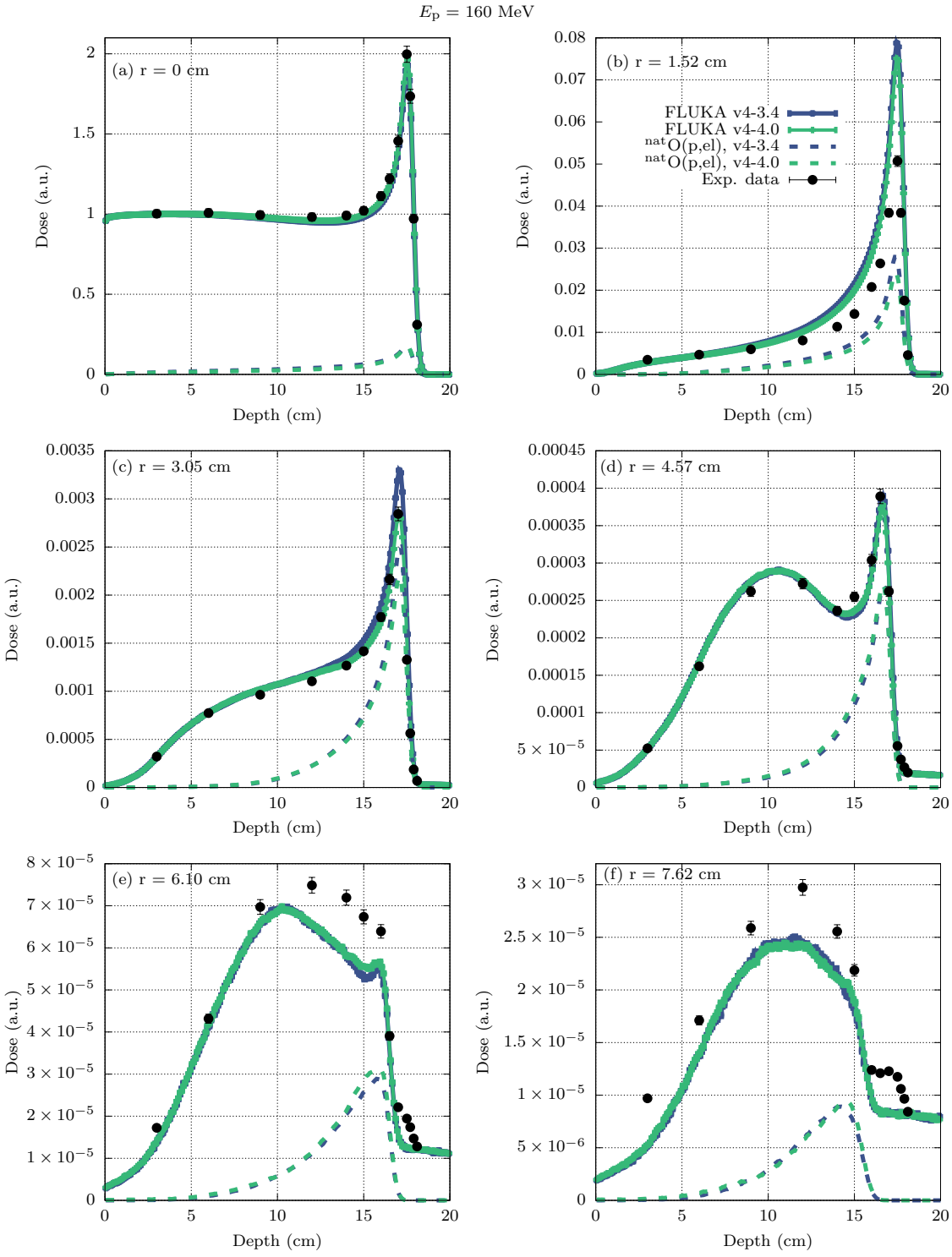

Figure 5.3: Same as Fig. 5.2 for 160 MeV protons.

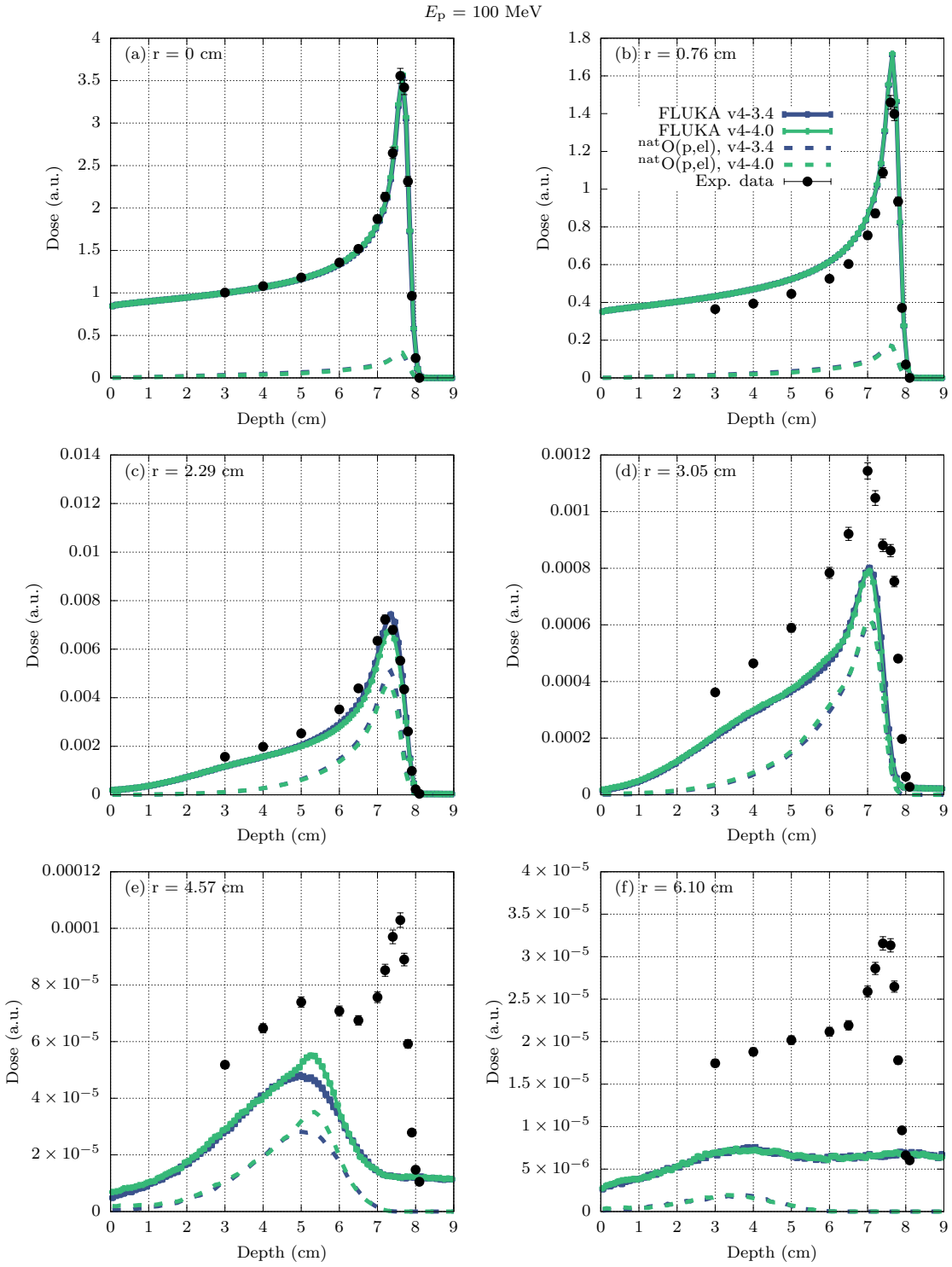

Figure 5.4: Same as Fig. 5.2 for 100 MeV protons.

proton beam, the physical origin of the improvements observed with FLUKA v4-4.0 is investigated. The particle-latching capabilities of FLUKA have been therefore employed to disentangle the contributions of different particle histories to the r-z dose maps. For the three considered energies, Figs. 5.2, 5.3, and 5.4 show the contribution to the total absorbed dose from particle histories where protons underwent a nuclear elastic scattering event on oxygen in FLUKA v4-3.4 (dashed blue curve) and in v4-4.0 (dashed green curve). The magnitude of these dashed curves confirms that the nuclear elastic scattering of protons plays a dominant role at large radial distances and it even contributes significantly on-axis towards the end of the proton range. The substantial increase in dose predicted by FLUKA v4-4.0, which helps to reduce the gap with experimental absorbed doses at large radial distances and depths for the 160 MeV and 225 MeV proton beams, is indeed due to a more accurate treatment of proton nuclear elastic scattering in FLUKA v4-4.0. Specifically, nuclear elastic scattering events of protons on oxygen are modelled more accurately, as FLUKA v4-4.0 relies on fits to experimental differential cross sections (DXSs) for light nuclei [37, 38]. A similar behavior is observed for the 100 MeV proton beam case.

The agreement between the doses simulated with FLUKA v4-3.4/v4-4.0 and the experimental absorbed dose at each radial distance is quantified by means of the relative root mean square deviation:

$$\delta(r_j) = \frac{\sqrt{\frac{1}{N}\sum_{i=1}^{N}\left(D_{ij}^{\mathrm{FLUKA}} - D_{ij}^{\mathrm{exp}}\right)^2}}{D_j^{\mathrm{exp,max}} - D_j^{\mathrm{exp,min}}}, \tag{5.5}$$

where N represents the number of experimental points along the z axis at each radial distance r_j, with $j = \{1, 2, 3, 4, 5, 6\}$. The quantities D_{ij}^{FLUKA} and D_{ij}^{exp} correspond to the FLUKA-simulated and experimental absorbed doses at each z_i and r_j, respectively. The maximum and minimum experimental absorbed doses at each r_j are denoted by $D_j^{\mathrm{exp,max}}$ and $D_j^{\mathrm{exp,min}}$, respectively. Table 5.3 displays $\delta(r_j)$ for FLUKA v4-3.4 and v4-4.0. For the 225 MeV proton beam, $\delta(r_j)$ confirms that FLUKA v4-4.0 achieves better agreement with the experimental absorbed dose across all radial distances compared to v4-3.4. Similarly for the 160 MeV proton beam, except at $r = 7.62$ cm, where both versions yield comparable $\delta(r_j)$. For the 100 MeV case, both FLUKA versions exhibit comparable $\delta(r_j)$.

5.4 Source term for the 100 MeV and 160 MeV proton beams

As presented in Section 5.3, the Fermi-Eyges theory describing the proton beam at the entrance of the water phantom is sufficiently accurate for simulating the experimental r-z dose maps [29] for 225 MeV protons at all the considered radial distances, as well as for 160 MeV and 100 MeV protons, but only on axis. Instead, ar large radial distances several underestimations and missing features are observed for the latter two proton energies. Similar challenges were reported in Ref. [29]. This section addresses the underlying issues and proposes an effective prescription to resolve them.

The Fermi-Eyges theory, briefly discussed in Section 5.2, effectively captures the dominant Gaussian core of the angular distribution of protons incident on the water phantom, resulting from multiple Coulomb scattering (MCS) as the protons pass through air on their way from the beamline to the water phantom. However, it does not account

Table 5.3: Relative root mean square deviation, Eq. (5.5), of the absorbed dose in water under 100 MeV, 160 MeV, and 225 MeV proton irradiation, simulated with FLUKA v4-3.4 and v4-4.0.

E (MeV)	r_j (cm)	$\delta(r_j)$	
		FLUKA **v4-3.4**	FLUKA **v4-4.0**
100	0	0.0274	0.0258
	0.76	0.0805	0.0823
	2.29	0.0544	0.0738
	3.05	0.3200	0.3299
	4.57	0.5639	0.5617
	6.10	0.6209	0.6196
160	0	0.0304	0.0269
	1.52	0.2938	0.2598
	3.05	0.0862	0.0327
	4.57	0.0332	0.0293
	6.10	0.1231	0.1128
	7.62	0.1652	0.1663
225	0	0.0153	0.0119
	1.52	0.0360	0.0332
	2.29	0.0726	0.0504
	7.62	0.0834	0.0296
	9.90	0.1098	0.0813
	10.67	0.1214	0.1029

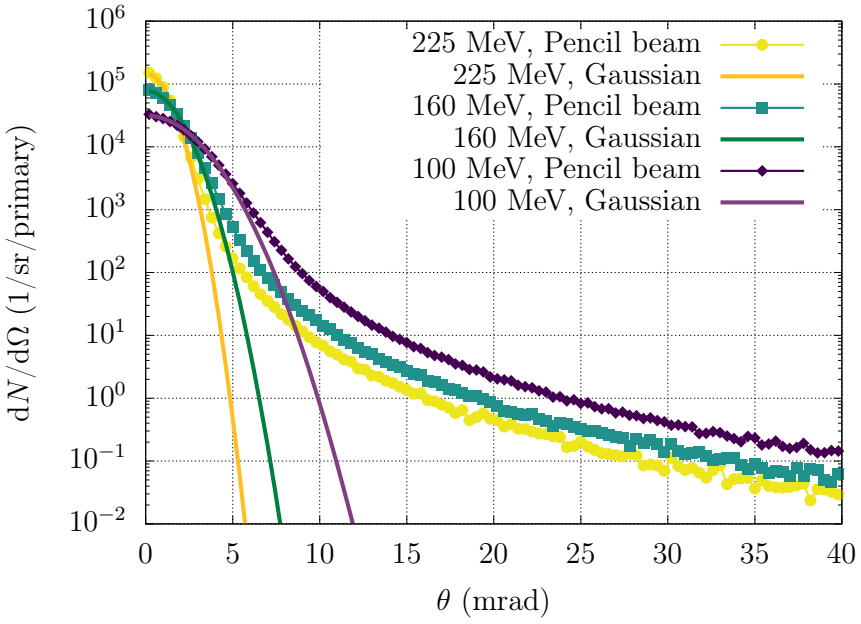

Figure 5.5: Comparison between FLUKA sampled angular distributions of pencil proton beams after 50 cm of air vs. fitted Gaussian distributions for proton energies of 225 MeV (yellow circles), 160 MeV (green squares), and 100 MeV (purple diamonds).

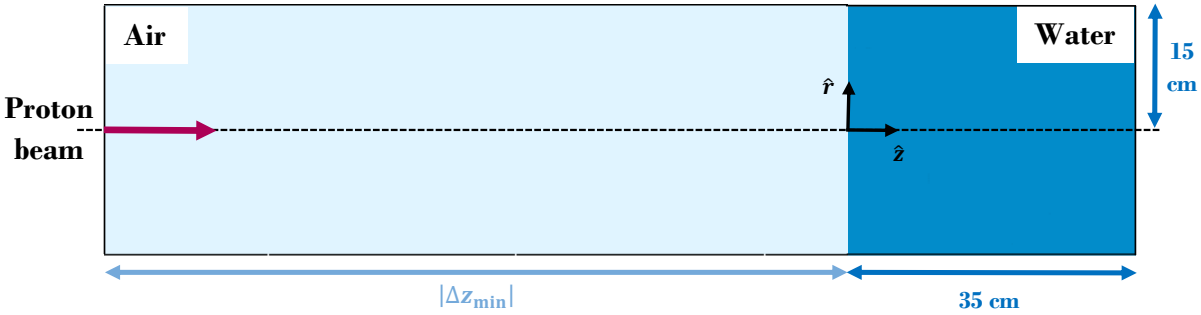

Figure 5.6: Schematic FLUKA simulation setup for the 100 MeV and 160 MeV proton beams, consisting of the water phantom and the impinging proton beam after traversing an air layer.

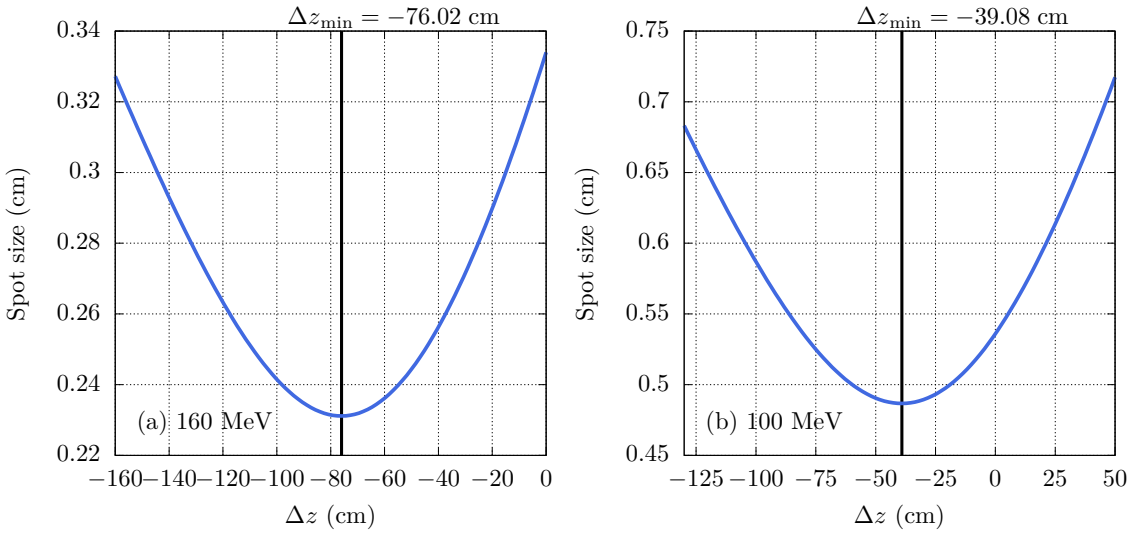

Figure 5.7: Beam spot size as a function of source displacement.

for contributions from large scattering angles (whether due to Coulomb or nuclear elastic scattering) that extend beyond the Gaussian core. To illustrate this point in a simplified manner, Fig. 5.5 shows angular distributions of 225 MeV (yellow circles), 160 MeV (green squares), and 100 MeV (purple diamonds) proton pencil beams after traversing 50 cm of air, sampled with FLUKA. These curves exhibit a dominant Gaussian structure around the incoming direction of the beam, but also display a tail corresponding to larger scattering angles. The solid curves of matching colors represent Gaussian fits to these angular distributions, demonstrating the extent to which such a fit can reproduce them. This analysis suggests that the Fermi-Eyges source model is insufficient to capture large-r features for the 160 MeV and 100 MeV cases, explaining the difficulties observed in Figs. 5.3 and 5.4.

To explicitly simulate deflections beyond the Gaussian core described by the Fermi-Eyges theory, an air layer has been introduced in front of the water phantom, as shown in Fig. 5.6, where protons can undergo nuclear elastic scattering. Consequently, the proton source must be retracted, and the corresponding Fermi-Eyges beam parameters must be evaluated. Since these parameters are known at the entrance of the water phantom [29], the new beam parameters can be derived following the method outlined in Ref. [85],

assuming that air is a weak scatterer, as follows:

$$\begin{aligned} A_0(z) &= A_0(z_1) + T\Delta z \\ A_1(z) &= A_1(z_1) + A_0(z_1)\Delta z + T\frac{\Delta z^2}{2} \\ A_2(z) &= A_2(z_1) + 2A_1(z_1)\Delta z + A_0(z_1)\Delta z^2 + T\frac{\Delta z^3}{3}, \end{aligned} \tag{5.6}$$

where $\Delta z = z - z_1$, with z_1 being the initial position of the source at the entrance of the water phantom, *i.e.*, 0 cm, and $z < 0$ representing the new position of the source. The beam parameters at the entrance of the water phantom [29], *i.e.*, $A_0(z_1)$, $A_1(z_1)$, and $A_2(z_1)$, are listed in Table 5.1. The scattering power [85]

$$T = \frac{\mathrm{d}\langle\theta^2\rangle}{\mathrm{d}z}, \tag{5.7}$$

assumed constant for air, has been estimated as follows. The angular distributions of 100 MeV and 160 MeV protons traversing air slabs of various thicknesses have been scored with FLUKA. The mean squared projected MCS angle has been evaluated for each thickness and T has been estimated using a finite difference approximation of Eq. (5.7). The beam spot size is

$$\sigma_x(z) = \sqrt{2A_2(z)}. \tag{5.8}$$

Figure 5.7 depicts $\sigma_x(z)$ as a function of the source displacement Δz for the 160 MeV (a) and 100 MeV (b) proton beam cases, respectively. The beam spot size reaches its minimum at $\Delta z_{\min} = z_{\min} - z_1 = -76.02$ cm for 160 MeV and -39.08 cm for 100 MeV, as indicated by the black vertical lines in Figs. 5.7a and 5.7b. The parameters of the retracted proton beams at the position of the minima are summarized in Table 5.4. Beyond these minima, it is not possible to farther retract the source using the Fermi-Eyges theory, as this approach only accounts for beam spreading [89], and does not incorporate beam focusing effects. Nonetheless, air layers thicker than $|\Delta z_{\min}|$ can still be simulated by adjusting the density of an air layer with thickness $|\Delta z_{\min}|$ as

$$\rho_{\text{equiv}} = \rho_{\text{air}}\frac{|\Delta z|}{|\Delta z_{\min}|}, \tag{5.9}$$

where $\rho_{\text{air}} = 1.20479 \times 10^{-3}$ g/cm^3 [90, 91] is the density of dry air at sea level and $|\Delta z| > |\Delta z_{\min}|$ is the thickness that yields the best agreement between simulated and experimental r-z dose maps (determined iteratively). This effective method allows one to simulate an air layer thicker than $|\Delta z_{\min}|$ without moving the source beyond the range where the Fermi-Eyges prescription remains valid.

Due to the displacement of the source, the simulated proton beam loses energy while passing through the additional air layer, causing a shift in the position of the Bragg peak. To ensure the correct depth of the Bragg peak, the beam energy is adjusted according to Ref. [92] as:

$$E' = \left(E^p - \frac{\Delta z}{\alpha}\right)^{1/p}, \tag{5.10}$$

where E is the initial beam energy at the entrance of the water phantom, and $p = 1.7589$ and $\alpha = 2.194$ MeV^{-p} cm are parameters obtained by fitting the energy-range power law $R = \alpha E^p$, where R represents the proton range in air [93, 94]. Since energy straggling in

Table 5.4: Parameters of the retracted source at the position at which the beam spot size minimum is attained for the 100 MeV and 160 MeV proton beams.

	100 MeV	**160 MeV**
T (rad^2/cm)	12×10^{-8}	4.8×10^{-8}
$\Delta z_{\min}$ (cm)	-39.08	-76.02
$\sqrt{2A_2(z_{\min})}$ (cm)	0.484	0.216
$2A_1(z_{\min})$ (cm mrad)	0.0916	0.133
$\sqrt{2A_0(z_{\min})}$ (mrad)	5.17	2.32

Table 5.5: Adjusted proton beam energy E' , thickness $|\Delta z|$ of the air layer, and equivalent density as per Eq. (5.9) employed for the 100 MeV and 160 MeV cases.

	100 MeV	**160 MeV**
E' (MeV)	101.167	161.450
$\|\Delta z\|$ (cm)	130	220
ρ_{equiv} (g/cm^3)	4.00755×10^{-3}	3.48663×10^{-3}

air is negligible, the energy spread σ_E of the proton beam at the water phantom entrance, listed in Table 5.1, remains unchanged. The corrected proton beam energy E', along with the equivalent air density ρ_{equiv}, and the air layer thickness $|\Delta z|$ needed to evaluate ρ_{equiv} are provided in Table 5.5.

Figures 5.8 and 5.9 illustrate the significant impact of introducing an additional air layer in front of the water phantom for 160 MeV and 100 MeV proton beams, particularly at larger radial distances from the beam axis. The experimental absorbed doses [29] are displayed in black symbols, while the FLUKA v4-4.0 simulations with and without the air layer are represented by the yellow and green curves, respectively. The dashed magenta and blue curves depict particle histories where protons underwent nuclear elastic scattering in air on nitrogen and oxygen, respectively. These interactions in the additional air layer are crucial: without their contribution (along with proton-induced nuclear reactions in air), the simulated dose is significantly lower than the experimental absorbed doses. For the 160 MeV case, particularly at $r = 6.10$ cm (panel 5.8e) and $r = 7.62$ cm (panel 5.8f), features observed in the experimental absorbed dose at depths between 15–20 cm are not captured when the air layer is absent (green curves). However, when the air layer is included, these features, originating from proton nuclear elastic scattering on nitrogen and oxygen in air, are accurately reproduced (yellow curves). The agreement with experimental absorbed doses at smaller radial distances (panels 5.8a–d) remains unaltered after retracting the source. Similarly, for the 100 MeV case, good agreement is maintained on-axis (panel 5.9a) and at $r = 0.76$ cm (panel 5.9b). At $r = 2.29$ cm (panel 5.9c), there is a slight improvement that helps reduce the discrepancy between FLUKA-simulated and experimental absorbed doses. However, at $r = 3.05$ cm (panel 5.9d) and $r = 4.57$ cm (panel 5.9e), the increase in simulated dose is still insufficient to match the experimental absorbed dose. The most

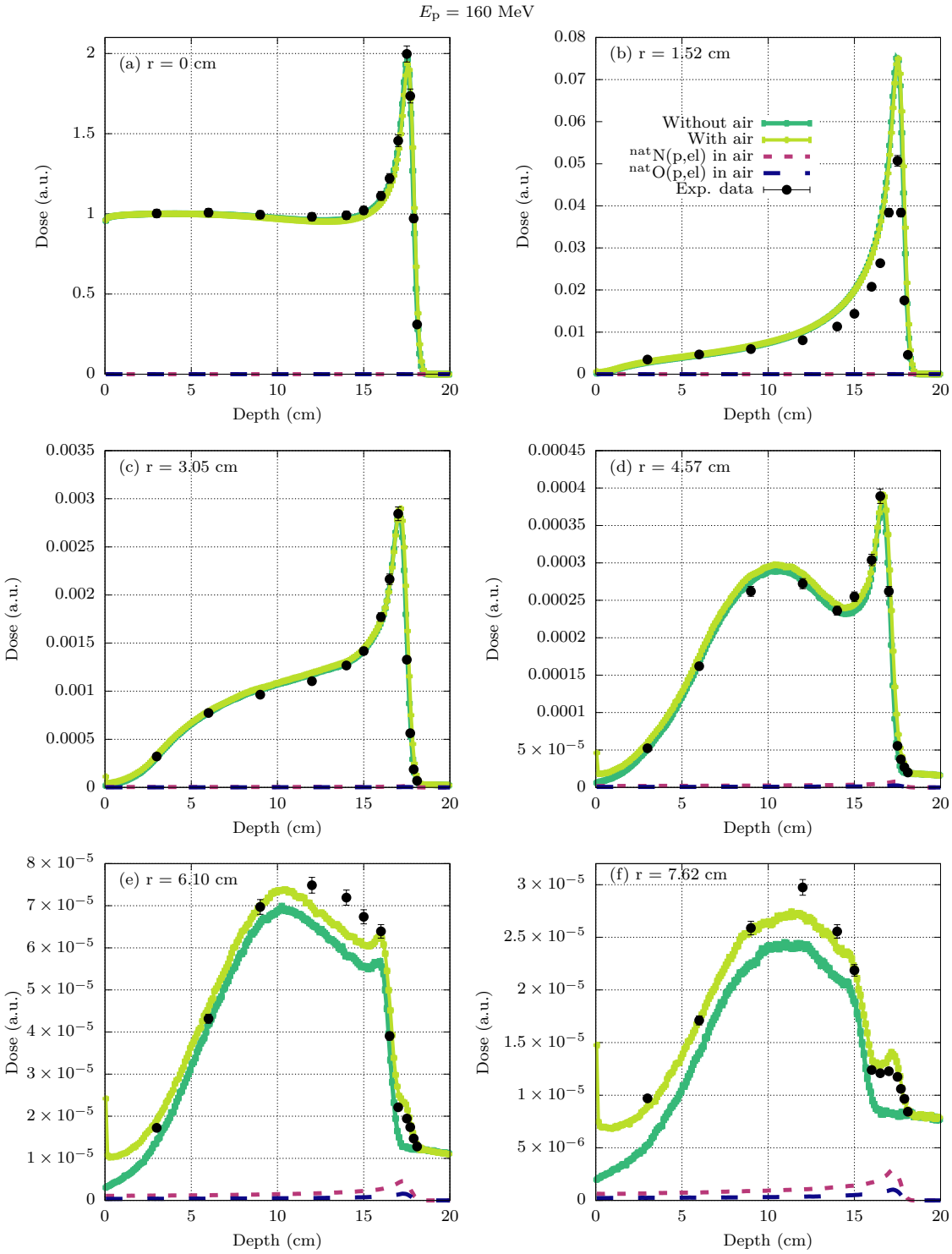

Figure 5.8: Absorbed dose in arbitrary units as a function of depth by 160 MeV protons in water scored with FLUKA v4-4.0 without (green) and with (yellow) the air layer. The black dots represent experimental absorbed doses [29]. The dashed curves correspond to contributions from particle histories where protons underwent a nuclear elastic scattering in air on nitrogen (magenta) and on oxygen (blue). In panels (a)-(c) these contributions are almost zero at the scale of the figure.

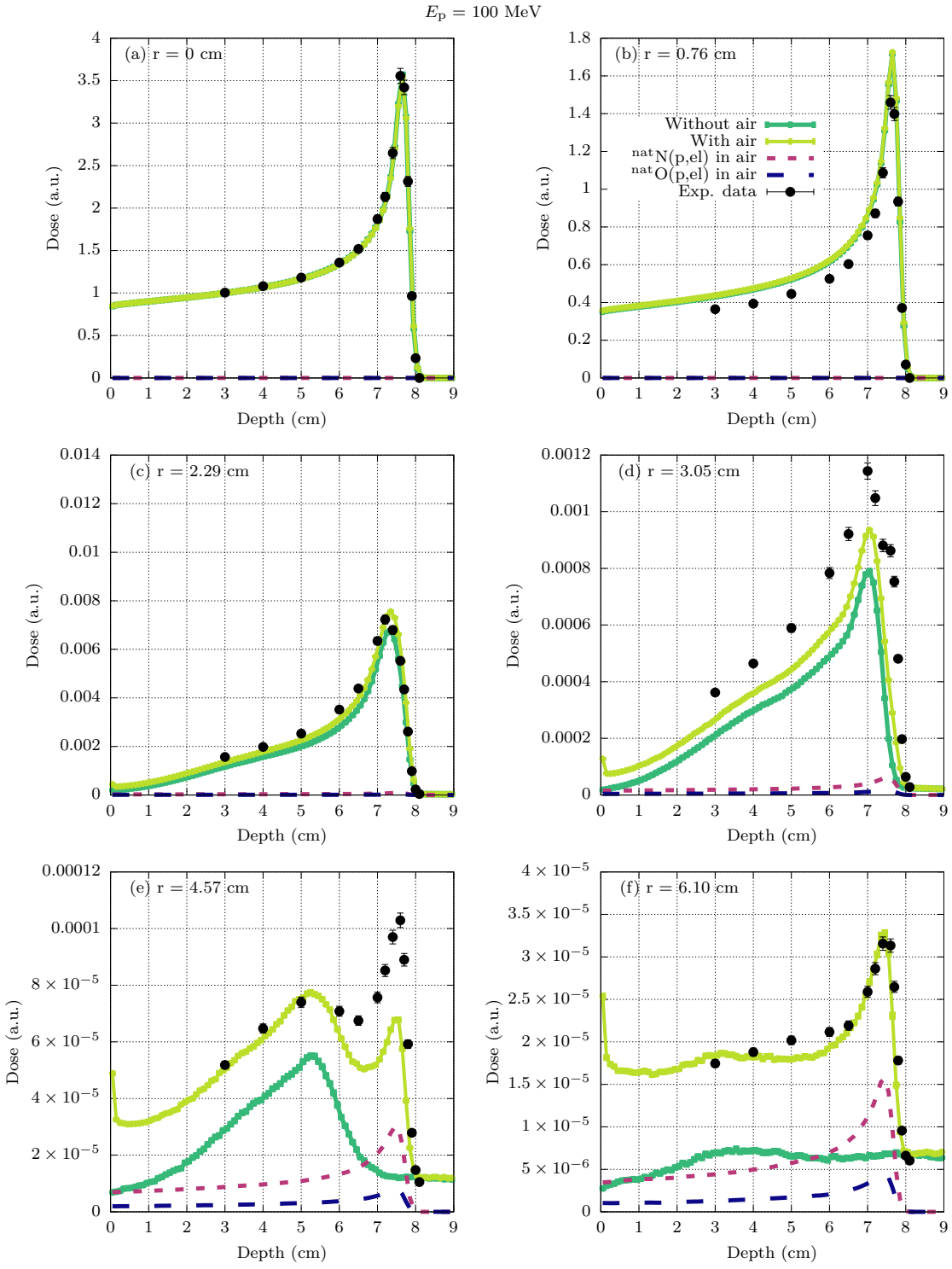

Figure 5.9: Same as Fig. 5.8 for 100 MeV.

striking improvement occurs at $r = 6.10$ cm (panel 5.9f), where proton nuclear elastic scattering on nitrogen in the air layer plays a substantial role, as indicated by the dashed magenta curve, leading to a satisfactory match with the experimental absorbed dose.

The mean free paths for nuclear elastic scattering of protons in air are 2.37×10^4 cm for 100 MeV, 6.75×10^4 cm for 160 MeV, and 2.34×10^5 cm for 225 MeV. While the mean free paths for 100 MeV and 160 MeV protons are similar, the mean free path for 225 MeV protons is one order of magnitude larger. This explains why the Fermi-Eyges source characterization works well for the 225 MeV proton beam, but it is not as effective for the 100 MeV and 160 MeV beams.

The features observed at $z = 0$ in Figs. 5.8 and 5.9, particularly at large radial distances, are attributed to δ rays produced by secondary particles in the air layer before the water phantom. These δ rays transition from a low-density medium (air) to a higher-density medium (water), where their range is significantly reduced. As a result, the δ rays generated in air deposit their energy over a shorter distance in water, leading to localized dose deposition at the entrance of the water phantom.

Table 5.6: Relative root mean square deviation, Eq. (5.5), of the absorbed dose in water under 100 MeV and 160 MeV proton irradiation, simulated with FLUKA v4-4.0 with and without the additional air layer.

E (MeV)	r_j (cm)	$\delta(r_j)$	
		Without air	**With air**
100	0	0.0258	0.0294
	0.76	0.0823	0.0890
	2.29	0.0738	0.0460
	3.05	0.3299	0.2301
	4.57	0.5617	0.2357
	6.10	0.6196	0.1163
160	0	0.0269	0.0616
	1.52	0.2598	0.2884
	3.05	0.0327	0.0718
	4.57	0.0293	0.0524
	6.10	0.1128	0.0625
	7.62	0.1663	0.0523

The measure $\delta(r_j)$, defined in Eq. (5.5), has been calculated for the FLUKA v4-4.0 absorbed doses, considering the additional air layer in front of the water phantom, and compared in Table 5.6 with the FLUKA v4-4.0 estimates from Table 5.3, where the air layer was not accounted for. For the 160 MeV proton beam, a slight deterioration in agreement with the experimental absorbed dose is observed at the first four radial distances when the air layer is added. However, at $r = 6.10$ cm and $r = 7.62$ cm, there is a significant improvement due to nuclear elastic and inelastic scattering of protons in air. The simulated dose not only increases in intensity throughout the depth of the water phantom, but also reproduces key features beyond 15 cm depth more accurately. For the 100 MeV case, at $r = 0$ cm and $r = 0.76$ cm, similar $\delta(r_j)$ are obtained regardless of whether the air layer is considered or not, as its effect on-axis is negligible at this lower proton energy. At larger radial distances, however, better agreement with experimental absorbed doses is achieved. The most notable impact of including the air layer occurs at $r = 6.10$ cm, where nuclear

elastic scattering of protons on nitrogen provides a substantial increase in the simulated dose, leading to a closer match with experimental absorbed doses.

Differences between FLUKA v4-4.0-simulated and experimental absorbed doses persist at the last two radial distances for the 225 MeV proton beam, as well as for the 160 MeV proton beam (even with the additional air layer). Moreover, for the 160 MeV case at $r = 1.52$ cm, a significant overestimation of the experimental absorbed dose by the simulated dose is observed with both FLUKA versions, and this overestimation remains when the air layer is added in front of the water phantom. For the 100 MeV case, discrepancies are still present at $r = 3.05$ cm and $r = 4.57$ cm. Similar differences to those mentioned above were also reported in the original study [29] for simulations performed with other MC codes. To explore whether nuclear interaction models could explain these discrepancies, the integrated cross section for both nuclear elastic and inelastic scattering of protons on oxygen has been varied by a considerable ±10% across the energy range of interest (100–225 MeV). However, this variation was insufficient to reduce the gap between simulated and experimental absorbed doses and compromised the good agreement at shallow depths. Thus, the remaining differences may be attributed to uncertainties in the experimental absorbed doses, in the original Fermi-Eyges proton beam parameters (which propagate into uncertainties in source parameters when retracted to its position at the start of the air layer), or due to simplifications of the actual experimental beamline layout.

5.5 Role of different interaction mechanisms in various regions of the *r*-*z* maps

To illustrate the contribution of different interaction mechanisms to dose absorption in the setup used in this work, the particle-latching capabilities of FLUKA have been exploited to score explicitly the contribution of various particle histories to different regions of the *r*-*z* dose maps. Figures 5.10, 5.11, and 5.12 show the total dose for 225 MeV, 160 MeV, and 100 MeV proton beams (the latter two with an additional air layer in front of the water phantom, as described in Section 5.4), as simulated with FLUKA v4-4.0 (teal). The total dose is further resolved into contributions from particle histories involving nuclear reactions (purple), with neutron interactions explicitly filtered out (orange), nuclear elastic scattering on hydrogen (yellow), oxygen (blue), and nitrogen (magenta), or no nuclear interactions. In all cases, Coulomb scattering and ionization are always active. For all considered energies, the dominant contribution on-axis throughout the depth of the water phantom comes from particle histories without nuclear interactions (green), as expected, albeit this contribution decreases with increasing distance from the beam axis. In contrast, secondaries produced by proton nuclear reactions (purple) contribute significantly at larger radial distances and intermediate depths. Among these secondaries, neutrons (and their subsequent secondaries generated from their nuclear interactions) are responsible for the plateau observed in the purple curves at greater depths. Interestingly, there are specific radial distances where nuclear elastic scattering of protons on hydrogen (yellow), which remains unchanged in FLUKA v4-4.0 compared to v4-3.4, becomes significant: $r = 7.62$ cm for 225 MeV, and $r = 3.05$ cm and $r = 4.57$ cm for 160 MeV. Nuclear elastic scattering on oxygen (blue) plays a crucial role both on-axis and out-of-field for all three energies, particularly at greater depths. Lastly, for both 160 MeV and 100 MeV cases, nuclear elastic scattering of protons on nitrogen (magenta) in the additional air layer in front of

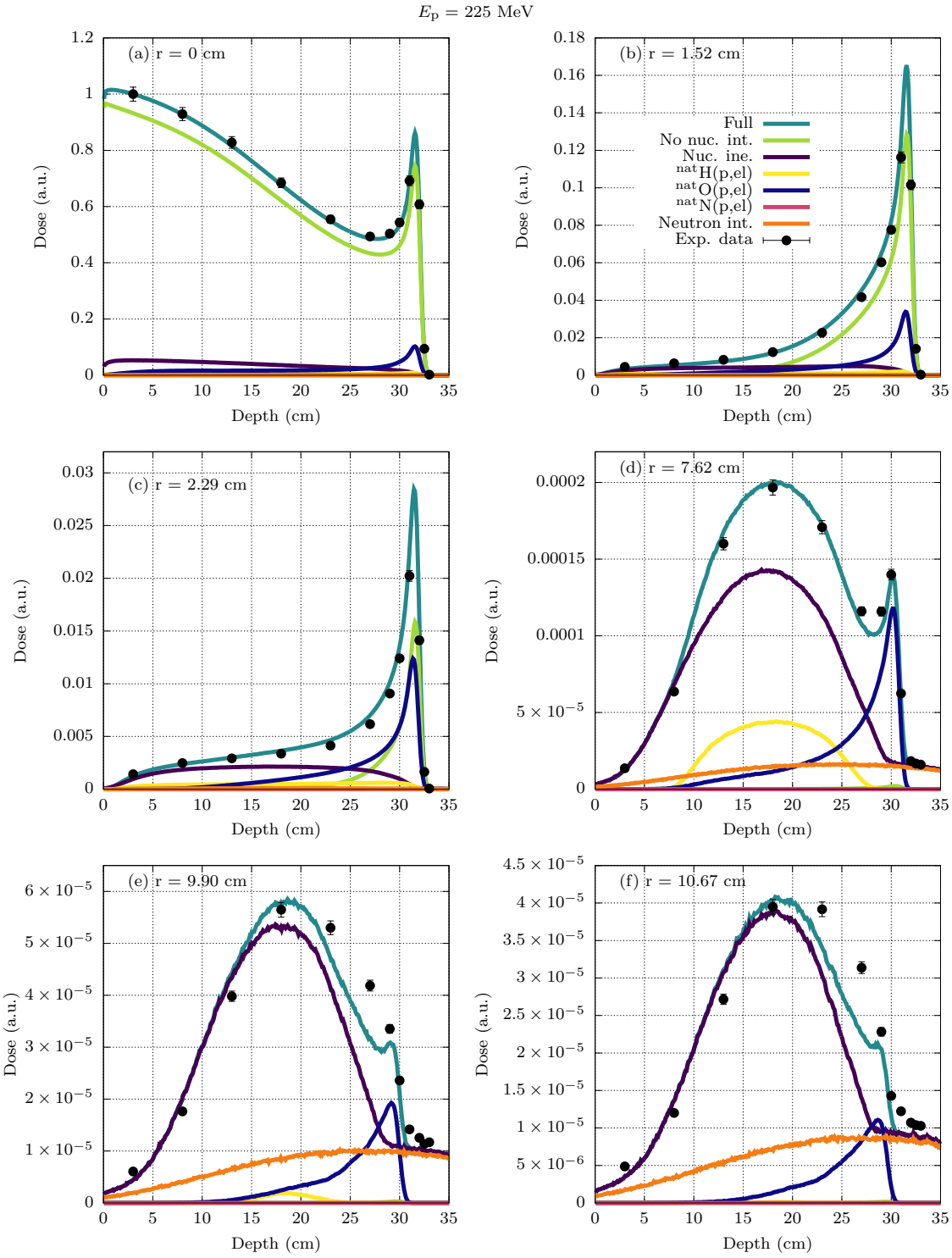

Figure 5.10: FLUKA v4-4.0 absorbed dose in arbitrary units as a function of depth by 225 MeV protons in water, resolved into the contribution of various kind of particle histories (see key and text).

the water phantom has a surprisingly significant impact.

To further quantify the contribution of different interaction mechanisms to the r-z dose maps, the ratio $D_i(r,z)/D(r,z)$ has been evaluated, where $D_i(r,z)$ represents the absorbed dose from particle histories having undergone a specific interaction interaction mechanism

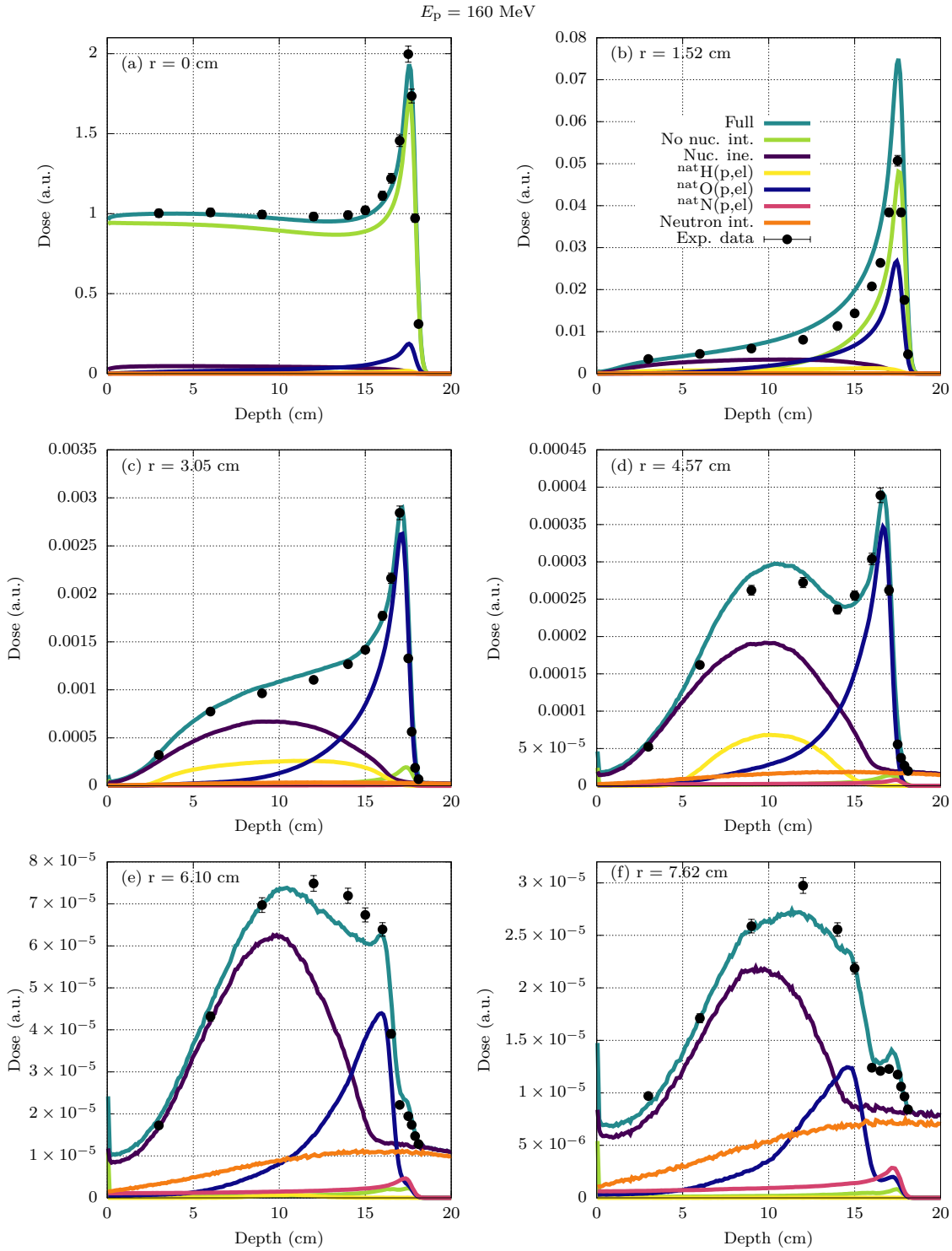

Figure 5.11: Same as Fig. 5.10 for 160 MeV protons.

of type i ={no nuclear interactions, nuclear elastic scattering, nuclear reactions, neutron interactions} and $D(r,z)$ is the total absorbed dose. Figures 5.13, 5.14, and 5.15 display this ratio as a function of radial distance from the beam axis and depth within the water phantom. These 2D maps have been generated by simulating 10.5×10^9 primary protons. The contribution from proton histories without nuclear interactions is shown in the upper left panels of these figures. This contribution is highest near the beam axis and decreases

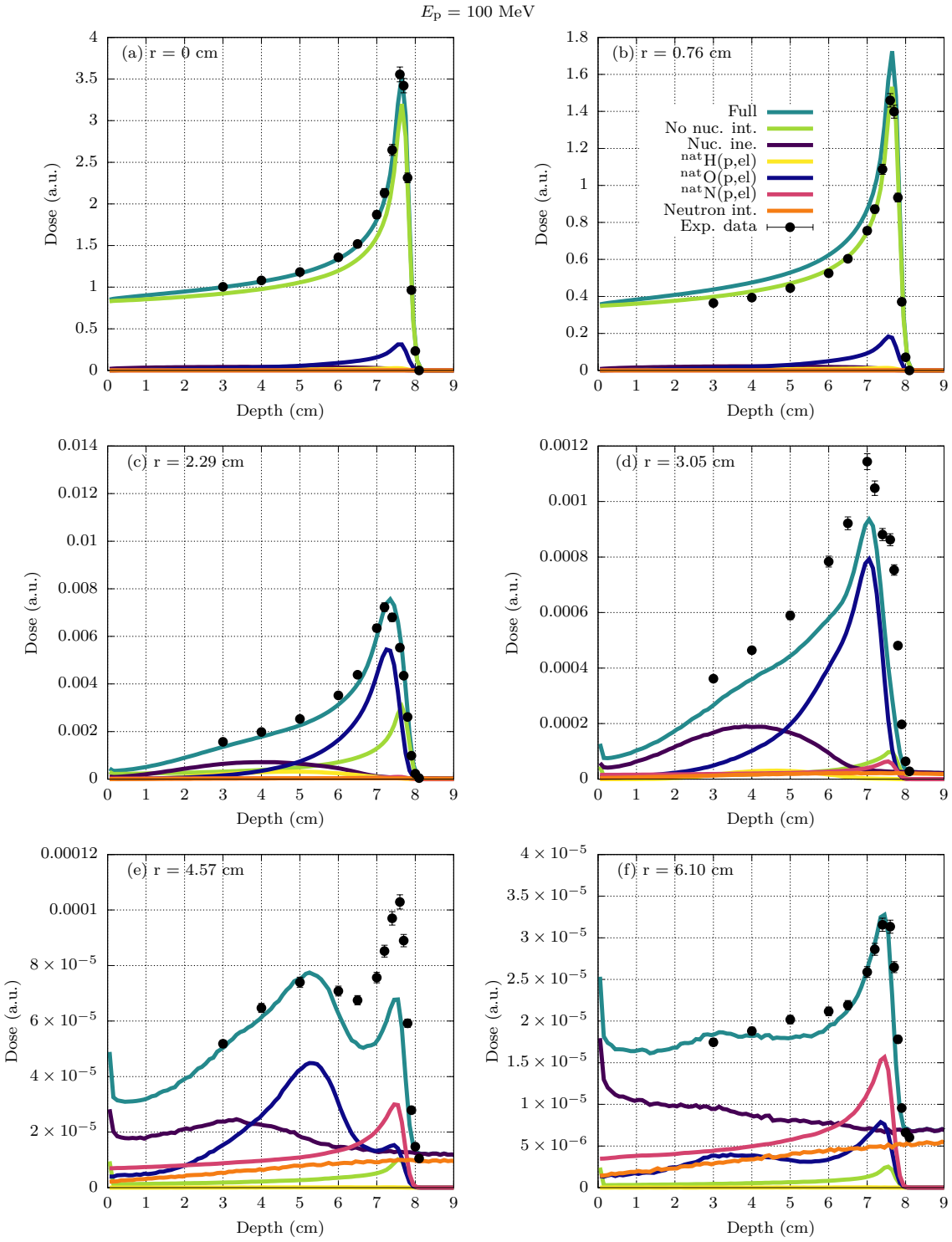

Figure 5.12: Same as Fig. 5.10 for 100 MeV protons.

sharply beyond the Bragg peak, which occurs around 30-35 cm for 225 MeV protons, 15-20 cm for 160 MeV protons, and 8-9 cm for 100 MeV protons. As expected, the radial spread of this contribution (driven by multiple Coulomb scattering) is relatively narrow, with most of the dose concentrated near the beam axis, broadening towards the end of the proton range. The maximum energy transfer to δ rays from 100 MeV, 160 MeV, and 225 MeV protons is approximately 229.19 keV, 377.79 keV, and 548.19 keV, respectively.

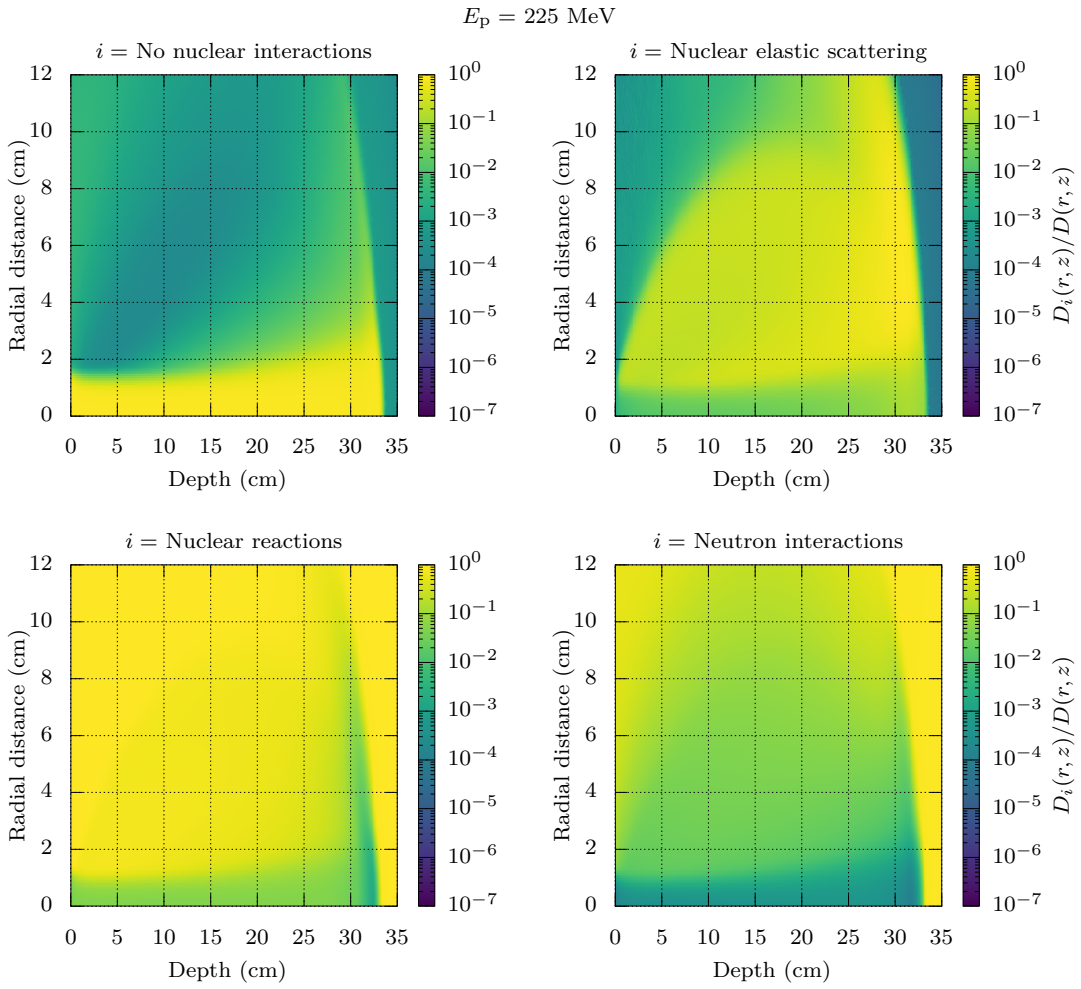

Figure 5.13: Ratio between the FLUKA v4-4.0 absorbed dose due to various interaction mechanisms (see key and text) and the total absorbed dose for 225 MeV protons in water.

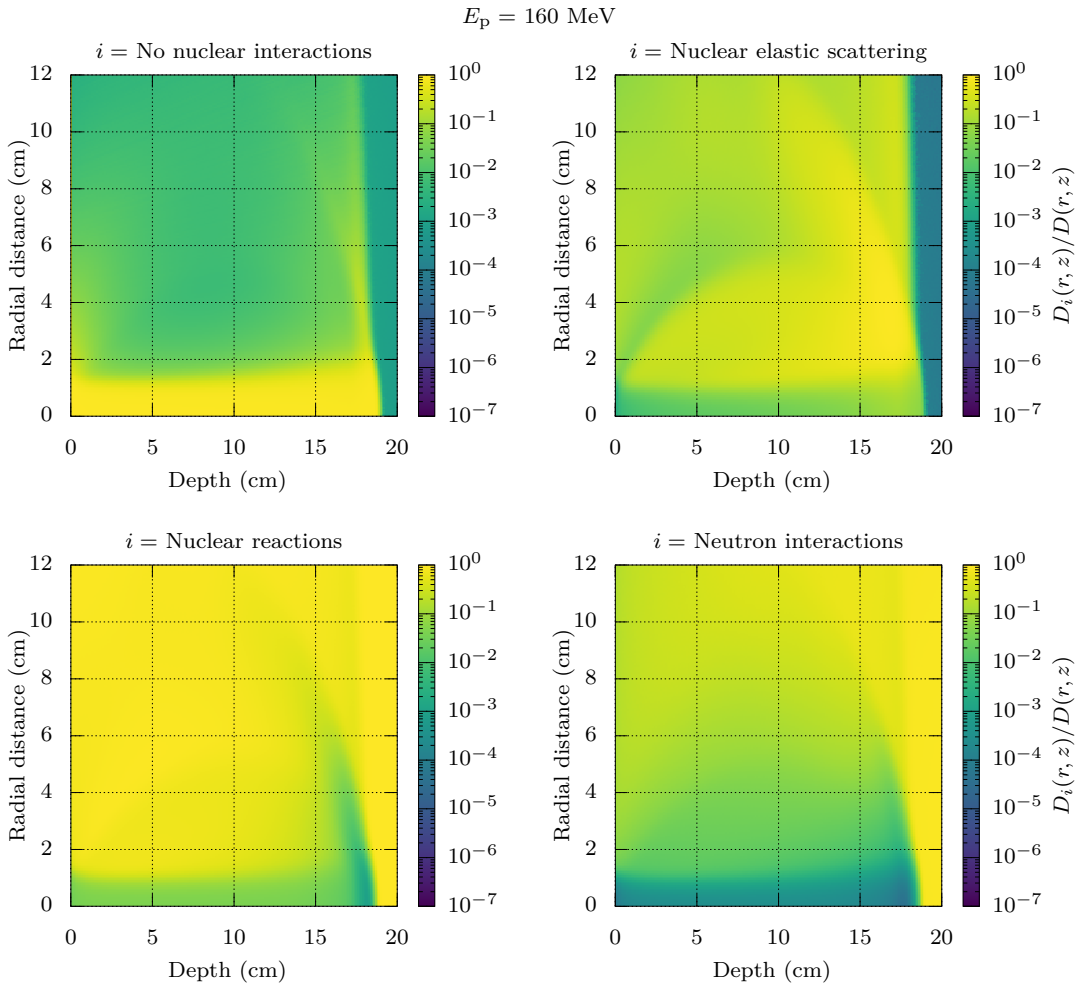

Figure 5.14: Same as Fig. 5.13 for 160 MeV protons.

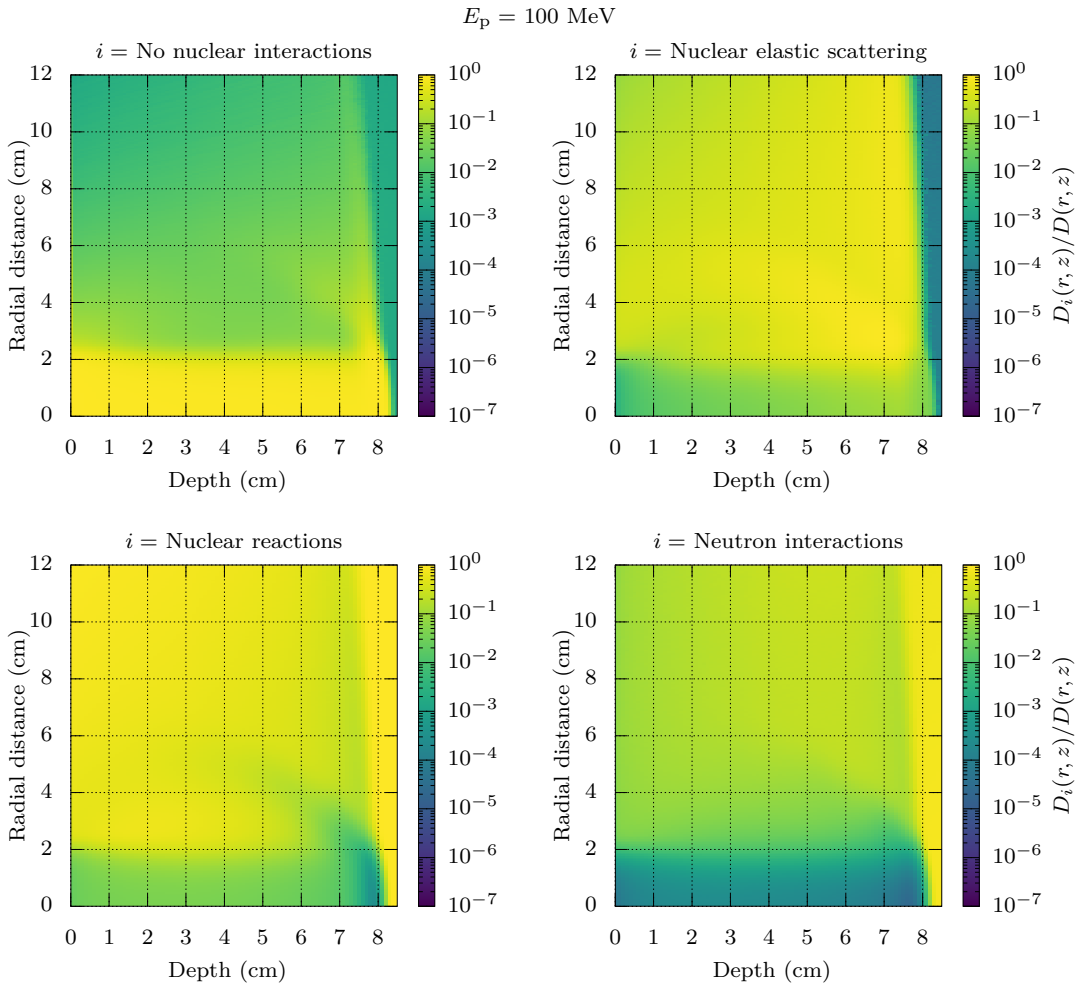

Figure 5.15: Same as Fig. 5.13 for 100 MeV protons.

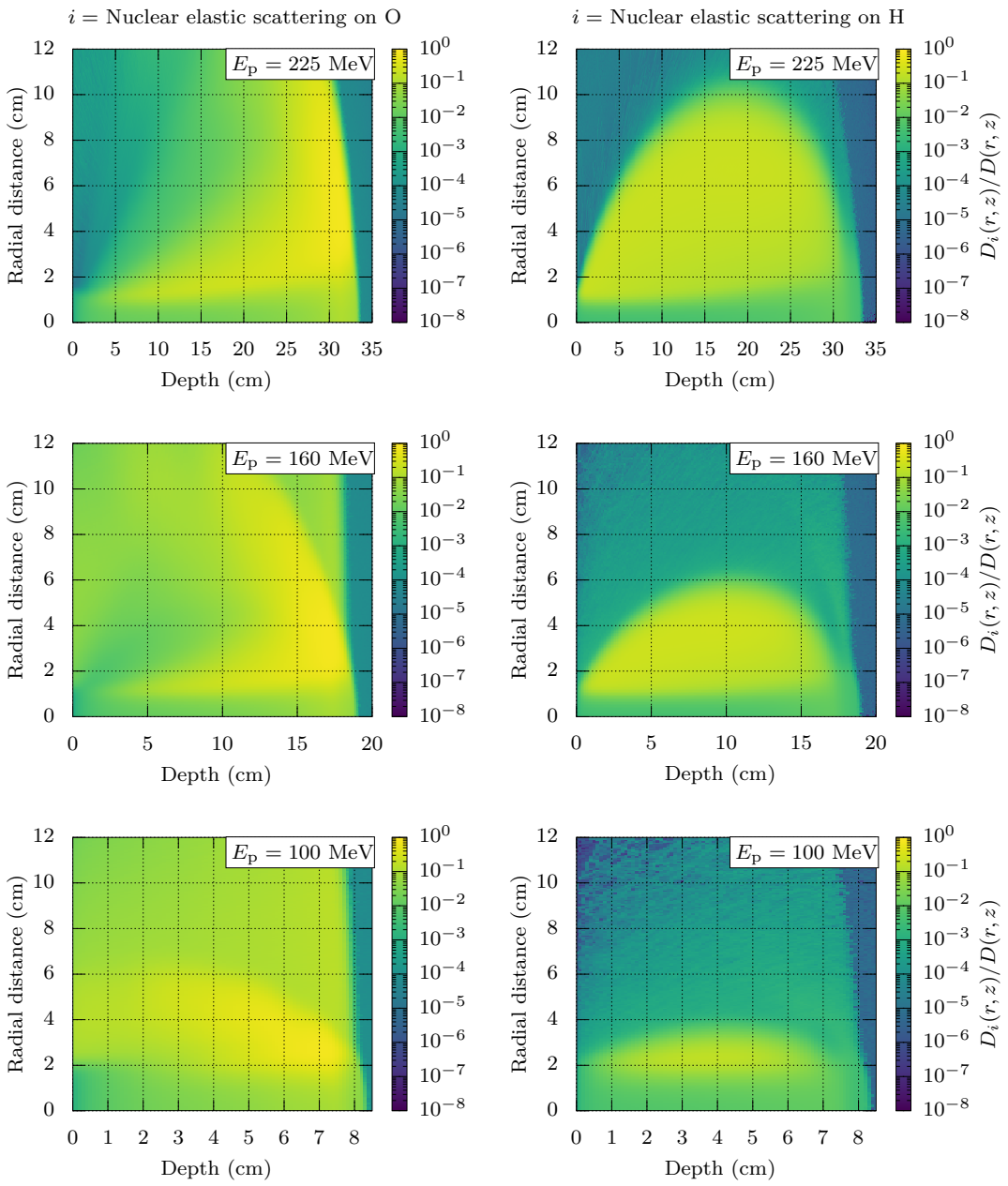

Figure 5.16: Ratio of the FLUKA v4-4.0 absorbed dose due to histories from nuclear elastic scattering of protons on oxygen (left panels) and hydrogen (right panels) to the total absorbed dose for 225 MeV, 160 MeV, and 100 MeV protons (first, second, and third row, respectively) in water.

At these energies, electrons can emit Bremsstrahlung photons that travel farther from the beam axis, explaining the non-zero dose ratio at large radial distances at all depths, even beyond the Bragg peak. Additionally, for both the 100 MeV and 160 MeV cases, particle tracks observed in the upper left panels are due to secondary electrons produced by Bremsstrahlung photons via Compton scattering or the photoelectric effect.

The contribution of particle histories involving nuclear elastic scattering, shown in the upper right panels, exhibits a wider radial spread than those without nuclear interactions for all three energies. This is due to the DXS for proton nuclear elastic scattering which is broader compared to that of Coulomb scattering [27]. Although the overall dose contribution from nuclear elastic scattering is smaller than that from particle histories without nuclear interactions, this mechanism plays a crucial role at greater depths across all radial distances.

The contribution from proton histories involving nuclear reactions, depicted in the bottom left panels, spans a broad range in both radial distance and depth. This contribution becomes more significant at larger radial distances compared to the contributions from particle histories without nuclear interactions or those involving nuclear elastic scattering. This increase is due to the production of secondary particles, which can travel farther from the primary beam path. Specifically, the contribution from histories where neutrons were produced, shown in the bottom right panels, is generally small but increases at larger depths for all radial distances. In water, neutrons undergo elastic scattering abundantly, losing energy until they thermalize. These thermal neutrons have a high capture cross section and lead to the emission of ~MeV photons that can travel $\mathcal{O}(10)$ cm within the water phantom, contributing to dose deposition at large depths.

The contribution of proton histories involving nuclear elastic scattering has been further resolved according to the atomic number of the target nucleus: oxygen or hydrogen. Figure 5.16 presents these two contributions in the left and right panels, respectively, for 225 MeV, 160 MeV, and 100 MeV proton beams. During proton-hydrogen nuclear elastic scattering events, due to their equal masses, a larger momentum transfer can occur compared to proton-oxygen elastic scattering. This larger momentum transfer explains the broader radial extent of absorbed dose observed for proton-hydrogen elastic scattering events (right panels), as opposed to proton-oxygen elastic scattering events (left panels) in Fig. 5.16.

Chapter 6

α-particle elastic scattering on $N = Z$ nuclei: beyond optical potential models

6.1 Motivation

Given an increasing interest in ^{4}He beams for applications in both hadron therapy [31] and single-event upset (SEU) production in electronic devices [32], α-scattering processes involving large-angle deflections (resulting in significant energy transfers from the α particle to the material), such as nuclear elastic scattering, may become particularly important. However, FLUKA currently lacks a model for the nuclear elastic scattering of α particles. While the approach used in this work for proton nuclear elastic scattering, based on a global optical potential model (OPM), is effective, its application to α particles becomes challenging: global OPMs face difficulties in accurately reproducing the angular distribution of α particles with energies of tens of MeV on $N = Z$ nuclei at large scattering angles. In this angular region, there is a pronounced enhancement of the differential cross section (DXS), known as the anomalous large-angle scattering (ALAS) [35, 95, 96]. Several studies [35, 36] suggest that ALAS may be linked to α-like correlations within $N = Z$ nuclei, and prior to undertaking a more comprehensive modelling of this interaction mechanism, this hypothesis has been explored as an initial step.

ALAS cannot be reasonably explained in the standard approach of global OPMs relying on Woods-Saxon (WS) potentials [33]. Modified WS potentials were also considered [95] and, although these phenomenological potentials can fit the experimental angular distributions, they depend on fit parameters which do not have a clear physical interpretation. Furthermore, various reaction models were proposed, such as L-dependent potentials [97], α exchange [98], Regge-poles [99], and quasi-molecular resonances [100], to name but a few. Since ALAS is mainly observed in the elastic scattering of α particles on $N = Z$ nuclei, assumed to exhibit α-type correlations in the ground state, in some studies [36, 101, 102] ALAS was associated to the scattering between the α-particle and the α clusters in the target nucleus. In more recent studies, ALAS was investigated in the framework of the single-folding model [103, 104]. In this approach, the real part of the interaction potential between the α particle and the nucleus is calculated by folding an α-nucleon interaction potential with the nuclear density of the target nucleus. The imaginary part is instead taken as a standard WS potential [103, 104]. The main conclusions of the single-folding calculations are the following: (a) the real scattering potential able to describe ALAS has a rather different shape than the WS potential; (b) a weak absorption of the incident α particles is needed to reproduce ALAS; this is commonly achieved by employing imaginary potentials with a small strength. How a reduced absorption could be related to ALAS

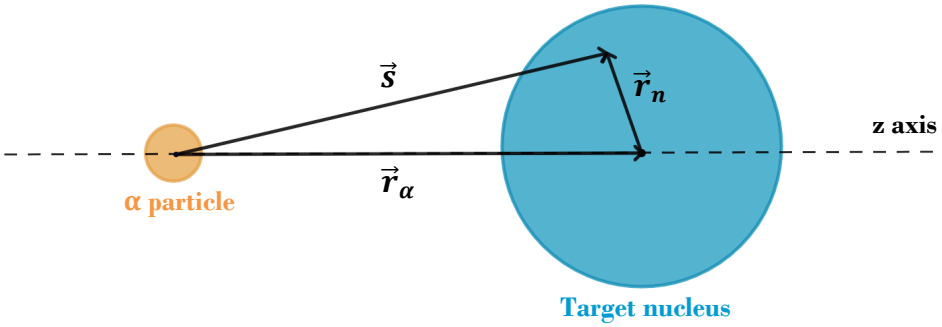

Figure 6.1: Schematic representation of the interaction between the α particle and the target nucleus.

is discussed in Refs. [105–107]. According to these studies, ALAS is generated by those α particles which, due to the weak absorption, can enter inside the nucleus and then be scattered back by the inner wall of the effective potential. This scenario is supported by semiclassical calculations which show that the trajectories of the α particles entering the nucleus are diverted in a unique focal point and, afterwards, some of these trajectories are emerging in the backward directions [107]. In the majority of the folding calculations which address ALAS, the real part of the interaction potential is derived by folding the α-nucleon interaction potential with phenomenological densities of a particular form, *e.g.*, modified Gaussian. These densities, which are fitted to nuclear root mean square radii, are not expected to provide a detailed description of the density profile across the whole nucleus.

In this chapter, both the real and imaginary parts of the α-nucleus interaction potential have been evaluated using the single-folding model in which realistic nuclear densities, derived from microscopic mean field models and explicitly incorporating correlations, have been employed. For the α-nucleon interaction potential a phenomenological energy- and density-dependent Gaussian form has been assumed [108]. To reduce the number of fit parameters, the energy dependence and the range of the real part of the α-nucleon interaction potential have been set from theoretical estimations [109]. The adopted single-folding approach allows one to probe the role of ground state correlations inside the target nucleus by means of the realistic mean-field nuclear densities. Furthermore, this prescription, which extends beyond global OPMs, provides a reasonable description of α elastic scattering from *sd*-shell nuclei across the full angular domain.

6.2 Single-folding potential

The total interaction potential between the α particle and the target nucleus is the sum of the electrostatic potential, $V_{\mathrm{C}}(r_\alpha)$, and the nuclear interaction potential, $V_{\alpha A}(r_\alpha)$:

$$V(r_\alpha) = V_{\mathrm{C}}(r_\alpha) + V_{\alpha A}(r_\alpha), \tag{6.1}$$

where r_α is the distance between the α particle and the center of the target nucleus, as illustrated in Fig. 6.1.

The electrostatic potential, modelled as the Coulomb interaction between a uniformly

charged sphere (the target nucleus) and a point charge (the α particle), is

$$V_{\mathrm{C}}(r_\alpha) = \begin{cases} \dfrac{Z_{\mathrm{p}} Z_{\mathrm{t}} e^2}{2R}\left(3 - \dfrac{r_\alpha^2}{R^2}\right), & r_\alpha < R, \\ \dfrac{Z_{\mathrm{p}} Z_{\mathrm{t}} e^2}{r_\alpha}, & r_\alpha \geq R, \end{cases} \tag{6.2}$$

where A is the mass number of the target nucleus, $R = 1.3A^{1/3}$ is its radius in fm, Z_{p} and Z_{t} are the atomic numbers of the projectile and of the target nucleus, respectively, and $e^2 = 1.44$ MeV fm is the square of the elementary charge.

In this work, the nuclear potential describing the interaction between the target nucleus and the point-like α particle is derived in the framework of the single-folding model (see, *e.g.*, Ref. [108]):

$$V_{\alpha A}(r_\alpha) = \int \rho(r_n)\, v_{\alpha n}(s)\, \mathrm{d}\boldsymbol{r_n}, \tag{6.3}$$

where r_n is the coordinate of a nucleon inside the nucleus, s is the distance between the α particle and that nucleon, as depicted in Fig. 6.1, ρ is the nuclear density of the target nucleus, and $v_{\alpha n}(s)$ is the α-nucleon interaction potential.

6.2.1 α-nucleon interaction potential

The phenomenological α-nucleon interaction potential adopted in this work is

$$v_{\alpha n}(s) = V e^{-(s/a_{\mathrm{R}})^2} + iW e^{-(s/a_{\mathrm{I}})^2}, \tag{6.4}$$

where V and W are the strengths of the real and the imaginary parts, respectively, while a_{R} and a_{I} are their corresponding ranges.

When the antisymmetrization between the nucleons of the target nucleus and those of the α particle is taken into account, the exchange term makes the α-interaction non-local. Nonetheless, this non-local interaction can be approximated by a local one [109]:

$$v_{\mathrm{eff}}(s, E_\alpha) \approx U_0(1 - \beta E_\alpha) e^{-(s/a_R)^2}, \tag{6.5}$$

which depends on the energy of the α particle, E_α. The parameters $U_0 = -47.3$ MeV, $\beta = 0.003$ MeV^{-1}, and $a_{\mathrm{R}} = 1.97$ fm were derived for the Brink and Boeker force [109].

Furthermore, the effective α-nucleon interaction potential is expected to depend also on the density of the nuclear matter in which nucleons interact. Typically, the density dependence is taken of the following form [104, 108]:

$$f(\rho) = (1 - \gamma\rho^{2/3}). \tag{6.6}$$

This density dependence is effectively reducing the folding potential inside the target nucleus, where the density is higher, without changing significantly the potential in the surface and tail regions. This is expected to improve the description of α elastic scattering at large angles [108].

Concerning the imaginary part of the α-nucleon interaction potential, Eq. (6.4), Ref. [110] provides a microscopic derivation. However, this imaginary potential is not suitable for ALAS studies since its derivation relies on approximations which are not valid at the low energies of the α particles where ALAS is observed. Other microscopic

derivations which could guide the construction of an effective potential suited for ALAS studies are not available. Due to this reason, in this work an energy and density dependence similar to that of the real part have been assumed also for the imaginary part of Eq. (6.4).

Thus, the following α-nucleon interaction potential has been adopted in this work:

$$v_{\alpha n}(s) = g_{\mathrm{R}} f_{\mathrm{R}}(E_\alpha, \rho) e^{-(s/a_{\mathrm{R}})^2} + i g_{\mathrm{I}} f_{\mathrm{I}}(E_\alpha, \rho) e^{-(s/a_{\mathrm{I}})^2}, \tag{6.7}$$

where the nuclear density ρ of the target is taken at the nucleon position. The energy and density dependence $f_k(E_\alpha, \rho)$ has the following form:

$$f_k(E_\alpha, \rho) = U_0(1 - \beta E_\alpha)(1 - \gamma_k \rho^{2/3}), \tag{6.8}$$

where $k = \{\mathrm{R}, \mathrm{I}\}$. Since the antisymmetrization argument is expected to apply in a similar manner to the real and the imaginary parts of the α-nucleon interaction potential, both terms have the same parameter β.

6.2.2 Nuclear density

The nuclear densities of the target nuclei employed in Eq. (6.3) to evaluate the interaction potential, were derived microscopically from non-relativistic and relativistic mean field models.

1. Nuclear densities derived from non-relativistic mean field calculations

The nuclear densities were obtained by performing axially-deformed Skyrme+QCM calculations [111] including both the isovector and the isoscalar pairing correlations, which are treated within the quartet condensation model (QCM) [112–114]. In this framework, the ground state of even-even $N = Z$ nuclei is described by the following wavefunction [114]:

$$|QCM\rangle = (Q^\dagger_{T=1} + \Delta^{\dagger 2}_0)^{n_q}|0\rangle, \tag{6.9}$$

where $n_q = (N+Z)/4$ is the number of quartets. The operator $Q^\dagger_{T=1}$ is the isovector quartet defined as

$$Q^\dagger_{T=1} = 2\Gamma^\dagger_1\Gamma^\dagger_{-1} - (\Gamma^\dagger_0)^2, \tag{6.10}$$

where

$$\Gamma^\dagger_t = \sum_{i=1}^{N_{\mathrm{levels}}} x_i P^\dagger_{i,t}, \quad t = \{-1, 0, 1\}, \tag{6.11}$$

are the collective pairs expressed in terms of the non-collective isovector pairs $P^\dagger_{i,t}$, where $t = \{-1, 0, 1\}$ are the projections of the isospin. The index i denotes the single particle double degenerate states, running from 1 to the number of levels, N_{levels}. The isoscalar pairing correlations are described by the collective isoscalar pair

$$\Delta^\dagger_0 = \sum_{i=1}^{N_{\mathrm{levels}}} y_i D^\dagger_{i,0}, \tag{6.12}$$

where $D^\dagger_{i,0} = (\nu^\dagger_i \pi^\dagger_{\bar{i}} - \pi^\dagger_i \nu^\dagger_{\bar{i}})/\sqrt{2}$ is the non-collective isoscalar proton-neutron pair operator; the operator $\nu^\dagger_i$ creates a neutron, while the operator $\pi^\dagger_i$ creates a proton. The bar over the single particle double degenerate states i indicates the time conjugate.

The QCM calculations were performed with an isovector-isoscalar pairing interaction of zero range of the form:

$$V^T(r_1, r_2) = V_0^T \delta(r_1 - r_2) \hat{P}^T_{S,S_z}, \tag{6.13}$$

where V_0^T is a constant coupling strength and $\hat{P}^T_{S,S_z}$ is the projection operator on the spin of the pairs, namely, $S = 0$ for the isovector force and $S = 1, S_z = 0$ for the isoscalar force. The Dirac delta function $\delta(r_1 - r_2)$ indicates that the pairing interaction is of zero range. More details about the Skyrme+QCM calculations can be found in Ref. [111] (as for Skyrme functionals, see Appendix F.1).

The ground state densities provided by the Skyrme+QCM calculations have axial symmetry. From these densities, the corresponding spherical symmetric densities can be constructed as follows:

$$\rho(r_n) = \frac{1}{2} \int_0^\pi \rho(r_n, \theta) \sin\theta \, \mathrm{d}\theta \tag{6.14}$$

where θ is the polar angle.

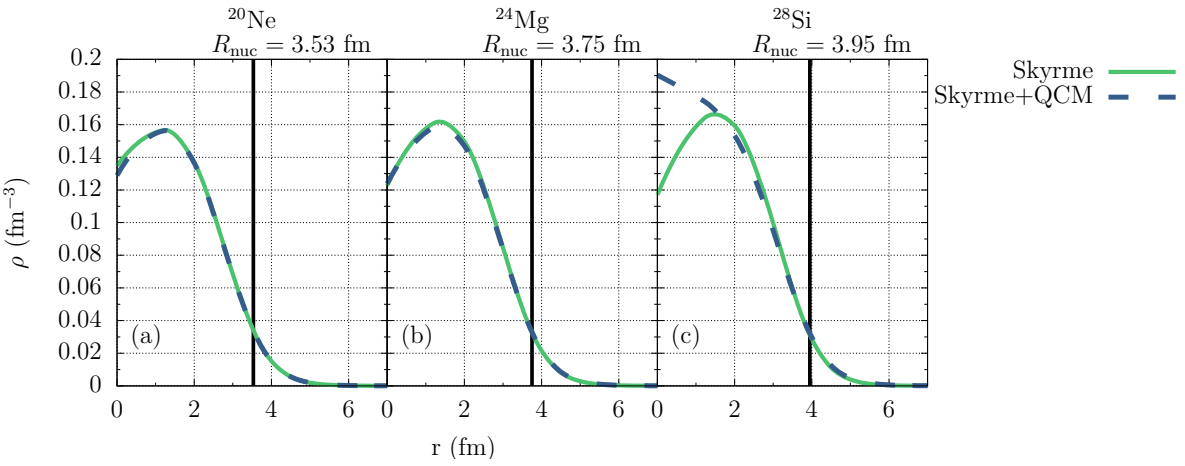

Figure 6.2: Spherically symmetric nuclear densities of ^{20}Ne, ^{24}Mg, and ^{28}Si with (dashed blue) and without (solid green) pairing correlations.

Note that these densities, calculated within the Skyrme+QCM approach, include 4-body α-type quartet correlations in the ground state of the nucleus. The impact of these correlations on the elastic scattering of α particles at energies where ALAS is present is discussed below. As an example, Fig. 6.2 displays the spherically symmetric nuclear density of ^{20}Ne, ^{24}Mg, and ^{28}Si with (dashed blue) and without (solid green) pairing correlations [115]. The vertical black lines indicate in each panel the nuclear radius. The differences between these densities are insignificant at the surface, while at the center they become more accentuated, especially for ^{28}Si, as displayed in Fig. 6.2c.

2. Nuclear densities derived from relativistic mean field calculations

The nuclear densities were calculated in the framework of the Relativistic-Hartree-Bogoliubov (RHB) approach [116], which treats simultaneously the particle-hole (ph) and the pairing correlations by combining two average potentials: a self-consistent mean field that incorporates all long-range ph correlations and a pairing field that accounts for the pairing correlations [117]. The ph correlations were calculated with the DD-PC1 functional [118], while pairing was described by a force derived from a separable interaction

in the momentum space [119, 120]:

$$\langle k|V|k'\rangle = -Gp(k)p(k'), \tag{6.15}$$

where $p(k) = e^{-a^2k^2}$ is a Gaussian ansatz. The parameters G and a were adjusted to reproduce the pairing gap in the nuclear matter calculated with the Gogny D1S force [121, 122]. The Dirac-Hartree-Bogoliubov equations were solved in a basis provided by axially-symmetric harmonic oscillator wavefunctions [123]. In this framework, the ground state of the nuclei do not have a well-defined angular momentum and parity. To restore these symmetries, a Hill-Wheeler [124] calculation was performed. More precisely, with the axially symmetric RHB functions $|\phi(q_i)\rangle$ of various deformations q_i (each representing a shape configuration of the nucleus), spherical symmetric wavefunctions were constructed:

$$|JM\pi;\alpha\rangle = \sum_i \sum_K f_\alpha^{JK\pi}(q_i) P^J_{MK} P^\pi |\phi(q_i)\rangle, \tag{6.16}$$

where $f_\alpha^{JK\pi}(q_i)$ are amplitudes corresponding to different deformations q_i; α is the Euler angle for a rotation around the z-axis, J is the total angular momentum, while K is its projection along its intrinsic symmetry axis, and π is the good parity quantum number. The total angular momentum projection operator is denoted by P^J_{MK}, where M is the projection of the total angular momentum along the z-axis, and the parity projection operator is denoted by P^π. Further details can be found in Ref. [117].

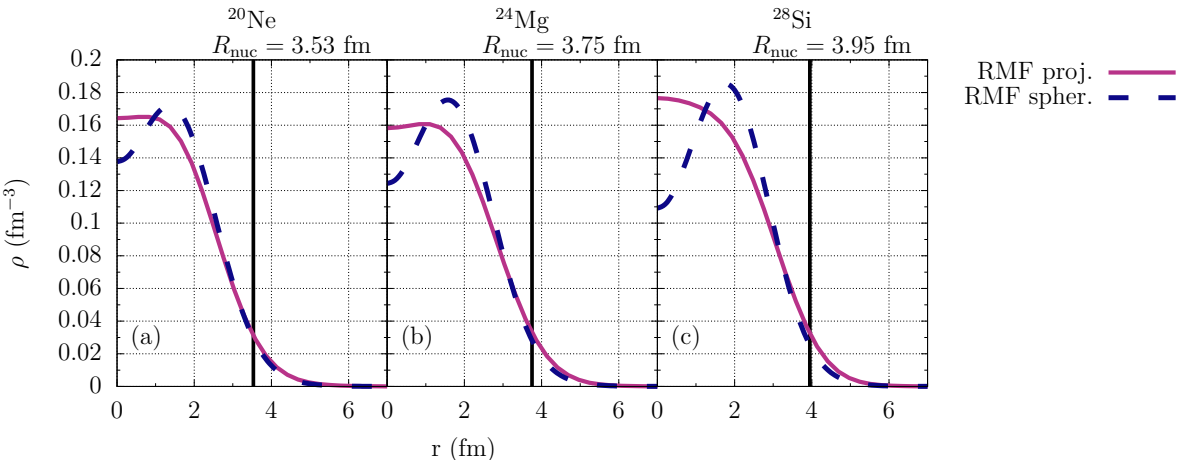

Figure 6.3: Nuclear densities of ^{20}Ne, ^{24}Mg, and ^{28}Si obtained within the projected relativistic mean field approach (solid magenta) and by imposing spherical symmetry (dashed blue).

As an example, Fig. 6.3 displays the nuclear density of ^{20}Ne, ^{24}Mg, and ^{28}Si obtained with the projected RMF approach (solid magenta) and by imposing a spherically symmetric nucleus from the beginning (dashed blue) [115]. The vertical black lines indicate in each panel the nuclear radius. While the differences between these densities are modest at the surface of the nucleus, they become more significant towards the center. The discrepancies are more accentuated the more deformed is the nucleus.

6.3 Evaluation of the interaction potential and of the differential cross section

The single-folding potential, Eq. (6.3), has been obtained by numerical integration in spherical coordinates. The calculation has been optimized by assuming the z-axis aligned with the distance r_α between the α particle and the target nucleus, as displayed in Fig. 6.1. This choice removes from the integral the dependence on the azimuthal angle φ:

$$V_{\alpha A}(r_\alpha) = 2\pi \int_0^{R_{\rm nuc}} \int_0^{\pi} \rho(r_n)\, v_{\alpha n}(s) r_n^2 \sin\theta \, \mathrm{d}r \, \mathrm{d}\theta. \tag{6.17}$$

The only dependencies that remain in the evaluation of the distance s between the α particle and the nucleon are on the radial coordinate r_n and the polar angle θ:

$$s = \sqrt{r_\alpha^2 + r_n^2 + 2 r_\alpha r_n \cos\theta}. \tag{6.18}$$

The radial Schrödinger equation, Eq. (2.4), has been solved numerically for the potential evaluated as prescribed in the foregoing section for each orbital angular momentum ℓ in the partial-wave series, using the RADIAL Fortran subroutine package [41], which provides the phase shifts δ_ℓ (see Section 2.1 and Appendix A for more detailed partial-wave analysis discussions). The differential cross section (DXS) for the elastic scattering of an α particle along a direction $\hat{\Omega} = (\theta, \varphi)$ with respect to the incident direction has been evaluated as:

$$\frac{\mathrm{d}\sigma}{\mathrm{d}\hat{\Omega}} = \left| f(\hat{\Omega}) \right|^2, \tag{6.19}$$

where the scattering amplitude is

$$f(\hat{\Omega}) = \frac{1}{2ik} \sum_{\ell=0}^{\infty} (2\ell+1) P_\ell(\cos\theta) \left(\mathrm{e}^{2i\delta_\ell} - 1 \right), \tag{6.20}$$

where k is the center-of-mass (CM) wavevector and $P_\ell(\cos\theta)$ are the Legendre polynomials. An explicit derivation of Eq. (6.20) can be found in Appendix A.

6.4 Calculation scheme and fitting procedure

The DXS depends on the input used in the single-folding calculations, *i.e.*, the nuclear densities and the α-nucleon interaction potential. The nuclear densities used as default in the folding calculations to fit the parameters of the α-nucleon interaction potential are those obtained within the projected RMF approach, as described in Section 6.2.2.

To reduce the number of fit parameters in the α-nucleon interaction potential, the parameters in the energy dependence are set equal to those provided by theoretical calculations: $U_0 = 47.3$ MeV and $\beta = 0.003$ MeV^{-1} [109]. Furthermore, the interaction range of the real part is set to $a_{\rm R} = 2$ fm, consistent with the theoretical estimation [125].

The rest of the parameters have been determined through a fitting procedure as follows. For each pair of target nucleus and α-particle energy considered in this work, the fit parameters have been varied initially on a coarse grid, as displayed in Table 6.1. Then, the

Table 6.1: Minimum and maximum of each parameter and the corresponding number of evaluation points for the first coarse fitting step.

Parameter	Min.	Max.	N_p
g_R	0.1	3.5	8
g_I	0.01	1.0	7
a_I (fm)	1.9	2.3	9
γ_R (fm^2)	1.7	2.1	5
γ_I (fm^2)	1.7	2.1	5

interaction potential, Eq. (6.1), has been evaluated for each combination of fit parameters. Next, the DXS has been calculated for each evaluated interaction potential, as discussed in Section 6.3.

For maximizing the agreement between the distorted-wave and the experimental DXS, the following measure has been adopted:

$$\chi^2 = \sum_{i=1}^{N} \left(\log \left. \frac{\mathrm{d}\sigma(\theta_i)}{\mathrm{d}\sigma_\mathrm{R}} \right|_\mathrm{DW} - \log \left. \frac{\mathrm{d}\sigma(\theta_i)}{\mathrm{d}\sigma_\mathrm{R}} \right|_\mathrm{exp} \right)^2 , \tag{6.21}$$

where $\left. \frac{\mathrm{d}\sigma(\theta_i)}{\mathrm{d}\sigma_\mathrm{R}} \right|_\mathrm{DW}$ is the distorted-wave DXS at scattering angle θ_i, $\left. \frac{\mathrm{d}\sigma(\theta_i)}{\mathrm{d}\sigma_\mathrm{R}} \right|_\mathrm{exp}$ is the experimental DXS [37, 38] at θ_i, both expressed as a ratio to the Rutherford DXS, and N is the number of experimental CM scattering angles. The combination of fit parameters which minimizes Eq. (6.21) is searched. Once this is found, the fitting procedure is restarted, employing a refined grid around the best found fit parameters.

Following the fitting procedure described above, the parameters $a_\mathrm{I} = 2.25$ fm, $\gamma_\mathrm{R} = 1.8$ fm^2, and $\gamma_\mathrm{I} = 1.7$ fm^2 were found to provide a very good fit for all the nuclei and all α-particle energies considered in this work. Thus, the only remaining energy- and nucleus-dependent parameters are the renormalization factors g_R and g_I of the strengths of the real and of the imaginary parts, respectively, of the α-nucleon potential. These are reported in Table 6.2, along with their correlation coefficient and their standard deviations, which have been evaluated by solving the covariance matrix, as detailed in Appendix E.

The variation of g_R and g_I with the kinetic energy of the incident α particle, E_α, is displayed in Fig. 6.4 for all target nuclei (except for ^{44}Ti, for which there is only one available experimental energy of the α particles in the energy range of interest). A stronger variation with E_α is exhibited by g_R compared to g_I. Nevertheless, the renormalization factors do not have a large spread across the considered α-particle energies, indicating that the adopted phenomenological α-nucleon potential is able to reasonably describe the elastic scattering of α particles at both low and high energies. It should be noted, however, that for some of the nuclei the considered experimental energies of the α particles are insufficient for a reliable interpolation.

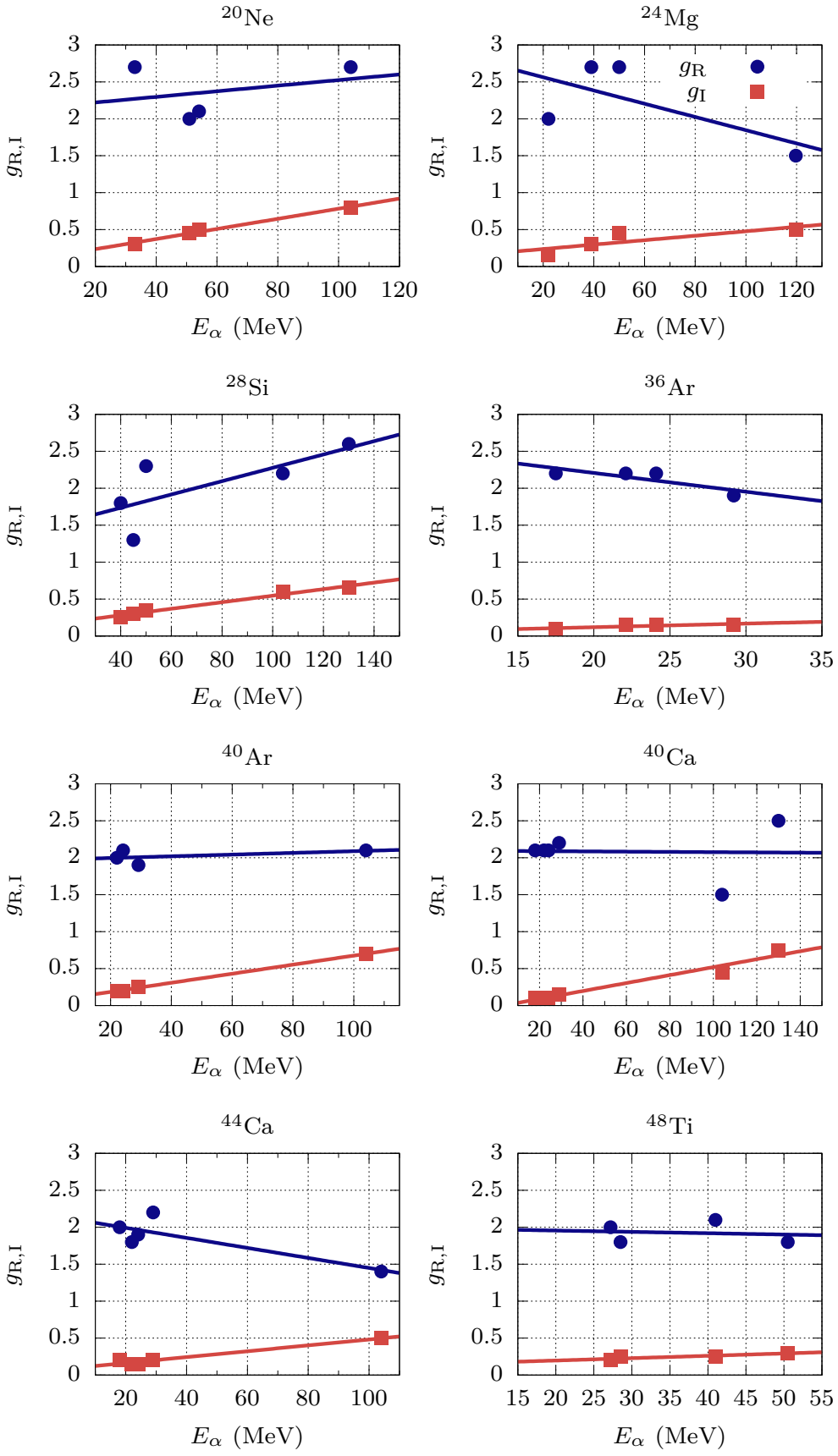

Figure 6.4: Variation of the renormalization factors g_{R} and g_{I} of the real and imaginary parts, respectively, of the α-nucleon potential with the kinetic energy of the incident α particles for the target nuclei considered in this work.

Nucleus	E_α (MeV)	g_R	g_I	Cor(g_R,g_I)	σ_{g_R}	σ_{g_I}
^{20}Ne	33.00	2.7	0.30	−0.34	0.26	0.21
	50.90	2.0	0.45	0.54	0.71	0.26
	54.10	2.1	0.50	0.53	0.68	0.30
	104.00	2.7	0.80	0.84	0.93	0.30
^{24}Mg	22.10	2.0	0.15	0.34	0.068	0.004
	39.00	2.7	0.30	0.014	0.036	0.019
	50.00	2.7	0.45	0.068	0.086	0.016
	119.70	1.5	0.50	0.90	0.060	0.029
^{28}Si	40.00	1.8	0.25	−0.20	0.064	0.023
	45.00	1.3	0.30	0.34	0.054	0.017
	50.00	2.3	0.35	0.24	0.062	0.015
	104.00	2.2	0.60	0.77	0.079	0.023
	130.00	2.6	0.65	0.91	0.142	0.034
^{36}Ar	17.50	2.2	0.09	0.061	0.020	0.002
	22.10	2.2	0.15	0.002	0.032	0.010
	24.10	2.2	0.15	0.455	0.041	0.014
	29.20	1.9	0.15	0.448	0.016	0.007
^{40}Ar	22.10	2.0	0.20	−0.213	0.037	0.026
	24.10	2.1	0.20	−0.216	0.097	0.063
	29.20	1.9	0.25	−0.275	0.192	0.116
	104.00	2.1	0.70	0.702	0.108	0.046
^{40}Ca	18.00	2.1	0.10	−0.04	0.022	0.005
	22.00	2.1	0.10	0.90	0.648	0.0029
	24.10	2.1	0.10	0.91	0.094	0.0098
	29.00	2.2	0.15	0.03	0.052	0.0053
	104.00	1.5	0.45	0.79	0.815	0.0228
	130.00	2.5	0.75	0.87	0.844	0.0361
^{44}Ca	18.00	2.0	0.20	−0.462	0.082	0.0677
	22.00	1.8	0.15	0.496	0.033	0.0129
	24.10	1.9	0.15	0.806	0.022	0.0109
	29.00	2.2	0.20	0.556	0.023	0.0199
	104.00	1.4	0.50	0.747	0.050	0.0244
^{44}Ti	21.80	0.9	0.1	0.557	0.070	0.013
^{48}Ti	27.20	2.0	0.20	0.365	0.095	0.073
	28.50	1.8	0.25	−0.294	0.393	0.209
	41.00	2.1	0.25	0.067	0.064	0.024
	50.50	1.8	0.30	0.317	0.018	0.056

Table 6.2: Fit parameters, their correlation coefficient and their standard deviation σ for the target nuclei and α-particle energies considered in this work.

6.5 Results

6.5.1 Accurate description of the differential cross section

Figures 6.5 and 6.6 display a comparison between partial-wave DXSs based on the single-folding potential evaluated as described in the foregoing sections (solid yellow curves) and DXSs obtained by employing a standard global OPM [33] (dashed blue curves) for a selection of target nuclei and α-particle energies. The black dots are experimental angular distributions [37, 38]. At low energies, where ALAS is typically observed, the partial-wave DXSs obtained using the global OPM [33] significantly underestimate the experimental DXS at intermediate and large scattering angles, see *e.g.*, Figs. 6.5a, 6.5c, and 6.5e and Figs. 6.6a, 6.6c, and 6.6e. Instead, the partial-wave DXSs evaluated relying on the single-folding potential succeed in capturing the prominent backscattering features exhibited by the experimental DXS. Furthermore, the adopted single-folding calculation scheme provides a reasonable description of the DXS also at higher energies of the α particles, as shown in Figs. 6.5d and 6.6d.

The differences observed between the DXSs which rely on the global OPM and those which rely on the single-folding potential can be better understood by comparing the interaction potentials of the two approaches. As an example, Fig. 6.7 depicts the interaction potential for the scattering of 33 MeV α particles on ^{20}Ne. The real and imaginary parts of the potentials are represented by red and blue, respectively. The single-folding potential is displayed in solid lines, while the potential relying on the global OPM of Ref. [33] is represented by dashed lines. On the one hand, the real parts of the two potentials have similar shapes, but different depths: the folding potential is much deeper than the OPM potential. On the other hand, the imaginary parts of the potential have completely different shapes and differ not only in the center, but also towards the surface of the nucleus.

6.5.2 Effect of the nuclear density on the differential cross section

To assess the effect of pairing correlations on the DXS obtained using the single-folding potential, the Skyrme and Skyrme+QCM nuclear densities have been considered. The fit parameters of the α-nucleon potential, reported in Table 6.2, have been kept constant. Figure 6.8 shows a comparison between the DXS obtained using the Skyrme density (solid green) and the Skyrme+QCM density (dashed blue) for a selection of α-particle energies on ^{20}Ne, ^{24}Mg, and ^{28}Si. For ^{20}Ne, no differences in the DXS are observed. Instead, for ^{24}Mg and ^{28}Si slight differences can be noticed around 120 deg. During an elastic collision at such low energies the α particle probes only the surface of the nucleus. Since the nuclear densities are very similar in the nuclear surface, as illustrated in Fig. 6.2, no notable differences are propagated to the angular distributions.

6.5.3 Effect of excess neutrons on the differential cross section

Experimental angular distributions show that the enhancement at large scattering angles is higher in $N = Z$ nuclei compared to nuclei which have an excess of neutrons, as clearly observed in Figs. 6.9 and 6.10, where the experimental DXSs [37, 38] for ^{36,40}Ar and ^{40,44}Ca are displayed in black dots. In the same figures are shown the DXSs resulting from the folding-model calculations obtained with the microscopical densities, which are

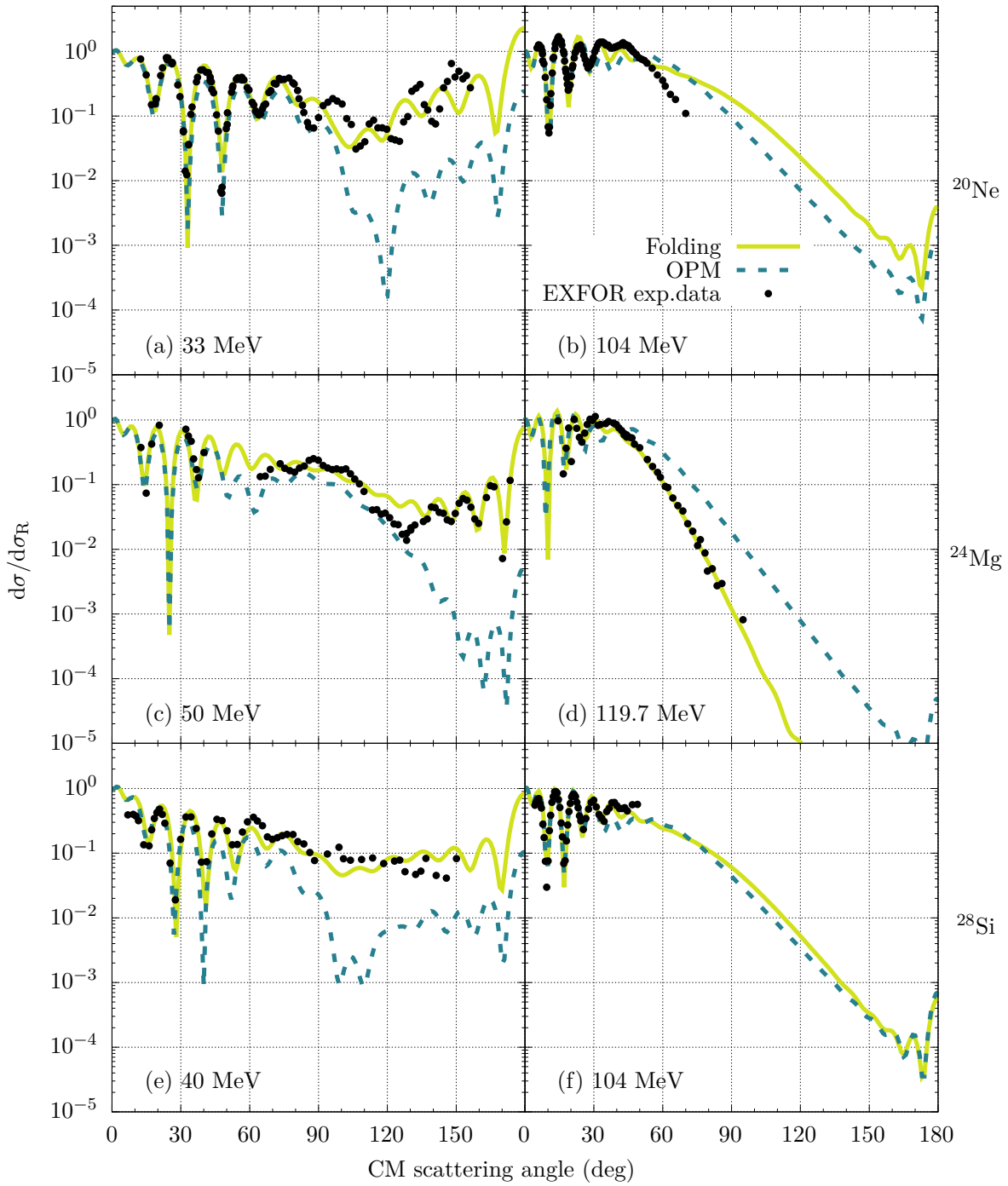

Figure 6.5: Comparison between DXSs obtained following the single-folding procedure adopted in this work (solid yellow) and DXSs obtained relying on a standard global OPM [33] (dashed blue) for ^{20}Ne, ^{24}Mg, and ^{28}Si, for a selection of α-particle energies. The black dots represent experimental angular distributions [37, 38].

able to properly describe the effect of the neutron excess on the DXS at large scattering angle.

In the calculations shown in Figs. 6.9 and 6.10 the parameters g_R and g_I for $N = Z$ and $N > Z$ nuclei are different (see Table 6.2). To elucidate how the changes in the nuclear

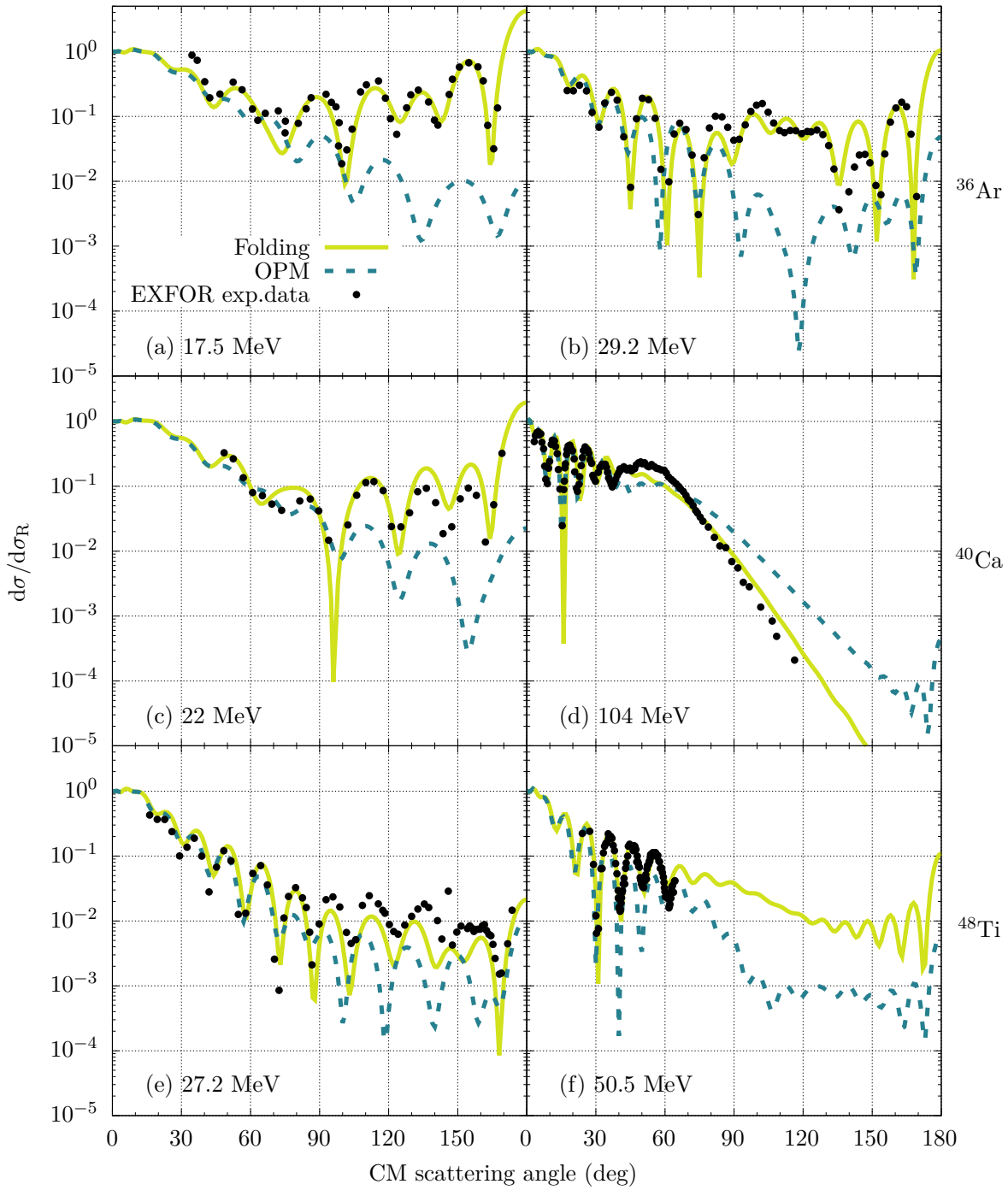

Figure 6.6: Same as Fig. 6.5 for ^{36}Ar, ^{40}Ca, and ^{48}Ti.

densities induced by the extra neutrons are impacting the DXS, folding calculations have been performed, in which the parameters of $N = Z$ nuclei have been employed for $N > Z$ nuclei. Figure 6.11 depicts the calculated DXS for ~50 MeV α particles on Ne, Mg and Si isotopes with $N = Z$ and $N - 4 = Z$, which decrease significantly for the $N - 4 = Z$ nuclei. The densities for each pair of isotopes are shown in Fig. 6.12. One can notice that the extra neutrons modify the density in the nuclear surface region, which is mainly probed by the elastic scattering of α particles at low energies.

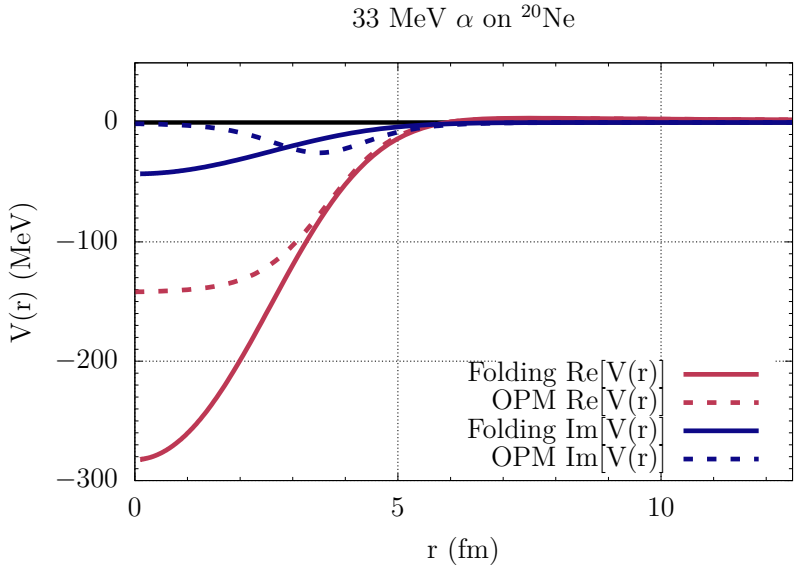

Figure 6.7: Interaction potential of 33 MeV α particles on ^{20}Ne.

6.6 Summary and open questions

The study presented in this chapter shows that the elastic scattering of low-energy α particles on $N = Z$ nuclei can be reasonably described within a single-folding formalism based on nuclear densities derived from self-consistent mean-field models. Both the real and the imaginary parts of the interaction potential have been obtained by folding the densities with a Gaussian-type interaction between the target nucleons and the α particle. This interaction is density dependent and it also includes an energy dependent factor extracted from microscopic estimations. All the parameters of the α-nucleon interaction potential are set for all the nuclei considered in this thesis either from theoretical predictions or from a fit on experimental angular distributions, with the exception of the strengths of the real and the imaginary parts of the potential which are allowed to be both energy- and nucleus-dependent.

The present calculations indicate that ALAS is not sensitive to the ground state correlations induced by pairing and quartetting correlations since these do not affect significantly the nuclear target densities in the surface and tail regions, which are probed by the low-energy α elastic scattering. On the other hand, ALAS is very sensitive to the strength of the imaginary part of the alpha-nucleon interaction potential. More precisely, as seen in Table 6.2, ALAS requires a weak absorption.

One of the open questions of the ALAS studies, including this work, is why ALAS is mainly present at low energies of the α-particles on $N = Z$ nuclei. One of the first proposed scenarios was that ALAS is generated by the scattering of the α particle with the α clusters present in the surface of $N = Z$ nuclei [36, 101, 102]. In these studies, the elastic scattering was considered between two α particles, which means that the α clusters were assumed analogous to the α particles. However, this assumption is not supported by microscopic calculations, including the quartet condensation model (QCM). In fact, in $N = Z$ nuclei the α-like clusters are 4-body structures correlated in spin and isospin, but not necessarily in coordinate space. These 4-body correlations have significant effects on the binding energies [111]. They can also change the ground state nuclear density,

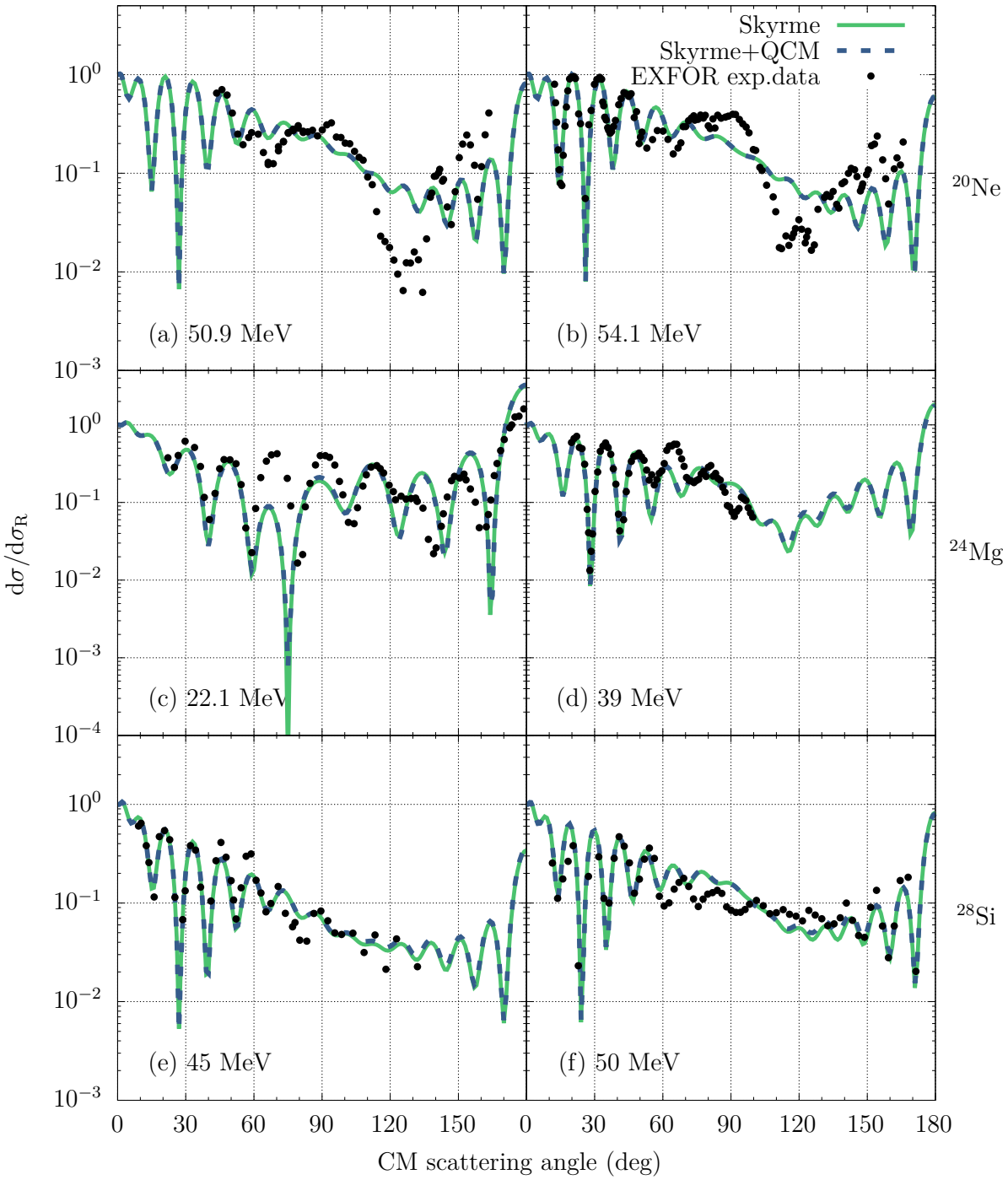

Figure 6.8: Differential cross section for the elastic scattering of α particles on ^{20}Ne, ^{24}Mg, and ^{28}Si (first, second, and third row, respectively), for a selection of α-particle energies with (dashed blue) and without (solid green) pairing correlations. The black dots represent experimental angular distributions [37, 38].

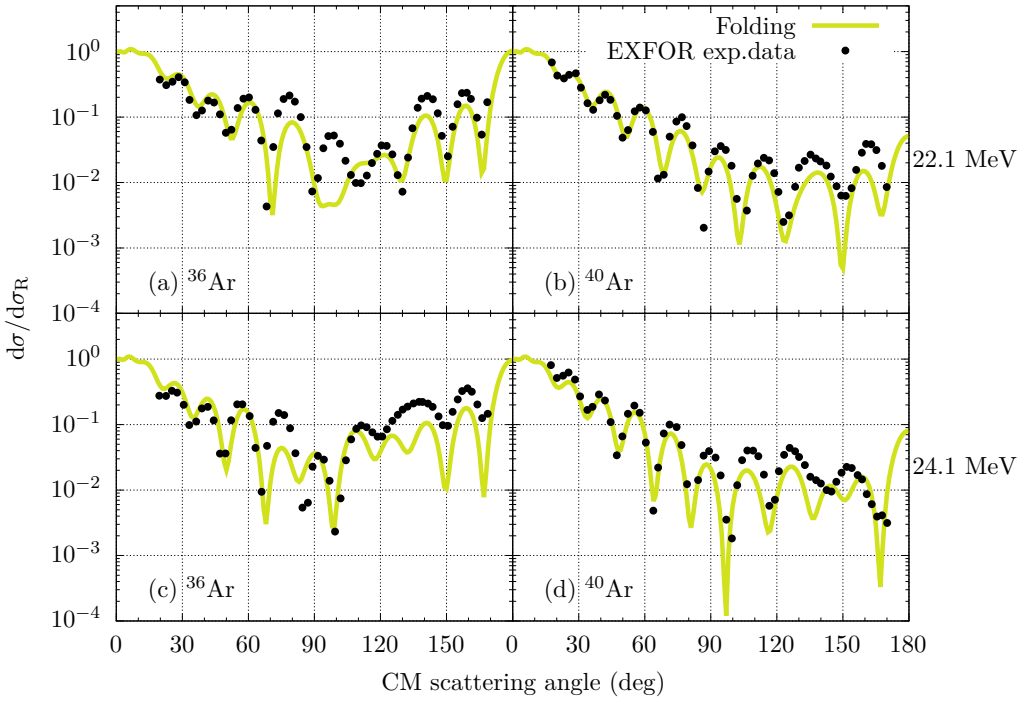

Figure 6.9: Effect of neutron excess on the differential cross section for the elastic scattering of α particles on ^{36}Ar (first column) and ^{40}Ar (second column), for a selection of α-particle energies. The black dots represent experimental angular distributions [37, 38].

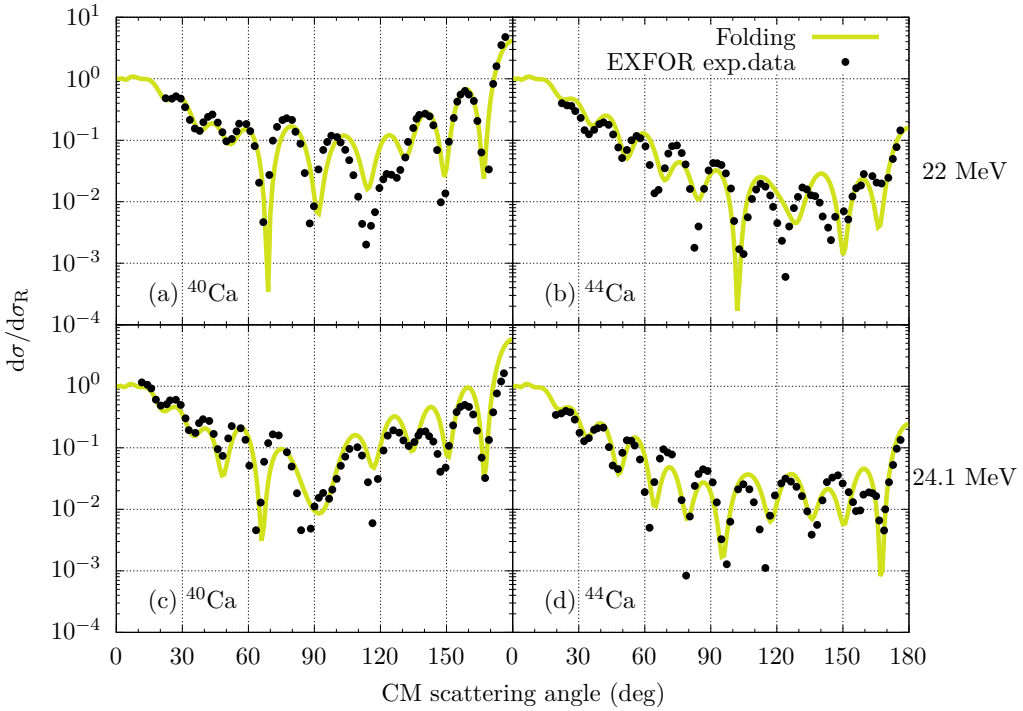

Figure 6.10: Same as Fig. 6.9 for α particles on ^{40}Ca (first column) and ^{44}Ca (second column).

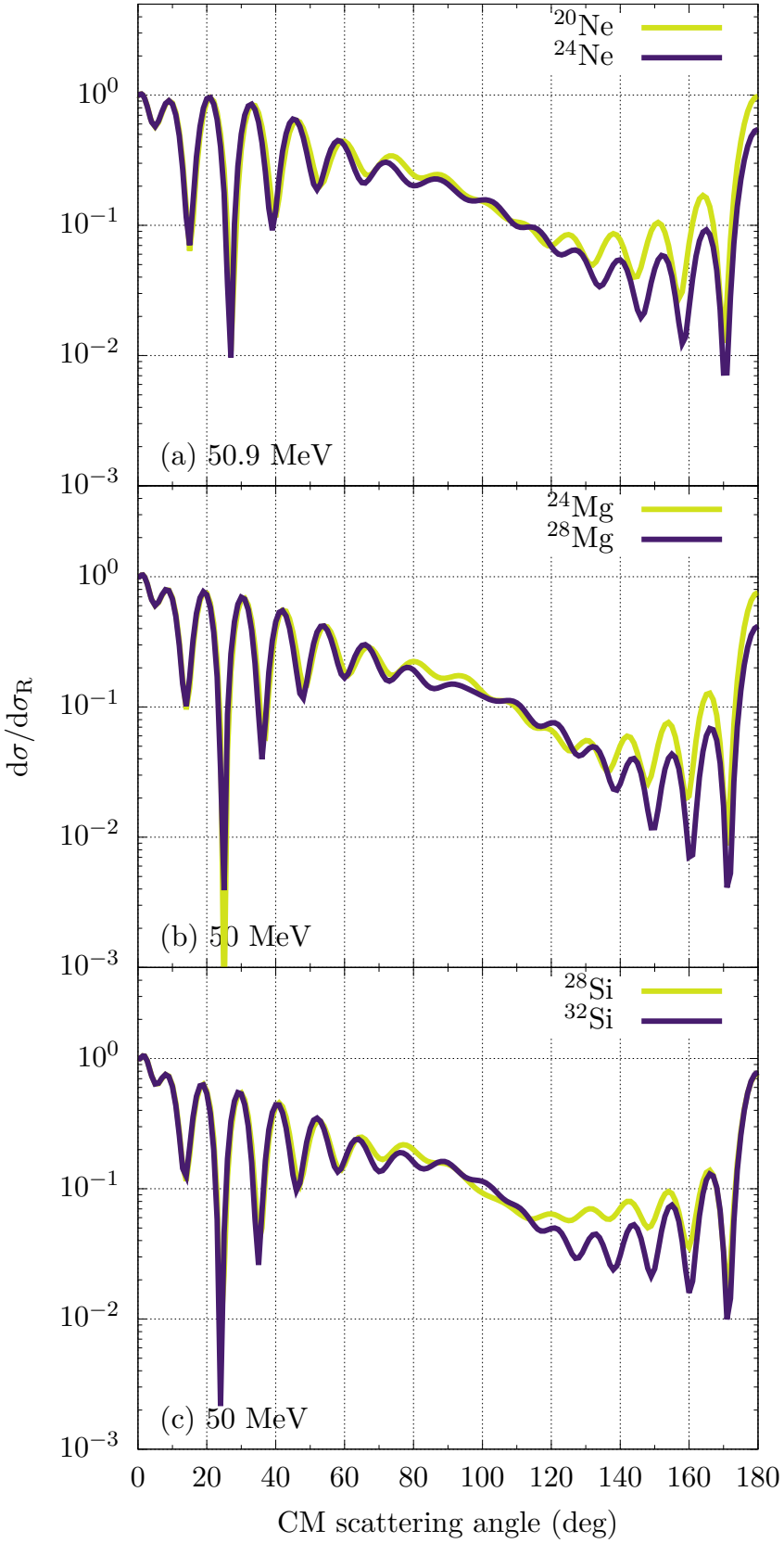

Figure 6.11: Effect of neutron excess on the differential cross section for the elastic scattering of α particles on Ne, Mg, and Si isotopes (top, middle, and bottom panel, respectively).

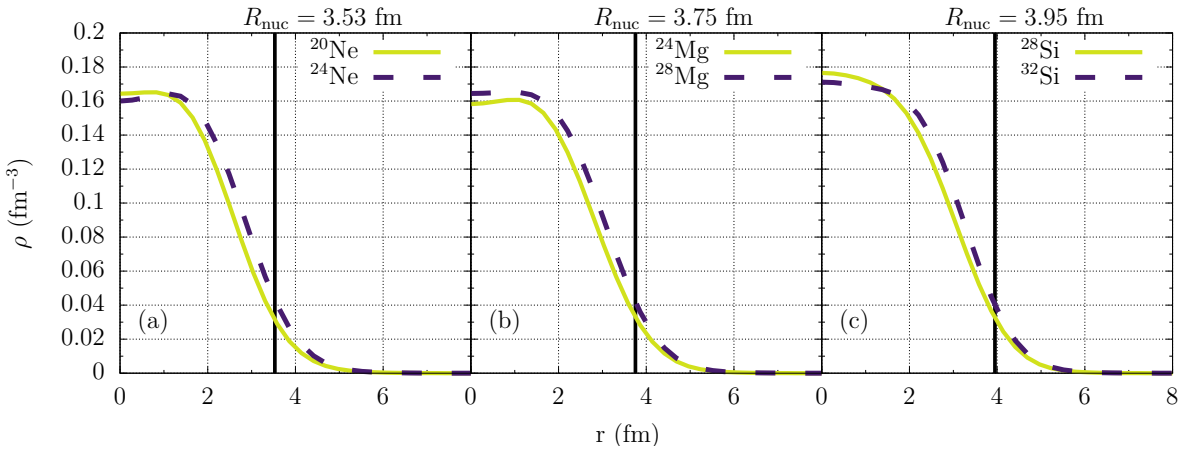

Figure 6.12: Comparison between nuclear densities of Ne (left panel), Mg (middle panel), and Si (right panel) isotopes.

but, as seen in this study, these changes do not affect significantly the single-folding calculations. Most probably ALAS is related to the excitations of the $N = Z$ nuclei, which are substantially influenced by the α-like correlations induced by proton-neutron (pn) pairing [126, 127]. More precisely, to excite the neutrons and/or protons in $N = Z$ nuclei, first the 4-body correlations (the α-like clusters) have to be broken, and only then the neutron-neutron (nn), proton-proton (pp) and/or the pn pairs can be broken. In contrast, in $N > Z$ only the nn pairs need to be broken. Moreover, in $N > Z$ nuclei the excess neutrons block the pn pairing, reducing the 4-body correlations and the binding energy of pn pairs. In view of these considerations, it is easier to excite $N > Z$ nuclei than $N = Z$ nuclei. Consequently, the incident flux of α particles is expected to be absorbed less in $N = Z$ nuclei than in $N > Z$ nuclei. This effect, which is related to ALAS, is taken into account phenomenologically in the single-folding model through the imaginary part of the α-nucleon interaction potential, which is reduced in $N = Z$ nuclei compared to $N > Z$ nuclei, as seen in Table 6.2 for, *e.g.*, Ar, Ca, and Ti isotopes. A suitable approach would be to evaluate the absorption microscopically, starting from the excitation spectra of $N = Z$ nuclei. However, this is a challenging task beyond the scope of this work.

Chapter 7

Conclusions

The work presented in this dissertation has led to the following findings:

1. Recent studies of single-event upset (SEU) production in a commercial random static access memory (SRAM) under proton irradiation revealed a discrepancy of up to two orders of magnitude below 10 MeV, where the SEU production cross section has a drastic rise, between experimental SEU production cross sections and estimations obtained with the general-purpose Monte Carlo (MC) code FLUKA (up to version v4-3.4). This underestimation was due to two main shortcomings: (1) the lack of nuclear elastic scattering of protons below 10 MeV and (2) an improper account of recoils in Coulomb single scattering. To address the first shortcoming, a new model for the nuclear elastic scattering of protons from Coulomb barrier up to 250 MeV has been developed. This new model relies on partial-wave analyses, as well as on experimental angular distributions, to evaluate a database of differential cross sections (DXS) for protons on nuclei with mass numbers ranging from $A = 2$ to $A = 252$. To reduce memory requirements, an effective analytical parametrized DXS has been found, relying only on 7 energy- and A-dependent fit parameters. A rejection sampling scheme has been implemented in FLUKA to sample proton nuclear elastic scattering events and the integrated cross section for this interaction mechanism has been consistently taken as the integral of the differential one. This newly developed model, included in FLUKA v4-4.0 (released on February 14, 2024), overcomes the unphysical lack of nuclear elastic scattering for protons below 10 MeV up to FLUKA v4-3.4 and it provides a more accurate description of large scattering angles compared to the legacy model employed hitherto.

2. While formally questionable, Coulomb and nuclear elastic scattering are treated as separate interaction mechanisms in FLUKA, since the code relies on the Molière multiple Coulomb scattering theory, whose underlying DXS is a screened Rutherford DXS, *i.e.*, purely electrostatic. In this work, special care has been devoted to the interplay between Coulomb and nuclear elastic scattering as follows. Below Coulomb barrier, where a Rutherford-like DXS is expected with no nuclear effects taken into account, the integrated cross section for proton nuclear elastic scattering has been set to 0 and the nuclear finite-size form factors (employed in FLUKA to effectively account for the charge distribution of the nucleus) have been set equal to 1. In an energy window of ±5% of the Coulomb barrier, the integrated cross section is allowed to gradually increase and the finite-size form factors are allowed to deviate from 1. Finally, at higher energies, both quantities take their full values. A systematic benchmark, comparing sampled Coulomb plus nuclear elastic scattering DXSs with partial-wave or experimental angular distributions, revealed a typically negligible error when treating separately these interaction mechanisms.

3. To address the second shortcoming of FLUKA for SEU production, an explicit

account of recoils in Coulomb single scattering has been implemented for proton projectiles in a development version of the code. If the generated elastic recoil has a kinetic energy below the transport threshold, its energy is deposited locally, otherwise the recoil is explicitly transported. This new feature allows one to quantify the event-by-event contribution of Coulomb-scattering recoils to SEU production induced by protons in commercial SRAMs.

4. With these two model developments implemented in FLUKA (a new model for proton nuclear elastic scattering and an explicit account of Coulomb recoils), SEU production induced by protons in a commercial ISSI (Integrated Silicon Solution Inc.) SRAM has been assessed both with FLUKA v4-3.4 and with the development version of the code. While the former exhibited the aforementioned underestimation of up to two orders of magnitude, with the latter additional intensity is brought to the FLUKA-estimated SEU production cross section, closing the gap with experimental SEU cross sections. Moreover, for SEU production induced by protons below 10 MeV, FLUKA has now similar performances to other MC codes used in such studies, such as Geant4.

5. Residual discrepancies still observed between experimental and FLUKA-predicted SEU production cross sections have been attributed to the adopted FLUKA simulation geometry. This is based on the rectangular parallelepiped (RPP) model which relies on two parameters: the sensitive volume (SV) in which the deposited energy is collected and the critical charge, which has to be exceeded to trigger an SEU. These two parameters are generally derived from a wealth of experimental SEU production cross sections induced by protons, as well as heavy ions. In this work, instead, optimal parameters which maximize the agreement between FLUKA-simulated and experimental SEU production cross sections have been found, not only for the aforementioned ISSI SRAM (40 nm), but also for two other bulk planar SRAMs manufactured on different complementary metal-oxide-semiconductor (CMOS) technology nodes: the Cypress SRAM (65 nm) and the ESA Monitor SRAM (250 nm). Hence, trends across technology nodes have been identified. These serve as practical guidelines for setting the RPP-model parameters for electronic devices for which only the technology node is known and no experimental SEU cross sections are readily available, *e.g.*, for novel devices which have not undergone irradiation.

6. Proton nuclear elastic scattering plays a significant role also in the out-of-field dose deposition by proton beams in water phantoms. For protons with energies of 100 MeV, 160 MeV and 225 MeV, experimental radial-depth dose maps have been simulated with two FLUKA versions: v4-3.4, relying on the legacy model for proton nuclear elastic scattering, and v4-4.0, where the new model developed in this work for this interaction mechanism has been included. This benchmark of absorbed dose as a function of depth at different radial distances from the beam axis has revealed that the excellent description of dose deposition provided by FLUKA has not only been preserved on axis, but substantial improvements have been achieved out-of-field thanks to the new model for proton nuclear elastic scattering implemented in FLUKA v4-4.0. Furthermore, the importance of the radiation source characterization and of the adopted scattering geometry for MC simulation purposes has been emphasized.

7. In the last chapter of the thesis, the elastic scattering of α particles on $N = Z$ nuclei

has been addressed to explore the physical origin of the strong enhancement of experimental angular distributions at large scattering angles, the so-called anomalous large-angle scattering (ALAS). While for protons the evaluation of the DXS has relied in this work on a global optical potential model (OPM), for α particles this effective approach becomes challenging since ALAS is not properly captured by global OPMs. Therefore, in this work the DXS evaluation has been extended beyond OPMs: a single-folding procedure has been adopted to calculate the interaction potential between the α particles and $N = Z$ nuclei. The latter relies on an α-nucleon potential, which depends only on two energy- and nucleus-dependent fit parameters, and on the target nucleon density, which was derived from microscopic mean field theories. The effect of pairing and quartetting correlations, accounted for explicitly by means of the target nucleon density, has been investigated and deemed minimal for ALAS. Nevertheless, in contrast with global OPMs, an accurate description of the experimental DXS throughout the full angular domain has been provided using the adopted single-folding model.

Chapter 8

List of contributions

8.1 List of publications

8.1.1 Publications in ISI journals

The Impact Factor (IF) and Article Influence Score (AIS) of each journal have been taken from the latest Journal Citation Reports (JCR) at the moment of writing (JCR 2023 and JCR 2024) published on the official website of the Romanian Executive Unit for the Financing of Higher Education, Research, Development and Innovation (UEFISCDI) [128].

1. **A.-G. Şerban**, A. Coronetti, R. García Alía, and F. Salvat-Pujol, Nuclear elastic scattering of protons below 250 MeV in FLUKA v4-4.0 and its role in single-event-upset production in electronics, Computer Physics Communications, 303 (2024) 109276, doi: https://doi.org/10.1016/j.cpc.2024.109276.
   IF = 7.2, **AIS = 2.086**.

2. G. Hugo, ..., **A.-G. Şerban**, *et al.*, Latest FLUKA developments, EPJ Nuclear Sciences & Technologies, 10 (2024) 20, doi: https://doi.org/10.1051/epjn/2024023.
   IF = 0.9, **AIS = 0.250**.

3. **A.-G. Şerban**, A. Coronetti, R. García Alía, and F. Salvat-Pujol, RPP-model trends across technology nodes for the MC simulation of SEUs in commercial bulk planar CMOS SRAMs under proton irradiation, IEEE Transactions on Nuclear Science, vol. 72, no. 2, pp. 133-146 (2025), doi: https://doi.org/10.1109/TNS.2024.3520506.
   IF = 1.9, **AIS = 0.384**.

4. **A.-G. Şerban**, J.A. De la Torre González, M. Anguiano, A.M. Lallena, F. Salvat-Pujol, On the improved performances of FLUKA v4-4.0 in out-of-field proton dosimetry, Radiation Physics and Chemistry, 237 (2025) 112947, doi: https://doi.org/10.1016/j.radphyschem.2025.112947.
   IF = 3.3, **AIS = 0.425**.

5. **A.-G. Şerban**, F. Salvat-Pujol, N. Sandulescu, P. Marevic, Anomalous large-angle α-scattering with a single-folding model based on densities derived from microscopic mean field models, ***in preparation***.

The total AIS (as of September 4, 2025) is 3.145.
The total IF (as of September 4, 2025) is 13.3.

8.1.2 Publications in non-ISI journals

1. C. Ahdida, ..., **A.-G. Şerban**, *et al.*, Developments of the present and future FLUKA generations, **submitted as proceedings** of the 16$^{\text{th}}$ workshop on Shielding aspects of Accelerators, Targets and Irradiation Facilities (SATIF-16) to EPJ Web of Conferences.

8.2 List of conferences

1. **A.-G. Şerban**, F. Salvat-Pujol, Overhaul of FLUKA's nuclear elastic scattering model for low-energy hadrons, 1$^{\text{st}}$ FLUKA.CERN collaboration meeting, 27–28 June 2022, CERN, Geneva, Switzerland.

2. **A.-G. Şerban**, On the contribution of nuclear interactions to the production of Single-Event-Upsets in electronics, 16$^{\text{th}}$ Varenna Conference on Nuclear Reaction Mechanisms, 11–16 June 2023, Varenna, Italy.

3. **A.-G. Şerban**, N. Sandulescu, Probing α clustering in $N = Z$ nuclei through elastic α scattering, ENST Experimental and Theoretical Aspects of Neutron-Proton Pairing and Quartet Correlations in Atomic Nuclei workshop, 4–8 September 2023, CEA Paris-Saclay, France.

4. **A.-G. Şerban**, F. Salvat-Pujol, Nuclear elastic scattering of protons below 250 MeV in FLUKA, 2$^{\text{nd}}$ FLUKA.CERN collaboration meeting, 26–28 September 2023, CERN, Geneva, Switzerland.

5. **A.-G. Şerban**, F. Salvat-Pujol, Role of proton nuclear elastic scattering in single-event-upset production and proton dosimetry applications, 3$^{\text{rd}}$ FLUKA.CERN collaboration meeting, 17–19 June 2024, ELI ERIC, Prague, Czech Republic.

6. **A.-G. Şerban**, N. Sandulescu, Elastic scattering of α particles: going beyond optical potential models, Advances in the investigation of weak and strong interactions workshop, 1–4 July 2024, Bucharest, Romania.

Appendices

A. Partial-wave analysis of elastic scattering

A.1 Spinless particles

Following Ref. [42], the elastic scattering of non-relativistic spinless particles on target nuclei can be described by solving the Schrödinger equation for an effective central interaction potential $\alpha V(r)$:

$$\left[-\frac{\hbar^2}{2\mu}\nabla^2 + \alpha V(r)\right]\psi_{\boldsymbol{k}}(\boldsymbol{r}) = E\psi_{\boldsymbol{k}}(\boldsymbol{r}), \tag{A.1}$$

where $\hbar$ is the reduced Planck constant, $\boldsymbol{k}$ is the CM wavevector, and

$$\mu = \frac{m_1 m_2}{m_1 + m_2} \tag{A.2}$$

is the reduced mass, where m_1 is the mass of the projectile and m_2 is the mass of the target nucleus. In Eq. (2.2) the CM motion has been already factored out via a separation of variables [40].

In the free particle limit $\alpha \to 0$, the eigenstates $\psi_{\boldsymbol{k}}(\boldsymbol{r})$ tend to plane waves $\mathrm{e}^{i\boldsymbol{k}\cdot\boldsymbol{r}}$. If the potential is gradually switched on (α becoming larger), the eigenstates gradually depart from the plane waves solutions. Therefore, $\psi_{\boldsymbol{k}}(\boldsymbol{r})$ is called a distorted wave and $\alpha V(r)$ is the distorting potential.

Since the distorting potential is central, the wavefunction $\psi_{\boldsymbol{k}}(\boldsymbol{r})$ can be expanded as spherical waves:

$$\psi_{\boldsymbol{k}}(\boldsymbol{r}) = 4\pi\frac{1}{kr}\sum_{\ell=0}^{\infty} i^\ell \mathcal{A}_\ell P_{E\ell}(kr) \sum_{m_\ell=-\ell}^{\ell} Y_{\ell m_\ell}(\hat{\boldsymbol{r}}) Y^*_{\ell m_\ell}(\hat{\boldsymbol{k}}), \tag{A.3}$$

where $P_{E\ell}(r)$ are unbound solutions of the radial equation for $V(r)$, $Y_{\ell m}(\hat{\boldsymbol{r}})$ are the spherical harmonics, ℓ is the orbital angular momentum, and m_ℓ is its projection along the quantization axis. The factor $1/r$ appears due to the expansion in terms of spherical waves, while the additional factor $1/k$ ensures dimensionlessness. The expansion coefficients $\mathcal{A}_\ell$ can be determined using the limit $r \to \infty$:

$$\lim_{r\to\infty}\frac{1}{kr}P_{E\ell}(r) \propto \frac{1}{kr}\sin\left(kr - \ell\frac{\pi}{2} + \delta_\ell\right), \tag{A.4}$$

where δ_ℓ are the phase shifts, which measure how much the introduction of an effective interaction potential shifts the radial functions with respect to the corresponding zero-potential solutions. Thus,

$$\lim_{r\to\infty}\left[\psi_{\boldsymbol{k}}(\boldsymbol{r}) - \mathrm{e}^{i\boldsymbol{k}\cdot\boldsymbol{r}}\right] = \frac{4\pi}{kr}\sum_{\ell=0}^{\infty} i^\ell \underbrace{\left[\mathcal{A}_\ell \sin\left(kr - \frac{\ell\pi}{2} + \delta_\ell\right) - \sin\left(kr - \frac{\ell\pi}{2}\right)\right]}_{\mathrm{X}} \sum_{m_\ell=-\ell}^{\ell} Y_{\ell m_\ell}(\hat{\boldsymbol{r}}) Y^*_{\ell m_\ell}(\hat{\boldsymbol{k}}). \tag{A.5}$$

$$
\begin{aligned}
i^\ell \mathrm{X} &= \frac{i^\ell}{2i}\left\{\mathcal{A}_\ell\left[\mathrm{e}^{ikr}\mathrm{e}^{-i\ell\pi/2}\mathrm{e}^{i\delta_\ell} - \mathrm{e}^{-ikr}\mathrm{e}^{i\ell\pi/2}\mathrm{e}^{-i\delta_\ell}\right] - \left[\mathrm{e}^{ikr}\mathrm{e}^{-i\ell\pi/2} - \mathrm{e}^{-ikr}\mathrm{e}^{i\ell\pi/2}\right]\right\} \\
&= \frac{i^\ell}{2i}\left\{\mathcal{A}_\ell\left[(-i)^\ell\mathrm{e}^{ikr}\mathrm{e}^{i\delta_\ell} - i^\ell\mathrm{e}^{-ikr}\mathrm{e}^{-i\delta_\ell}\right] - \left[(-i)^\ell\mathrm{e}^{ikr} - i^\ell\mathrm{e}^{-ikr}\right]\right\} \\
&= \frac{1}{2i}\left\{\mathcal{A}_\ell\left[\mathrm{e}^{ikr}\mathrm{e}^{i\delta_\ell} - (-1)^\ell\mathrm{e}^{-ikr}\mathrm{e}^{-i\delta_\ell}\right] - \left[\mathrm{e}^{ikr} - (-1)^\ell\mathrm{e}^{-ikr}\right]\right\} \\
&= \frac{1}{2i}\left[\mathrm{e}^{ikr}\left(\mathcal{A}_\ell\mathrm{e}^{i\delta_\ell} - 1\right) + (-1)^\ell\mathrm{e}^{-ikr}\left(1 - \mathcal{A}_\ell\mathrm{e}^{-i\delta_\ell}\right)\right].
\end{aligned}
\tag{A.6}
$$

The spherical waves can be either incoming (with a factor e^{-ikr}) or outgoing (with a factor e^{ikr}) with respect to the scattering center. An outgoing wave implies $\mathcal{A}_\ell^+ = \mathrm{e}^{i\delta_\ell}$, while an incoming wave implies $\mathcal{A}_\ell^- = \mathrm{e}^{-i\delta_\ell}$. Thus,

$$
\mathcal{A}_\ell^\pm = \mathrm{e}^{\pm i\delta_\ell}. \tag{A.7}
$$

Equation (A.5) becomes:

$$
\begin{aligned}
\lim_{r\to\infty}\left[\psi_{\boldsymbol{k}}(\boldsymbol{r}) - \mathrm{e}^{i\boldsymbol{k}\cdot\boldsymbol{r}}\right] = \frac{4\pi}{kr}\sum_{\ell=0}^{\infty}\frac{1}{2i}\left[\mathrm{e}^{ikr}\left(\mathrm{e}^{\pm i\delta_\ell}\mathrm{e}^{i\delta_\ell} - 1\right) + (-1)^\ell\mathrm{e}^{-ikr}\left(1 - \mathrm{e}^{\pm i\delta_\ell}\mathrm{e}^{-i\delta_\ell}\right)\right] \\
\times \sum_{m_\ell=-\ell}^{\ell} Y_{\ell m_\ell}(\hat{\boldsymbol{r}})Y^*_{\ell m_\ell}(\hat{\boldsymbol{k}}).
\end{aligned}
\tag{A.8}
$$

Using the addition theorem of spherical harmonics

$$
\sum_{m_\ell=-\ell}^{\ell} Y_{\ell m_\ell}(\hat{\boldsymbol{r}})Y^*_{\ell m_\ell}(\hat{\boldsymbol{k}}) = \frac{2\ell+1}{4\pi}P_\ell(\hat{\boldsymbol{k}}\cdot\hat{\boldsymbol{r}}), \tag{A.9}
$$

where $P_\ell(x)$ are the Legendre polynomials, yields

$$
\lim_{r\to\infty}\left[\psi_{\boldsymbol{k}}(\boldsymbol{r}) - \mathrm{e}^{i\boldsymbol{k}\cdot\boldsymbol{r}}\right] = \frac{1}{2ikr}\sum_{\ell=0}^{\infty}(2\ell+1)P_\ell(\hat{\boldsymbol{k}}\cdot\hat{\boldsymbol{r}})\left[\mathrm{e}^{ikr}\left(\mathrm{e}^{\pm i\delta_\ell}\mathrm{e}^{i\delta_\ell} - 1\right) + (-1)^\ell\mathrm{e}^{-ikr}\left(1 - \mathrm{e}^{\pm i\delta_\ell}\mathrm{e}^{-i\delta_\ell}\right)\right]. \tag{A.10}
$$

The outgoing wavefunction is:

$$
\lim_{r\to\infty}\left[\psi^+_{\boldsymbol{k}}(\boldsymbol{r}) - \mathrm{e}^{i\boldsymbol{k}\cdot\boldsymbol{r}}\right] = \frac{\mathrm{e}^{ikr}}{r}\frac{1}{2ik}\sum_{\ell=0}^{\infty}(2\ell+1)P_\ell(\hat{\boldsymbol{k}}\cdot\hat{\boldsymbol{r}})\left(\mathrm{e}^{2i\delta_\ell} - 1\right) = \frac{\mathrm{e}^{ikr}}{r}f(\hat{\boldsymbol{k}}\cdot\hat{\boldsymbol{r}}), \tag{A.11}
$$

where $f(\hat{\boldsymbol{k}}\cdot\hat{\boldsymbol{r}})$ is the scattering amplitude in direction $\hat{\boldsymbol{k}}$.

The differential cross section is then the modulus square of the scattering amplitude:

$$
\frac{\mathrm{d}\sigma}{\mathrm{d}\hat{\Omega}} = \left|f(\hat{\boldsymbol{k}}\cdot\hat{\boldsymbol{r}})\right|^2. \tag{A.12}
$$

A.2 Particles with spin 1/2

Analogously to the derivation presented in the foregoing section and following Ref. [42], the differential cross section for an unpolarized beam and a spin-independent detector is given by

$$
\frac{\mathrm{d}\sigma}{\mathrm{d}\hat{\Omega}} = \left|f(\hat{\Omega})\right|^2 + \left|g(\hat{\Omega})\right|^2, \tag{A.13}
$$

where the direct and the spin flip scattering amplitudes are

$$\begin{aligned} f(\hat{\Omega}) &= f_{\mathrm{C}}(\theta) + \frac{1}{2ik}\sum_{\ell=0}^{\infty} P_\ell(\cos\theta)\mathrm{e}^{i2\Delta_\ell}\left[(\ell+1)\mathrm{e}^{i2\tilde{\delta}_{\ell,\ell+1/2}} + \ell\mathrm{e}^{i2\tilde{\delta}_{\ell,\ell-1/2}} - (2\ell+1)\right] \\ g(\hat{\Omega}) &= \frac{1}{2ik}\mathrm{e}^{i\varphi}\sum_{\ell=1}^{\infty} P_\ell^1(\cos\theta)\left(\mathrm{e}^{i2\delta_{\ell,\ell+1/2}} - \mathrm{e}^{i2\delta_{\ell,\ell-1/2}}\right), \end{aligned} \tag{A.14}$$

where $P_\ell(\cos\theta)$ are the Legendre polynomials and $P_\ell^m(\cos\theta)$ are the associated Legendre polynomials; $\Delta_\ell = \arg\Gamma(\ell+1+i\eta)$, where Γ is the Gamma function, and $\tilde{\delta}_{\ell j}$ are the Coulomb and the inner phase shifts, respectively, verifying $\delta_{\ell j} = \Delta_\ell + \tilde{\delta}_{\ell j}$. The Coulomb scattering amplitude on a point nucleus is

$$f_{\mathrm{C}}(\theta) = -\eta\frac{\exp\left[2i\Delta_0 - i\eta\ln\left(\sin^2\dfrac{\theta}{2}\right)\right]}{2k\sin^2\dfrac{\theta}{2}}, \tag{A.15}$$

where the Sommerfeld parameter is

$$\eta = \frac{Z_{\mathrm{p}}Z_{\mathrm{t}}e^2}{\hbar v}, \tag{A.16}$$

where Z_{p} and Z_{t} are the atomic numbers of the projectile and of the target nucleus, respectively, e is the elementary charge, and v is the non-relativistic velocity of the proton far from the origin of the coordinates [41].

B. Proton nuclear elastic scattering integrated cross section

To evaluate numerically the integrated cross section for proton nuclear elastic scattering as the integral of the differential one, Eq. (2.18) has been split, for simplicity, into four terms which have been evaluated separately:

$$\begin{aligned}\frac{\mathrm{d}\sigma(\theta,\boldsymbol{\alpha})}{\mathrm{d}\hat{\Omega}} &= \left[\alpha k^2 R^4 \left(\frac{J_1(Rq\delta_1)}{Rq}\right)^2 e^{-\beta_1 Rq}\right] + \left[\alpha k^2 R^4 \gamma J_0^2(Rq\delta_0) e^{-\beta_0 Rq}\right] \\ &+ \zeta\left[\alpha k^2 R^4 \left(\frac{J_1(Rq'\delta_1)}{Rq'}\right)^2 e^{-\beta_1 Rq'}\right] + \zeta\left[\alpha k^2 R^4 \gamma J_0^2(Rq'\delta_0) e^{-\beta_0 Rq'}\right] \\ &= f_1 + f_0 + \zeta f_1' + \zeta f_0'.\end{aligned} \tag{B.1}$$

The first term can be rewritten as:

$$f_1 = \alpha k^2 R^4 \frac{J_1^2(Rq\delta_1)}{R^2 q_{\mathrm{CM}}^2} e^{-\beta_1 Rq} = \alpha k^2 R^4 \delta_1^2 \frac{J_1^2(x_1)}{x_1^2} e^{-\frac{\beta_1}{\delta_1} x_1}, \tag{B.2}$$

while the second term becomes:

$$f_0 = \alpha k^2 R^4 \gamma J_0^2(Rq\delta_0)\, e^{-\beta_0 Rq} = \alpha k^2 R^4 \gamma J_0^2(x_0) e^{-\frac{\beta_0}{\delta_0} x_0}, \tag{B.3}$$

where $x_{0,1} = Rq\delta_{0,1}$. Analogously, the third and fourth terms are

$$f_1' = \alpha k^2 R^4 \delta_1^2 \frac{J_1^2(x_1')}{{x_1'}^2} e^{-\frac{\beta_1}{\delta_1} x_1'}, \tag{B.4}$$

and

$$f_0' = \alpha k^2 R^4 \gamma J_0^2(x_0') e^{-\frac{\beta_0}{\delta_0} x_0'}, \tag{B.5}$$

where $x_{0,1}' = Rq'\delta_{0,1}$.

Having removed all the dependencies on the fit parameters from the integrand, the integral of Eq. (2.18) is

$$\int \mathrm{d}\hat{\Omega} \frac{\mathrm{d}\sigma(\theta,\boldsymbol{\alpha})}{\mathrm{d}\hat{\Omega}} = 2\pi \int_0^\pi \sin\theta \mathrm{d}\theta \frac{\mathrm{d}\sigma(\theta,\boldsymbol{\alpha})}{\mathrm{d}\hat{\Omega}} = 2\pi \int_0^\pi 2\sin\frac{\theta}{2}\cos\frac{\theta}{2}\mathrm{d}\theta \left(f_1 + f_0 + \zeta f_1' + \zeta f_0'\right). \tag{B.6}$$

Using $q = 2k\sin\dfrac{\theta}{2}$ and $q' = 2k\sin\dfrac{\pi-\theta}{2} = 2k\cos\dfrac{\theta}{2}$, the above integral can be written as:

$$\begin{aligned}\int \mathrm{d}\hat{\Omega} \frac{\mathrm{d}\sigma(\theta,\boldsymbol{\alpha})}{\mathrm{d}\hat{\Omega}} &= \left[\frac{2\pi}{k^2}\int_0^{2k} q\mathrm{d}q f_1\right] + \left[\frac{2\pi}{k^2}\int_0^{2k} q\mathrm{d}q f_0\right] + \left[\frac{2\pi\zeta}{k^2}\int_0^{2k} q'\mathrm{d}q' f_1'\right] + \left[\frac{2\pi\zeta}{k^2}\int_0^{2k} q'\mathrm{d}q' f_0'\right] \\ &= I_1 + I_0 + \zeta I_1' + \zeta I_0'.\end{aligned} \tag{B.7}$$

The integral I_1 yields

$$I_1 = \frac{2\pi}{k^2}\int_0^{2k} q\,\mathrm{d}q f_1 = \frac{2\pi}{k^2R^2\delta_1^2}\int_0^{2kR\delta_1} x_1\,\mathrm{d}x_1 f_1 = 2\pi\alpha R^2\int_0^{2kR\delta_1}\frac{1}{x_1}J_1^2(x_1)\,e^{-\frac{\beta_1}{\delta_1}x_1}\mathrm{d}x_1. \tag{B.8}$$

Analogously,

$$\begin{aligned} I_0 &= \frac{2\pi\alpha R^2\gamma}{\delta_0^2}\int_0^{2kR\delta_0} x_0 J_0^2(x_0)\,e^{-\frac{\beta_0}{\delta_0}x_0}\mathrm{d}x_0, \\ I_1' &= 2\pi\alpha R^2\zeta\int_0^{2kR\delta_1}\frac{1}{x_1'}J_1^2(x_1')\,e^{-\frac{\beta_1}{\delta_1}x_1'}\mathrm{d}x_1', \\ I_0' &= \frac{2\pi\alpha R^2\gamma}{\delta_0^2}\int_0^{2kR\delta_0} x_0' J_0^2(x_0')\,e^{-\frac{\beta_0}{\delta_0}x_0'}\mathrm{d}x_0'. \end{aligned} \tag{B.9}$$

With all the dependencies on the scattering angle and the fit parameters outside of the integral, the integration variable becomes a dummy variable. Thus, Eq. (B.7) can be written as:

$$\begin{aligned} \int \mathrm{d}\hat{\mathbf{\Omega}}\,\frac{\mathrm{d}\sigma}{\mathrm{d}\hat{\mathbf{\Omega}}} = (1+\zeta)\,2\pi\alpha R^2\int_0^{2kR\delta_1}\frac{1}{x_1}J_1^2(x_1)\,e^{-\frac{\beta_1}{\delta_1}x_1}\mathrm{d}x_1 \\ + (1+\zeta)\,\frac{2\pi\alpha R^2\gamma}{\delta_0^2}\int_0^{2kR\delta_0} x_0 J_0^2(x_0)\,e^{-\frac{\beta_0}{\delta_0}x_0}\mathrm{d}x_0, \end{aligned} \tag{B.10}$$

which is a form preconditioned for numerical integration.

C. Sampling in Coulomb single scattering

The scheme used in FLUKA to sample the scattering angle in the laboratory frame for Coulomb single scattering has been revisited in view of the evaluation of the recoil kinetic energy in Section 3.2. For the purposes of this appendix, the Molière differential cross section (DXS) (3.3) can be simplified as:

$$\frac{\mathrm{d}\sigma}{\mathrm{d}\hat{\Omega}} = \left[\frac{Z_\mathrm{p}^2 Z_\mathrm{t}^2 e^4}{4c^4\beta^2 E^2 \sin^4\frac{\tilde{\theta}}{2}}\right]\left[\frac{(1-\cos\tilde{\theta})^2}{\left(1-\cos\tilde{\theta}+\frac{\chi_\mathrm{a}^2}{2}\right)^2}\right] = \frac{\alpha}{\left(1-\cos\tilde{\theta}+\frac{\chi_\mathrm{a}^2}{2}\right)^2}, \tag{C.1}$$

where $\alpha = \dfrac{Z_\mathrm{p}^2 Z_\mathrm{t}^2 e^4}{c^4\beta^2 E^2}$. The normalization constant of this DXS is

$$\mathcal{N} = \int \mathrm{d}\hat{\Omega}\,\frac{\mathrm{d}\sigma}{\mathrm{d}\hat{\Omega}} = 2\pi\alpha\int_0^\pi \sin\tilde{\theta}\,\mathrm{d}\tilde{\theta}\,\frac{1}{\left(1-\cos\tilde{\theta}+\frac{\chi_\mathrm{a}^2}{2}\right)^2} = \frac{16\pi\alpha}{\chi_\mathrm{a}^2\left(4+\chi_\mathrm{a}^2\right)}. \tag{C.2}$$

The sampling equation for the normalized Molière DXS is

$$\xi = \int \mathrm{d}\hat{\Omega}\,\frac{1}{\mathcal{N}}\frac{\mathrm{d}\sigma}{\mathrm{d}\hat{\Omega}} = \frac{\chi_\mathrm{a}^2\left(4+\chi_\mathrm{a}^2\right)}{8}\int_0^{\tilde{\theta}} \sin\tilde{\theta}'\,\mathrm{d}\tilde{\theta}'\,\mathrm{d}\varphi\,\frac{1}{\left(1-\cos\tilde{\theta}'+\frac{\chi_\mathrm{a}^2}{2}\right)^2} = \frac{\left(1-\cos\tilde{\theta}\right)\left(4+\chi_\mathrm{a}^2\right)}{4\left(1-\cos\tilde{\theta}+\frac{\chi_\mathrm{a}^2}{2}\right)^2}, \tag{C.3}$$

where $\xi \sim \mathcal{U}[0,1)$ is a random number. Rearranging the terms yields:

$$\cos\tilde{\theta} = 1 - \frac{2\xi\chi_\mathrm{a}^2}{4+\chi_\mathrm{a}^2-4\xi}. \tag{C.4}$$

FLUKA evaluates $\cos\tilde{\theta}$ relying on the following trigonometric identity:

$$\cos\tilde{\theta} = \frac{1-\tan^2\frac{\tilde{\theta}}{2}}{1+\tan^2\frac{\tilde{\theta}}{2}} = 1 - \frac{2\tan^2\frac{\tilde{\theta}}{2}}{1+\tan^2\frac{\tilde{\theta}}{2}}. \tag{C.5}$$

Equating Eqs. (C.4) and (C.5) and rearranging the terms one can identify:

$$\tan^2\frac{\tilde{\theta}}{2} = \frac{\xi\chi_\mathrm{a}^2}{(1-\xi)\left(4+\chi_\mathrm{a}^2\right)}, \tag{C.6}$$

which is the quantity sampled by FLUKA in Coulomb single scattering.

D. Transforming scattering angles and angular distributions from lab to CM

To deduce the expressions for transforming both scattering angles and angular distributions from the laboratory frame to the center-of-mass (CM) frame, one considers an inertial frame where a projectile particle with mass m_p and momentum $\tilde{p}_\mathrm{p}$ scatters elastically on a target nucleus with mass m_t at rest. The following derivations are restricted to the case in which there is a unique correspondence between the lab emission angle $\tilde{\theta}$ of the projectile after the collision and the CM emission angle θ.

D.1 Lab to CM scattering angles

The starting point is the Lorentz boost giving the four-momentum of the projectile in the laboratory frame:

$$\mathcal{P}'_\mathrm{p} = \begin{pmatrix} E_\mathrm{p} \\ p\sin\theta \\ 0 \\ p\cos\theta \end{pmatrix} = \begin{pmatrix} \gamma & 0 & 0 & -\beta\gamma \\ 0 & 1 & 0 & 0 \\ 0 & 0 & 1 & 0 \\ -\beta\gamma & 0 & 0 & \gamma \end{pmatrix} \begin{pmatrix} \tilde{E}'_\mathrm{p} \\ \tilde{p}'_\mathrm{p}\sin\tilde{\theta} \\ 0 \\ \tilde{p}'_\mathrm{p}\cos\tilde{\theta} \end{pmatrix} = \begin{pmatrix} \gamma\tilde{E}'_\mathrm{p} - \beta\gamma\tilde{p}'_\mathrm{p}\cos\tilde{\theta} \\ \tilde{p}'_\mathrm{p}\sin\tilde{\theta} \\ 0 \\ \gamma\tilde{p}'_\mathrm{p}\cos\tilde{\theta} - \beta\gamma\tilde{E}'_\mathrm{p} \end{pmatrix}, \tag{D.1}$$

from which one can extract:

$$\begin{aligned} p\sin\theta &= \tilde{p}'_\mathrm{p}\sin\tilde{\theta} \\ p\cos\theta &= \gamma\tilde{p}'_\mathrm{p}\cos\tilde{\theta} - \gamma\beta\tilde{E}'_\mathrm{p}. \end{aligned} \tag{D.2}$$

Dividing these expressions yields

$$\tan\theta = \frac{\tilde{p}'_\mathrm{p}\sin\tilde{\theta}}{\gamma\tilde{p}'_\mathrm{p}\cos\tilde{\theta} - \gamma\beta\tilde{E}'_\mathrm{p}} = \frac{\sin\tilde{\theta}_1}{\gamma\cos\tilde{\theta} - \gamma\dfrac{\beta\tilde{E}'_\mathrm{p}}{\tilde{p}'_\mathrm{p}}}, \tag{D.3}$$

where and $\tilde{E}'_\mathrm{p} = \sqrt{\tilde{p}'^2_\mathrm{p} + m^2_\mathrm{p}}$.

D.2 Lab to CM differential cross section

The chain rule is applied for the transformation of the differential cross section from the lab (as it is sampled by FLUKA) to the CM:

$$\frac{\mathrm{d}\sigma}{\mathrm{d}\hat{\Omega}_\mathrm{CM}} = \frac{\mathrm{d}\sigma}{\mathrm{d}\hat{\Omega}_\mathrm{lab}}\frac{\mathrm{d}\hat{\Omega}_\mathrm{lab}}{\mathrm{d}\hat{\Omega}_\mathrm{CM}} = \frac{\mathrm{d}\sigma}{\mathrm{d}\hat{\Omega}_\mathrm{lab}}\frac{\mathrm{d}(\cos\tilde{\theta})}{\mathrm{d}(\cos\theta)}. \tag{D.4}$$

Analogously to Eq. (D.3), the tangent of the lab scattering angle can be written in terms of the CM scattering angle as:

$$\tan\tilde{\theta} = \frac{\sin\theta}{\gamma(\cos\theta + \xi)}, \tag{D.5}$$

where $\xi = \dfrac{\beta E'_{\mathrm{p}}}{p}$, E'_{p} is the total CM energy of the projectile after the collision and p is the CM momentum after the collision. Equation (D.5) can be rewritten as

$$1 + \tan^2\tilde{\theta} = \frac{\gamma^2(\cos\theta + \xi)^2 + \sin^2\theta}{\gamma^2(\cos\theta + \xi)^2}, \tag{D.6}$$

and the trigonometric identity

$$1 + \tan^2\tilde{\theta} = \frac{1}{\cos^2\tilde{\theta}}, \tag{D.7}$$

can be employed, yielding:

$$\frac{1}{\cos^2\tilde{\theta}} = \frac{\gamma^2(\cos\theta + \xi)^2 + \sin^2\theta}{\gamma^2(\cos\theta + \xi)^2}. \tag{D.8}$$

It follows that

$$\cos\tilde{\theta} = \frac{\gamma(\cos\theta + \xi)}{\sqrt{\gamma^2(\cos\theta + \xi)^2 + \sin^2\theta}}. \tag{D.9}$$

Differentiating with respect to $\cos\theta$ yields

$$\begin{aligned}
\frac{\mathrm{d}(\cos\tilde{\theta})}{\mathrm{d}(\cos\theta)} &= \frac{1}{\gamma^2(\cos\theta + \xi)^2 + \sin^2\theta}\left\{\gamma\sqrt{\gamma^2(\cos\theta + \xi)^2 + \sin^2\theta}\right. \\
&\left.-\gamma(\cos\theta + \xi)\frac{1}{2}\left[\gamma^2(\cos\theta + \xi)^2 + \sin^2\theta\right]^{-1/2}\left[\gamma^2 2(\cos\theta + \xi) - 2\cos\theta\right]\right\} \\
&= \frac{1}{\left[\gamma^2(\cos\theta + \xi)^2 + \sin^2\theta\right]^{3/2}}\left\{\gamma\left[\gamma^2(\cos\theta + \xi)^2 + \sin^2\theta\right]\right. \\
&\left.-\gamma(\cos\theta + \xi)\left[\gamma^2(\cos\theta + \xi) - \cos\theta\right]\right\} \\
&= \frac{\gamma}{\left[\gamma^2(\cos\theta + \xi)^2 + \sin^2\theta\right]^{3/2}}\left[\sin^2\theta + (\cos\theta + \xi)\cos\theta\right] \\
&= \frac{\gamma(1 + \xi\cos\theta)}{\left[\gamma^2(\cos\theta + \xi)^2 + \sin^2\theta\right]^{3/2}}.
\end{aligned} \tag{D.10}$$

Thus, the CM differential cross section can be evaluated as

$$\frac{\mathrm{d}\sigma}{\mathrm{d}\hat{\Omega}_{\mathrm{CM}}} = \frac{\mathrm{d}\sigma}{\mathrm{d}\hat{\Omega}_{\mathrm{lab}}}\frac{\gamma(1 + \xi\cos\theta)}{\left[\gamma^2(\cos\theta + \xi)^2 + \sin^2\theta\right]^{3/2}}. \tag{D.11}$$

E. Correlation between fit parameters

For a model that depends on n parameters, $\boldsymbol{p} = \{p_1, p_2, ..., p_n\}$, the best fit parameters, $\boldsymbol{p}_0$, can be found by minimizing

$$\chi^2(\boldsymbol{p}) = \sum_{i=1}^{N} \left(y_i^{\text{exp}} - y_i^{\text{eval}}(\boldsymbol{p}) \right)^2, \tag{E.1}$$

where N is the number of experimental data points, y_i^{exp} are the experimental quantities at each experimental data point i, and $y_i^{\text{eval}}(\boldsymbol{p})$ are the corresponding fitted quantities at each experimental data point i, depending on the fit parameters $\boldsymbol{p}$.

After finding the best-fit parameters $\boldsymbol{p}_0$ by minimizing $\chi^2(\boldsymbol{p})$, the covariance matrix of the parameters can be evaluated as [129]:

$$\boldsymbol{C} = \frac{\chi^2(\boldsymbol{p}_0)}{N - n} \left(\boldsymbol{J}^T \boldsymbol{J} \right)^{-1}, \tag{E.2}$$

where $N - n$ is the number of degrees of freedom and $\boldsymbol{J}$ is the Jacobian matrix, with dimensions $N \times n$. This matrix consists of the first-order derivatives of the residuals, $r_i(\boldsymbol{p}) = y_i^{\text{exp}} - y_i^{\text{eval}}(\boldsymbol{p})$, with respect to the parameters:

$$J_{ij} = \frac{\partial r_i(\boldsymbol{p})}{\partial p_j}. \tag{E.3}$$

When an explicit analytical form of the derivatives is not available, finite differences can be used to approximate them:

$$J_{ij} = \frac{\partial r_i(\boldsymbol{p})}{\partial p_j} \approx \frac{r_i(\boldsymbol{p_0} + \Delta \boldsymbol{p_j}) - r_i(\boldsymbol{p_0})}{\Delta p_j}. \tag{E.4}$$

Once the covariance matrix $\boldsymbol{C}$ is known, the correlation coefficient ρ_{ij} between the parameters p_i and p_j is

$$\rho_{ij} = \frac{C_{ij}}{\sqrt{C_{ii} C_{jj}}}, \tag{E.5}$$

where C_{ij} is the covariance between p_i and p_j, and C_{ii} and C_{jj} are their variances.

The correlation coefficients can take values between -1 and 1:

- $\rho_{ij} = -1$ indicates a perfect negative correlation, *i.e.*, when one parameter increases, the other decreases.

- $\rho_{ij} = 0$ shows that there is no correlation between the parameters.

- $\rho_{ij} = 1$ indicates a perfect positive correlation, *i.e.*, when one parameter increases, the other increases as well.

F. Microscopic mean field theories

For self-consistency, this appendix provides the main ingredients for the target nuclear densities calculated and employed in Chapter 6. The model descriptions presented in a few relevant scientific papers (cited throughout the appendix) have been closely followed, without presenting any original contributions.

F.1 Non-relativistic Hartree-Fock calculations with the Skyrme force

Microscopic mean field theories are based on the assumption that each nucleon (proton or neutron) inside the nucleus is moving independently in an average mean-field potential created by all other nucleons. The aim is to extract such a single-particle potential from the sum of effective two-body nucleon-nucleon (NN) interactions [130]. In the non-relativistic case, the starting point is the many-body Schrödinger equation, which describes the NN-particle quantum system:

$$\hat{\mathcal{H}}|\Psi(\boldsymbol{r}_1, \boldsymbol{r}_2, \ldots, \boldsymbol{r}_A)\rangle = E|\Psi(\boldsymbol{r}_1, \boldsymbol{r}_2, \ldots, \boldsymbol{r}_A)\rangle, \tag{F.1}$$

where $\Psi(\boldsymbol{r}_1, \boldsymbol{r}_2, \ldots, \boldsymbol{r}_A)$ is the many-body wavefunction of all particles and E is the total energy of the system. The Hamiltonian of the system is

$$\hat{\mathcal{H}} = \sum_{i=1}^{A} \frac{\boldsymbol{p}_i^2}{2m} + \frac{1}{2} \sum_{i \neq j}^{A} V_{ij}^{\text{eff}}, \tag{F.2}$$

where $\boldsymbol{p}_i$ is the momentum operator for the i^{th} nucleon, m is the mass of a single nucleon, and A is the number of nucleons. The effective two-body NN interaction is denoted by V_{ij}^{eff} and it is generally built in a phenomenological way.

In the Hartree-Fock (HF) approximation, the ground state wavefunction of the nucleus $\Psi(\boldsymbol{r}_1, \boldsymbol{r}_2, \ldots, \boldsymbol{r}_A)$ is approximated by a Slater determinant of single-particle wavefunctions $\psi(\boldsymbol{r})$:

$$\Psi(\boldsymbol{r}_1, \boldsymbol{r}_2, \ldots, \boldsymbol{r}_A) = \frac{1}{\sqrt{A!}} \begin{vmatrix} \psi_1(\boldsymbol{r}_1) & \psi_2(\boldsymbol{r}_1) & \cdots & \psi_A(\boldsymbol{r}_1) \\ \psi_1(\boldsymbol{r}_2) & \psi_2(\boldsymbol{r}_2) & \cdots & \psi_A(\boldsymbol{r}_2) \\ \vdots & \vdots & \ddots & \vdots \\ \psi_1(\boldsymbol{r}_A) & \psi_2(\boldsymbol{r}_A) & \cdots & \psi_A(\boldsymbol{r}_A) \end{vmatrix}. \tag{F.3}$$

The variational principle is employed to determine the optimal single-particle wavefunctions $\psi(\boldsymbol{r})$ by minimizing the total energy of the nucleus:

$$E = \frac{\langle \Psi | H | \Psi \rangle}{\langle \Psi | \Psi \rangle}, \tag{F.4}$$

leading to a set of A coupled integro-differential equations (the HF equations):

$$h\psi_i = \left(-\frac{\hbar^2}{2m} \boldsymbol{\nabla}^2 + U_{\text{HF}}[\psi] \right) \psi_i = \varepsilon_i \psi_i, \quad i = 1, \ldots, A. \tag{F.5}$$

This self-consistent system of HF equations is typically solved by iteration until convergence is attained, resulting in a set of single-particle wavefunctions ψ, their energies ε and the HF mean field $U_{\mathrm{HF}}[\psi]$. Once the single-particle states are known, the nuclear density is evaluated as:

$$\rho(\boldsymbol{r}) = \sum_{i=1}^{A} |\psi_i(\boldsymbol{r})|^2. \tag{F.6}$$

To properly describe the properties of nuclei, in particular the binding energies and the radii, density-dependent energy functionals are commonly used, based on Gogny [121, 122] or Skyrme [131, 132] interactions. In this section the HF equations for the Skyrme interaction are briefly presented, closely following [131, 132], where the Skyrme-HF formalism was first introduced.

The Skyrme-HF calculations are performed with the zero-range two-body force:

$$\begin{aligned} v_{12} = {} & t_0 \left(1 + x_0 P_\sigma\right) \delta(\boldsymbol{r}_1 - \boldsymbol{r}_2) + \frac{1}{2} t_1 \left[\delta(\boldsymbol{r}_1 - \boldsymbol{r}_2) k^2 + k'^2 \delta(\boldsymbol{r}_1 - \boldsymbol{r}_2)\right] \\ & + t_2 \boldsymbol{k}' \cdot \delta(\boldsymbol{r}_1 - \boldsymbol{r}_2) \boldsymbol{k} + i W_0 (\boldsymbol{\sigma}_1 + \boldsymbol{\sigma}_2) \cdot \boldsymbol{k}' \times \delta(\boldsymbol{r}_1 - \boldsymbol{r}_2) \boldsymbol{k}, \end{aligned} \tag{F.7}$$

where $\boldsymbol{k} = (\nabla_1 - \nabla_2)/(2i)$ is the operator of the relative momentum. In addition to this two-body force, in the original Skyrme calculations [131, 132] a three-body force of zero-range was also introduced:

$$v_{123} = t_3 \delta(\boldsymbol{r}_1 - \boldsymbol{r}_2) \delta(\boldsymbol{r}_2 - \boldsymbol{r}_3), \tag{F.8}$$

For even-even nuclei this force is equivalent to a two-body density-dependent interaction:

$$v_{123}(\rho) = \frac{1}{6} t_3 (1 + P_\sigma) \delta(\boldsymbol{r}_1 - \boldsymbol{r}_2) \rho\left(\frac{\boldsymbol{r}_1 + \boldsymbol{r}_2}{2}\right). \tag{F.9}$$

Later on, the following more general density-dependent term was introduced:

$$v_{123}(\rho) = \frac{1}{6} t_3 (1 + P_\sigma) \delta(\boldsymbol{r}_1 - \boldsymbol{r}_2) \rho^\gamma\left(\frac{\boldsymbol{r}_1 + \boldsymbol{r}_2}{2}\right). \tag{F.10}$$

where γ is a parameter mainly related to the compressibility of nuclear matter. Since this density-dependent term cannot be further related to a nucleon-nucleon force, the formalisms which include this term are commonly referred to as Skyrme energy-density functionals.

The Skyrme-HF equations presented below are derived for even-even $N = Z$. Neglecting the Coulomb interaction and taking $\gamma = 1$, the total energy can be written as

$$E = \int H(\boldsymbol{r}) \, \mathrm{d}\boldsymbol{r}, \tag{F.11}$$

where

$$\begin{aligned} H(\boldsymbol{r}) = {} & \frac{\hbar^2}{2m} \tau + \frac{3}{8} t_0 \rho^2 + \frac{1}{16} t_3 \rho^3 + \frac{1}{16} (3t_1 + 5t_2) \rho \tau \\ & + \frac{1}{64} (9t_1 - 5t_2) (\boldsymbol{\nabla} \rho)^2 - \frac{3}{4} W_0 \rho \boldsymbol{\nabla} \cdot \boldsymbol{J} + \frac{1}{32} (t_1 - t_2) \boldsymbol{J}^2. \end{aligned} \tag{F.12}$$

The nucleon density $\rho(\boldsymbol{r})$, the kinetic energy density $\tau(\boldsymbol{r})$, and the spin-orbit densities $\boldsymbol{J}(\boldsymbol{r})$ depend on the single particle states ψ_i which define the Slater-determinant wavefunction

Ψ:

$$\rho(\boldsymbol{r}) = \sum_{i,s,t} |\psi_i(\boldsymbol{r}, s, t)|^2, \tag{F.13}$$

$$\tau(\boldsymbol{r}) = \sum_{i,s,t} |\boldsymbol{\nabla}\psi_i(\boldsymbol{r}, s, t)|^2, \tag{F.14}$$

$$\boldsymbol{J}(\boldsymbol{r}) = -i \sum_{i,s,s',t} \varphi_i^*(\boldsymbol{r}, s, t) \left[\boldsymbol{\nabla}\psi_i(\boldsymbol{r}, s', t) \times \boldsymbol{\sigma}_{s,s'}\right]. \tag{F.15}$$

The sums are taken over all occupied single-particle states. The spin and isospin coordinates are denoted by s and t.

Varying the total energy E with respect to the single-particle states ψ_i (with the additional constraint that the latter are normalized):

$$\frac{\delta}{\delta\psi_i}\left(E - \sum_i \varepsilon_i \int |\psi_i(\boldsymbol{r})|^2 \mathrm{d}\boldsymbol{r}\right) = 0, \tag{F.16}$$

yields the HF equations:

$$\left[-\boldsymbol{\nabla} \cdot \frac{\hbar^2}{2m^*(\boldsymbol{r})}\boldsymbol{\nabla} + U(\boldsymbol{r}) + \boldsymbol{W}(\boldsymbol{r})\frac{1}{i} \cdot (\boldsymbol{\nabla} \times \boldsymbol{\sigma})\right]\psi_i = \varepsilon_i\psi_i, \tag{F.17}$$

where the effective mass is

$$m^*(\boldsymbol{r}) = m\left(1 + \frac{2m}{\hbar^2}\frac{1}{16}(t_1 + 5t_2)\rho(\boldsymbol{r})\right)^{-1}, \tag{F.18}$$

the effective potential is

$$U(\boldsymbol{r}) = \frac{3}{4}t_0\rho + \frac{3}{16}t_3\rho^2 + \frac{1}{16}(3t_1 + 5t_2)\tau + \frac{1}{32}(5t_2 - 9t_1)\boldsymbol{\nabla}^2\rho - \frac{3}{4}W_0\boldsymbol{\nabla} \cdot \boldsymbol{J}, \tag{F.19}$$

and the one-body spin-orbit potential is

$$\boldsymbol{W}(\boldsymbol{r}) = \frac{3}{4}W_0\boldsymbol{\nabla}\rho. \tag{F.20}$$

The HF equations are solved iteratively and the parameters t_0, t_1, t_2, t_3, x_0 and W_0 are fitted to experimental binding energies and radii.

For deformed nuclei with axial symmetry, the Skyrme-HF equations are usually solved in the intrinsic system. In this case, the single-particle wave functions are

$$\psi_i(\boldsymbol{r}, s, t) = \chi_{t_i}(t)\left[\psi_i^+(r, z)e^{i\Lambda^-}\varphi_{\chi+1/2}(s) + \psi_i^-(r, z)e^{i\Lambda^+}\varphi_{\chi-1/2}(s)\right], \tag{F.21}$$

where $\Lambda^\pm = \Omega_i \pm \frac{1}{2}$, Ω_i is the eigenvalue of the component J_z of the total angular momentum, which is a good quantum number for the single-particle state ψ_i; the eigenvalues of the component τ_z of the isospin are $t_i = +\frac{1}{2}$ for protons and $t_i = -\frac{1}{2}$ for neutrons. Therefore, the nucleon and kinetic energy densities depend only on the coordinates r and z:

$$\begin{aligned}
\rho(r, z) &= \sum_i \left[|\psi_i^+(r, z)|^2 + |\psi_i^-(r, z)|^2\right] \\
\tau(r, z) &= \sum_i \Bigg(|\nabla_r\psi_i^+(r, z)|^2 + |\nabla_z\psi_i^+(r, z)|^2 + \frac{1}{r^2}|\Lambda^-\psi_i^+(r, z)|^2 \\
&\quad + |\nabla_r\psi_i^-(r, z)|^2 + |\nabla_z\psi_i^-(r, z)|^2 + \frac{1}{r^2}|\Lambda^+\psi_i^-(r, z)|^2\Bigg).
\end{aligned} \tag{F.22}$$

In open-shell nuclei one needs to take into account also the correlations induced by the pairing force. In this case, the single-particle states have an occupation probability which is different from 1 and 0. As such, the nuclear density becomes:

$$\rho(\boldsymbol{r}) = \sum_i v_i^2 |\psi_i(\boldsymbol{r})|^2, \tag{F.23}$$

where v_i^2 is the occupation probability of the state i. The kinetic energy density and spin-orbit density are calculated in the same manner.

In the majority of the calculations for open-shell nuclei, the occupation probabilities are calculated within the BCS (Bardeen-Cooper-Schrieffer) approximation. For the even-even $N = Z$ nuclei considered in this thesis, in which the proton-neutron pairing is significant, the occupation probabilities were evaluated in the framework of QCM (quartet condensation model).

F.2 Relativistic mean field theory

Contrary to non-relativistic mean-field theories, the relativistic mean field (RMF) approach fulfills the special relativity requirements and, as such, it strictly obeys the causality principle. In this section the main ingredients of RMF are briefly presented, closely following [133].

In RMF the nucleons are considered point-like particles which interact by exchanging mesons. In the case of nucleon-nucleon interactions in free space, one of the most important mesons is the pion (π), characterized by the angular momentum $J = 0$, the isospin $T = 1$, and the parity $P = -1$. However, due to the negative parity, its inclusion in the RMF theory would break parity symmetry at the Hartree level. Since parity is conserved in real nuclei, the pion is typically not included explicitly in the RMF theory. Instead, an effective scalar field, the σ-meson, is introduced, characterized by $J = 0$, $T = 0$, and $P = +1$. The σ-meson is usually considered as a phenomenological approximation of a two-pion resonance and it is introduced to generate the long-range attractive part of the nucleon-nucleon interaction. The repulsive short-range interaction is modelled by the ω-meson, which has quantum numbers $J = 1$, $T = 0$, and $P = -1$. This meson generates a vector field ($\omega^\mu(\boldsymbol{x})$) analogous to the electromagnetic field of the photon, with its time-like component contributing to a repulsive force similar to Coulomb repulsion. The isospin dependence of the nuclear interaction is generated by the exchange of the ρ-meson characterized by $J = 1$, $T = 1$, and $P = -1$. The masses and coupling constants of the σ, ω, and ρ mesons are treated as adjustable parameters that are fine-tuned to reproduce observed nuclear properties.

The equations of motion for the fields are derived from the Lagrangian density through the classical variation principle. The mean-field approximation is adopted: the meson fields are replaced by their classical expectation values obeying the Klein-Gordon equations and the nucleons are described as single-particle wavefunctions obeying the Dirac equation. To describe the ground-state nuclear properties, such as the nuclear density, static solutions are sought for the equations of motion, under the following assumptions:

- The meson fields are time-independent.
- The nucleon spinors have a time dependent phase of the form $\exp(i\epsilon_i t)$.
- Time-reversal invariance and good parity are considered, which are particularly applicable to the ground states of even-even nuclei.

The stationary RMF equations are then:

$$[-i\boldsymbol{\alpha}\nabla + \beta(m+S) + V]\psi_i = \varepsilon_i\psi_i \tag{F.24}$$

$$(-\Delta + m_\sigma)\sigma = -g_\sigma\rho_s - g_2\sigma^2 - g_3\sigma^3 \tag{F.25}$$

$$(-\Delta + m_\omega)\omega^0 = g_\omega\rho_v \tag{F.26}$$

$$(-\Delta + m_\rho)\rho_3^0 = g_\rho\rho_3 \tag{F.27}$$

$$-\Delta\rho_c^0 = e\rho_c, \tag{F.28}$$

where the scalar density is

$$\rho_s = \sum_{i=1}^{A} \bar{\psi}_i\psi_i, \tag{F.29}$$

the usual (baryon) density is

$$\rho_v = \sum_{i=1}^{A} \psi_i^\dagger\psi_i, \tag{F.30}$$

the isovector density is

$$\rho_3 = \sum_{i=1}^{A} \psi_i^\dagger\tau_3\psi_i, \tag{F.31}$$

and the charge density is

$$\rho_c = \sum_{i=1}^{A} \psi_i^\dagger\frac{1}{2}(1+\tau_3)\psi_i. \tag{F.32}$$

In Eq. (F.24), the vector potential is

$$V(\boldsymbol{r}) = g_\omega\omega^0(\boldsymbol{r}) + g_\rho\tau_3\rho_3^0(\boldsymbol{r}) + eA^0(\boldsymbol{r}), \tag{F.33}$$

which is the time-like component of a Lorentz vector (and it corresponds to the Coulomb field in electrodynamics), and the scalar potential is

$$S(\boldsymbol{r}) = g_\sigma\sigma(\boldsymbol{r}), \tag{F.34}$$

contributing to the effective Dirac mass $m^*(\boldsymbol{r}) = m + S(\boldsymbol{r})$. The stationary RMF equations are solved self-consistently by iteration, as follows:

1. An initial guess is made for the potentials V and S;
2. The Dirac equations for the spinors ψ_i are solved;
3. The densities ρ_s, ρ_v, ρ_3, and ρ_c are calculated;
4. The meson fields are computed;
5. The potentials are updated;
6. The steps above are repeated until convergence is achieved.

The procedure is equivalent to the Hartree approximation employed in the non-relativistic case [134].

One relevant aspect of the RMF approach is the way in which the effective mean field is generated. This can be seen by neglecting the Laplacian in Eqs. (F.25) and (F.26). In this case, the scalar (σ) and vector (ω) meson fields (with masses of approximately 500 MeV and 780 MeV, respectively) are proportional to the scalar and vector fields, respectively, as in infinite nuclear matter. For finite nuclei, σ and ω meson fields exhibit a Wood-Saxon shape, vanishing outside the nucleus. Inside the nucleus, these fields remain nearly constant, with $S \approx -400$ MeV for the σ-field and $V \approx 350$ MeV for the ω-field. Consequently, the nucleon potential depth is $(V + S) \approx -50$ MeV. On the other hand, the anti-nucleon potential is significantly larger, $(V - S) \approx 750$ MeV. Due to this reason, in the majority of the RMF calculations, the contribution of the negative-energy solutions of the Dirac equations is neglected.

Another important aspect of the RMF approach is the mechanism by which the saturation of nuclear matter is preserved. This mechanism is based on the special structure of the scalar and vector densities, which determine the attractive scalar and repulsive vector potentials. The scalar density

$$\rho_s(r) = \sum_{i=1}^{A} \left(|f_i(r)|^2 - |g_i(r)|^2 \right), \tag{F.35}$$

depends on the difference between the large (f_i) and small (g_i) components of Dirac spinors, while the vector density

$$\rho_v(r) = \sum_{i=1}^{A} \left(|f_i(r)|^2 + |g_i(r)|^2 \right), \tag{F.36}$$

depends on their sum. As small components become significant during a potential collapse (*e.g.*, when the energy gap in Dirac equations diminishes), ρ_s decreases. Since ρ_s drives the attractive scalar potential S, this reduction mitigates excessive attraction and stabilizes the nucleus.

Bibliography

[1] G.C. Messenger and M.S. Ash. *Single Event Phenomena I*, chapter 6, pages 179–231. Springer US, 1997. doi: 10.1007/978-1-4615-6043-2_6. URL https://doi.org/10.1007/978-1-4615-6043-2_6.

[2] J. Barak and N. Yitzhak. SEU Rate in Avionics: From Sea Level to High Altitudes. *IEEE Trans. Nucl. Sci.*, 62:3369–3380, 12 2015. doi: 10.1109/TNS.2015.2495324. URL https://doi.org/10.1109/TNS.2015.2495324.

[3] M. Huhtinen and F. Faccio. Computational method to estimate Single Event Upset rates in an accelerator environment. *Nucl. Instrum. Meth. A*, 450(1):155–172, 2000. ISSN 0168–9002. doi: 10.1016/S0168-9002(00)00155-8. URL https://doi.org/10.1016/S0168-9002(00)00155-8.

[4] R. García Alía. *Radiation fields in high energy accelerators and their impact on single event effects*. PhD thesis, Montpellier Univ., Montpellier, France, 2014. [Online]. Available: https://cds.cern.ch/record/2012360. Accessed on: Sep. 20, 2024.

[5] D. Binder, E.C. Smith, and A.B. Holman. Satellite Anomalies from Galactic Cosmic Rays. *IEEE Trans. Nucl. Sci.*, 22(6):2675–2680, 1975. doi: 10.1109/TNS.1975.4328188. URL https://doi.org/10.1109/TNS.1975.4328188.

[6] T.C. May and M.H. Woods. A New Physical Mechanism for Soft Errors in Dynamic Memories. In *Proc. 16th International Reliability Physics Symposium*, pages 33–40, San Diego, California, USA, 1978.

[7] J.F. Ziegler and W.A. Lanford. Effect of Cosmic Rays on Computer Memories. *Science*, 206(4420):776–788, 1979. doi: 10.1126/science.206.4420.776. URL https://doi.org/10.1126/science.206.4420.776.

[8] R. García Alía et al. Single event effects in high-energy accelerators. *Semicond. Sci. Technol.*, 32(3):034003, 2017. doi: 10.1088/1361-6641/aa5695. URL https://doi.org/10.1088/1361-6641/aa5695.

[9] B.D. Sierawski et al. Impact of Low-Energy Proton Induced Upsets on Test Methods and Rate Predictions. *IEEE Trans. Nuc. Sci.*, 56(6):3085–3092, 2009. doi: 10.1109/TNS.2009.2032545. URL https://doi.org/10.1109/TNS.2009.2032545.

[10] E.H. Cannon et al. Heavy Ion, High-Energy, and Low-Energy Proton SEE Sensitivity of 90-nm RHBD SRAMs. *IEEE Trans. Nucl. Sci.*, 57(6):3493–3499, 2010. doi: 10.1109/TNS.2010.2086482. URL https://doi.org/10.1109/TNS.2010.2086482.

[11] P. Caron et al. Physical Mechanisms of Proton-Induced Single-Event Upset in Integrated Memory Devices. *IEEE Trans. Nucl. Sci.*, 66(7):1404–1409, 2019. doi: 10.1109/TNS.2019.2902758. URL https://doi.org/10.1109/TNS.2019.2902758.

[12] A. Coronetti. *Relevance and Guidelines of Radiation Effect Testing Beyond the Standards for Electronic Devices and Systems Used in Space and at Accelerators.*

PhD thesis, Jyväskylä Univ., Jyväskylä, Finland, 2021. [Online]. Available: https://cds.cern.ch/record/2799812. Accessed on: Sep. 20, 2024.

[13] A. Coronetti et al. Assessment of Proton Direct Ionization for the Radiation Hardness Assurance of Deep Submicron SRAMs Used in Space Applications. *IEEE Trans. Nucl. Sci.*, 68(5):937–948, 2021. doi: 10.1109/TNS.2021.3061209. URL https://doi.org/10.1109/TNS.2021.3061209.

[14] A. Akkerman, J. Barak, and N.M. Yitzhak. Role of Elastic Scattering of Protons, Muons, and Electrons in Inducing Single-Event Upsets. *IEEE Trans. Nucl. Sci.*, 64 (10):2648–2660, 2017. doi: 10.1109/TNS.2017.2747658. URL https://doi.org/10.1109/TNS.2017.2747658.

[15] Z. Wu et al. Recoil-Ion-Induced Single Event Upsets in Nanometer CMOS SRAM Under Low-Energy Proton Radiation. *IEEE Trans. Nucl. Sci.*, 64(1):654–664, 2017. doi: 10.1109/TNS.2016.2633405. URL https://doi.org/10.1109/TNS.2016.2633405.

[16] https://www.issi.com/WW/pdf/61-64WV204816BLL.pdf, 2016. Accessed on: Sep. 20, 2024.

[17] T.C. Slaba and K. Whitman. The Badhwar-O'Neill 2020 Model. Technical Report NASA/TP-2019-220419, NASA Langley Research Center, Hampton, VA, USA, 2019. [Online]. Available: https://spaceradiation.larc.nasa.gov/nasapapers/NASA-TP-2019-220419.pdf. Accessed on: Nov. 22, 2024.

[18] NASA Langley Research Center. On-Line Tool for the Assessment of Radiation in Space (OLTARIS). https://oltaris.nasa.gov, 2024. Accessed: Nov. 22, 2024.

[19] https://fluka.cern. Accessed on: Sep. 23, 2024.

[20] G. Battistoni et al. Overview of the FLUKA code. *Ann. Nucl. Energy*, 82:10–18, 2015. ISSN 0306-4549. doi: 10.1016/j.anucene.2014.11.007. URL https://doi.org/10.1016/j.anucene.2014.11.007.

[21] C. Ahdida et al. New Capabilities of the FLUKA Multi-Purpose Code. *Front. Phys.*, 9, 2022. ISSN 2296-424X. doi: 10.3389/fphy.2021.788253. [Online]. Available: https://www.frontiersin.org/journals/physics/articles/10.3389/fphy.2021.788253. Accessed on: Sep. 20, 2024.

[22] G. Lerner et al. Analysis of the Photoneutron Field Near the THz Dump of the CLEAR Accelerator at CERN With SEU Measurements and Simulations. *IEEE Trans. Nucl. Sci.*, 69(7):1541–1548, 2022. doi: 10.1109/TNS.2022.3157404. URL https://doi.org/10.1109/TNS.2022.3157404.

[23] M. Cecchetto et al. 0.1-10 MeV Neutron Soft Error Rate in Accelerator and Atmospheric Environments. *IEEE Trans. Nucl. Sci.*, 68(5):873–883, 2021. doi: 10.1109/TNS.2021.3064666. URL https://doi.org/10.1109/TNS.2021.3064666.

[24] R. Alía García et al. SEU Measurements and Simulations in a Mixed Field Environment. *IEEE Trans. Nucl. Sci.*, 60(4):2469–2476, 2013. doi: 10.1109/TNS.2013.2249096. URL https://doi.org/10.1109/TNS.2013.2249096.

[25] P. Caron et al. New SEU Modeling Method for Calibrating Target System to Multiple Radiation Particles. *IEEE Trans. Nucl. Sci.*, 67(1):44–49, 2020. doi: 10.1109/TNS.2019.2953995. URL https://doi.org/10.1109/TNS.2019.2953995.

[26] S. Lüdeke and A. Javanainen. Proton Direct Ionization in Sub-Micron Technologies: Numerical Method for RPP Parameter Extraction. *IEEE Trans. Nucl. Sci.*, 69(3): 254–263, 2022. doi: 10.1109/TNS.2022.3147592. URL https://doi.org/10.1109/TNS.2022.3147592.

[27] A.-G. Şerban, A. Coronetti, R. García Alía, and F. Salvat Pujol. Nuclear elastic scattering of protons below 250 MeV in FLUKA v4-4.0 and its role in single-event-upset production in electronics. *Computer Physics Communications*, page 109276, 2024. ISSN 0010-4655. doi: 10.1016/j.cpc.2024.109276. URL https://doi.org/10.1016/j.cpc.2024.109276.

[28] J.H.L. Mott and J.M. Daniel. Interactions of Electromagnetic Radiation and Subatomic Particles with Matter - Part 2. *Clin. Oncol.*, 33(7):455–460, 2021. doi: 10.1016/j.clon.2021.02.005. URL https://doi.org/10.1016/j.clon.2021.02.005.

[29] N. Verbeek et al. Single pencil beam benchmark of a module for Monte Carlo simulation of proton transport in the PENELOPE code. *Med. Phys.*, 48(1), 2021. doi: 10.1002/mp.14598. URL https://doi.org/10.1002/mp.14598.

[30] J. Ranft. Estimation of radiation problems around high-energy accelerators using calculations of the hadronic cascade in matter. *Part. Accel.*, 3:129–161, 1972.

[31] J. Ströbele, T. Schreiner, H. Fuchs, and D. Georg. Comparison of basic features of proton and helium ion pencil beams in water using GATE. *Z. Med. Phys.*, 22:170–8, 01 2012. doi: 10.1016/j.zemedi.2011.12.001. URL https://doi.org/10.1016/j.zemedi.2011.12.001.

[32] P. Roche et al. Comparisons of soft error rate for SRAMs in commercial SOI and bulk below the 130-nm technology node. *IEEE Trans. Nucl. Sci.*, 50(6):2046–2054, 2003. doi: 10.1109/TNS.2003.821588. URL https://doi.org/10.1109/TNS.2003.821588.

[33] X.-W. Su and Y.-L. Han. Global optical model potential for alpha projectile. *Int. J. Mod. Phys. E*, 24(12), 2015. doi: 10.1142/S0218301315500925. URL https://doi.org/10.1142/S0218301315500925.

[34] A. Budzanowski et al. Glory effect in the optical-model analysis of 39K(α,α)39K elastic scattering. *Nucl. Phys. A*, 126(2):369–380, 1969. ISSN 0375-9474. doi: 10.1016/0375-9474(69)90472-2. URL https://www.sciencedirect.com/science/article/pii/0375947469904722.

[35] G. Gaul et al. Effects of α-particle correlations in elastic α-scattering. *Nucl. Phys. A*, 137:177–92, 1969. doi: 10.1016/0375-9474(69)90081-5. URL https://doi.org/10.1016/0375-9474(69)90081-5.

[36] H. Schmeing and R. Santo. Backward-angle anomalies in inelastic alpha-particle scattering on ^{40}Ca. *Phys. Lett. B*, 33(3):219–221, 1970. ISSN 0370–2693. doi: 10.1016/0370-2693(70)90577-0. URL https://doi.org/10.1016/0370-2693(70)90577-0.

[37] N. Otuka et al. Towards a More Complete and Accurate Experimental Nuclear Reaction Data Library (EXFOR): International Collaboration Between Nuclear Reaction Data Centres (NRDC). *Nucl. Data Sheets*, 120:272–276, 2014. ISSN 0090-3752. doi: 101016/jnds201407065. URL https://doi.org/101016/jnds201407065.

[38] V.V. Zerkin and B. Pritychenko. The experimental nuclear reaction data (EXFOR): Extended computer database and Web retrieval system. *Nucl. Instrum. Meth. A*, 888:31–43, 2018. ISSN 0168-9002. doi: 10.1016/j.nima.2018.01.045. URL https://doi.org/10.1016/j.nima.2018.01.045.

[39] A.J. Koning and J.P. Delaroche. Local and global nucleon optical models from 1 keV to 200 MeV. *Nuc. Phys. A*, 713:231–310, 2003. doi: 10.1016/S0375-9474(02)01321-0. URL https://doi.org/10.1016/S0375-9474(02)01321-0.

[40] A. Messiah. *Quantum Mechanics*. Number Bd. 1 in Quantum Mechanics. North-Holland Publishing Company, 1961. ISBN 9780471597667. URL https://books.google.ch/books?id=5XcfAQAAMAAJ.

[41] F. Salvat and J.M. Fernández-Varea. RADIAL: A Fortran subroutine package for the solution of the radial Schrödinger and Dirac wave equations. *Comp. Phys. Comm.*, 240:165–177, 2019. doi: 10.1016/j.cpc.2019.02.011. URL https://doi.org/10.1016/j.cpc.2019.02.011.

[42] F. Salvat. *Mecánica cuántica*. Aula Magna Proyecto Clave McGraw Hill, 2006.

[43] A. Ferrari and P. Sala. The physics of high energy reactions. *Proceed. Workshop on Nucl. Reaction Data and Nuclear Reactor Physics, Design and Safety*, 2, 1998. [Online]. Available: https://cds.cern.ch/record/682497/files/phys-97-113.pdf. Accessed on: Oct. 29, 2024.

[44] I.M. Dremin. Elastic scattering of hadrons. *Phys.-Usp*, 56(1):3, 2013. doi: 10.3367/UFNe.0183.201301a.0003. URL https://doi.org/10.3367/UFNe.0183.201301a.0003.

[45] V.M. Grichine. Geant4 hadron elastic diffuse model. *Comp. Phys. Comm.*, 181(5):921–927, 2010. doi: 10.1016/j.cpc.2010.01.004. URL https://doi.org/10.1016/j.cpc.2010.01.004.

[46] B. Watson, P.P. Singh, and R.E. Segel. Optical-Model Analysis of Nucleon Scattering from 1p-Shell Nuclei between 10 and 50 MeV. *Phys. Rev.*, 182:977–989, 1969. doi: 10.1103/PhysRev.182.977. URL https://doi.org/10.1103/PhysRev.182.977.

[47] J.W. Wilson et al. Nucleon-nucleus interaction data base-total nuclear and absorption cross sections, 1988. [Online]. Available: https://ntrs.nasa.gov/api/citations/19880017551/downloads/19880017551.pdf. Accessed on: Oct. 29, 2024.

[48] W.H. Press et al. *Numerical Recipes in C: the Art of Scientific Computing*. Cambridge University Press, 1992.

[49] G. Moliere. Theorie der Streuung schneller geladener Teilchen II Mehrfach-und Vielfachstreuung. *Z. Naturforsch. A*, 3(2):78–97, 1948. doi: 10.1515/zna-1948-0203. URL https://doi.org/10.1515/zna-1948-0203.

[50] J.M. Fernández-Varea, R. Mayol, J. Baró, and F. Salvat. On the theory and simulation of multiple elastic scattering of electrons. *Nucl. Instrum. Methods Phys. Res. B*, 73(4):447–473, 1993. ISSN 0168-583X. doi: https://doi.org/10.1016/0168-583X(93)95827-R. URL https://www.sciencedirect.com/science/article/pii/0168583X9395827R.

[51] H. A. Bethe. Molière's Theory of Multiple Scattering. *Phys. Rev.*, 89:1256–1266, 1953. doi: 10.1103/PhysRev.89.1256. URL https://link.aps.org/doi/10.1103/PhysRev.89.1256.

[52] A. Ferrari et al. An improved multiple scattering model for charged particle transport. *Nucl. Instrum. Meth. B*, 71(4):412–426, 1992. ISSN 0168-583X. doi: 10.1016/0168-583X(92)95359-Y. URL https://doi.org/10.1016/0168-583X(92)95359-Y.

[53] Y.-S. Tsai. Pair production and bremsstrahlung of charged leptons. *Rev. Mod. Phys.*, 46:815–851, 1974. doi: 10.1103/RevModPhys.46.815. URL https://doi.org/10.1103/RevModPhys.46.815.

[54] R. García Alía et al. Heavy Ion Energy Deposition and SEE Intercomparison Within the RADNEXT Irradiation Facility Network. *IEEE Trans. Nucl. Sci.*, 70(8):1596–1605, 2023. doi: 10.1109/TNS.2023.3260309. URL https://doi.org/10.1109/TNS.2023.3260309.

[55] R. Velazco. Error-rate prediction for programmable circuits: methodology, tools and studied cases, 2022. [Online]. Available: https://indico.cern.ch/event/1098043/contributions/4954313/attachments/2479339. Accessed on: Sep. 23, 2024.

[56] P. Roche et al. SEU response of an entire SRAM cell simulated as one contiguous three dimensional device domain. *IEEE Trans. Nucl. Sci.*, 45(6):2534–2543, 1998. doi: 10.1109/23.736495. URL https://doi.org/10.1109/23.736495.

[57] P. Roche et al. Determination of key parameters for SEU occurrence using 3-D full cell SRAM simulations. *IEEE Trans. Nucl. Sci.*, 46(6):1354–1362, 1999. doi: 10.1109/23.819093. URL https://doi.org/10.1109/23.819093.

[58] J.-M. Palau et al. Device simulation study of the SEU sensitivity of SRAMs to internal ion tracks generated by nuclear reactions. *IEEE Trans. Nucl. Sci.*, 48(2):225–231, 2001. doi: 10.1109/23.915368. URL https://doi.org/10.1109/23.915368.

[59] T. Merelle et al. Criterion for SEU occurrence in SRAM deduced from circuit and device Simulations in case of neutron-induced SER. *IEEE Trans. Nucl. Sci.*, 52(4):1148–1155, 2005. doi: 10.1109/TNS.2005.852319. URL https://doi.org/10.1109/TNS.2005.852319.

[60] S. Abe et al. Multi-scale Monte Carlo simulation of soft errors using PHITS-HyENEXSS code system. In *Proc. RADECS 2011*, pages 390–395, Sevilla, Spain, 2011. doi: 10.1109/RADECS.2011.6131413. URL https://doi.org/10.1109/RADECS.2011.6131413.

[61] R.A. Weller et al. Monte Carlo Simulation of Single Event Effects. *IEEE Trans. Nucl. Sci.*, 57(4):1726–1746, 2010. doi: 10.1109/TNS.2010.2044807. URL https://doi.org/10.1109/TNS.2010.2044807.

[62] G. Hubert et al. Operational SER Calculations on the SAC-C Orbit Using the Multi-Scales Single Event Phenomena Predictive Platform (MUSCA SEP^3). *IEEE Trans. Nucl. Sci.*, 56(6):3032–3042, 2009. doi: 10.1109/TNS.2009.2034148. URL https://doi.org/10.1109/TNS.2009.2034148.

[63] G. Hubert, L. Artola, and D. Regis. Impact of scaling on the soft error sensitivity of bulk, FDSOI and FinFET technologies due to atmospheric radiation. *Integr. VLSI J.*, 50:39–47, 2015. ISSN 0167-9260. doi: 10.1016/j.vlsi.2015.01.003. URL https://doi.org/10.1016/j.vlsi.2015.01.003.

[64] R. García Alía et al. Direct Ionization Impact on Accelerator Mixed-Field Soft-Error Rate. *IEEE Trans. Nucl. Sci.*, 67(1):345–352, 2020. doi: 10.1109/TNS.2019.2951307. URL https://doi.org/10.1109/TNS.2019.2951307.

[65] C. Inguimbert and S. Duzellier. SEU rate calculation with GEANT4 (comparison with CREME 86). *IEEE Trans. Nucl. Sci.*, 51(5):2805–2810, 2004. doi: 10.1109/TNS.2004.836524. URL https://doi.org/10.1109/TNS.2004.836524.

[66] P. Caron et al. Physical Mechanisms of Proton-Induced Single-Event Upset in Integrated Memory Devices. *IEEE Trans. Nucl. Sci.*, 66(7):1404–1409, 2019. doi: 10.1109/TNS.2019.2902758. URL https://doi.org/10.1109/TNS.2019.2902758.

[67] S. Agostinelli et al. GEANT4–a simulation toolkit. *Nucl. Instrum. Meth. A*, 506: 250–303, 2003. doi: 10.1016/S0168-9002(03)01368-8. URL https://doi.org/10.1016/S0168-9002(03)01368-8.

[68] D. Lucsányi et al. G4SEE: A Geant4-Based Single Event Effect Simulation Toolkit and Its Validation Through Monoenergetic Neutron Measurements. *IEEE Trans. Nuc. Sci.*, 69(3):273–281, 2022. doi: 10.1109/TNS.2022.3149989. URL https://doi.org/10.1109/TNS.2022.3149989.

[69] J. Fang et al. Understanding the Average Electron–Hole Pair-Creation Energy in Silicon and Germanium Based on Full-Band Monte Carlo Simulations. *IEEE Trans. Nucl. Sci.*, 66(1):444–451, 2019. doi: 10.1109/TNS.2018.2879593.

[70] https://www.infineon.com/dgdl/Infineon-CY62167G30_CY62167GE30_16_Mbit_(1M_words_X_16_bit_2M_words_X_8_bit)_Static_RAM_with_Error-Correcting_Code_(ECC)-DataSheet-v07_00-EN.pdf?fileId=8ac78c8c7d0d8da4017d0ee9e49f72cf, 2020. Accessed on: Sep. 20, 2024.

[71] http://ww1.microchip.com/downloads/en/DeviceDoc/doc7747.pdf, 2007. Accessed on: Sep. 20, 2024.

[72] A.-G. Şerban, A. Coronetti, R. García Alía, and F. Salvat Pujol. RPP-model trends across technology nodes for the MC simulation of SEUs in commercial SRAMS under proton irradiation. *IEEE Trans. Nucl. Sci.*, 2024. doi: 10.1109/TNS.2024.3520506. URL https://doi.org/10.1109/TNS.2024.3520506.

[73] R. Harboe-Sorensen, F.-X. Guerre, and A. Roseng. Design, Testing and Calibration of a "Reference SEU Monitor" System. In *Proc. RADECS 2005*, pages B3–1–B3–7, Cap d'Agde, France, 2005. doi: 10.1109/RADECS.2005.4365561. URL https://doi.org/10.1109/RADECS.2005.4365561.

[74] https://www.issi.com/WW/pdf/Asynch_Fast_SRAM_32Mb_REV02.pdf, 2016. Accessed on: Sep. 20, 2024.

[75] N. A. Dodds et al. Hardness Assurance for Proton Direct Ionization-Induced SEEs Using a High-Energy Proton Beam. *IEEE Trans. Nucl. Sci.*, 61(6):2904–2914, 2014. doi: 10.1109/TNS.2014.2364953. URL https://doi.org/10.1109/TNS.2014.2364953.

[76] N. A. Dodds et al. New Insights Gained on Mechanisms of Low-Energy Proton-Induced SEUs by Minimizing Energy Straggle. *IEEE Trans. Nucl. Sci.*, 62(6): 2822–2829, 2015. doi: 10.1109/TNS.2015.2488588. URL https://doi.org/10.1109/TNS.2015.2488588.

[77] N. A. Dodds et al. The Contribution of Low-Energy Protons to the Total On-Orbit SEU Rate. *IEEE Trans. Nucl. Sci.*, 62(6):2440–2451, 2015. doi: 10.1109/TNS.2015.2486763. URL https://doi.org/10.1109/TNS.2015.2486763.

[78] D. Lambert, F. Desnoyers, and D. Thouvenot. Investigation of neutron and proton SEU cross-sections on SRAMs between a few MeV and 50 MeV. In *Proc. RADECS 2009*, pages 148–154, Bruges, Belgium, 2009. doi: 10.1109/RADECS.2009.5994571. URL https://doi.org/10.1109/RADECS.2009.5994571.

[79] F. Faccio, C. Detcheverry, and M. Huhtinen. First evaluation of the Single Event Upset (SEU) risk for electronics in the CMS experiment, 1998. [Online]. Available: https://cds.cern.ch/record/687587. Accessed on: Sep. 20, 2024.

[80] J.F. Ziegler, M.D. Ziegler, and J.P. Biersack. SRIM – The stopping and range of ions in matter (2010). *Nucl. Instrum. Meth. B*, 268(11):1818–1823, 2010. ISSN 0168-583X. doi: 10.1016/j.nimb.2010.02.091. URL https://doi.org/10.1016/j.nimb.2010.02.091.

[81] F. Wrobel, J.-M. Palau, M.-C. Calvet, and P. Iacconi. Contribution of SiO_2 in neutron-induced SEU in SRAMs. *IEEE Trans. Nucl. Sci.*, 50(6):2055–2059, 2003. doi: 10.1109/TNS.2003.821596.

[82] A.-G. Şerban et al. On the improved performances of FLUKA v4-4.0 in out-of-field proton dosimetry. ***Submitted for publication to Rad. Phys. Chem.***, 2024. URL https://arxiv.org/abs/2412.18314.

[83] L. Eyges. Multiple Scattering with Energy Loss. *Phys. Rev.*, 74:1534–1535, 1948. doi: 10.1103/PhysRev.74.1534. URL https://link.aps.org/doi/10.1103/PhysRev.74.1534.

[84] B. Rossi and K. Greisen. Cosmic-Ray theory. *Rev. Mod. Phys.*, 12:240–309, 1941. doi: 10.1103/RevModPhys.13.240. URL https://doi.org/10.1103/RevModPhys.13.240.

[85] B. Gottschalk. Techniques of Proton Radiotherapy: Transport Theory. https://arxiv.org/abs/1204.4470, 2012.

[86] V. Vlachoudis. FLAIR: A Powerful But User Friendly Graphical Interface For FLUKA. In *Proc. Int. Conf. on Mathematics, Computational Methods & Reactor Physics*, Saratoga Springs, New York, USA, 2009.

[87] A. Donadon, G. Hugo, C. Theis, and V. Vlachoudis. FLAIR3 – recasting simulation experiences with the Advanced Interface for FLUKA and other Monte Carlo codes. *EPJ Web Conf.*, 302:11005, 2024. doi: 10.1051/epjconf/202430211005. URL https://doi.org/10.1051/epjconf/202430211005.

[88] S.M. Seltzer et al. Key data for ionizing-radiation dosimetry: measurement standards and applications, ICRU Report 90. 2016. doi: 10.1093/jicru/ndw029. URL https://doi.org/10.1093/jicru/ndw029.

[89] B. Gottschalk, E.W. Cascio, J. Daartz, and M.S. Wagner. On the nuclear halo of a proton pencil beam stopping in water. *Phys. Med. Biol.*, 60(14):5627–5654, 2015. doi: 10.1088/0031-9155/60/14/5627. URL https://doi.org/10.1088/0031-9155/60/14/5627.

[90] R. Zhang, P.J. Taddei, M.M. Fitzek, and W.D. Newhauser. Water equivalent thickness values of materials used in beams of protons, helium, carbon and iron ions. *Phys. Med. Biol.*, 55:2481, 2010. doi: 10.1088/0031-9155/55/9/004. URL https://doi.org/10.1088/0031-9155/55/9/004.

[91] A.L. Burin, I.S.L. Branco, and H. Yoriyaz. Determination of WER and WET equivalence estimator for proton beams in the therapeutic energy range using MCNP6.1 and TOPAS codes. *Rad. Phys. Chem.*, 203:110606, 2023. doi: 10.1016/j.radphyschem.2022.110606. URL https://doi.org/10.1016/j.radphyschem.2022.110606.

[92] T. Bortfeld. An analytical approximation of the Bragg curve for therapeutic proton beams. *Med. Phys.*, 24(12):2024–2033, 1997. doi: 10.1118/1.598116. URL https://doi.org/10.1118/1.598116.

[93] M.J. Berger, J.S. Coursey, and M.A. Zucker. ESTAR, PSTAR, and ASTAR: Computer Programs for Calculating Stopping-Power and Range Tables for Electrons, Protons, and Helium Ions (version 1.21). http://physics.nist.gov/Star, 1999. Accessed: September 12, 2024.

[94] https://physics.nist.gov/PhysRefData/Star/Text/PSTAR.html. Accessed: September 12, 2024.

[95] F. Michel and R. Vanderpoorten. Optical model description of anomalous elastic and inelastic $\alpha - ^{40}$Ca scattering between 20 and 50 MeV. *Phys. Rev. C*, 16:142–152, 1977. doi: 10.1103/PhysRevC.16.142. URL https://doi.org/10.1103/PhysRevC.16.142.

[96] R. Planeta, H. Daabrowski, L. Freindl, and K. Grotowski. Explanation of the anomalously small absorption of α-particles in ^{40}Ca nuclei. *Nucl. Phys. A*, 326 (1):97–107, 1979. ISSN 0375-9474. doi: 10.1016/0375-9474(79)90369-5. URL https://doi.org/10.1016/0375-9474(79)90369-5.

[97] K.A. Eberhard. An explanation of the anomalous backward enhancement of elastic α-scattering cross sections near A=40 in terms of an extended optical model. *Phys. Lett. B*, 33(5):343–346, 1970. ISSN 0370-2693. doi: 10.1016/0370-2693(70)90249-2. URL https://doi.org/10.1016/0370-2693(70)90249-2.

[98] D. Agassi and N.S. Wall. Exchange Interpretation of the Large-Angle Scattering of Alpha Particles from Nuclei. *Phys. Rev. C*, 7:1368–1382, 1973. doi: 10.1103/PhysRevC.7.1368. URL https://doi.org/10.1103/PhysRevC.7.1368.

[99] K.W. McVoy. Regge Poles and Strong Absorption in Heavy-Ion and α-Nucleus Scattering. *Phys. Rev. C*, 3:1104–1117, 1971. doi: 10.1103/PhysRevC.3.1104. URL https://doi.org/10.1103/PhysRevC.3.1104.

[100] A.S. Rinat (Reiner). Evidence for the existence of highly excited bands of intermediate resonances describing quasi-molecular rotations. *Phys. Lett. B*, 38(5):281–285, 1972. ISSN 0370-2693. doi: 10.1016/0370-2693(72)90246-8. URL https://doi.org/10.1016/0370-2693(72)90246-8.

[101] F. Michel. α-clustering in the ground state of ^{40}Ca. *Phys. Lett. B*, 60(3):229–231, 1976. ISSN 0370-2693. doi: 10.1016/0370-2693(76)90287-2. URL https://doi.org/10.1016/0370-2693(76)90287-2.

[102] Z.M.M. Mahmoud et al. Analysis of Alpha Scattering from α-Conjugate Nuclei. *J. Phys. Soc. Jpn.*, 88(2):024201, 2019. doi: 10.7566/JPSJ.88.024201. URL https://doi.org/10.7566/JPSJ.88.024201.

[103] H.P. Gubler et al. Large-angle alpha scattering from ^{40}Ca is not anomalous. *Phys. Lett. B*, 74(3):202–206, 1978. ISSN 0370-2693. doi: 10.1016/0370-2693(78)90553-1. URL https://doi.org/10.1016/0370-2693(78)90553-1.

[104] K.O. Behairy, Z.M.M. Mahmoud, and M. Anwar. α-particle elastic scattering from ^{12}C, ^{16}O, ^{24}Mg, and ^{28}Si. *Nucl. Phys. A*, 957:332–346, 2017. ISSN 0375-9474. doi: 10.1016/j.nuclphysa.2016.09.008. URL https://doi.org/10.1016/j.nuclphysa.2016.09.008.

[105] F. Michel, S. Ohkubo, and G. Reidemeister. Local Potential Approach to the Alpha-Nucleus Interaction and Alpha-Cluster Structure in Nuclei. *Prog. Theor. Phys. Supp.*, 132:7–72, 03 1998. ISSN 0375-9687. doi: 10.1143/PTP.132.7. URL https://doi.org/10.1143/PTP.132.7.

[106] J. Albiński and F. Michel. Quantum calculation of the barrier and internal wave contributions to light- and heavy-ion elastic scattering. *Phys. Rev. C*, 25:213–225, 1982. doi: 10.1103/PhysRevC.25.213. URL https://doi.org/10.1103/PhysRevC.25.213.

[107] F. Brau, F. Michel, and G. Reidemeister. Barrier and internal wave contributions to the quantum probability density and flux in light heavy-ion elastic scattering. *Phys. Rev. C*, 57:1386–1397, 1998. doi: 10.1103/PhysRevC.57.1386. URL https://doi.org/10.1103/PhysRevC.57.1386.

[108] G.R. Satchler and W.G. Love. Folding model potentials from realistic interactions for heavy-ion scattering. *Phys. Rep.*, 55(3):183–254, 1979. ISSN 0370-1573. doi: 10.1016/0370-1573(79)90081-4. URL https://doi.org/10.1016/0370-1573(79)90081-4.

[109] M. Lassaut and N.Vinh Mau. Low-energy nucleon-alpha scattering: Microscopic potentials and phase shifts. *Nucl. Phys. A*, 349(3):372–396, 1980. ISSN 0375-9474. doi: 10.1016/0375-9474(80)90295-X. URL https://doi.org/10.1016/0375-9474(80)90295-X.

[110] M. Lassaut and N.Vinh Mau. The imaginary part of the local potential equivalent to the non-local α-nucleus optical potential. *Nucl. Phys. A*, 391(1):118–136, 1982. ISSN 0375-9474. doi: 10.1016/0375-9474(82)90222-6. URL https://doi.org/10.1016/0375-9474(82)90222-6.

[111] D. Negrea, N. Sandulescu, and D. Gambacurta. Proton-neutron pairing and binding energies of nuclei close to the $N = Z$ line. *Phys. Rev. C*, 105:034325, 2022. doi: 10.1103/PhysRevC.105.034325. URL https://doi.org/10.1103/PhysRevC.105.034325.

[112] N. Sandulescu, D. Negrea, J. Dukelsky, and C. W. Johnson. Quartet condensation and isovector pairing correlations in $N = Z$ nuclei. *Phys. Rev. C*, 85:061303, 2012. doi: 10.1103/PhysRevC.85.061303. URL https://doi.org/10.1103/PhysRevC.85.061303.

[113] N. Sandulescu, D. Negrea, and C. W. Johnson. Four-nucleon α-type correlations and proton-neutron pairing away from the $N = Z$ line. *Phys. Rev. C*, 86:041302, 2012. doi: 10.1103/PhysRevC.86.041302. URL https://doi.org/10.1103/PhysRevC.86.041302.

[114] N. Sandulescu, D. Negrea, and D. Gambacurta. Proton–neutron pairing in N=Z nuclei: Quartetting versus pair condensation. *Phys. Lett. B*, 751:348–351, 2015. ISSN 0370-2693. doi: 10.1016/j.physletb.2015.10.063. URL https://doi.org/10.1016/j.physletb.2015.10.063.

[115] A.-G. Şerban, F. Salvat Pujol, N. Sandulescu, and P. Marevic. Anomalous large-angle α-scattering with a single-folding model based on densities derived from microscopic mean field models. ***In preparation***, 2025.

[116] P. Ring. Relativistic mean field theory in finite nuclei. *Progress in Particle and Nuclear Physics*, 37:193–263, 1996. ISSN 0146-6410. doi: 10.1016/0146-6410(96)00054-3. URL https://doi.org/10.1016/0146-6410(96)00054-3.

[117] P. Marević et al. Quadrupole and octupole collectivity and cluster structures in neon isotopes. *Phys. Rev. C*, 97:024334, 2018. doi: 10.1103/PhysRevC.97.024334. URL https://doi.org/10.1103/PhysRevC.97.024334.

[118] T. Nikšić, D. Vretenar, and P. Ring. Relativistic nuclear energy density functionals: Adjusting parameters to binding energies. *Phys. Rev. C*, 78:034318, 2008. doi: 10.1103/PhysRevC.78.034318. URL https://doi.org/10.1103/PhysRevC.78.034318.

[119] T. Duguet. Bare vs effective pairing forces: A microscopic finite-range interaction for Hartree-Fock-Bogolyubov calculations in coordinate space. *Phys. Rev. C*, 69:054317, 2004. doi: 10.1103/PhysRevC.69.054317. URL https://doi.org/10.1103/PhysRevC.69.054317.

[120] Y. Tian, Z.Y. Ma, and P. Ring. A finite range pairing force for density functional theory in superfluid nuclei. *Physics Letters B*, 676(1):44–50, 2009. ISSN 0370-2693. doi: 10.1016/j.physletb.2009.04.067. URL https://doi.org/10.1016/j.physletb.2009.04.067.

[121] J. Dechargé and D. Gogny. Hartree-Fock-Bogolyubov calculations with the $D1$ effective interaction on spherical nuclei. *Phys. Rev. C*, 21:1568–1593, 1980. doi: 10.1103/PhysRevC.21.1568. URL https://doi.org/10.1103/PhysRevC.21.1568.

[122] J.F. Berger, M. Girod, and D. Gogny. Time-dependent quantum collective dynamics applied to nuclear fission. *Comp. Phys. Comm.*, 63(1):365–374, 1991. ISSN 0010-4655. doi: 10.1016/0010-4655(91)90263-K. URL https://doi.org/10.1016/0010-4655(91)90263-K.

[123] Y.K Gambhir, P. Ring, and A. Thimet. Relativistic mean field theory for finite nuclei. *Ann. Phys.*, 198(1):132–179, 1990. ISSN 0003-4916. doi: 10.1016/0003-4916(90)90330-Q. URL https://doi.org/10.1016/0003-4916(90)90330-Q.

[124] D.L. Hill and J.A. Wheeler. Nuclear Constitution and the Interpretation of Fission Phenomena. *Phys. Rev.*, 89:1102–1145, 1953. doi: 10.1103/PhysRev.89.1102. URL https://doi.org/10.1103/PhysRev.89.1102.

[125] R.A. Serway and J.W. Jewett. *Physics for Scientists and Engineers with Modern Physics*. Brooks Cole, 9th edition, 2015. ISBN 9781133954057.

[126] M. Sambataro and N. Sandulescu. α-Like quartetting in the excited states of proton-neutron pairing Hamiltonians. *Physics Letters B*, 820:136476, 2021. ISSN 0370-2693. doi: 10.1016/j.physletb.2021.136476. URL https://doi.org/10.1016/j.physletb.2021.136476.

[127] M. Sambataro and N. Sandulescu. Intrinsic quartet states and band-like structures in $N = Z$ nuclei. *Eur. Phys. J. A*, 59:87, 2023. doi: 10.1140/epja/s10050-023-01003-w. URL https://doi.org/10.1140/epja/s10050-023-01003-w.

[128] https://uefiscdi.gov.ro/scientometrie-baze-de-date. Accessed on: Oct. 25, 2024.

[129] M. Kortelainen et al. Nuclear energy density optimization. *Phys. Rev. C*, 82:024313, 2010. doi: 10.1103/PhysRevC.82.024313. URL https://doi.org/10.1103/PhysRevC.82.024313.

[130] K. Bennaceur, P. Bonche, and J. Meyer. Mean field theories and exotic nuclei. *C. R. Phys.*, 4(4):555–570, 2003. ISSN 1631-0705. doi: https://doi.org/10.1016/S1631-0705(03)00060-4. URL https://www.sciencedirect.com/science/article/pii/S1631070503000604.

[131] T.H.R. Skyrme. CVII. The Nuclear Surface. *Philos. Mag.*, 1(11):1043–1054, 1956. doi: 10.1080/14786435608238186. URL https://doi.org/10.1080/14786435608238186.

[132] T.H.R. Skyrme. The effective nuclear potential. *Nucl. Phys.*, 9(4):615–634, 1958. ISSN 0029-5582. doi: 10.1016/0029-5582(58)90345-6. URL https://www.sciencedirect.com/science/article/pii/0029558258903456.

[133] P. Ring. Relativistic mean field theory in finite nuclei. *Prog. Part. Nucl. Phys.*, 37:193–263, 1996. ISSN 0146-6410. doi: https://doi.org/10.1016/0146-6410(96)00054-3. URL https://www.sciencedirect.com/science/article/pii/0146641096000543.

[134] Y.K. Gambhir and P. Ring. Relativistic mean-field description of the ground-state nuclear properties. *J. Phys.*, 32:389–404, 1989. ISSN 0973-7111. doi: 10.1007/BF02845972. URL https://doi.org/10.1007/BF02845972.